The Road goes ever on and on
Down from the door where it began.
Now far ahead the Road has gone,
And I must follow it, if I can,
Pursuing it with eager feet,
Until it joins some larger way
Where many paths and errands meet.
And whither then? I cannot say.

– J.R.R. Tolkien

University of Alberta

Kinetic Models for a Diesel Oxidation Catalyst

by

Stephen John Salomons ©

A thesis submitted to the Faculty of Graduate Studies and Research
in partial fulfillment of the requirements for the degree of

Doctor of Philosophy

in

Chemical Engineering

Department of Chemical and Materials Engineering

Edmonton, Alberta
Spring, 2008

Library and
Archives Canada

Published Heritage
Branch

395 Wellington Street
Ottawa ON K1A 0N4
Canada

Bibliothèque et
Archives Canada

Direction du
Patrimoine de l'édition

395, rue Wellington
Ottawa ON K1A 0N4
Canada

Your file Votre référence
ISBN: 978-0-494-45591-3
Our file Notre référence
ISBN: 978-0-494-45591-3

NOTICE:
The author has granted a non-exclusive license allowing Library and Archives Canada to reproduce, publish, archive, preserve, conserve, communicate to the public by telecommunication or on the Internet, loan, distribute and sell theses worldwide, for commercial or non-commercial purposes, in microform, paper, electronic and/or any other formats.

The author retains copyright ownership and moral rights in this thesis. Neither the thesis nor substantial extracts from it may be printed or otherwise reproduced without the author's permission.

AVIS:
L'auteur a accordé une licence non exclusive permettant à la Bibliothèque et Archives Canada de reproduire, publier, archiver, sauvegarder, conserver, transmettre au public par télécommunication ou par l'Internet, prêter, distribuer et vendre des thèses partout dans le monde, à des fins commerciales ou autres, sur support microforme, papier, électronique et/ou autres formats.

L'auteur conserve la propriété du droit d'auteur et des droits moraux qui protège cette thèse. Ni la thèse ni des extraits substantiels de celle-ci ne doivent être imprimés ou autrement reproduits sans son autorisation.

In compliance with the Canadian Privacy Act some supporting forms may have been removed from this thesis.

While these forms may be included in the document page count, their removal does not represent any loss of content from the thesis.

Conformément à la loi canadienne sur la protection de la vie privée, quelques formulaires secondaires ont été enlevés de cette thèse.

Bien que ces formulaires aient inclus dans la pagination, il n'y aura aucun contenu manquant.

Canada

Abstract

Automotive-based exhaust is a major contributor to air pollution, and legislation controls the emission of several components. Catalytic converters are used to reduce these emissions to acceptable levels. As legislation becomes more stringent, better catalysts are required, and better kinetic models can accelerate the design of these models.

This work considers the kinetics of the oxidation of CO and hydrogen on a Pt monolith diesel oxidation catalyst under lean conditions. The study of CO oxidation alone, while well documented in the literature, is a necessary step in the development of a complete model. CO oxidation is studied using both temperature ramp and concentration step experiments. These experiments are modelled and discussed.

The selectivity of the catalyst toward CO is observed during light-off experiments of CO and hydrogen mixtures. Literature models are modified to correctly model this selectivity, improving the validity of the modified model.

The hydrogen-promotion effect, whereby the presence of hydrogen promotes CO oxidation during light-off, is discussed and modelled. Experimental and numerical results are shown and compared, and modifications to the standard literature models are proposed. These modifications model the behaviour of the catalyst for mixtures of CO (up to 2000 ppm), hydrogen (up to 2000 ppm) and oxygen (6%), including the catalyst selectivity and the hydrogen promotion effect.

for Sibylle

Acknowledgements

Special Thanks,

- to Prof. Dr. R.E. Hayes, University of Alberta, whose guidance and support has been invaluable
- to Dr. Martin Votsmeier and Umicore AG & Co. KG, who supported this project both financially and with their expertise
- to Prof. H. Vogel and Dr. Alfons Drochner at the Technical University of Darmstadt, who supported this project with facilities and with their expertise
- to Felix Knoth, Wulf Hauptmann and Anke Schuler (Technical University of Darmstadt), who worked on this project and are continuing to build on this work
- to Walter David (Technical University of Darmstadt), who helped with the construction of the experimental apparatus, and without whom the experimental apparatus would perhaps not have been built
- to Bob Barton and Computing Resources in the Department of Chemical and Materials Engineering, University of Alberta, who provided research computing facilities
- to Dr. Samy Mukadi, who wrote the simualtor and assisted with simulations
- to Dr. Ralph Scheinbein, who helped with proofreading

Table of Contents

1 **Introduction** 1
1.1 Automotive-Based Emissions 1
1.2 Current Legislated Limits on Automotive Exhaust 2
1.3 Automotive Catalysis 5
1.4 Kinetic Models 6
1.5 Contributions of the Current Work 7
1.6 Layout of the Thesis 8

2 **Experimental Apparatus** 9
2.1 Overview of the Experimental Apparatus 9
2.2 Gas Mixing Unit 9
2.2.1 Gas Sources 10
2.2.2 Valves 13
2.2.3 Flow controllers 13
2.2.4 Water Evaporator 13
2.3 Heater 14
2.4 Reactor 14
2.4.1 Monolith Core 15
2.5 Analyzers 16
2.6 Other Sensors 18
2.7 Electronics 19
2.8 Signal Stability and Noise 20

2.9 LabVIEW Control System 21
2.9.1 LabVIEW Fundamentals 21
2.9.2 Queueing System 22
2.10 SQL Measurement Database 23
2.11 Safety System 24
2.11.1 Watchdog 24
2.11.2 Computer Checks 25
2.12 Post-Processing of Results 25
2.13 Types of Experiments Performed 26
2.13.1 Temperature Programmed Reactions or Light-Off Curves 26
2.13.2 Concentration Programmed Reactions 27
2.14 Summary 29

3 Modelling 30
3.1 Introduction to Computer Modelling 30
3.2 Kinetic Modelling 31
3.3 Classical LHHW-Type Model 31
3.3.1 CO Oxidation 31
3.4 Mechanistic Model Based on Langmuir-Hinschelwood Assumptions 33
3.4.1 CO Oxidation 33
3.4.2 H_2 and H_2O Adsorption and Desorption 34
3.4.3 H_2 and H_2O Reactions 36
3.5 Langmuir-Hinschelwood plus Eley-Rideal Model 38
3.5.1 CO Oxidation 38
3.6 Simulator 40
3.7 Objective Function 41
3.8 Solving Differential Equations 42
3.8.1 Initial Conditions 42
3.9 Input Files and Parameters 42
3.9.1 Reactor Physics 42
3.9.2 Mechanisms 43
3.9.3 Washcoat 45
3.9.4 Numerical Solver Parameters 45
3.9.5 Reactor Conditions 45
3.9.6 Simulator Keywords 46
3.10 Simulation Output and Post-Processing 46
3.11 Comparisons With Other Catalysts Made Using Other Preparation Methods 47

4 CO Oxidation over Platinum 48
4.1 CO Oxidation on Platinum Catalysts 48
4.1.1 Platinum Catalysts 48
4.1.2 Structured Catalysts 48
4.1.3 Models of CO Oxidation on Pt Catalysts 49

4.1.4 Effect of Catalyst Preparation . . . 49
4.1.5 Deactivation . . . 49
4.1.6 Adsorption of Species onto the Active Surface . . . 50
4.1.7 Surface Mass Transfer . . . 53
4.1.8 Oxidation of CO on Pt . . . 54
4.1.9 Unsteady Behaviour . . . 54
4.2 Experimental Results - CO Light-Off Curves . . . 59
4.2.1 Inlet Gas Temperature Ramp . . . 59
4.2.2 Light-off At Various CO Concentrations . . . 61
4.2.3 Moving Extinction Fronts . . . 65
4.3 CO Step Functions . . . 68
4.3.1 Reproducibility of Results for CO Step Functions . . . 68
4.3.2 Experimental Results - CO Steps . . . 68
4.4 Comparison of Experimental and Simulation Results for CO Light-off . . . 77
4.4.1 Optimization of the Loading Factor . . . 77
4.4.2 CO Light Offs . . . 80
4.4.3 Effect of the Sticking Coefficients . . . 85
4.4.4 Effect of Modelling the Washcoat . . . 87
4.4.5 Initial Parameter Optimization . . . 87
4.5 Modelling CO Concentration Steps . . . 90
4.5.1 Simulating Step Functions with the Subsurface Oxygen Model . . . 93
4.5.2 Simulating Step Functions with the AB Model . . . 100
4.5.3 Simulating Step Functions with the classical LH Model and Irreversible Oxygen . . . 100
4.5.4 Simulating Step Functions with the Compressed Oxygen Model . . . 104
4.5.5 Simulating Step Functions with the Compressed Oxygen Model and Oxidized Platinum . . . 110
4.5.6 Factors Influencing the Steady-State Conversion . . . 110
4.5.7 Factors Influencing the Peak Conversion . . . 112
4.5.8 Carbon Deposition . . . 114
4.5.9 Effect of Reactor Length . . . 120
4.5.10 Limited Surface Coverage . . . 121
4.6 Summary . . . 126
4.6.1 CO Light-Off Curves . . . 126
4.6.2 CO Concentration Steps . . . 126
4.7 Requirements for an Acceptable Model . . . 126
4.8 Future Work . . . 127

5 CO+H_2 Oxidation **129**
5.1 CO+H_2 Literature Review . . . 129
5.1.1 Hydrogen on the Pt Surface . . . 129
5.1.2 CO and Hydrogen on the Pt Surface (no reaction) . . . 131
5.1.3 Oxidation of Hydrogen . . . 131

5.1.4 Water Gas Shift 133
5.2 $CO+H_2$ - Selectivity 134
5.2.1 Selectivity of Pt Catalysts Towards Oxidation of Carbon Monoxide . 134
5.3 Experimental Light-Off Curve 135
5.3.1 1000 ppm CO and 500 ppm H_2 136
5.4 Selectivity and Order of Ignition 140
5.4.1 Rate of Reaction of First Hydrogen Oxidation Step: O^*+H^* 141
5.5 Conclusions on Catalyst Selectivity 148
5.6 Hydrogen Promotion Effect 149
5.7 The Oxidation of Carbon Monoxide and Hydrogen 149
5.8 $CO + H_2$ Experimental Light-Off Curves 152
5.8.1 $CO + H_2$ Steps 153
5.8.2 Mechanism 157
5.8.3 Modelling $CO+H_2$ Light-Off 159
5.9 Hydrogen Promotion Of CO Oxidation 159
5.9.1 Role of Adiabatic Temperature Rise 159
5.9.2 CO Desorption Dependence on Gas-Phase Hydrogen 161
5.9.3 The Limit of Hydrogen Promotion 165
5.9.4 Hydrogen Promotion and Selectivity 165
5.10 Summary of $CO+H_2$ 181

6 Summary and Conclusions **182**
6.1 Conclusions 182
6.2 Future Work 184

A Basic Equations **185**
A.1 Heat and Mass Transfer 185
A.1.1 Gas Hourly Space Velocity 185
A.1.2 Reynolds Number 185
A.1.3 Prandtl Number 185
A.1.4 Peclet Number 186
A.2 Mass Transfer 186
A.2.1 Knudson Diffusion 186
A.2.2 Fuller Equation 186
A.2.3 Effective Diffusivity 187
A.2.4 Effective Diffusion 187
A.3 Selectivity and Conversion 187
A.3.1 Conversion 187
A.3.2 Selectivity 188
A.4 Dew Point 188
A.4.1 Antoine Equation 189
A.5 Adiabatic Temperature Rise 190

B Kinetic Expressions **192**
- B.1 Eindhoven Approach 192
  - B.1.1 Arrhenius Equation 193
  - B.1.2 Elovich Equation 193
  - B.1.3 Source Term - Eindhoven 194
  - B.1.4 Steps to Calculate Eindhoven Source Terms 194
- B.2 DETCHEM Approach 194
  - B.2.1 Species Concentration 195
  - B.2.2 Thermodynamic Equilibrium 195
  - B.2.3 Calculation of the Rate Constant 196
  - B.2.4 Source Term - DETCHEM 196
  - B.2.5 Steps for Calculating DETCHEM source terms 197
- B.3 Bimolecular Surface Reaction Rate 197
- B.4 Unimolecular Surface Reaction Rate Example 199
- B.5 Sticking Coefficients 201
- B.6 Unimolecular Adsorption Rate Example 202
- B.7 Bimolecular Adsorption Rate Example 204

C Reaction Mechanisms **206**
- C.1 Classical LHHW-Type Model 206
  - C.1.1 CO Oxidation 206
- C.2 Mechanistic Model Based on Langmuir-Hinschelwood Assumptions 207
  - C.2.1 CO Oxidation 208
  - C.2.2 H_2 and H_2O Adsorption and Desorption 209
  - C.2.3 H_2 and H_2O Reactions 211
- C.3 Langmuir-Hinschelwood plus Eley-Rideal Model 211
  - C.3.1 CO Oxidation 211
- C.4 Strong and Weakly Adsorbed Oxygen Mechanism 216
- C.5 Multiple Binding Sites: A and B-Type Sites 216
- C.6 Subsurface Oxygen Sub-Mechanism 220
- C.7 Compressed Oxygen Sub-Mechanism 221
- C.8 Vlachos Mechanism for H_2 + CO Oxidation 222
  - C.8.1 Hydrogen Oxidation on Pt 222
- C.9 CO-H 224
- C.10 Carbon Deposition 225

D Simulator Input Files and Parameters **226**
- D.1 Gas Properties 226
- D.2 Site Species 227
- D.3 Surface Species Properties 228
- D.4 Solid Material Properties 228
- D.5 Mechanisms 229
  - D.5.1 Surface Reaction 230

D.6 Washcoat . . . 230
D.7 Numerical Solver Parameters . . . 230
D.8 Reactor Conditions . . . 231
  D.8.1 Initial Temperature and Gas-Phase Concentrations in the Reactor . 231
  D.8.2 Initial Surface Concentrations . . . 231
  D.8.3 Inlet Concentrations over Time . . . 231
D.9 Simulator Keywords . . . 232

E Staging Queues Software **233**
E.1 Introduction to LabVIEW . . . 233
E.2 User Interface . . . 233
E.3 Communication with Laboratory Equipment . . . 234
E.4 Queueing System . . . 234
E.5 Parallel Routines . . . 234
E.6 Input Scriptfiles . . . 235
  E.6.1 Global Operational Parameters . . . 235
E.7 Output Files . . . 235
E.8 Basic Queueing Script Commands . . . 236

F Parameters Summary **242**

G Experiments Performed **246**

References **249**

List of Tables

1.1 Typical Diesel Emissions 3
1.2 EURO Regulations 3
1.3 Passenger vehicle exhaust classification bins 4
1.4 Fleet Average NOx Limits 4
1.5 California Regulations 5

2.1 Gas Sources and Associated Purities 13
2.2 Thermocouple locations 17
2.3 Measurement Ranges of Analytic Equipment 19

3.1 Voltz Model Parameters 32
3.2 LH Mechanism Parameters - CO Oxidation 35
3.3 LH Mechanism Parameters - H_2 Oxidation 37
3.4 LH+ER Mechanism Parameters - CO Oxidation 40

4.1 CO Desorption Values 52
4.2 Surface Phases during Oscillations in CO Oxidation 56
4.3 Experimental CO Light-Off and Light-Out Temperatures 63
4.4 Classical LH Simulation CO Light-Off and Light-Out Temperatures 86
4.5 Effect of Oxygen and CO Sticking Coefficients 86
4.6 Effect of the Washcoat 87
4.7 Optimizing Parameters 88
4.8 Values used to study Boudouard equation. 120
4.9 Surface coverage limits 125

5.1 Sticking Coefficients 130
5.2 Experimental CO Light-Off and Light-Out Temperatures in the presence of Hydrogen 136
5.3 Literature Values for O^*+H^* 146
5.4 Integrated CO Steps 157

5.5 Effect of Exothermicity 161
5.6 Light-Off Temperatures vary with dEa/H of CO desorption 162
5.7 Effect of CO-H Submechanism at 1000 ppm CO 163
5.8 Effect of CO-H Submechanism at 2000 ppm CO 164
5.9 Effect of Ea_{H+OH} on CO-H Selectivity 166

B.1 Differences between Eindhoven and DETCHEM methods 195
B.2 Parameters used for example surface reaction 198
B.3 Parameters used for example surface reaction 200
B.4 Ideal Gas Constant 203
B.5 Parameters used for Adsorption Example 203
B.6 Parameters used for Adsorption Example 2 205

C.1 Voltz Model Parameters 207
C.2 LH Mechanism Parameters - CO Oxidation 210
C.3 LH Mechanism Parameters - H_2 Oxidation 212
C.4 LH+ER Mechanism Parameters - CO Oxidation 215
C.5 Multiple Oxygen Sites - CO Oxidation 219
C.6 Subsurface Oxygen Parameters - CO Oxidation 220
C.7 Compressed Oxygen Parameters - CO Oxidation 222
C.8 Vlachos Model Parameters 223
C.9 CO-H Submechanism Parameters 224

D.1 Gas Phase Heat Capacity 227
D.2 Gas Phase Properties 227
D.3 Surface Species Properties 228
D.4 Washcoat and Solid Material Physical Properties 229
D.5 Washcoat and Solid Material Physical Properties 229

F.1 Parameter Set 243
F.2 Carbon Deposition Parameter Set 244
F.3 Compressed Oxygen Parameters 244
F.4 CO-H_2 coupling 244
F.5 Boudouard Parameters 244
F.6 Platinum Oxidation Parameters 245

G.1 CO Light-Off Experiments Performed 247
G.2 CO Concentration Step Experiments Performed 247
G.3 CO + H_2O Light-Off Experiments Performed 248
G.4 CO + H_2 Light-Off Experiments Performed 248
G.5 CO + H_2 Concentration Step Experiments Performed 248

List of Figures

2.1 Experimental Apparatus (simplified) 10
2.2 Experimental Apparatus (photo) 11
2.3 Experimental Apparatus Flowsheet 12
2.4 Re and Pe in open tube 15
2.5 Re and Pe in monolith channel 16
2.6 Thermocouple Placement 17
2.7 Monolith support material 18
2.8 Electrical System (simplified) 20
2.9 Control System 21
2.10 Reporting value code 23
2.11 Sample Light-Off and Light-Out Points 28

4.1 Typical Feed Temperature 60
4.2 Typical Feed Temperature 61
4.3 Standard CO Light-Off Curves 62
4.4 CO and O covered Surfaces 65
4.5 Temperature profile during extinction 66
4.6 1000 ppm CO Step at 391 K 71
4.7 CO Step-Up Functions, 1000 ppm, 391 K 72
4.8 Reproducibility of 1000 ppm CO Step Functions 73
4.9 500 ppm CO Step Down at 373 K 74
4.10 500 ppm CO Step Up at 373 K 75
4.11 1000 ppm CO Step Up Temperature Profile 76
4.12 Sum of Δ T Residuals 78
4.13 Sum of LSQ 79
4.14 Sum of Weighted LSQ 80
4.15 Effect of Pt Loading Factor 81
4.16 CO Light-Off Curves Simulated with Global Model 82
4.17 CO Light-Off Voltz Sims 83

4.18 CO Light-Off LH+ER Sims 84
4.19 CO Light-Off Curves Simulated with LH Model 85
4.20 Effect of k_{CO+O} 89
4.21 CO Step using Voltz Kinetics 91
4.22 1000 ppm CO Step - LH Model 94
4.23 1000 ppm CO Step - LH Model 95
4.24 500 ppm CO step - subsurface oxygen model 96
4.25 1000 ppm CO step - subsurface oxygen model 97
4.26 500 ppm CO step - subsurface oxygen model 98
4.27 1000 ppm CO step - subsurface oxygen model 99
4.28 1000 ppm CO Step Up at 383 K, using AB model 101
4.29 1000 ppm CO Step Down at 383 K, using AB model 102
4.30 Simulation of CO step with classical LH 103
4.31 500 ppm CO step - compressed oxygen model 107
4.32 1000 ppm CO Step - LH Mechanism 108
4.33 Comparison of compressed oxygen model for 1500 ppm CO light off 109
4.34 Effect of CO Desorption on CO Step 111
4.35 Effect of CO Adsorption on CO Step 112
4.36 Effect of Oxygen Adsorption on CO Step 113
4.37 Effect of OO reaction on CO Step 114
4.38 CO Light-Off without oxygen 116
4.39 CO Step Functions without Oxygen 118
4.40 CO Step Function 119
4.41 Effect of Boudouard Reaction 121
4.42 Effect of Reactor Length 122
4.43 Modified sticking coefficients 124

5.1 1000 ppm CO + H_2 Light-Off Curves 137
5.2 2000 ppm CO + H_2 Light-Off Curves 138
5.3 Experimental CO+H_2 Light-Off 139
5.4 CO step in H_2 at room temperature 142
5.4 Effect of Ea for first H oxidation step 143
5.5 Experimental Light-off: 1000 ppm CO + 500ppm H_2 145
5.6 Comparison of Selectivity in Experiment and Simulation 147
5.7 Simulated CO Light-off with and without H_2 149
5.8 Simulated CO Light-off with and without H_2 - Exotherm 150
5.9 CO-H Desorption 152
5.10 Effect of H_2 on CO Light-Off 153
5.11 Effect of H_2 on CO Light-Off 154
5.12 Effect of H_2 on CO Light-Off 155
5.13 H_2 steps at constant CO concentration 168
5.14 500 ppm CO step up in 100 ppm H_2 169
5.15 500 ppm CO step down in 100 ppm H_2 170

5.16 CO Steps in the presence of hydrogen 171
5.17 CO-H mechanism: 1000 ppm CO and 500 ppm H_2 172
5.18 CO-H mechanism: 1000 ppm CO and 2000 ppm H_2 173
5.19 CO-H mechanism: 1000 ppm CO and various H_2 174
5.20 CO-H mechanism: 1000 ppm CO LO Temperatures 175
5.21 CO-H mechanism: 2000 ppm CO LO Temperatures 176
5.22 Limits of Hydrogen Promotion 177
5.23 Experimental light-off: 2000 ppm CO and 2000 ppm H_2 178
5.24 Influence of Ea_{O*+H*} on CO promotion and selectivity 179
5.25 Promoted and Selective Simulation 180

A.1 Adiabatic Temperature Rise 191

List of Nomenclature

Latin Letters

A	reactant	
a	stoichiometric coefficent of associated reactant	dimensionless
a	heat capacity coefficient	$J \cdot mol^{-1} \cdot K^{-1}$
$A_{lowcoverage}$	value of rate factor at low coverage	dimensionless
A_0	pre-exponential factor	$mol_i\ mol_{cat}^{-1}\ s^{-1}$
a_{cat}	specific surface area of the catalyst	$m_{NM}^2 \cdot m_{cat}^{-3}$
$B_{highcoverage}$	value of rate factor at high coverage	dimensionless
b	heat capacity coefficient	$J \cdot mol^{-1} \cdot K^{-2}$
C_{steep}	steepness of the transition between values of A and B	dimensionless
$C_{ps,1}$	solid heat capacity first coefficient	$J \cdot kg^{-1} \cdot K^{-1}$
C_i	concentration of component i in gas phase	
c	heat capacity coefficient	$J \cdot mol^{-1} \cdot K^{-3}$
C_p	Heat capacity	$J \cdot mol^{-1} \cdot K^{-1}$
$C_{ps,2}$	solid heat capacity first coefficient	$J \cdot kg^{-1} \cdot K^{-2}$
$C_{ps,3}$	solid heat capacity first coefficient	$J \cdot kg^{-1} \cdot K^{-3}$

d	heat capacity coefficient	$J\cdot kg^{-1}\cdot K^{-4}$
$D_{A,eff}$	Effective diffusion of component A through a pore	$m^2\cdot s^{-1}$
D_{AB}	Diffusivity of component A through B	$m^2\cdot s^{-1}$
$D_{inflectionpoint}$	inflection point where transition between A and B occurs	fractional surface coverage
D_{KA}	Knudsen Diffusivity	$m^2\cdot s^{-1}$
D'_{NA}	Effective diffusivity of component A	$m^2\cdot s^{-1}$
e	heat capacity coefficient	$J\cdot kg^{-1}\cdot K^{-5}$
$E_{a,i}$	Activation Energy of reaction i	$J\cdot mol^{-1}$
F	flowrate	$mol\cdot s^{-1}$
Factor	Rate factor used for modifying sticking coefficients	dimensionless
GHSV	Gas Hourly Space Velocity	h^{-1}
H	Humidity	$g_{H2O}\cdot g_{dryair}^{-1}$
H_S	Saturation Humidity	$g_{H2O}\cdot g_{dryair}^{-1}$
H_P	Percent Humidity	%
k	reaction rate constant	$mol_i\ mol_{cat}^{-1}\ s^{-1}$
$k_{s,1}$	thermal conductivity first coefficient	$W\cdot m^{-2}\cdot K^{-1}$
$k_{s,2}$	thermal conductivity second coefficient	$W\cdot m^{-2}\cdot K^{-2}$
$k_{s,3}$	thermal conductivity third coefficient	$W\cdot m^{-2}\cdot K^{-3}$
k_s	thermal conductivity	$W\cdot m^{-2}\cdot K^{-1}$
K_{Eq}	thermodynamic equilibrium constant	
L	characteristic length	m
L_A	concentration of active sites per unit surface area	$mol_{NM}\cdot m_{cat}^{-3}$
L_t	density of active sites per unit surface area	$mol_{NM}\cdot m_{NM}^{-2}$
M_i	molar mass of component i	$g\cdot mol^{-1}$

N_i	flux of component i	$mol\cdot m^{-2}s^{-1}$
n	reaction order	dimensionless
Pr	Prandtl number	dimensionless
P	product	
p	stoichiometric coefficent of associated product	dimensionless
Pe	Peclet number	dimensionless
P_{abs}	Pressure, absolute	atm
P_{atm}	atmospheric pressure	kPa
P_{vap}	vapour pressure	bar
P_{AS}	partial pressure of water in air at saturation	kPa
$\bar{r}$	average pore radius	m
R	Ideal Gas Constant	$8.314\ J\cdot mol^{-1}\cdot K^{-1}$
r	rate of formation of product	$mol\cdot s^{-1}$ or $mol_A\cdot m_{NM}^{-2}\cdot s^{-1}$
Re	Reynolds number	dimensionless
RH	Relative Humidity	%
S_0	modified sticking coefficient	dimensionless
s	source term	$mol_A\cdot m_{cat}^{-3}\cdot s^{-1}$
S	sticking coefficent	dimensionless
T	Temperature	K
T_0	Reference Temperature	300 K
V	fluid velocity	$m\cdot s^{-1}$
X	conversion	dimensionless
$x_{A,av}$	average molar fraction of component A	dimensionless
x_i	molar fraction of gas component i	dimensionless fraction

Greek Letters

β	Temperature exponent	dimensionless
γ	Surface site density	$\mathrm{mol}_{NM} \cdot m_{NM}^{-2}$
ϵ	Void fraction	dimensionless
ν	Diffusion volume	$cm^3 \cdot mol^{-1}$
ζ_i	Fractional surface coverage of component i on $\star$	fraction of monolayer
θ_i	Fractional surface coverage of component i	fraction of monolayer
μ	Reaction order correction	dimensionless
τ	Tortuosity	dimensionless

Subscripts

AB	denotes usage of multiple binding sites model. See section C.5.
Bou	denotes usage of strong and weakly adsorbed oxygen model. See section C.4.
cLH	denotes classical Langmuir-Hinschelwood model. See section C.2.
NM	Nobel Metal
$subsO$	denotes usage of subsurface oxygen model. See section C.6.
V	denotes usage of global model. See section C.1.

Superscripts

b	designates reverse reaction, as in k^b
f	designates forward reaction, as in k^f
$*$	Platinum surface site
$\bullet$	Pseudo-site for hydrogen (see section C.9)
$\dagger$	Subsurface site (see section C.6)
$\star$	Alternate Pt surface site (see section C.5)

List of Acronyms

AES Atomic Emission Specstroscopy

CLD Chemiluminescence Detector

CPSI Cells Per Square Inch of a monolith (in^{-2})

ER Eley-Rideal

ESD Electron Stimulated Desorption

FID Flame Ionization Detector

FTIR Fourier-Transform InfraRed

FTP Federal Test Procedure

GHSV Gas Hourly Space Velocity

GMRES Generalized Minimal Residual Method

LEV Low Emissions Vehicle

LH Langmuir-Hinshelwood

MFC Mass Flow Controller

MLT MuLTi-component and multi-method analyzer

OFA Open Frontal Area of a monolith (fraction)

OLE Object Linking and Embedding

OPC OLE for Process Control

NMOG Non-Methane Organic Gases

PM Particulate Matter

PROX PReferential OXidation

PZEV Partial Zero Emissions Vehicle

STM Scanning Tunnel Microscopy

SQL Structured Query Language

SULEV Super Ultra Low Emissions Vehicle

SV Space Velocity (h^{-1})

TPR Temperature Programmed Reaction

TPD Temperature Programmed Desorption

TFID Thermo Flame Ionization Detector

TLEV Transitional Low Emissions Vehicle

ULEV Ultra Low Emissions Vehicle

UHV Ultra High Vacuum

USI Umicore Simulation Interface

ZEV Zero Emissions Vehicle

1

Introduction

1.1 Automotive-Based Emissions

Transportation-based air pollution is a growing problem, as the number of automobiles globally on the road has increased from 40 to 700 million over the last 60 years [1, 2]. On-road automobile engines account for 59 % of Canada's CO emissions and 53 % of NO_x emissions [3].

As many as 40-60 % of all new Western-European passenger automobiles sold are diesel powered, compared to 4-7 % in Canada [4, 5]. Market share of diesel passenger cars is growing, reflecting recent increases in fuel prices and decreases in manufacturing costs, and the global market share of diesel passenger vehicles is expected to double in the next 10 years [6].

Diesel engine exhaust contains many different components (see Table 1.1), some of which are pollutants regulated by legislation [7]. However, with both the market share and absolute number of diesel passengers cars growing, these regulations are becoming more stringent.

As part of an effort to combat this pollutant problem, governments have established emission regulations that define the maximum allowed emissions for particular classes of vehicles. Regulations for gasoline-powered vehicles are becoming very strict, and regulations for diesel-powered vehicles are following.

The production and use of cleaner alternative fuels, especially hydrogen, have the potential to reduce emissions [8, 9, 10]; however they do not have the market share that is currently held by petroleum-based internal combustion engines (gasoline and diesel). Significant changes to the design of modern automobiles (hybrid or electric cars) will require time to reduce in price and achieve significant market share. Currently, and in the near-future (20-30 years), internal-combustion engines fueled by gasoline or diesel are likely to remain the most important means of transport [11], and to reduce transportation-based emissions, this design must be targeted. Work has also been done to modify diesel fuel into a lower emissions fuel by reducing the mono-aromatic content [12], which lowers the NO_x and particulate emissions compared to standard diesel fuel. Biodiesel shows promise to reduce CO, hydrocarbon and particulate emissions [13], as well as a potentially more sustainable ultimate carbon balance [14], however, current production levels of biodiesel cannot meet a significant portion of the diesel demand, and will not be a major fuel source in the short term until production costs are brought down [15]. Biodiesel will likely not make a significant volume contribution in the near future. Dimethyl ether is another potential future fuel, but current production levels are not comparable to traditional gasoline and diesel fuel production. In addition, even with "clean" or biofuels, additional treatment of the exhaust gas is still required to meet legislative limits.

Although much is being done to improve combustion engines [16], the dominant method for reducing transportation-based emissions (without affecting demand economics) is through the use of catalytic converters. Meeting strict legislative requirements (such as California Super Ultra Low Emissions Vehicle (SULEV) requirements) many be attained through advancements in current designs [17] without radical departures. Catalytic aftertreatment of exhaust gases shows much potential in meeting legislated limits [18, 19, 20, 21, 22, 23, 24]. Much has already been done to meet limits in the past quarter century since automotive catalysts were first introduced [1, 25, 26, 27, 28, 29], but there are still many challenges to meet to meet future emission limits [30].

Table 1.1 shows the typical composition of diesel emissions. The main pollutants are hydrocarbons and carbon monoxide (both resulting from incomplete combustion), and NO_x, a product of nitrogen reacting with oxygen at the high temperatures in the engine during the combustion process.

1.2 Current Legislated Limits on Automotive Exhaust

Legislation requires that all vehicles sold in an economic region meet the allowable emission standards. In the EU, these regulations take the form of the EURO II, III, IV and soon to be V standards (see Table 1.2). These standards represent the maximum allowable emissions for a light-duty diesel engine, and are increasingly stringent. In early versions of the Euro specification, there was a distinction between direct and indirect injection methods, however, that distinction was not made after 2000.

Exhaust Component	Typical Range Diesel [1]	Typical Range Gasoline[20]	Units
O_2	10-15	0.5	%
CO_2	7	10	%
H_2O	1.4 - 7	10	%
CO	300 - 1200	5000	ppm
NO_x	350 - 1000	900	ppm
HC	50 - 330	350	ppm
H_2	100 - 400	1700	ppm
SO_x	10 - 100		ppm
Particulate	65		mg m^{-3}
N_2	rest	rest	
Temperature	r.t. - 650		°C
Pressure	atmospheric	atmospheric	
GHSV	30 000 - 100 000		h^{-1}
λ (A/F)	$\sim$ 1.8 (26 by mass)	$\sim$ 1 (14.6 by mass)	

Table 1.1: Typical Diesel Emissions [1]. The Air-to-Fuel ratio (λ) is typically expressed as a molar ratio, with stoichiometric composition being $\lambda = 1$. The mass ratio at equimolar stoichiometry is ~ 14.6. When the molar ratio is 1.8, the mass ratio is ~ 26.

Year		CO g/km	HC + NO_x g/km	NO_x g/km	Particulates g/km
1996	(Euro II, IDI[a])	1.00	0.70		0.08
1996	(Euro II, DI[b])	1.00	0.90		0.10
2000	(Euro III)	0.64	0.56	0.50	0.05
2005	(Euro IV)	0.50	0.30	0.25	0.025
2009 [c]	(Euro V)	0.50	0.23	0.18	0.005
2014 [c]	(Euro VI)	0.50	0.17	0.08	0.005

---

[a] indirect injection

[b] direct injection

[c] proposed

Table 1.2: EURO regulations for a light-duty diesel vehicle. From [31, 32, 33, 34].

Bin	NO_x	NMOG	CO	Formaldehyde	PM
11	0.559	0.1739	4.5333	0.0199	0.0745
10	0.373	0.0969 / 0.01428	2.61 / 3.97	0.0112 / 0.0168	0.0497
9	0.186	0.0559 / 0.1118	2.6082	0.0112	0.0373
8	0.124	0.0776 / 0.0969	2.6082	0.0112	0.0124
7	0.093	0.0559	2.6082	0.0112	0.0124
6	0.062	0.0559	2.6082	0.0112	0.0062
5	0.043	0.0559	2.6082	0.0112	0.0062
4	0.025	0.0435	1.3041	0.0068	0.0062
3	0.019	0.0342	1.3041	0.0068	0.0062
2	0.012	0.0062	1.3041	0.0025	0.0062
1	0.000	0.0000	0.0000	0.0000	0.0000

Table 1.3: Passenger vehicle exhaust classification bins ($g \cdot km^{-1}$). From [7, 35].

Model Year	Light Duty Vehicles	Heavy Duty Vehicles
2004	0.25	0.53
2005	0.19	0.43
2006	0.13	0.33
2007	0.07	0.20
2008	0.07	0.14
2009 and later	0.07	0.07

Table 1.4: Fleet average NOx requirements, ($g \cdot mile^{-1}$). From [35, 36].

Due to the interdependence of the Canadian and American markets, legislators have moved to harmonize laws. Canadian limits are split into multiple bins (see Table 1.3), emphasizing fleet averages instead of individual vehicle performance [7]. Each vehicle sold in North America is placed in a bin by the manufacturer based on the vehicle's performance during emissions testing. The sales-weighted average of all vehicles sold by the manufacturer must then meet the fleet averages such as the NO_x requirements in Table 1.4.

Automobiles produced in 2009 must be classified into bins 1-8, as bins 9 and 10 are not available to light-duty passenger cars after 2006 and after 2008 for heavy-duty vehicles. The same emission limits apply to all vehicles, irrespective of the fuel. The regulations are in effect for the full useful life of a vehicle. The useful life of a light-duty vehicle is 10 years or 192 000 km (120 000 miles), and the useful life of a medium- or heavy-duty vehicle is defined as 11 years or 192 000 km (120 000 miles). The emissions of NO_x, Non-Methane Organic Gases (NMOG), CO, formaldehyde and Particulate Matter (PM) are considered.

	50,000 miles/5 years				
	NMOG g/mi	CO g/mi	NOx g/mi	PM g/mi	HCHO g/mi
LEV	0.075	3.4	0.05	-	0.015
ULEV	0.040	1.7	0.05	-	0.008
SULEV	-	-	-	-	-

	120,000 miles/11 years				
	NMOG g/mi	CO g/mi	NOx g/mi	PM g/mi	HCHO g/mi
LEV	0.090	4.2	0.07	0.01	0.018
ULEV	0.055	2.1	0.07	0.01	0.011
SULEV	0.010	1.0	0.02	0.01	0.004

Table 1.5: California regulations for a light-duty diesel vehicle. From [37].

California has its own vehicle regulations (see Table 1.5), and these regulations include limits after extended travel in a vehicle, regulating performance out to 11 years or 120 000 miles. As catalysts can slowly poison or foul over time, meeting Californian regulations requires careful attention to the fouling and deactivation mechanisms in a catalyst over time.

1.3 Automotive Catalysis

A catalytic converter is placed in the exhaust system after the engine.When an engine starts from a cold state, the exhaust manifold and catalytic converter are typically also cold. As the reactions on the catalyst in a cold state are kinetically limited, the conversion of the gases of interest is typically incomplete. As the engine runs, hot exhaust gas warms the exhaust manifold and catalytic converter.

As most of the harmful products from exhaust gas are released before the catalyst has had a chance to reach a state where high-conversion of the gases occurs (above the light-off point), allowing the catalyst to warm up quickly is important in reaching cold-start emission regulations and reducing overall emissions. The light-off point is defined as the inlet temperature at which conversion exceeds 50 %. It is a strong function of operating conditions, especially temperature ramp rate.

When a catalyst is placed closer to the engine, the thermal mass of the exhaust system is lowered, and heat losses between the engine and catalytic converter are minimized. However, if a catalyst is placed too close to the engine, the exhaust gas temperature is relatively high, and the catalyst may reach temperatures where sintering (see subsection 4.1.5) is significant. Thus, the catalyst may prematurely deactivate and have a shorter useful life. The durability and useful life of a catalyst are specified in environmental regulations, and are becoming more stringent. SULEV regulations require lower emission levels at 120 000 miles than Low Emissions Vehicle (LEV) and Ultra Low Emissions Vehicle (ULEV) required after 50 000 miles, as shown in Table 1.5. If the catalyst is placed too far back, then the heat losses in the exhaust system reduce the operating temperature of the catalyst, and light-off occurs much later.

Platinum is the most common metal used for diesel oxidation catalysis, due to its high activity. Palladium is also widely-used, but more often applied to catalytic converters for gasoline engines, which run at a lower oxygen-to-fuel ratio. Other metals have also been applied to automotive catalysis. Gold is active towards CO [38], less expensive and as it has a large available supply, it is less susceptible to supply issues [39]. However, platinum is much more active, and when a catalyst is well-prepared (with respect to optimizing catalyst coverage, dispersion, and activity and minimizing the amount of platinum used), platinum can be more cost-effective than gold. As well, platinum is typically more resistant to poisoning than gold, an important factor when considering the useful life of a catalytic converter.

1.4 Kinetic Models

Models of the reactions that occur in a catalytic converter come in many forms, depending on the underlying assumptions that have been made. Elementary models attempt to consider every significant chemical step that may occur in the catalytic converter. As these models typically include gas phase and surface reactions, mass transfer steps between the phases must also be modelled. These models are apt to better describe the catalyst behaviour over a wider range of conditions, but require more complex computer programs to solve and typically require more computing time to reach a solution. Global models make an assumption about the rate-determining step, and simplify the underlying equations, often to a single equation. While this greatly simplifies the equations that must be solved, these models run the risk of having a limited range of validity. The present work will focus on elementary models.

Voltz et al. [40] proposed a model to describe CO oxidation in the presence of oxygen, propylene and NO. This global model was based on experimental observations of a pelleted Pt-alumina catalyst using a synthetic gas mixture and a varied inlet temperature. Oh and

Cavendish [41] modelled the oxidation of CO, propene and hydrogen, using the specific reaction rate expressions developed by Voltz et al. [40] and modifying the pre-exponential factors. This model was later tested against bench engine tests [42, 43] in converter warmup tests. Koltsakis and Stamatelos [44] added an oxygen-storage submechanism to the model, assisting in modelling reactions where the ratio of oxygen to fuel is close to 1. Dubien et al. [45] used light-off experiments with CO and hydrocarbons to estimate rate parameters for a reaction model based on modified Voltz equations. Siemund et al. [46] based their global model on the work of others [47, 48], obtaining good agreement for light-off with the exception of an sensitivity around light-off and a transient state that was not modelled.

Global models [40] are still used [45, 49] in research and development to describe the reactions within a catalytic converter. However, as will be shown, a global model does not consider the surface-dependent phenomena that are critical in describing the catalyst behaviour under transient conditions. The performance of a catalyst is dependent upon the thermal and surface history of the catalyst, as well as current coverage, and in real-world operation, the inlet conditions to the catalyst are constantly changing. A global model may not predict transient responses (such as those to be discussed later) that result from concentration steps, as these responses are often dependent on the surface coverage. An elementary mechanism can consider surface composition and more complex chemical reactions, and can more reliably predict transient responses.

1.5 Contributions of the Current Work

CO oxidation on single crystals [50, 51, 52, 53, 54, 55, 56, 57, 58, 59, 60, 61, 62] has been extensively studied, however most single-crystal experiments are performed under high vacuum, or at temperatures outside the range of normal catalytic converter operation. Much work has also been done on generalized models using Federal Test Procedure (FTP) cycles [63] and engine bench experiments. As most FTP cycles are performed with complex mixtures, it is exceptionally difficult to discern between the contributions of various components. Between these two areas of research, there is a gap [64] and more work must be done to understand the surface reactions under real-world conditions.

Within this knowledge gap, this work focuses on the oxidation of CO in a diesel oxidation catalyst. Studies using controlled inlet gas temperatures and compositions in the presence and absence of hydrogen are also described. Experimental and numerical studies of the transient behaviour are discussed, with an end of improving the current literature models for use in the design and control of automotive catalytic converters.

CO oxidation has been extensively studied already, however its mechanism is still not completely understood. Most notable modelling studies [65, 66] focus almost exclusively on light-off behaviour, and light-out behaviour and concentration steps are currently neither well described nor understood. Some studies of concentration steps are available in the literature [67, 68], but these same studies are not complete, as is demonstrated. No published model can describe light-off/light-out behaviour as well as concentration step behaviour for CO and hydrogen mixtures under conditions of interest for diesel oxidation. Current models do not model the promotion effect observed when hydrogen is added to a CO mixture, and the light-off temperature is reduced.

Experimental verification of elementary models from literature is presented in this work. As CO is a significant component of transportation-based emissions, classified as a primary pollutant and most prevalent component studied in the literature, this is the component that was chosen to be the first studied. Descriptions of CO and H_2 mixtures and their interactions are also presented, modelled and described.

1.6 Layout of the Thesis

This thesis is divided into 6 chapters. The first chapter (this one) introduces the problem of automotive emissions, and steps taken to reduce those from diesel engines. Chapter 2 describes the experimental apparatus that was built to perform the necessary experiments to study diesel oxidation catalysis. Chapter 3 focuses on the development of the simulator and steps taken to model the appropriate kinetic reactions and mass transport. The oxidation of CO, experiments performed to study CO oxidation and the subsequent modelling of these experiments is discussed in chapter 4.

In chapter 5, hydrogen is added to the mixture and the interactions between H_2 and CO are experimentally observed and subsequently simulated. This chapter discusses the selectivity of the catalyst used, and introduces a new means by which hydrogen promotion of CO oxidation may be modelled. Chapter 6 summarizes this work, and restates the conclusions made.

2

Experimental Apparatus

2.1 Overview of the Experimental Apparatus

The purpose of this work is to understand and model the the oxidation of CO and CO/H_2 mixtures on a monolith reactor. To this end, the ability to study systems where the inlet gas concentration is fixed and the inlet gas temperature is transient (or vice versa) is required. This gas needs to be directed into the monolith reactor, and the outlet gas composition analyzed. All components need to be computer controlled and all essential measurements recorded. Such an experimental apparatus was built.

The exhaust gas from an engine is the inlet gas to the catalytic converter. This system may be thought of as reactors in series, where the outlet of the first reactor is controlled such that a study of the second reactor may proceed. In the present work, the engine exhaust gas is artificially created with the assistance of a gas mixing unit such that the transient response of the second reactor, a Pt/Al_2O_3-coated monolith, may be investigated.

The experimental apparatus consists of four main parts: the gas mixing unit, the heater/reactor, the analyzers, and a computer control and datalogging system. A simplified diagram of the experimental apparatus is shown in Figure 2.1, and a flow diagram is detailed in Figure 2.3. A photograph of the system is shown in Figure 2.2. The apparatus was built in the laboratories of the Technische Universität Darmstadt, in Darmstadt, Germany.

2.2 Gas Mixing Unit

The gas mixing unit is designed to control the input concentrations of all gases into the reactor. Pure gases are used, and valves and mass flow controllers control the flow rates to

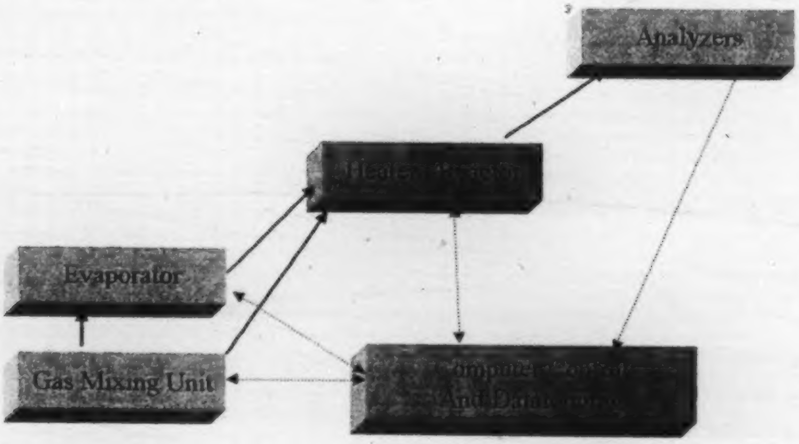

Figure 2.1: Experimental apparatus (simplified).

create the desired gas composition.

Stainless steel lines of diameter 6 mm, $\frac{1}{4}$ inch and $\frac{1}{2}$ inch, supplied by CS-Chromatographie Service GmbH., were used within the system whenever possible. Polyamide lines, supplied by Riegler & Co. KG, were used where stainless steel lines were not practical. Fittings were supplied by Swagelok and by Hoke Handelsges. mbH.

2.2.1 Gas Sources

Liquid nitrogen was purchased in bulk from Linde AG., and stored in a large storage tank for various uses across the campus. Linde AG. installed an evaporator unit next to the storage tank, capable of handling up to 10 000 $\text{L}\cdot\text{h}^{-1}$ of nitrogen gas. A direct stainless steel line between the storage tank and the laboratory was installed. This line was cleaned upon installation, and has been used as the primary nitrogen source. Linde claimed that the liquid nitrogen is of 6.0 purity (99.9999 % pure). A portable enclosed liquid nitrogen Dewar was also available on hand, should the need arise. Before the nitrogen line was installed, this portable tank was the primary nitrogen source, however, the bulk of the experiments

Figure 2.2: Photograph of the experimental apparatus. From left to right is the gas mixing unit, water evaporator, oven, insulated reactor and analyzers.

presented here were performed using the direct line. This portable storage tank was filled from the same large storage tank, and was flushed clean with every fill.

Gas bottles of pure and calibration gases were purchased from Messer Greisheim GmbH.. Gas purities are detailed in Table 2.1. All bottles, with the exception of NO and calibration gas, were stored and placed into service in an outdoor shed. This shed allowed adequate ventilation in the unlikely event of a gas leak. Stainless steel tubes of diameter $\frac{1}{4}$ inch (for CO, H_2, C_3H_8 and C_3H_6) and 6 mm (for O_2 and CO_2) were installed and cleaned to allow direct usage of these gases. A pressure reducer, supplied by DruVa GmbH & Co. KG, for each gas was placed at the bottle source, and another pressure reducer was placed in the laboratory, directly before entering the gas mixing unit. The pressure of a typical gas after the first pressure reducer was 20 bar, and gases entered the gas mixing unit at approximately 3.5 bar.

Due to outdoor temperatures (NO tends to adsorb to the stainless steel walls below 10°C, and calibration certificates were not valid under 10°C), NO and calibration gases, when in use, were placed in a ventilated gas safety cabinet inside the laboratory. Calibration gas

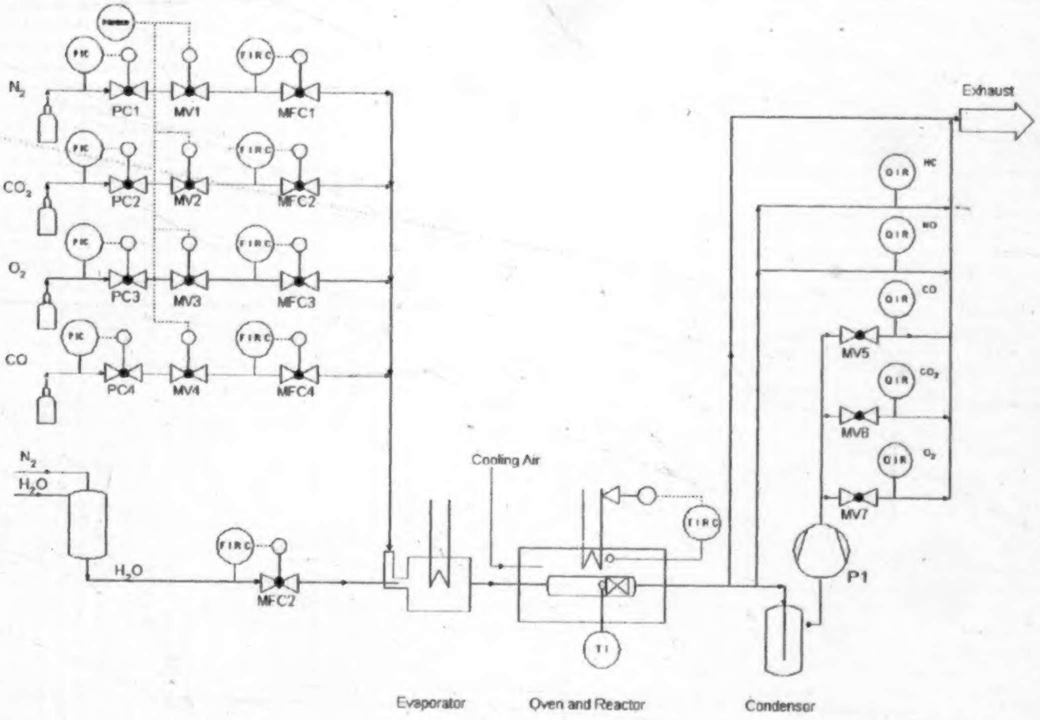
PIC
FIRC
N_2
CO_2
O_2
CO
PC1
MV1
MFC1
PC2
MV2
MFC2
PC3
MV3
MFC3
PC4
MV4
MFC4
Exhaust
QIR
HC
NO
CO
CO_2
O_2
MV5
MV6
MV7
P1
N_2
H_2O
H_2O
MFC2
Cooling Air
TIRC
TI
Evaporator
Oven and Reactor
Condensor

Figure 2.3: Experimental Apparatus Flowsheet

bottles not in use were stored outside. When the calibration gases were used on warmer days, they were simply brought indoors. However, when the outdoor temperature was below 10°C, these bottles were brought indoors and placed in the gas safety cabinet overnight before being placed into service. This ensured that the gas bottles and mixtures were at room temperature when the calibrations were performed. Calibration gases purchased in winter were also "winter mix" gases, having a lower fill pressure and being more likely to remain as a homogeneous mixture at lower temperatures.

Upon changing of gas bottles, a rigorous cleaning of the line in between the bottle and the pressure reducer was performed. This line was flushed seven times with high pressure pure gas from the cylinder before allowing the gas to flow further through the system.

Gas Type	Bottle Size (L)	Purity	Typical Flowrate ($L \cdot h^{-1}$)	Source Pressure (bar)
N_2	direct line	6.0	1000	5
CO_2	40	4.5	200	20
O_2	40	3.5	100	180
CO	40	2.5	2	200
H_2	50	3.0	~ 1	200
NO	10	2.5	~ 1	40
C_3H_6	40	2.5	~ 1	10.3
C_3H_8	40	2.5	~ 1	8.3
CH_4	50	2.5	~ 1	200

Table 2.1: Gas Sources and Associated Purities. A gas that is 99.9999% pure is defined as having a purity of 6.0, whereas a gas that is 99.5% pure is graded as 2.5.

2.2.2 Valves

Solenoid valves were supplied by Buerkert Fluid Control Systems. These control all gas flows before the gas reaches the mass flow controllers, and require 24 VDC to open. All valves were normally-closed for safety, with the exception of a N_2 valve that is normally-open to allow an inert environment inside the reactor in the event of a power failure.

2.2.3 Flow controllers

The flow rate of each gas entering the reactor was controlled and measured using a Mass Flow Controller (MFC). All the MFCs were supplied by Bronkhorst High-Tech B.V., with the exception of two MFCs, which were supplied by Brooks Instrument B.V. (Emerson Process Management). The Bronkhorst MFCs functioned using 0-10 VDC analog input and output signals. The two Brooks MFCs used 0-5 VDC analog signals. MFCs were calibrated at the factory, and calibration curves were supplied. MFC accuracy, as reported by the manufacturer, is ±0.5% of the measured value plus ±0.1% of the full scale value.

2.2.4 Water Evaporator

Water vapour was added to the mixture using an Controlled Evaporation and Mixing system (model W-303-330-P) supplied by Bronkhorst High-Tech B.V.. The incoming gas was mixed with liquid water in the inlet of the evaporator, and the water was vapourized inside the evaporator. A dosing meter (model M1P2-FAC-33-0) was used to measure the rate of water inflow, and the inlet valve controlled the flow rate to meet the desired setpoint, up to

241 g·h^{-1}. Distilled water was supplied from a 10 L water tank that was pressurized to 4 bar. A filter placed before the dosing meter removed all particles greater than 15 microns in size.

2.3 Heater

A large split-tube oven of length 100 cm was supplied by Arnold Schröder Industrieofen GmBH. The oven temperature regulator was supplied by Eurotherm. Although oven temperatures of up to 1100°C were possible with the oven and controller, much of the other equipment was not rated for such high temperatures and the heater was electronically limited to temperatures less than 600°C. Communication between the computer and the oven controller was via a PROFIBUS [69] connection.

Inside the oven was a stainless steel tube with an inner diameter of 37 mm. Static mixers have been found to enhance mass-transfer [70], and as such, three static mixers (provided by Herbert Ott Vertriebsgesellschaft MbH. + Co. KG) were included in the tube in the heater, to enhance the mixing of the gas and ensure that the gas composition and temperature is homogeneous.

Experiments were performed at a constant gas flow rate. The Gas Hourly Space Velocity (GHSV) (see Equation A.1) was kept constant at 25000 h^{-1}, or 0.965 m^3·h^{-1}. This is equivalent to 43 mol·h^{-1} under the conditions at which the flow controllers were calibrated and used.

Reynolds numbers and Peclet numbers in the reactor and in the monolith have been calculated, and are shown in Figure 2.4 and Figure 2.5. Within the range of experiments performed, the Re number was in a laminar flow region. With the exception of with the aid of the static mixers, turbulence is not achieved. Laminar flow is assumed for all calculations inside the monolith.

2.4 Reactor

Placement of the thermocouples in and around the reactor is shown in Figure 2.6 and Table 2.2.

Heating tape and insulation, supplied by Horst GmbH., were wrapped around the reactor outside the oven to ensure not only that heat losses were minimal, but also to prevent water condensation.

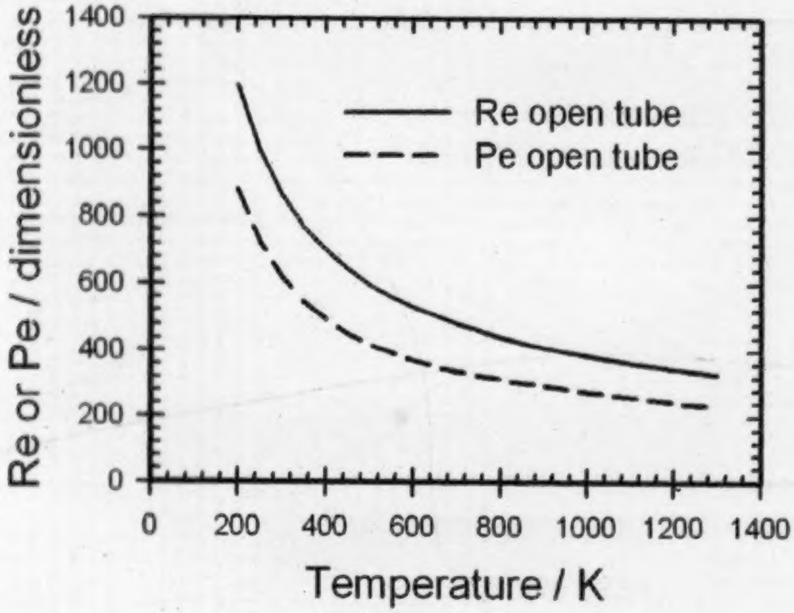

Figure 2.4: Reynold and Peclet Numbers in flow over various temperatures, calculated for N_2. The open tube was ~26 mm in diameter. A space velocity of 25 000 hr^{-1} was used in these calculations.

2.4.1 Monolith Core

The Pt catalyst was supplied by Umicore AG & Co. KG, and was aged at 600°C for 10 h prior to use. The catalyst was prepared by applying a Pt/Al_2O3 washcoat to a cordierite monolith support [71]. Platinum loading was 80 g per ft^3 of monolith volume. A core sample (26 mm in diameter and 76 mm in length) was taken from the larger catalyst, and this core sample was used for the experiments presented here. The sample had hexagonal channels with a channel density of 400 CPSI and a wall thickness of 4.3 mil (or 109 microns).

Type K thermocouples were placed at various places within and around the monolith. One thermocouple was placed immediately in front of the monolith, allowing for measurement of the inlet gas temperature. When possible, thermocouple cement was used to fix thermocouples into the channel and to block the channel to gas flow and minimize thermocouple error.

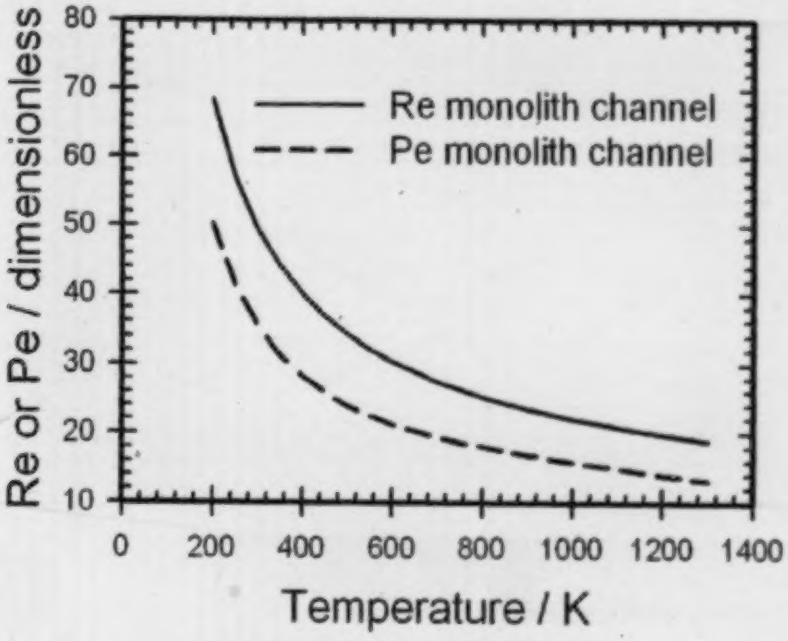

Figure 2.5: Reynold and Peclet Numbers in flow over various temperatures, calculated for N_2. A typical monolith channel of 1 mm and an OFA of ~0.7 was used. A space velocity of 25 000 hr^{-1} was used in these calculations.

2.5 Analyzers

Gas was sampled directly behind the catalyst, and routed along a 3 m line before entering the analyzer cabinet. This line was heated so as to prevent water condensation. Upon entering into the analyzer cabinet, the sample is split into multiple streams.

One stream was diverted to the Thermo Flame Ionization Detector (TFID). This analyzer was supplied by Emerson Process Management Manufacturing GmbH & Co. OHG, and is combined with a NGA 2000 platform for data reporting and communication. The gas input to the analyzer is heated (~ 150 °C) sample gas. A supplementary stream of H_2 was also provided to the analyzer, to ensure the flame did not extinguish. Air, from either a filter/catalyst system built into the analyzer or an in-house utility air, was also provided as fuel for the flame.

A MuLTi-component and multi-method analyzer (MLT) unit, also supplied by Emerson Process Management, was used to measure concentrations of CO, CO_2, and O_2 in the

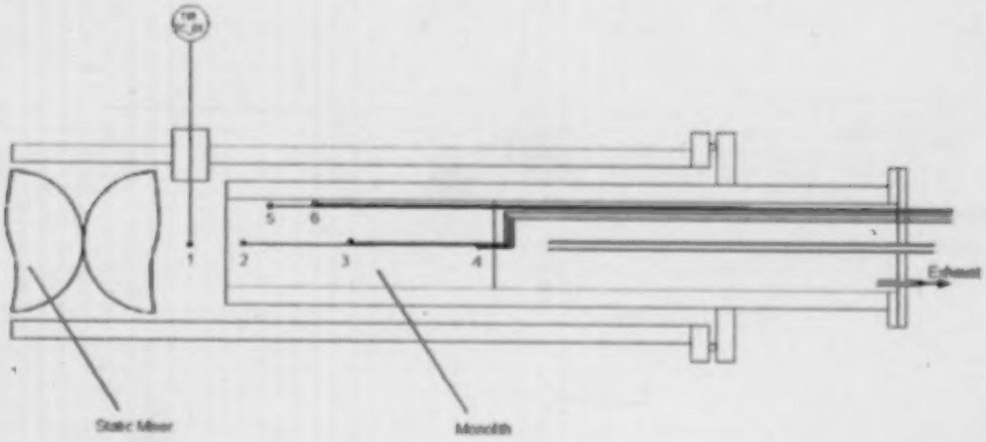

Figure 2.6: Placement of thermocouples in and around the monolith. See also Table 2.2. Insulation and heating tape not shown.

gas stream. CO and CO_2 measurements utilized an infrared (IR) technique, and oxygen measurements used a paramagnetic sensor. As the MLT unit is sensitive to flow rate, the flow rate into the unit was controlled to be constant at $0.5\ \mathrm{l{\cdot}min^{-1}}$.

A cooler/condenser is located along the sample path before the infra-red spectrometers, to remove water to prevent erosion of the IR sample cell. Thus, all CO, CO_2 and O_2 measurements are dry measurements. Condensed water is removed from the analyzers by a series of pumps. CO and CO_2 measurements were performed using an IR detector (NGA 2000 MLT) supplied by Emerson Process Management GmbH. & Co. OHG. O_2 measurements used the same device (NGA 2000 MLT), but using a paramagnetic sensor.

Label	Location
TC_01	3 mm in front of monolith
TC_02	7 mm from front of monolith, along the centreline
TC_03	37 mm from front of monolith, along the centreline
TC_04	71 mm from front of monolith, along the centreline
TC_05	6 mm behind catalyst in bulk gas
TC_06	38 mm from front of monolith, along the wall
TC_07	along the wall, precise position unknown
TC_08	ambient temperature in laboratory

Table 2.2: Locations of thermocouples shown in Figure 2.6.

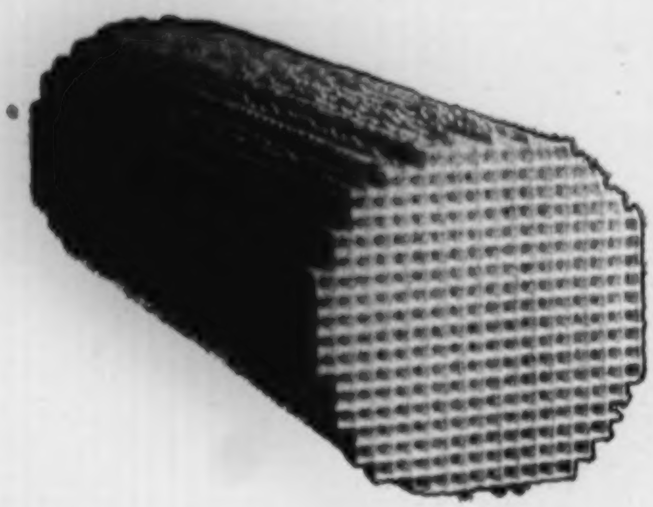

Figure 2.7: A typical monolith support material. This cordieriete monolith has 400 cells per square inch (CPSI).

An Eco-Physics CLD 822 M h unit measured NO, NO_2 and NO_x concentrations using chemiluminescence. As NO_x was not used for the experiments presented in this work, nothing further is mentioned regarding NO_x measurements.

Hydrocarbon measurements were performed with a Flame Ionization Detector (FID).

A H-Sense Hydrogen Monitoring System, a H_2 mass spectrometer, from V&F Analyse- und Messtechnik GmbH was used to perform a number of experiments with CO and H_2. This mass spectrometer has a range of 0-10000 ppm H_2. A water condenser in the spectrometer removes all water before water enters the main analytical system, and thus all measurements were also dry measurements.

2.6 Other Sensors

As many as 8 type K thermocouples were used in any experiment. While there is a limit in the number of thermocouples that may be practically placed inside the monolith, a thermoelement has been placed to measure the gas temperature immediately before (~5 mm) the monolith.

Analyzer	Channel	Gas	Method	Low	High	Units
MLT	1	CO	IR	0	30000	ppm
	2	CO	IR	0	2500	ppm
	3	CO_2	IR	0	25	%
	4	CO_2	IR	0	1000	ppm
	5	O_2	paramagnetic	0	25	%
TFID	1	equiv CH_4	FID	0	10000	ppm
CLD	1	NO	CL	0	500	ppm
	2	NO_2	CL	0	500	ppm
	3	NO_x	CL	0	500	ppm
HS-MS	1	H_2	mass-spec	0	10000	ppm

Table 2.3: Measurement Ranges of Analytic Equipment

A pressure sensor (supplied by Wagner Mess- und Regeltechnik GmbH), capable of measuring 0-4 bar absolute, was employed. Normally, this sensor measures the pressure immediately before the catalyst, however it was also employed in other locations in some experiments. Typical pressure measurements before the catalyst during experimentation were between 1.07 and 1.10 bar.

2.7 Electronics

Electronic input/output devices were supplied by Elektro Beckhoff GmbH. The Beckhoff system was designed to provide 8 channels of thermocouple inputs, and 32 channels each of analog input, analog output, and digital output. Analog input and analog output devices are capable of 0-10 VDC input and output, at a digital resolution of 12-bits. At 12-bit resolution, the error associated with a digital signal is:

$$100\%/2^{12} = 0.024\% = \pm 0.024 \text{ VDC} \tag{2.1}$$

This uncertainty was considered to be insignificant. Analog output devices were used to control mass flow controllers, and analog input devices were used to record signals from mass flow controllers, analyzers, and other devices (i.e. the pressure sensor).

Digital output devices were typically used for controlling valves (but also for the watchdog signal detailing in subsection 2.11.1), and produce a 0 or 24 VDC signal. 8 Type K thermocouples were connected via Beckhoff modules, and may be read by the computer system.

Communication between the controlling computer and the Beckhoff device, as well as with the oven regulator, was via a PROFIBUS [69] connection. A Beckhoff bus coupler module provided a backplane for communication with all Beckhoff modules, and allows the single PROFIBUS connection to function with all the Beckhoff modules and channels. An OLE for Process Control (OPC) server ran on the controlling computer, and this server provided the necessary interface between hardware and software. Channels on the OPC server were accessible to the LabVIEW software, and the appropriate device on the PROFIBUS network was addressed.

A simplified diagram of the electrical system is shown in Figure 2.8. Figure 2.9 details the control system, including hardware and software connections.

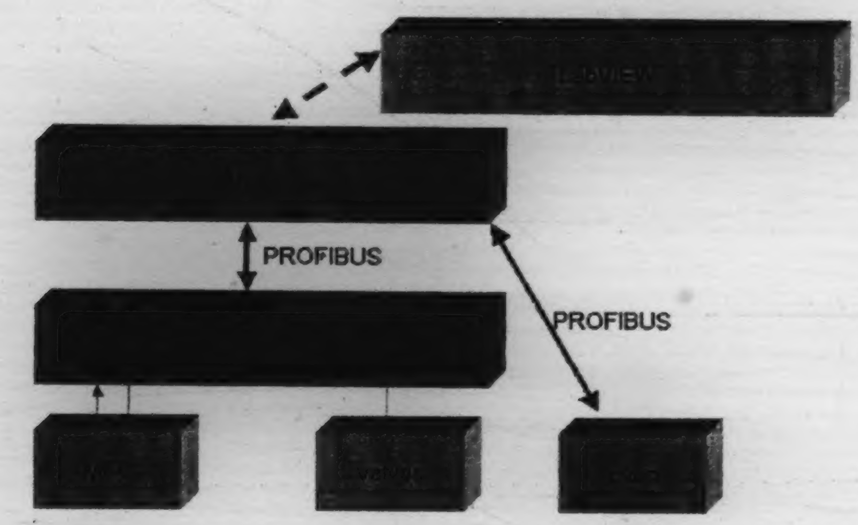

Figure 2.8: Electrical system (simplified).

2.8 Signal Stability and Noise

Electronic signals were typically very stable with minimal noise. A LabVIEW program was written to monitor a measurement for signal stability and to determine the degree of noise

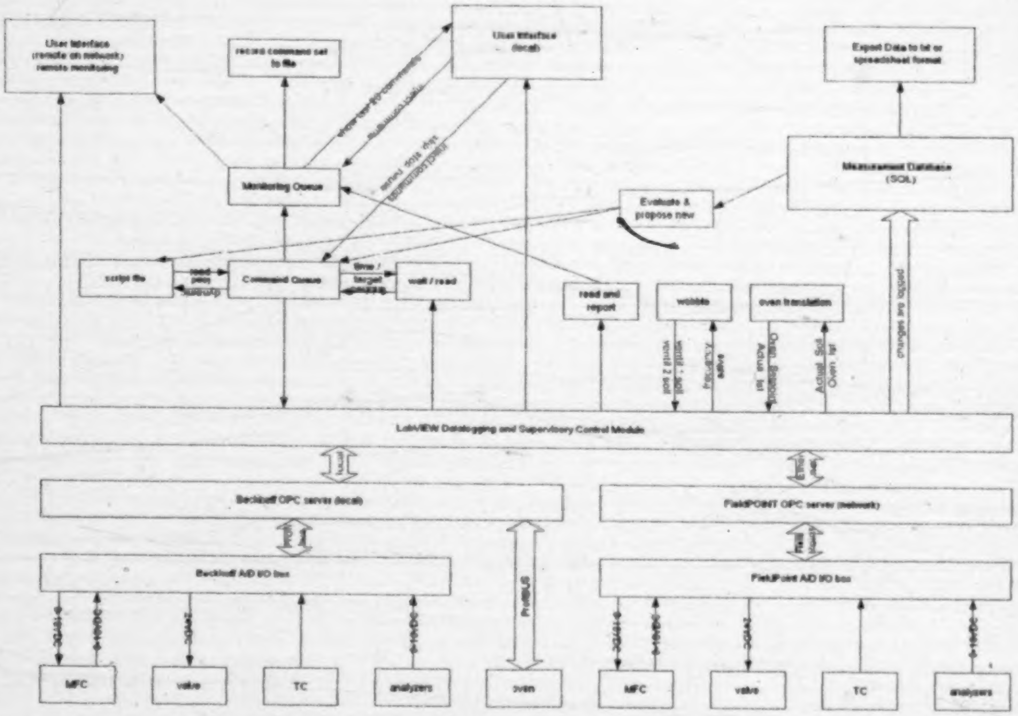
User interface
(remote on network)
remote monitoring
record command set
to file
User interface
(local)
Export Data to txt or
spreadsheet format
Monitoring Queue
Measurement Database
(SQL)
Evaluate &
propose new
script file
read
Command Queue
time /
target
wait / read
read and
report
wobble
oven translation
changes are logged
Actual_Sol
Oven_txt
Actua_txt
LabVIEW Datalogging and Supervisory Control Module
Beckhoff OPC server (local)
FieldPOINT OPC server (network)
Beckhoff A/D I/O box
ProfiBUS
FieldPoint A/D I/O box
MFC
valve
TC
analyzers
oven
MFC
valve
TC
analyzers

Figure 2.9: Control system (including all software and hardware) used to control and monitor all inputs and outputs in the system.

in the signal, and signals were found to be quite clean. The standard deviation of 1000 thermocouple measurements in a thermally stable environment was 0.7 K.

2.9 LabVIEW Control System

A computer control and data-logging system was built to control and record measurements as necessary. National Instruments LabVIEW 7.0 [72] was used as the programming environment for the control system.

2.9.1 LabVIEW Fundamentals

LabVIEW is a programming environment designed with for use in scientific laboratories. This flow programming language provides the user with many tools to interface and control typical laboratory equipment. Additional toolboxes and modules are available to add functionality.

The Datalogging and Supervisory Control Module for LabVIEW was employed for raw data storage and management. This module allows all addressable inputs and outputs in the system, especially those available on the OPC server, to be easily addressed by a tag name. Although the tag name is a simple string, the tag is configured to address the appropriate hardware channel with appropriate limits and logging options. All tags are logged to a Structured Query Language (SQL) database as often as the OPC server sees a new value. Tags values that do not change for a relatively long period of time (i.e. valve settings) are logged to the database a minimum of once every 30 seconds.

2.9.2 Queueing System

A scriptable program and an associated series of subroutines to control the experimental apparatus was written by the author of this thesis. This program reads in a text file and executes the commands found therein in series or parallel. Commands may involve defining new setpoints, waiting for a condition (time of measurement) to be met, data output functions, or functions that modify the current command queue.

The command queue is a dynamic list of commands to be executed in series. While the queue is not empty, a loop in the system is always executing a command. This loop reads the command at the front of the queue, removes it from the queue, and executes it. When that command is complete, the loop returns to the queue and process the next command, found at the front of the queue.

New commands may be added to either the end or the front of the queue, allowing for modifications to be made to a running set of commands. These modifications may be performed by an operator, be planned modifications (for example, loading another command script), or unplanned changes to the queue (for example, in response to a failure signal or the loss of a gas source). More detail regarding input files and basic commands for the control software may be found in section E.6.

Several other loops run in parallel in the background, monitoring the system progress and, in some cases, making changes. Perhaps the most visible background loop in the monitoring loop, which allows the operator to monitor the time-resolved progress of any selected tags in the system. This loop is a read-only loop, and does not modify and setpoints in the system. Standard graphs showing temperature measurements over time as well as analyzer readings over time are included here, as well as a basic interface showing data from the Fourier-Transform InfraRed (FTIR) OPC server.

Other loops that run in the background include an loop that calculates the overall gas consumption of an experiment by integrating the measurements from mass flow controllers over time.

Sample LabVIEW code of a scriptable command, reading a tag value and reporting that value to the operator, is shown in Figure 2.10.

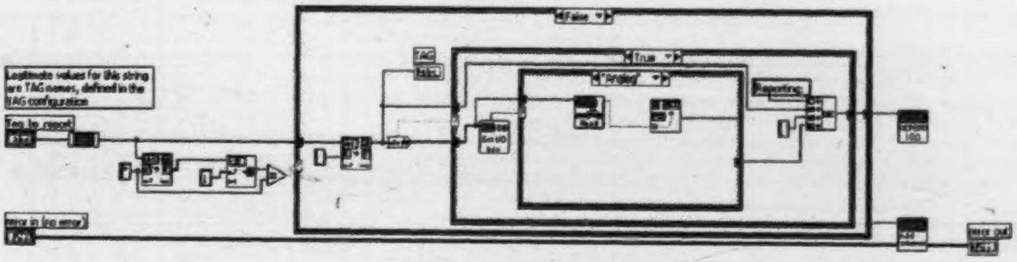

Figure 2.10: Sample LabVIEW code, reporting the value of a tag to the operator. Shown is the flow of commands, case structures, as well as a subroutine reference.

2.10 SQL Measurement Database

All measurements were recorded in a SQL database managed by the LabVIEW software. Data values were extracted as needed, typically at the end of an experiment. Measured values were stored in the database whenever a new value was measured. That is, when the system detected a new measurement that was different from the most recent value, the new value was stored. If there was no new value (as is the case for valves and setpoints that remain constant for extended periods of time), the database does not normally record the same value repeatedly. This saves on disk space and minimizes the number of SQL transactions. However, as data extracted from the database was step-interpolated between known values, all values were recorded in the database a minimum of once every 30 seconds, regardless of whether the value had changed or not. Thus, valves that were open for extended periods of time could still be accurately step-interpolated. Disk space was not a significant issue - large disk drives are readily available. Although additional SQL transactions slowed down the data extraction phase, data extraction usually occurred during the time between two experiments, and thus this was not a critical point or would have significantly influenced any results.

2.11 Safety System

The system is designed to run safely, such that it may be allowed to run overnight with minimal risk. The system was designed to fail in a safe mode, and any of a number of unsafe events may trigger the system to fall into this safe mode.

The oven, heating bands, evaporator, gas mixing unit, and all flow controllers and valves are powered through the same master switch. All computers and analyzers are on a separate master switch. When the switch controlling the oven and gases is turned off, all power to the heating and gas flow devices is removed, and all heating and dangerous gas flow is stopped. A single valve for N_2 is normally open (that is, when all power is removed, this valve opens, allowing a flow of N_2), and this valve flows into a flow restrictor and then to the main reactor gas feed. Thus, when power is removed, all gases except N_2 are prevented from flowing, and a flow of $\sim$ 1200 $L{\cdot}h^{-1}$ N_2 is allowed to flow through the reactor, inerting the gas and cooling the reactor internals. This N_2 flow rate is also low enough that it will not inert the room atmosphere at the same time, should a leak occur.

2.11.1 Watchdog

A watchdog computer supervises the general safety of the system. The watchdog monitors 5 separate signals, and when any one signal fails, the watchdog stops all power to the gas mixing unit and to the reactor, placing the system in fail-safe mode. The monitored signals are:

- N_2 source pressure sensor. If the N_2 pressure in the source line drops below a predetermined value (e.g. 4 bar), then the signal sent to the watchdog changes, and the watchdog may act. This protects against running the system with insufficient N_2 resources.

- A temperature sensor inside the oven reports the value to a safety switch. If the measured temperature exceeds a pre-determined rate (e.g. 550°C), then the watchdog will be alerted and will act. This prevents overheating the system beyond safe levels, risking damage to equipment or sintering the catalyst.

- Two gas sensors monitor the O_2 and CO levels in the room. If the atmospheric oxygen levels drop below 19%, then a warning light blinks. Should the oxygen level drop to more dangerous levels, such as 17%, then the watchdog acts and stops the system, closing all solenoid valves in the process. The same process for warning and shutdown occurs when the atmospheric CO level exceeds 30 and 60 ppm, respectively. This is designed to protect the people inside the lab from a gas leak.

- Every 10 seconds that the queueing system (described in subsection 2.9.2) is running on the computer, a pulse signal is sent through one of the digital channels. If this signal is not read by the watchdog for 60 seconds, then the watchdog considers this to be an alarm and acts. Thus, computer crashes are not allowed to bring the system into an unsafe state. A grace period of three minutes is allowed when first starting the watchdog, to simplify a manual start-up.

2.11.2 Computer Checks

The computer control system constantly monitors the flowrates of the N_2, O_2, CO_2 and CO flow controllers. Every two seconds, the current measured flow rate is compared to the desired setpoint. If the measured flow rate is less than 90% of the setpoint, then an alarm message is set to the operator. If the measured flow rate is chronically below 90% of the setpoint (e.g. for more than 15 seconds, or more than 7 alarm messages in a row), then the system will act on this failure and set all setpoints to zero and close all valves. This is also useful in the case of an empty gas bottle. As the bottle approaches a low pressure, the flow rate drops. If the flow rate is low for a long period of time, then the desired concentration profiles will not be met. The system stops the experiment, and the operator can change the bottle and restart or resume the experiment. The volume of gas wasted on undesired experiments is minimized.

2.12 Post-Processing of Results

Post-processing of experimental data was performed using a series of BASH [73] scripts coupled with MathWorks MATLAB 7 [74]. The scripts extracted columns of data from the experimental into a form that MATLAB could import. Mat Lab then proceeded to perform numerous calculations to obtain useful graphs. Microsoft Excel was also used. Final plotting of the data was performed with Sigmaplot [75].

A time correction was made for each analyzer, such that the time for events at the mass-flow controller could be compared to measurements at the analyzer, and the travel time discounted. The time correction factor was determined using a three-way valve, switching between N_2 and a calibration gas mixture. The three-way valve appeared at the same position as the reactor would normally appear in the flow diagram. Both gases were at the same pressure (~1.1 bar atmospheric), and the pressure was the same as usually measured in the reactor. When the gases were not directed to the analyzers, they were directed toward the exhaust system. In this manner, by switching between the two gas streams, the time between the reactor and the analyzer could be determined for each analyzer, and the appropriate time correction applied.

When necessary, a correction was made for the CO, CO_2, and O_2 measurements, as these measurements were made under dry conditions. This factor is based on the ratio of dry to wet total measured inlet flow. Error attributed to H_2O that has formed as a result of reaction (i.e. due to combustion of hydrocarbons) is considered to be minimal: when water is intentionally added to the mixture, it is added on the order of 6% to 10% (60 000 ppm to 100 000 ppm), whereas water formed as a result of hydrocarbon combustion is on the order of 1000 ppm (i.e. for total combustion of 1000 ppm inlet H_2).

2.13 Types of Experiments Performed

2.13.1 Temperature Programmed Reactions or Light-Off Curves

As many driving trips are short-distance and begin with cold engines [76, 77], efforts to reduce overall emissions typically focus on reducing the emissions during start-up. When an engine and the catalytic converter are warm, the efficiency of the catalytic converter is very high. However, until the catalytic converter is warm, the efficiency can be very low and the emissions are relatively high. Thus, much effort is made to study the temperature at which a transition from low to high reaction rate occurs. These are are typically referred to as light-off experiments [78, 79, 80], wherein the inlet gas concentrations are held fixed and the temperature of the reactor is slowly increased and then decreased. A plot of conversion (or outlet concentration) versus inlet gas temperature is produced by a light-off experiment.

The temperature typically begins at a lower value (between 30 and 75°C in the experiments presented here), and is increased at a rate of 7.5°C per minute. The light-off point occurs when the temperature is increased, and is defined as the inlet gas temperature at which conversion reaches 50%. This point may also be referred to as the ignition point. During the cooling phase, the reaction rate, and hence the conversion, will decrease. The point at which the conversion drops below 50% is referred to as the light-out, or extinction, point. Typical light-off and light-out points are shown in Figure 2.11. The light-off curve, Figure 2.11(a), is often referred to as the low-rate branch, and the light-out curve, Figure 2.11(b), is referred to as the high-rate branch.

Knowledge of light-off and light-out points during temperature programmed reactions are important, as during typical operation of a diesel engine (or during an FTP cycle), the catalyst may pass through ignition and extinction phases several times. Thus, for the overall reduction of emissions, maintaining the catalyst on high-rate branch is essential. A detailed knowledge of the catalyst behaviour can assist in controlling the catalysts such that the time at which the catalyst is on the low-rate branch is minimized.

Repeated light-off curves showed an insignificant change in the result between subsequent experiments involving simply CO, O_2, N_2, H_2 and CO_2. A pretreatment of the catalyst before each run was not required for those experiments, but is noted when performed. However, for experiments involving H_2O, a pre-treatment improved reproducibility of the experiments. Sirijaruphan et al. [81] reported that a pretreatment with hydrogen at a temperature above 300°C completely regenerated their Pt catalyst.

2.13.2 Concentration Programmed Reactions

Step functions have been performed, typically by increasing the CO concentration from a low (or zero) value to a high value (up to 2500 ppm), and then back again. At the instant a step was performed, commands to increase (or decrease) the flow rate of CO, open (or close) the CO valve (if required, the valve was closed for zero setpoints), and adjust the inert gas flow accordingly were sent is short succession. The time between steps was varied between 5 and 20 minutes, and this was not found to have a significant influence on the results.

Several experiments with respect to concentration ramps were performed, whereby the concentration (or flow rate) of a component was slowly increased or decreased. As the concentration of the species that was varied is typically low (on the order of 2000 ppm), there was no correction for changes in overall space velocity in early experiments during concentration ramps. As the concentration of the ramped component was typically on the order of 0.2% of the total mixture, the error in space velocity would be similar. This assumption appears valid, especially in light of the manufacturer's stated accuracy of ±1% for flow controller measurements.

In later experiments, functionality was added such that two controllers could be simultaneously ramped, at the same or different rates. This allows the reaction composition and overall space velocity to be kept under stricter control.

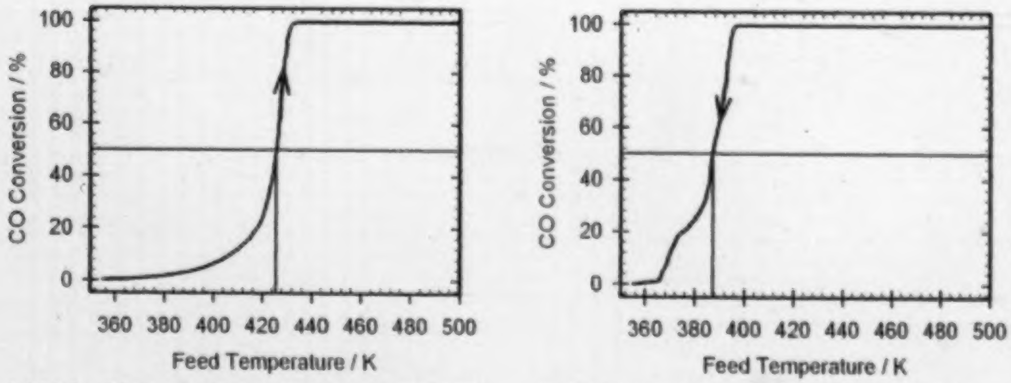

(a) Light-Off Curve. The light-off point is defined as the point at which conversion reaches 50%.

(b) Light-Out Curve. The light-out point is defined as the point at which conversion drops below 50%.

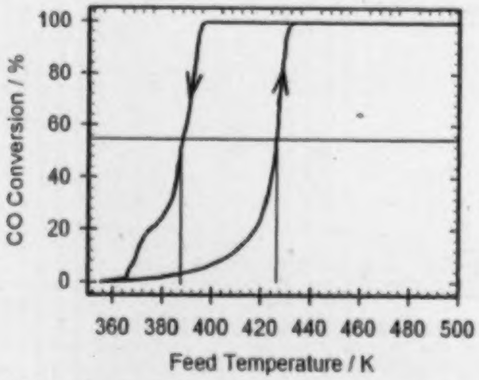

(c) Complete Light-Off Curve (with both light-off and light-out)

Figure 2.11: Sample Light-Off and Light-Out Points: (a) light-off is observed during an increasing temperature ramp, and (b) light-out is observed during a decrease in temperature; (c) typical experiments involve both.

2.14 Summary

Many experiments in CO oxidation have been performed by others on single crystal catalysts, typically under vacuum, which can look in detail at micro-phenomena but are fairly removed from real-world catalytic converter conditions. Engine test-benches running FTP cycles [63], as defined by the United States Environmental Protection Agency, are also used to study the performance of a catalytic converter. In these experiments, an automobile engine is run at specified loads over time and the exhaust gas directed through a catalytic converter and then analyzed. However, the single-crystal studies are performed under conditions far removed from those of real-world catalysts, and FTP cycle studies are performed in a manner that makes interpretation of surface kinetics very difficult to separate from other variables in the engine performance. By carefully controlling the inlet composition and temperature, information about the dynamics of this process under conditions closer to real-world conditions may be gained that would not be possible by studying FTP cycles. In this study, the exhaust gases from an automobile are artificially produced with selected components, such that phenomena on the catalyst may be more closely studied.

An experimental apparatus to control the inlet gas temperature and composition and measure and record the temperature in the catalyst and outlet gas composition has been built. This system has been described in detail.

3

Modelling

3.1 Introduction to Computer Modelling

Computer models, verified by experimental data, can be a powerful tool for the interpretation of real-world phenomena. Computer models allow the user to change parameters or observe variables that may otherwise be very difficult or expensive to do experimentally. This may allow insight into the underlying chemical reactions. By better understanding the underlying mechanisms, we can optimize the on-board control computers for automobiles, as well as make better use of computer based-simulations when making decisions regarding catalyst design.

However, computer models are not perfect and must usually make some simplifying assumptions to allow execution of the model within reasonable time and memory requirements given the current state of computing power. The limits of the model applied must be understood, and assumptions carefully chosen so as to consider transfer of thermal energy and mass when appropriate [82].

Kinetic modelling in automotive catalysis is not new, as many others have previously worked in this area [83, 84]. The pioneering work of Voltz et al. [40] is considered the first published attempt to model the behaviour of an automotive catalytic converter. While this method was able to describe some results, the nature of the global method limits its usefulness. These models are typically empirical equations and not based on elementary mechanisms. As these models are steady-state, their applicability to transient experiments is questionable, as important parameters such as storage and catalyst surface history are not considered. Other works have used this approach [85, 86] , however, the global method typically does not consider surface effects. The current work shows that considering surface reactions is essential when understanding and modelling automotive catalysis and developing a robust model.

Elementary models [87, 66] typically make fewer simplifying assumptions than global models and are more likely to describe experimental results, as these models consider the basic chemical reactions that occur in a stepwise manner, and can also include the surface phenomena that determines the dominant pathways under different conditions. These models work well in specific situations, such as the rising temperature portion of a light-off curve, but do not describe all phenomena that has been experimentally observed. While complex mixtures have been modelled in other works, it is not believed that all relevant effects were considered, and that these models would not work well when only a subset of the components are studied.

3.2 Kinetic Modelling

The chemical reaction steps that take place in the system are defined in the model. These steps may either be lumped together into a single global model (such as the Voltz model), or may consider individual elementary steps (such as a Langmuir-Hinshelwood or Eley-Rideal mechanism), or some variation of these models. Every adsorption, desorption, surface migration and surface reaction step may be defined for each surface type and component involved.

3.3 Classical LHHW-Type Model

Voltz et al. [40] proposed a model to describe CO oxidation in the presence of oxygen, propylene and NO. This model was based on experimental observations of a pelleted Pt-alumina catalyst using a synthetic gas mixture and a varied inlet temperature.

The original model included inhibition effects of propylene and NO. As these components are not used in the present work, these effects have been removed. This model uses a global reaction scheme, lumping parameters together and assuming that the rate-determining step is the reaction between CO and oxygen. This model does not consider surface effects, nor does it consider the catalyst history.

3.3.1 CO Oxidation

The overall reaction for the oxidation of CO can be written as shown in Equation 3.1:

Equation	Parameter	Value	Units
3.2	$A_{V,1}$	1×10^{16}	$mol_{CO}\ mol_{cat}^{-1}\ s^{-1}$
	$Ea_{V,1}$	9000	$kJ\ mol^{-1}$
	K_{a1}	65.5	$m^3\ mol^{-1}$

Table 3.1: Voltz Model Parameters

$$CO + \frac{1}{2}O_2 \rightleftharpoons CO_2 \tag{3.1}$$

Equation 3.2 was proposed as the rate of reaction, where G1 is an inhibition term (defined in Equation 3.3).

$$r_{V,CO} = \frac{k_{V,1} \cdot X_{g,CO} \cdot X_{g,O_2}}{G1} \tag{3.2}$$

$$\begin{aligned} G1 &= T \cdot (1 + K_{a1} \cdot X_{g,CO} + K_{a2} \cdot X_{g,C3H6})^2 \\ &\quad \cdot \left(1 + K_{a3} \cdot X_{g,CO}^2 \cdot X_{g,C3H6}^2\right) \\ &\quad \cdot \left(1 + K_{a4} \cdot X_{g,NO}^{0.7}\right) \end{aligned} \tag{3.3}$$

As NO and C_3H_6 are not used in the present work, Equation 3.3 simplifies to Equation 3.4.

$$G1 = T \cdot (1 + K_{a1} \cdot X_{g,CO})^2 \tag{3.4}$$

The rate of CO consumption may be calculated using Equation 3.5 and the parameters in Table 3.1.

$$r_{V,CO} = \frac{A_{V,1} \cdot e^{\left(-Ea_{V,1}/RT\right)} \cdot X_{g,CO} \cdot X_{g,O_2}}{T \cdot (1 + K_{a1} \cdot X_{g,CO})^2} \tag{3.5}$$

Since initial publication, the Voltz rate expression has been used in many different models, often while modified.

3.4 Mechanistic Model Based on Langmuir-Hinschelwood Assumptions

Models that attempt to account for each elementary step in the oxidation reaction have recently been presented in the literature. Chatterjee et al. presented a mechanism in the literature [66]. This mechanism considers CO, O_2, H_2, H_2O, C_3H_6 and other hydrocarbons. Rate parameters are derived from literature sources and thermodynamic data. The method for calculating the rate coefficients is presented in section B.2.

Other groups [88] have also published similar models, however the Chatterjee et al model is most familiar to the automotive catalysis community, and is one of the most studied. The Chatterjee et al. implementation is the implementation discussed the most in this work.

3.4.1 CO Oxidation

Before any surface reaction may take place, the respective components must first adsorb to the surface. Oxygen is considered to adsorb in a dissociative manner, as shown in Equation 3.6a. The rate equation for the chemical step (Equation 3.6a) is shown immediately below (Equation 3.6b).

$$O_2 + 2^* \underset{k^f_{cLH,8}}{\overset{k^f_{cLH,1}}{\rightleftharpoons}} 2O^* \tag{3.6a}$$

$$r_{cLH,1} = k^f_{cLH,1} C_{O_2} \theta_*^2 - k^f_{cLH,8} \theta_{O^*}^2 \tag{3.6b}$$

Although in this case oxygen adsorption is modelled as reversible, it is considered by many to be irreversible below 700 K [89, 90].

CO_2 may easily adsorb to or desorb from the surface.

$$CO_2 + ^* \underset{k^f_{cLH,14}}{\overset{k^f_{cLH,6}}{\rightleftharpoons}} CO_2^* \tag{3.7a}$$

$$r_{cLH,6} = k^f_{cLH,6} C_{CO_2} \theta_* - k^f_{cLH,14} \theta_{CO_2^*} \tag{3.7b}$$

The general consensus in the literature is that CO_2 desorption is practically instantaneous after the surface reaction. However, Han et al. [91] claim to have discovered a CO_2 intermediate species that is stable up to 300 K. They state a desorption activation energy of

46±3 kJ mol^{-1}, compared to an activation energy of 75±4 kJ mol^{-1} for the direct formation of gaseous CO_2 from adsorbed CO and O. This intermediate species is not considered to be significant in the present work, as the temperatures considered here are above 300 K.

CO adsorption is fully reversible.

$$\mathrm{CO} + {}^{*} \underset{k^{f}_{cLH,13}}{\overset{k^{f}_{cLH,7}}{\rightleftharpoons}} \mathrm{CO}^{*} \tag{3.8a}$$

$$r_{cLH,7} = k^{f}_{cLH,7} C_{CO} \theta_{*} - k^{f}_{cLH,13} \theta_{CO^{*}} \tag{3.8b}$$

The surface reaction between adsorbed CO and O is:

$$\mathrm{CO}^{*} + \mathrm{O}^{*} \underset{k^{f}_{cLH,45}}{\overset{k^{f}_{cLH,44}}{\rightleftharpoons}} \mathrm{CO}_2^{*} + {}^{*} \tag{3.9a}$$

$$r_{cLH,44} = k^{f}_{cLH,44} \theta_{CO_2^{*}} - k^{f}_{cLH,45} \theta_{CO_2^{*}} \theta_{*} \tag{3.9b}$$

If there is any carbon present on the catalyst surface, that carbon may also oxidize.

$$\mathrm{C}^{*} + \mathrm{O}^{*} \underset{k^{f}_{cLH,47}}{\overset{k^{f}_{cLH,46}}{\rightleftharpoons}} \mathrm{CO}^{*} + {}^{*} \tag{3.10a}$$

$$r_{cLH,46} = k^{f}_{cLH,46} \theta_{C^{*}} \theta_{O^{*}} - k^{f}_{cLH,47} \theta_{CO^{*}} \theta_{*} \tag{3.10b}$$

The rate parameters proposed by Chatterjee et al. are given in Table 3.2. Other parameter values have been reported [92, 93]. For example, Kasemo and Törnqvist [89] reported sticking coefficients of 0.62, 0.54 and 0.38 for hydrogen, CO and oxygen respectively.

3.4.2 H_2 and H_2O Adsorption and Desorption

The oxidation of hydrogen on platinum proceeds in a similar manner as that of CO, whereby the components all adsorb to the surface, react, and subsequently desorb. Oxidation of hydrogen on a Pt surface has been known to proceed at temperatures as low as 120 K [94], and when the surface is oxygen covered, the reaction is limited by the rate of adsorption of

Equation	Parameter	Value	Units [a]	Source
3.6b	$k^f_{cLH,1}$			[66]
	S_0	0.07	unitless	
	γ	2.72×10^{-5}	$\text{mol}_{NM}\ \text{m}_{NM}^{-2}$	
	$k^f_{cLH,8}$			
	A_0	1.006×10^{13}	mol cm^{-1} s	
	E_A	232.2	kJ mol^{-1}	
	$\frac{dE_A}{d\theta_O}$	90	kJ mol^{-1}	
3.7b	$k^f_{cLH,6}$			[66]
	S_0	0.005	unitless	
	γ	2.72×10^{-5}	$\text{mol}_{NM}\ \text{m}_{NM}^{-2}$	
	$k^f_{cLH,14}$			
	A_0	1×10^{13}	mol cm^{-1} s	
	E_A	27.1	kJ mol^{-1}	
3.8b	$k^f_{cLH,6}$			[66]
	S_0	0.84	unitless	
	γ	2.72×10^{-5}	$\text{mol}_{NM}\ \text{m}_{NM}^{-2}$	
	k^f_{14}			
	A_0	1×10^{13}	mol cm^{-1} s	
	E_A	126.4 [c]	kJ mol^{-1}	
	$\frac{dE_A}{d\theta_{CO}}$	33	kJ mol^{-1}	
3.9b	$k^f_{cLH,44}$			[66]
	A_0	1.006×10^{12}	mol cm^{-1} s	
	E_A	108	kJ mol^{-1}	
	$\frac{dE_A}{d\theta_{CO}}$	33	kJ mol^{-1}	
	$\frac{dE_A}{d\theta_{NO}}$	-90	kJ mol^{-1}	
	k^f_{45}			
	A_0	1.006×10^{13}	mol cm^{-1} s	
	E_A	165.1	kJ mol^{-1}	
	$\frac{dE_A}{d\theta_O}$	-45	kJ mol^{-1}	
3.10b	$k^f_{cLH,46}$			[66]
	A_0	1.006×10^{12}	mol cm^{-1} s	
	E_A	0	kJ mol^{-1}	
	$\frac{dE_A}{d\theta_{CO}}$	-33	kJ mol^{-1}	
	k^f_{47}			
	A_0	1.006×10^{13}	mol cm^{-1} s	
	E_A	218.5	kJ mol^{-1}	
	$\frac{dE_A}{d\theta_O}$	-45	kJ mol^{-1}	

---

[a] units converted from literature source. For example, 3.70×10^{21} mol cm s $\times$ 2.72×10^{-9} mol cm^{-2} = 1.006×10^{13} mol s cm^{-2}. In the original literature source, surface site density $\Gamma = 2.72\times 10^{-9}\ \text{mol}_{NM}\ \text{cm}_{NM}^{-2}$, where the subscript $_{NM}$ refers to the Nobel Metal.

[c] Literature values for activation energy for CO desorption vary as shown in Table 4.1. All these equations do have general agreement that the activation energy is 104 kJ mol^{-1} on a CO saturated surface.

Table 3.2: LH Mechanism Parameters for CO Oxidation

hydrogen [95].

$$H_2 +^* +^* \underset{k^f_{11}}{\overset{k^f_4}{\rightleftharpoons}} H^* + H^* \tag{3.11a}$$

$$r_4 = k^f_4 C_{H_2} \theta^2_{*} - k^f_{11} \theta^2_{H^*} \tag{3.11b}$$

$$H_2O +^* \underset{k^f_{12}}{\overset{k^f_5}{\rightleftharpoons}} H_2O^* \tag{3.12a}$$

$$r_5 = k^f_5 C_{H_2O} \theta_* - k^f_{12} \theta_{H_2O^*} \tag{3.12b}$$

3.4.3 H_2 and H_2O Reactions

The surface reactions involving adsorbed hydrogen are given as:

$$H^* + O^* \underset{k^f_{39}}{\overset{k^f_{38}}{\rightleftharpoons}} OH^* +^* \tag{3.13a}$$

$$r_{38} = k^f_{38} \theta_{H^*} \theta_{O^*} - k^f_{39} \theta_{OH^*} \theta_* \tag{3.13b}$$

$$H^* + OH^* \underset{k^f_{41}}{\overset{k^f_{40}}{\rightleftharpoons}} H_2O^* +^* \tag{3.14a}$$

$$r_{40} = k^f_{40} \theta_{H^*} \theta_{OH^*} - k^f_{41} \theta_{H_2O^*} \theta_* \tag{3.14b}$$

$$OH^* + OH^* \underset{k^f_{43}}{\overset{k^f_{42}}{\rightleftharpoons}} H_2O^* + O^* \tag{3.15a}$$

$$r_{42} = k^f_{42} \theta^2_{OH^*} - k^f_{43} \theta_{H_2O^*} \theta_{O^*} \tag{3.15b}$$

Equation	Parameter	Value	Units [a]	Source
3.11b	$k^f_{cLH,4}$			[66]
	S_0	0.046	unitless	
	γ	2.72e-5	$mol_{NM}\ m_{NM}^{-2}$	
	$k^f_{cLH,11}$			
	A_0	1.006E+13	mol s cm^{-1}	
	E_A	67.4	kJ mol^{-1}	
	$\frac{dE_A}{d\theta_H}$	6.0	kJ mol^{-1}	
3.12b	$k^f_{cLH,5}$			[66]
	S_0	0.75	unitless	
	γ	2.72e-5	$mol_{NM}\ m_{NM}^{-2}$	
	$k^f_{cLH,12}$			
	A_0	1.00E+13	mol s cm^{-1}	
	E_A	40.3	kJ mol^{-1}	
3.13b	$k^f_{cLH,38}$			[66]
	A_0	1.006E+13	mol s cm^{-1}	
	E_A	11.5	kJ mol^{-1}	
	$k^f_{cLH,39}$			
	A_0	1.569E+14	mol s cm^{-1}	
	E_A	74.9	kJ mol^{-1}	
3.14b	$k^f_{cLH,40}$			[66]
	A_0	1.006E+13	mol s cm^{-1}	
	E_A	17.4	kJ mol^{-1}	
	$k^f_{cLH,41}$			
	A_0	9.955E+12	mol s cm^{-1}	
	E_A	73.6	kJ mol^{-1}	
3.15b	$k^f_{cLH,42}$			[66]
	A_0	1.006E+13	mol s cm^{-1}	
	E_A	48.2	kJ mol^{-1}	
	$k^f_{cLH,43}$			
	A_0	6.392E+11	mol s cm^{-1}	
	E_A	41.0	kJ mol^{-1}	

---

[a] units converted from literature source. For example, 3.70×10^{21} mol cm s $\times$ 2.72×10^{-9} mol cm^{-2} = 1.006×10^{13} mol s cm^{-1}. In the original literature source, surface site density $\Gamma = 2.72\times 10^{-9}$ mol cm^{-2}.

Table 3.3: LH Mechanism Parameters for H_2 Oxidation

3.5 Langmuir-Hinschelwood plus Eley-Rideal Model

This model, proposed by Nibbelke et al. [96], also uses elementary kinetics as a foundation. Here, a Langmuir-Hinshelwood (LH) mechanism has an additional Eley-Rideal step. Gas-phase carbon monoxide can react with adsorbed oxygen to form carbon dioxide. While many in the literature argue that the Eley-Rideal step does not occur, a mechanism for reacting gas phase carbon monoxide on a surface fully covered by an oxygen monolayer is critical to explaining some behaviour. The Eley-Rideal step is one means of providing this step. There is discussion in the literature about the Eley-Rideal step, with several groups suggesting that it does not occur on a platinum oxidation catalyst, and others suggesting that there is such a step [97].

3.5.1 CO Oxidation

In this model, CO adsorbs to the surface in a single step. Oxygen adsorbs to the surface, and then splits to form two separate adsorbed oxygen atoms. Both adsobed and gas-phase CO are allowed to react with adsobed oxygen

$$\mathrm{CO} + * \underset{k_1^b}{\overset{k_1^f}{\rightleftharpoons}} \mathrm{CO}^* \tag{3.16a}$$

$$r_1 = k_1^f C_{CO}\theta_* - k_1^b\theta_{CO^*} \tag{3.16b}$$

Oxygen adsorbs and subsequently dissociates.

$$\mathrm{O}_2 + * \xrightarrow{k_2^f} \mathrm{O}_2^* \tag{3.17a}$$

$$r_{2/3} = k_2^f C_{O_2}\theta_* \tag{3.17b}$$

$$\mathrm{O}_2 * + * \xrightarrow{k_2^f} 2\mathrm{O}^* \tag{3.18a}$$

$$r_{2/3} = k_2^f C_{O_2}\theta_* \tag{3.18b}$$

The oxidation reaction may occur with either both CO and oxygen adsorbed to the surface, or with only oxygen adsorbed. The product of oxidation, CO_2, quickly desorbs.

$$CO^* + O^* \xrightarrow{k_4^f} CO_2 + 2* \tag{3.19a}$$

$$r_4 = k_4^f \theta_{CO^*} \theta_{O^*} \tag{3.19b}$$

$$CO + O^* \underset{k_5^b}{\overset{k_5^f}{\rightleftharpoons}} OCO^* \tag{3.20a}$$

$$r_5 = k_5^f C_{CO^*} \theta_O - k_5^b \theta_{OCO^*} \tag{3.20b}$$

$$OCO^* \xrightarrow{k_6^f} CO_2 + * \tag{3.21a}$$

$$r_6 = k_6^f \theta_{OCO^*} \tag{3.21b}$$

$$O_2 + s \xrightarrow{k_7^f} O_2s \tag{3.22a}$$

$$r_{7/8} = k_7^f C_{O_2} \xi_S \tag{3.22b}$$

$$O_2s + s \xrightarrow{k_8^f} 2Os \tag{3.23a}$$

$$r_{7/8} = k_8^f C_{O_2} \xi_S \tag{3.23b}$$

$$CO^* + Os \xrightarrow{k_9^f} CO_2 + s + * \tag{3.24a}$$

Equation	Parameter	Value	Units	Source
3.16b	A_1^f	9×10^5	$m^3\ mol^{-1}\ s^{-1}$	[98, 99]
	A_1^b	5.65×10^{14}	s^{-1}	
	E_1^b	113	$kJ\ mol^{-1}$	
	$\frac{dE_A}{d\theta_{CO}}$	-8.5	$kJ\ mol^{-1}$	
3.16b	Alternative Value			[100] [a]
	A_1^b	8.16×10^9	s^{-1}	
	$E_1^{b'}$	86.5	$kJ\ mol^{-1}$	
	$\frac{dE_A}{d\theta_{CO}}$	-4.15	$kJ\ mol^{-1}$	
3.17b	A_2^f	1×10^5	$m^3\ mol^{-1}\ s^{-1}$	[98, 99]
3.18b	A_3^f	1×10^5	$m^3\ mol^{-1}\ s^{-1}$	[98, 99]
3.19b	A_4^f	2.81×10^{13}	s^{-1}	[99]
	E_1^b	96.8	$kJ\ mol^{-1}$	
3.20b	A_5^f	4.6×10^3	$m^3\ mol^{-1}\ s^{-1}$	[98, 99]
	E_5^f	0.0	$kJ\ mol^{-1}$	
	A_5^b	248	s^{-1}	
	E_5^b	20.3	$kJ\ mol^{-1}$	
3.21b	A_6^f	20.5	s^{-1}	[98, 99]
	E_6^f	12.1	$kJ\ mol^{-1}$	

---

[a] page 131, Table 6.5 [100]

Table 3.4: LH+ER Mechanism Parameters for CO Oxidation

$$r_9 = k_9^f C_{CO^*} \xi_O \tag{3.24b}$$

$$CO_2 + \gamma \underset{k_{10}^b}{\overset{k_{10}^f}{\rightleftharpoons}} CO_2\gamma \tag{3.25a}$$

$$r_{10} = k_{10}^f C_{CO_2} \delta_\gamma - k_{10}^b \delta_{CO_2} \tag{3.25b}$$

3.6 Simulator

Testing of the kinetics models against the data from experiments required a computer-based simulator. There are many different possible models that can be used, the most common of which is the single channel reactor model. This model assumes that a single channel is representative of the entire monolith, assuming that there are no radial temperature or concentration gradients, and that the reactor is perfectly insulated.

Single channel models may be one-dimensional, assuming no radial gradients and only considering axial variations in temperature and concentration. Cylindrical symmetry may be assumed, allowing for radial gradients and making the model two-dimensional. Should the true geometry of the channel be used, a three-dimensional model would need to be employed. While three-dimensional models may be truer to the experimental reactor, these models are expensive to run. One-dimensional models are simpler, and require fewer computer resources (CPU time and memory).

In this work, a simulator previously developed by Mukadi and Hayes [99] was used to model the reaction kinetics. This model assumes that the reactor is adiabatic and that the flow distribution is uniform; thus, a single channel is representative of the entire monolith reactor. Radial symmetry was assumed, allowing a significant reduction in the amount of computing power required.

The simulator models the fluid and solid phases separately, with coupling between the two phases occurring at the gas-solid interface. Either phase may be modelled in either 1 or 2 dimensions, independent of how the other phase is modelled. Axial symmetry was assumed in the channel (gas phase). Typical simulations performed in this work were 1D in the gas phase and 1D on the surface. Modelling the washcoat is optional, and requires considerably more CPU time to simulate. Due to the additional computation load, the washcoat was not typically used in this work, and is discussed more in subsection 4.4.4. All modelling modes may be run as transient simulations.

The relevant mass and energy conservation equations are solved in the simulator using the finite volume method [101]. The resulting set of non-linear equations was solved using a Newton-Krylov method with a pre-conditioned Generalized Minimal Residual Method (GMRES) algorithm. The simulator was written in Fortran 95 [102], and allowed for adaptive time-stepping. This model was used "off-the-shelf", and the source code was not modified. Elementary kinetic equations in the system could be defined by the user via a chemistry module.

3.7 Objective Function

To determine the best agreement between experimental and simulation data, the light-off temperature was typically used. For some comparisons, the observed and predicted results were compared by calculating the error by the least squares method, and then the error was compared for various values of coefficients.

3.8 Solving Differential Equations

The reactor is assumed to be adiabatic and with no radial temperature or concentration gradients. This allows the model to be simplified to a 1D single channel model, vastly improving the execution speed of the simulation. Plug flow is assumed with no radial concentration gradients inside the monolith channels

3.8.1 Initial Conditions

The initial reactor conditions were imposed with the assumption that there are no gradients in the system. The imposed initial solid temperature profile was uniform in temperature, as was the imposed initial gas concentration profile. Initial fractional surface concentrations were defined as stated in the simulation discussions, and were assumed to be uniform throughout the catalyst.

The solver progressed through the time range in steps. The defined initial conditions were used when solving over the first time step. When the solver reached a solution for a point in time, that solution was then used as the initial condition when solving over the following time step.

3.9 Input Files and Parameters

3.9.1 Reactor Physics

The simulated catalyst was defined as being a monolith 0.0762 m (3 inches) in length and 0.0254 m (1 inch) in diameter, consistent with the monolith used in the experimental studies. A cell density of 400 Cells Per Square Inch of a monolith (in^{-2}) (CPSI), or 62 cells per cm^2, was used. As radial symmetry was assumed, a single-channel was modelled, and the cell density and monolith dimensions were used to calculate the dimensions of the channel. 30 axial elements were used to model the axial dimension. Physical properties of the solid material and washcoat (such as the thermal conductivity, heat capacity, density, pore size diameter, porosity and tortuosity) were defined for the simulator. These values are shown in section D.4.

Gas phase components, surface sites and surface species were all defined in the simulator, and assigned properties. When those properties were temperature dependent, the appropriate equations were used to calculate the correct property value under the conditions at that point in space and time.

Every gas phase component had associated properties, and the thermodynamic, heat capacity, molar mass and diffusion volume (used to calculate diffusion using the Fuller equation as in Equation A.6) were defined. These properties and parameters are shown in more detail in section D.1.

Every component that adsorbs to or is formed on an active site is defined as a surface species. The thermodynamic properties of the various combinations of active site and the reacting component are shown with parameters in section D.3. Site and surface species were defined, as were the thermodynamic interactions between them for adsorption and desorption.

3.9.2 Mechanisms

All reaction steps and associated parameters and reaction stoichiometry were defined in the input files. The reaction stoichiometry is defined in this step, as well as the type of reaction. Reactions may be either reversible or irreversible, and may be either an elementary sticking step (which calls the sticking function), an elementary step (which uses the Arrhenius equation), or a user-defined step. The Arrhenius equation is shown in Equation 3.26. These reaction steps and parameters are shown in more detail in Appendix C and Appendix F.

$$k_i = A_i \cdot e^{\left(\frac{E_i}{RT}\right)} \tag{3.26}$$

A noble metal loading factor was defined in the model, to represent the concentration of surface sites. This value defines the overall activity of the catalyst, and would be influenced by such factors as preparation method, catalyst loading and ageing. While this value may be determined for a single catalyst, if the simulator were to attempt to model another catalyst with a different preparation method, this value may differ. As only one catalyst was used in the present work, this value only needed to be determined once. It is not the goal of the present work to determine a parameter set for all oxidation catalysts, but to develop a model that predicts the correct trends under varying conditions.

The noble metal loading factor affects not only all the activities, but also the accumulation of adsorbed species. When this value is set too high, there is the possibility of a large amount of a reactant being present on the surface. When the reaction ignites, much of this reactant may react, yielding a much larger exotherm (~200 K) than is normally seen in experiments. This large exotherm may also be attributed in part to the numerical solver.

To ensure that the initial surface coverages in the simulator were acceptable, sufficient time was allowed such that the system would be settled before significant events occurred. In a typically light-off simulation, light-off did not occur in the first 1200 times-steps (where 1 time-step = 1 second), affording the system sufficient time to come to an acceptable equilibrium state well in advance. In concentration step simulations, a typical step occurred after 400 time-steps, ensuring that surface coverages were constant and that any small errors in the initial estimate would not influence the final result.

Adsorption

Adsorption is modelled using sticking coefficients, and the standard model for calculating sticking coefficients (see section B.5) makes a number of assumptions with respect to the surface of the catalyst. These assumptions are outlined below:

- Each surface site is the same, and all components may bind to the site. This assumption disregards the differences between bridging and linearly adsorbed CO, as well as the differences between difference crystal surfaces (Pt(111), Pt(110), and Pt(100)). This assumption is assumed to be valid, as due to the relatively large number of available sites (compared to studies on a single crystal), the surfaces average out. Also, at higher temperatures, bridging CO is assumed to play a minor role and CO bonds dominately in a linear fashion [103].

- The heat of adsorption is assumed to be independent of surface coverage in the model. Although literature studies show that this is not entirely true [104, 105], the dependency of heat of adsorption on surface coverage is neglected.

- One component adsorbs to one surface site, and all components may adsorb up to monolayer coverage. The compressed oxygen submechanism (see section C.7) tests this assumption for oxygen, as in the referenced submechanism, adsorbed oxygen is allowed to form species that take up less than one surface site each. As well, preliminary tests limiting coverage to less than a monolayer are discussed in subsection 4.5.10.

- The dispersion of active catalyst particles is assumed to be equally distributed throughout the catalyst, a factor that has been shown in the literature to be important [106]. However, as no measurements of the dispersion are available and standard established methods were used to prepare the catalyst, as well to simplify the simulator and minimize required computing time, the dispersion of the particles was assumed to be equally distributed.

The equation for calculating the rate for an adsorption step is shown in the equation for sticking coefficients, shown here in Equation 3.27, and described more in section B.5.

$$k_i^{''} = \frac{S_0}{L_i^n}\sqrt{\frac{RT}{2\pi M_i}}\left(\frac{T}{T_0}\right)^{\beta_i} \cdot e^{\left(-\frac{E_i}{RT}\right)} \tag{3.27}$$

The temperature dependence term ($\left(\frac{T}{T_0}\right)^{\beta_i} \cdot e^{\left(-\frac{E_i}{RT}\right)}$) is explicitly stated here, but is not typically used. The density of active sites per unit surface area is as described in subsection B.1.2.

Simulations studying the effects of the sticking coefficients are discussed in 5.1.1.

Surface Reaction

Surface reactions are modelled based on elementary mechanisms which are outlined in section B.1 and section B.2. Additions and changes to these models are described in subsection 4.5.4, section 5.4 and section 5.9.

The equations used to calculate rates are described in more detail in Appendix B.

3.9.3 Washcoat

A thickness of 2.33×10^{-5} m was assigned to the washcoat on the catalyst support.

3.9.4 Numerical Solver Parameters

The numerical solver required a relative error (between two iterations) of less than 1×10^{-6} before considering the solution for that time step to have converged and to move onto the next step. If convergence was not reached, the simulation would end with an error and not proceed to the next timestep.

Although the simulator used variable timestep sizes, a solution was outputted and saved to a datafile for every 1 second. This allowed easier comparison to experimental data, which was also written in 1 second increments.

3.9.5 Reactor Conditions

The inlet and initial conditions were defined in simple text files, with each line representing a point in time. The simulator read these files in, and linearly interpolated between the defined points to determine the appropriate inlet conditions for the point in time that was currently being considered. Initial conditions were also defined in the input files. When the

MATLAB interface to the simulator, Umicore Simulation Interface (USI), was used, this program generated the necessary input files from data defined by the user in the interface.

Inlet Conditions

The inlet concentration profile over time for a temperature programmed reaction was defined in an input file. At any given timestep in the simulation, the simulator linearly interpolated between the two most appropriate time steps (the defined point before and the defined point later than the current point in time) to determine the current inlet concentrations.

The inlet temperature over time for a simulation was defined in an input file. This profile was linearly interpolated by the simulator between points in time in a similar manner as the inlet concentration was handled. When simulating a previously run experiment, the inlet temperature profile used for light-off simulations was taken from corresponding experimentally recorded data. The thermocouple immediately before the catalyst was used, as will be discussed in subsection 4.2.1.

3.9.6 Simulator Keywords

Keywords were available in the simulator to accomplish specific tasks. The keyword 'nonexothermic' allowed the user to quickly and easily redefine the heat of reaction of all reactions to be zero. This keyword was used for select simulations during investigations into the role of adiabatic temperature rise on the promotion of CO light-off by the presence of H_2 (subsection 5.9.1).

3.10 Simulation Output and Post-Processing

The simulations were performed using either a typical Windows XP laptop computer, or utilizing a binary compiled and executed on a Linux cluster (to increase simulation throughput). The Linux cluster was owned and operated by the Department of Chemical and Materials Engineering at the University of Alberta.

After successful completion of a simulation, the simulator wrote a series of output files detailing the results. These output files were then processed with a series of scripts. BASH [73] scripts and Microsoft Excel were used initially, however once the USI interface became available, post-processing of the results was performed within the MATLAB [74] framework. Final plotting and presentation of the data was performed with Origin [107] and Sigmaplot [75]. A series of scripts were written to assist in the running of a large number of simulations on the Linux cluster, greatly increasing the throughput and effectiveness of the cluster.

3.11 Comparisons With Other Catalysts Made Using Other Preparation Methods

It is understood that after finding agreement between this model and experimental data in this work, that if the catalyst is changed, that agreement may not be retained. However, the differences are expected to be in the catalyst loading and preparation. These steps may be accounted for by re-performing experiments and simulations to determine an optimized platinum loading factor. However, the model is expected to remain intact and able to describe the same trends and observations on a different catalyst using slightly different parameters (which have changed due to the catalyst preparation method). The goal of the current work is not to determine an optimized parameter set for all oxidation catalysts, but to use various models to determine the strengths and weaknesses of each, and build on those models such that they predict the correct trends under various conditions.

4

CO Oxidation on Platinum*

4.1 CO Oxidation on Platinum Catalysts

4.1.1 Platinum Catalysts

Platinum was first found to be useful as a catalyst by Langmuir in 1922 [110, 111]. Since this time, Pt has found uses in many applications. Automotive exhaust catalysis is perhaps the single most common usage of platinum catalysts.

γ-alumina (Al_2O_3) is the most common material used as a support for the washcoat, the material used to bind the catalyst particles to the ceramic monolith walls. At approximately 1050°C, γ-alumina changes structure to form δ-alumina, followed by a transition to θ-alumina at 1150°C and to α-alumina at approximately 1200°C [112]. Each of these transitions during the sintering process will affect the surface area of the alumina, with the sintering process decreasing the surface area available to the catalyst. With decreasing surface area, the number of available sites will also decrease, and the catalyst performance will diminish. However, these temperatures are significantly higher than those under typical oxidation catalysis reactions, and are thus not expected to be of significant influence.

4.1.2 Structured Catalysts

Monoliths have many applications as gas phase and gas-liquid reactors [113, 114], and are of particular use in environmental applications [115]. By far, the largest single application of monolith catalysis is in automotive catalysis. Monolith catalysts, such as that shown in

---

*a portion of this chapter has been published [108] in *Applied Catalysis B: Environmental*, and has been presented [109] at IWEC4, the 4th International Workshop on Environmental Catalysis in Heidelberg, Germany in June 2005.

Figure 2.7, allow for a relatively high surface area with a low pressure drop [116], compared to traditional packed bed catalysts. The low pressure drop makes the catalyst advantageous in an automobile, as less power is then lost to moving the exhaust gas. The high surface area allows a larger amount of active catalyst to be available for reaction in an effective manner.

Monoliths are often made from cordierite ($Mg_2Al_4Si_5O_{18}$) [118, 119], a material that is typically quite resistant to thermal shock.

4.1.3 Models of CO Oxidation on Pt Catalysts

Several different models of CO oxidation on Pt catalysts have been proposed in the literature. A global model was proposed by Voltz et al. [40] (section 3.3) as mentioned earlier.

Among them, LH (section C.2) and Eley-Rideal (ER) (introduced in section 3.5) are the most common models in current use. Other models include strong and weakly adsorbed oxygen (section C.4), multiple binding sites (section C.5), subsurface oxygen (section C.6), and carbon deposition (section C.10). These models are discussed in more detail in the following sections and in Appendix C.

4.1.4 Effect of Catalyst Preparation

The preparation of the catalyst may have a significant impact on its performance. The effects of altering the noble metal and washcoat [120], and different preparation methods and doping [121] have been documented in the literature. Arnby et al. reported that the sample with Pt distributed most heterogeneously (or most localized) was the most active towards CO oxidation in a distribution effect that was not caused by heat effects [122], but were inconclusive if this was a kinetic or a mass transfer effect. The effect of catalyst preparation was not studied in the present work.

4.1.5 Deactivation

Deactivation [123, 124] of monolith catalysts is typically due to thermal sintering and poisoning [125]. Thermal sintering occurs when the catalyst temperature rises too high, at which point the catalyst active sites are irreversibly altered and no longer active towards their intended uses. Reactivation of sintered catalysts may be achieved via oxychlorination [126] in some cases, however this is not a viable option for an installed automotive catalyst.

Poisoning of a catalyst may be either reversible, as in the case of CO poisoning, or irreversible poisoning by other agents. Lead was once used in fuel as an anti-knocking agent, however, lead deposits on catalysts covers active sites, fouling the catalyst over time. Beginning in 1973, lead has been banned as a gasoline additive in most districts.

4.1.6 Adsorption of Species onto the Active Surface

N_2 and CO_2 Adsorption

Adsorption of nitrogen and carbon dioxide on the surface can be ignored. Langmuir was unable to measure any nitrogen or carbon dioxide adsorption on a platinum surface [110]. Ford et al. [61] placed nitrogen (N_2) as the weakest binding molecular species on Pt(111). They continued to state that experimentally, nitrogen has not been found to adsorb to Pt(111) surfaces without defects. Nitrogen adsorption on the surface is not considered to be significant in the experiments presented here.

CO_2 adsorption at low temperatures (50-250 K) has been extensively discussed in the literature [127], and CO_2 has been described [128] as lowering the amount of available oxygen-storage sites, and slightly inhibiting oxygen adsorption. However, generally, adsorption of carbon dioxide to the catalyst surface is not considered to be significant under the conditions of interest for diesel oxidation. CO_2 is held weakly at surface, and will immediately desorb at room temperature [129, 130]. CO_2 adsorption is not considered to be significant in the experiments and simulations presented herein.

CO Adsorption

General consensus in the literature shows that, under the conditions of interest for diesel oxidation, CO binds to Pt in a terminally-bound, on-top site [130, 131]. Makowka and Slichter used ^{195}Pt NMR studies to confirm this, showing that the bond between CO and Pt is typically through the C atom [132].

Other studies [133] have shown CO binding to Pt not only in an on-top linear formation, but also bridge-bound and 3-fold hollow configurations. Bourane et al. observed linear, bridged and threefold coordinated on Pt/Al_2O_3 at 300 K in Temperature Programmed Desorption (TPD) experiments [104]. Ford et al. performed many calculations of adsorption on Pt, and reported that CO will bind in both the on-top and bridged configurations [61]. Szabó et al. showed that CO may adsorb in different configurations on Pt surfaces, but that the oxidation reaction was structure sensitive. Geometrically, the distance between adsorbed CO and adsorbed O is smaller when the reaction occurs on the terraced sites of stepped Pt(112), showing a geometrical ground for a favoured pathway through this configuration [134]. Craig and Hock performed Electron Stimulated Desorption (ESD) studies of CO on a recrystallised Pt ribbon, and observed that CO desorbed from only a single state [135]. For the purposes of the present modelling study, CO is assumed to bind only in the linear configuration.

The dependence of CO adsorption on surface coverages has been seen to be quite non-linear [136], with the rate slightly decreasing with increasing coverage at low coverages, but decreasing rapidly as saturation coverage is approached. Bourane et al. have measured the heat of adsorption of linear CO species on Pt, finding that the heat of adsorption decreased linearly with coverage, with 206 kJ·mol^{-1} at θ=0 to 115 kJ·mol^{-1} at θ=1 [137]. Ertl et al. assigned this observation to interactions between adsorbed particles, and stated that these interactions are important above $\theta = 0.5$ [138]. Schubert et al. considered adsorption energies for CO at high-coverage [139] and reported values of 85 kJ·mol^{-1} (Pt(111)), 97 kJ·mol^{-1} for Pt(533) and 151 kJ·mol^{-1} on Pt(321).

Saturation Coverage

Bissett et al. assumed that CO could completely saturate ($\theta_{CO} = 1$) the surface under PReferential OXidation (PROX) conditions [140]. Schubert et al. state that in all cases studied, CO coverage was close to saturation ($\theta_{CO} > 0.9\theta_{sat}$) [139], and stayed close to saturation even at lower CO partial pressures. However, others [141, 142] have reported saturation coverages as low as 0.44 monolayer (see Table 4.9). This topic is discussed in more detail in subsection 4.5.10.

CO Desorption

The rate of CO desorption is critical to the light-off temperature (as will be shown later in subsection 5.9.2). During a typical CO light-off experiment, with only CO, N_2 and O_2 present, the surface is typically CO covered, as shown in Figure 4.4. In order for oxidation to occur, oxygen must be afforded the opportunity to adsorb to the surface, and that opportunity is regulated by the rate of CO ad/desorption.

Values for activation energy for CO desorption vary in the literature, as shown in Table 4.1. The literature values have general agreement that the activation energy is 104 kJ·mol^{-1} on a CO saturated surface, however, they differ vastly on the value for low CO coverage. Zafiris and Gorte [143] showed that the particle size can also influence the activation energy of desorption, reporting values of 125.5 and 172 kJ·mol^{-1} for 14 and 1.7 nm particles, respectively. As the observed activation energy is typically close to the binding energy, and this energy may be more easily measured, the binding energy is often the value reported in literature.

Reference	E_a $kJ\cdot mol^{-1}$	$\frac{dE_a}{\theta_{CO}}$ $kJ\cdot mol^{-1}$	Comments
[143]	172 ± 16.7		1.7 nm particles
[144]	167.4	-62.8	
[145, 146]	146.4	-33	
[147]	137		Pt(100), 500-725 K
[66, 145]	136.4	-33	
[147, 111]	133		Pt wire
[66]	130.5		TPD
[148]	125.5		
[96, 149]	125	-27.2	
[143]	125.5 ± 12.6		14 nm particles
[150, 99, 151]	113	-8.5	
[136]	100		
[136]	84		
[147]	56.1		Pt/SiO_2 <450 K
[147]	54.2		Pt(100) <440 K
[147]	50.2		Pt/SiO_2 310-322 K
[147]	33.5-50.2		Pt/Aerosil 273-355 K

Table 4.1: CO desorption values from literature sources.

If CO desorption is too fast, then at high temperatures, insufficient CO will bind to the surface and the reaction will be incomplete. Experimentally, we know that this is not what is happening, as we see complete conversion above the light-off point under the conditions in this work.

Oxygen Adsorption

Oxygen typically adsorbs dissociatively onto a platinum surface under the conditions of interest in this work. At low temperatures (< 150 K), oxygen will adsorb molecularly to a platinum surface, and will desorb associatively at approximately 800 K [90]. However, above ~140 K, no adsorbed O_2 was found on the surface [53], and oxygen adsorbs dissociatively [89, 130]. Due to these observations, oxygen adsorption is assumed to be dissociative and irreversible in the range of temperatures in the present study.

At low temperatures, many different configurations are available to adsorbed oxygen on Pt surfaces. Stipe et al. have outlined several configurations available on Pt(111), including both molecular and atomic adsorbed species [152].Others [135, 153] have published results of multiple states of oxygen adsorption on specific surfaces. This has been echoed in high-temperature mechanisms proposed by Bianchi and coworkers [154, 155] and others (see section C.4). The true nature of oxygen adsorption on Pt under the conditions of interest for diesel catalysis are still under debate, but the general consensus is that oxygen adsorbs dissociatively and irreversibly in the temperature range 250-800 K.

Surface coverages of oxygen have been reported in the range of 0.25 [156] to 0.82 [89] of saturation coverage (values summarized in Table 4.9). Légaré found that, on a Pt(111) surface, no adsorption is stable beyond $\theta = 0.5$ monolayer, with the exception of a subsurface tetrahedral site [157]. However, even this site was not stable past $\theta = 0.75$ monolayer. Parker et al. used Atomic Emission Specstroscopy (AES) to determine surface coverages of oxygen atoms on a Pt(111) surface [54], producing a saturated chemisorped surface at 0.75 monolayer by use of NO_2 exposure.

At low coverages, oxygen tends to form islands on the surface [158, 95], however, studies using radiolabelled oxygen atoms show that there is no preferential reaction at the island perimeters [53]. Oxide formation [159, 60], oxygen compression [159] and subsurface oxygen [160] have also been discussed in the literature. Typical studies of these phenomena were performed under Ultra High Vacuum (UHV).

4.1.7 Surface Mass Transfer

Particles have been know to be able to diffuse on surfaces for quite some time now [161], and this diffusion may influence the distribution of molecules on the surface, the average proximity of a molecule to a nearby reactant, and thus the reaction rate. As diffusion occurs from regions of high concentration to regions of low concentration, surface diffusion helps to keep the distribution of adsorbed molecules more equally distributed on the surface. More mobile atoms, such as adsorbed hydrogen, may be very quickly and easily distributed along the surface, reducing the influence of adsorbed islands of concentration.

Diffusion by thermal random walk typically begins to appear at 200 K. Another mechanism, a 'hot' atom diffusion mechanism, was reported for oxygen atoms adsorbed onto Pt(111) [162]. It is expected that at elevated temperatures the thermal random walk is the more significant of the two surface diffusion mechanisms. As the activation energy of migration of oxygen atoms is approximately 20% of the metal-oxygen bond strength, the surface mobility of adsorbed oxygen atoms is much lower than that of adsorbed carbon monoxide [130]. If this is significant, it is expected to be more influential during times of low oxygen surface coverage.

4.1.8 Oxidation of CO on Pt

Recently, much debate on CO oxidation on Pt catalysis has centred upon whether the mechanism proceeds via an ER or a LH model. While the ER mechanism was favoured in early studies [163, 164], general consensus in recent studies have favoured a LH based mechanism [163, 50, 52, 165, 166, 66, 65, 87, 167, 62, 168, 144, 169, 170]. The difference being that in an LH mechanism, all components adsorb to the surface first, and then react, whereas in an ER mechanism, gas phase CO is permitted to react with adsorbed oxygen. It has also been stated [171] that when the Pt surface is partially covered with CO and exposed to O_2, the oxidation proceeded by LH, while the ER mechanism was the dominant pathway when the surface was saturated with oxygen and exposed to CO. Campbell and co-workers [50] confirmed by molecular-beam experiments that the LH reaction occurs on the surface [62], and this has been confirmed with theoretical studies [172].

However, these models on their own do not explain all observed phenomena, as will be shown, and ER models are still in current use [97, 65, 87, 99, 173, 174, 175]. In the present study, both the ER and LH models are considered and tested (see section 4.5), and modified mechanisms will be presented that build on these mechanisms to describe the observed results.

4.1.9 Unsteady Behaviour

Various types of unsteady behaviour have been observed in oxidation experiments, both in the present study and in literature. Perhaps the first to detect oscillatory behaviour [176] of CO + O_2 on a Pt surface were Hugo and Jakubith [177] and Beusch et al. [178].

Poisoning Fronts

A monolith system is much more complex than a single-crystal system, and not all points in a monolith may necessarily be under the same temperature and concentration conditions at the same time. It is entirely possible that a reaction is occurring at a relatively high rate in one region of the monolith, and at a relatively slow rate in another part. This must be considered when interpreting the experimental results.

Poisoning of the monolith by CO typically occurs starting at the entrance to the catalyst, and proceeds towards the rear. This follows the direction of flow, and as the inlet concentration is usually the highest CO concentration in the system, the inlet is the first to be poisoned by CO. This process is said to be accelerated when CO levels exceed 50 ppm [179], and this work will show the effect of CO in concentrations up to 2000 ppm.

Non-Linear Dynamics and Surface Effects

Many studies have been performed on crystal surfaces [180, 88], showing oscillations and other phenomena on the surface. Oscillations may arise from several varied phenomena, and have been described in the literature using various models (see 4.1.9 and 4.1.9).

Ertl et al. reported oscillations in the oxidation of CO on clean Pt surfaces [181], and attributed these oscillations to variations in the sticking coefficient of oxygen on each phase. Lynch and Wanke presented a mechanism for these oscillations [182], which is presented here in Equation 4.1 through Equation 4.5.

$$CO_{(g)} + M^{*} \rightarrow CO - M^{*} \tag{4.1}$$

$$O_{2(g)} + 2M_{1}^{*} \rightarrow 2O - M^{*} \tag{4.2}$$

$$O_{2(g)} + 2M_{2}^{*} \rightarrow 2O - M^{*} \tag{4.3}$$

$$CO - M^{*} + O - M^{*} \rightarrow CO_{2(g)} + 2M^{*} \tag{4.4}$$

$$CO_{2(g)} + S \rightleftharpoons CO_{2} - S \tag{4.5}$$

According to Lynch and Wanke [182], only one of Equation 4.2 and Equation 4.3 will be active at any one time, depending on the phase of the metal catalyst. The surface coverage of CO on the surface influences the metal phase and therefore determines which step is dominant. As the oxygen sticking coefficient is higher when adsorbing to a (1x1) surface (Equation 4.3) than to a (5x20) surface (Equation 4.2), the rate of oxidation of CO is also affected, being higher on the (1x1) surface. On a CO dominated surface, adsorbed oxygen available to react with CO is relatively scarce, compared to an oxygen dominated surface, where adsorbed oxygen is readily available for oxidation. The sticking coefficient of CO onto Pt is generally accepted to be much higher than the same for oxygen (Table 5.1).

The transition from the (5x20) phase to the (1x1) phase occurs when the fractional surface coverage of CO exceeds some critical value ($\theta_{CO,critical,A}$). Above this value, the surface is in the (1x1) phase and reactivity is high. When the surface coverage of CO decrease below some other critical value ($\theta_{CO,critical,B}$, where $\theta_{CO,critical,B} < \theta_{CO,critical,A}$), the surface transitions back from (5x20) → (1x1) and to lower reactivity.

Hendriksen et al. studied CO oxidation by switching between CO-rich and O_2-rich feed mixtures and monitoring the catalyst using scanning tunnelling microscopy. The mechanism of oscillation was observed to be dependent upon the pressure, where the effects responsible for low-pressure oscillations were not significant at atmospheric pressure [183].

Surface Structure	(5x20)	(1x1)
Reactivity	low	high
Dominant surface species	CO-Pt	O-Pt
Fraction of surface with large O_2 sticking coefficient	low	high

Table 4.2: Surface Phases during CO Oscillations on Pt(100).

At atmospheric pressures, the generally accepted explanation for CO oscillations on polycrystalline surfaces is that proposed by Sales et at. [184], whereby switching between the two reactive branches is caused by the formation of a non-reactive oxide. An oxide forms during periods of high oxygen coverage (and thus high reactivity), blocking sites from reaction with other species. As sufficient sites become blocked, the system reverts to the low-reactivity state. CO on the surface then may react with the oxide and reduce the surface, unblocking reactive sites [183]. Once some critical value of available sites is reached, the reaction may jump to the higher reactive state and begin the cycle once again. In this model, the reduction rate of oxide sites is thought to vary directly on CO coverage, whereas the oxidation rate is thought to not depend significantly on CO coverage.

As a large monolith is used in the studies in this work, and not a single crystal, it is not likely that surface oscillations will be observable. Due to the large number of active sites available on a monolith, and the scale on which surface oscillations are typically observed, these oscillations are expected to average out and not be significant under the conditions of interest to diesel oxidation catalysts.

Oxygen Islands

Islands of oxygen have been proposed to form on the catalyst surface. These islands have been described in Monte Carlo simulations [62] and in surface studies [53]. Akhter and White claim that not only is the reaction rate dependent on the square root of oxygen coverage [53], but that the reaction rate depends on the initial coverage and the history of oxygen islands on the surface.

Wintterlin et al. [185] proposed that CO oxidation reaction occurs exclusively on the edge of the oxygen islands [186], however, Akhter and White used radiolabelled oxygen atoms to show that there is no preferential reaction at the island perimeters [53]. They stated that CO is be able to diffuse into and out of the oxygen islands, as well as adsorb into and desorb from these islands. CO desorption from within an oxygen island was stated to be negligible, and at the conditions of interest in the present work, the temperature would be sufficient that oxidation would occur much more often than CO desorption from within the island.

These oxygen islands are described as able to be compressed [159] to occupy less than one surface site per atom. This phenomenon is discussed in more detail in subsection 4.5.4 and section C.7.

Reduction Model

The reduction model was first described in by Sales et al. [184], where adsorbed oxygen on the platinum surface was described as slowly forming an oxide state [187] in a subsurface layer. This layer can deactivate the surface by blocking adsorption of other species, but the oxide can be removed by reaction with adsorbed CO [188]. Above an upper-threshold value, the rate of reaction decreases, allowing the surface to reduce. Once a lower oxide threshold is attained, the reaction switches back to the higher reaction rate, allowing the rate of oxidation to become larger than the rate of reduction. This effect manifests itself as an oscillating reaction.

The concept of subsurface oxygen has appeared in several other studies [189, 190, 153, 191, 192] as well.

Carbon Model

The slow catalyst deactivation by atomic carbon impurities blocking adsorption sites characterizes the carbon model [193]. The source of the carbon may be either atomic carbon diffusing along the surface, or carbon from gas-phase hydrocarbons. Surface carbon is removed via one of three steps: reaction between adsorbed carbon and an adsorbed oxygen atom to form CO, reaction between adsorbed carbon and gas-phase oxygen to form CO_2, and the reaction of a gas-phase oxygen with two adjacent adsorbed carbon atoms to form two CO molecules [188]. The cyclic nature of the carbon model stems from oscillations in the rates of site activation and deactivation.

Both the carbon model and the reduction model are not expected to have a significant influence on the results of light-off temperatures. When a light-off experiment begins, there may be oxygen adsorbed to the surface. This adsorbed oxygen may begin to undergo the cyclic oxidation-reduction cycle when both oxygen and CO are present in the system, however it is expected that at low temperatures, the cycle will be quickly extinguished by CO dominating surface sites and new oxygen not being able to adsorb in significant quantities before ignition. In addition, the cyclic nature of many active sites may cancel out any observable effect, as each cycle is out of sync with the others, and the average rate (which is relatively constant over a large number of active sites) is that which is observed.

The formation of carbon is tested for in concentration step experiments, which is discussed in subsection 4.5.8.

Self-Exclusion Model

Exclusion models proposed by Herz and Marin [149] were based on the same basic reactions (Equation 3.6a, Equation 3.7a, Equation 3.8a and Equation 3.9a). They cited evidence [194, 195, 129] that maximum coverage of CO and oxygen were 1.0 and 0.5, respectively, and proposed two models. The rate expressions for their first model were:

Adsorption of CO:

$$r_{exc,ads,CO} = F_{CO} \cdot S_{CO} \cdot (1 - \theta_{CO} - \theta_O) \tag{4.6}$$

Desorption of CO:

$$r_{exc,des,CO} = k_{exc,des,CO} \cdot exp\left[\frac{E_2 - \beta\theta_{CO}}{RT}\right] \cdot \theta_{CO} \tag{4.7}$$

Adsorption of O:

$$r_{exc,ads,O} = 2F_{O_2} \cdot S_O \cdot (1 - f\theta_{CO} - N\theta_O)^2 \tag{4.8}$$

Surface reaction:

$$r_{exc,surf} = k_{exc,surf} \cdot exp\left[\frac{E_4}{RT}\right] \cdot \theta_{CO} \cdot \theta_O \tag{4.9}$$

In the above equations, F is the frequency of collision of gas phase molecules (here for either CO or O_2 molecules) with metal surface atoms, S is the sticking coefficient (see 3.9.2) for the respective CO or O species, β is a constant that depends on the CO-metal bond strength (coverage dependence of the heat of adsorption), and N is a constant which depends on the maximum surface coverage of each species (to which they assigned a value of 2). θ_{CO} and θ_O represent the fractional surface coverage of CO and O, respectively, and the rate constants for the desorption of CO from the surface and the surface reaction are represented by $k_{exc,des,CO}$ and $k_{exc,surf}$, respectively. As the rate constants are in units of s^{-1}, the rate of reaction is also stated in units of s^{-1}. The factor f is given by:

$$f = \left(\frac{1 - N\theta_O}{1 - \theta_O}\right) \tag{4.10}$$

In their second model, they proposed a different equation for the adsorption of oxygen:

$$r_{exc,ads,O} = 2F_{O_2} \cdot S_O \cdot (1 - f\theta_{CO} - N\theta_O)(1 - N\theta_O) \tag{4.11}$$

Lynch and Wanke [196] also used a model similar to this second form, with N ∈ [1,2].

4.2 Experimental Results - CO Light-Off Curves

In the CO light-off experiment performed using the forementioned Pt catalyst, the reactor and feed gas had an initial temperature of approximately 350 K. The temperature of the feed gas was then increased at approximately 0.133 $K \cdot s^{-1}$ (8 $K \cdot min^{-1}$) from 350 to approximately 623 K, where it was held constant for approximately 30 min, after which all temperatures in the monolith were higher than approximately 570 K. The feed temperature was then lowered by approximately 0.038 $K \cdot s^{-1}$. The cooling rate was governed by the cooling rate of the furnace used to heat the feed gas.

The first experiment performed used an inert gas (N_2) to measure the temperature profile in the monolith for the purpose of determining the appropriate inlet temperature to use for simulations.

4.2.1 Inlet Gas Temperature Ramp

The inlet temperature over time for light-off curve simulations was defined by the measured temperatures from the experimental run with which the data was to be compared. The temperature profiles measured during each temperature ramp were used to create the inlet temperature profiles for the corresponding temperature-programmed simulations.

When simulating a previously run experiment, the inlet temperature profile used for light-off simulations was taken from corresponding experimentally recorded data. The thermocouple immediately before the catalyst was used.

When the measured value from the thermocouple (TC_01) directly in front (5 mm) of the monolith is compared to the thermocouple inside the monolith (TC_02) that is closest to the front of the monolith (7 mm), the measured values can be seen to be quite similar, as shown in Figure 4.1. Errors due to gas temperature measurements and radiation adsorbed by the thermocouple in front of the monolith appear to be relatively small. This was a consistent observation for these two thermocouples for the experimental light-off curves. In addition, during step-up experiments, the heat of reaction did not have a significant influence on the measurement in front of the catalyst (TC_01).

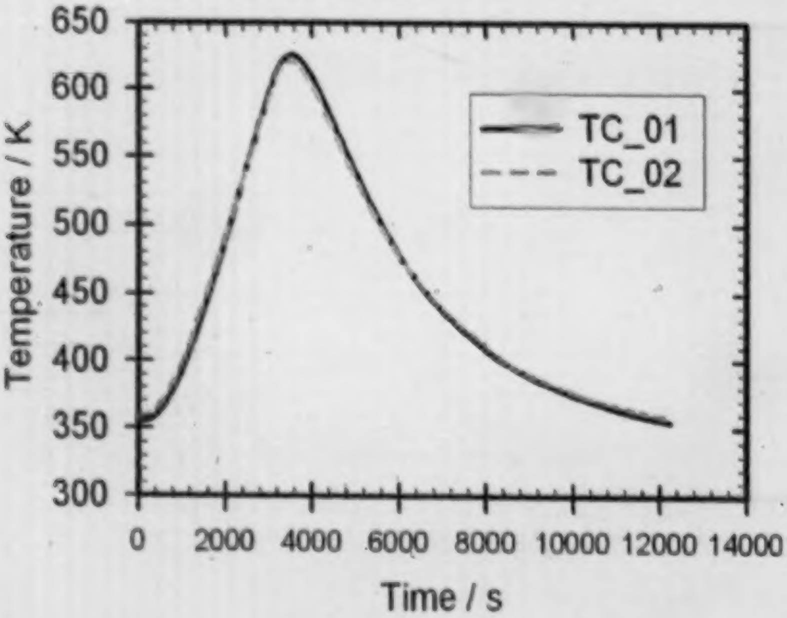

Figure 4.1: Typical feed temperature imposed upon light-off simulations. This temperature profile is from the 500 ppm CO light-off experiment.

The effect of the ramp rate on light-off temperature was assumed to be very low. When the light-off rate is very fast, the determined light-off temperature may be inaccurate due to temperature effects and movement of thermal energy inside the monolith. However, as the ramp rate was relatively slow (typically ~7.5°C·min^{-1}), the monolith was assumed to be in a pseudo-steady state. The same ramp-rate was used for all light-off experiments presented in this work.

The experimentally measured value for TC01, the inlet gas thermocouple which is ~5 mm in front of the monolith in the gas stream was used for each respective simulation of an experiment. That is, for the 1500 ppm CO temperature-programmed simulation, the measured gas inlet temperature for the corresponding 1500 ppm CO temperature-programmed experiment were used as the gas inlet temperature for the simulation.

The profile for all seven thermocouples is shown in Figure 4.2. While this shows a difference in the temperatures at higher temperatures, it is important to note that the light-off temperature is typically around 400-440K, and above the light-off temperature we see complete conversion. As well, both light-off and light-out begin at the front of the

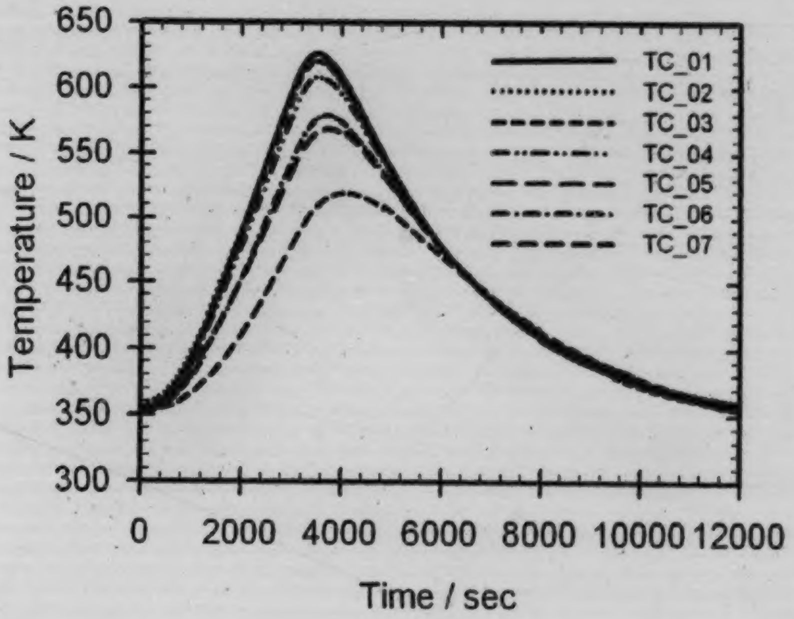

Figure 4.2: Typical feed temperature imposed upon light-off simulations. This temperature profile is from the 500 ppm CO light-off experiment.

monolith and move back. Heating bands were placed around the outside of the reactor to minimize heat losses at the temperatures near the light-off point.

Figure 4.1 also shows that the rate of cooling is slower than the rate of heating. This is due to the thermal mass of the oven and the relative strengths of active electrical heating and air cooling. Cooling air was available for cooling the oven, and was controlled by an electric valve.

4.2.2 Light-off At Various CO Concentrations

Four light-off experiments were performed at various CO concentrations. In all cases the feed contained 6 vol.% oxygen, with either 500, 1000, 1500, or 2000 ppm of CO. In each case, the start-up procedure was first to flush with nitrogen for 1 min, followed by addition of oxygen, which was allowed to flow for a further minute, and finally addition of CO. This condition was held for 8 min before commencing the temperature ramp. The results are shown in Figure 4.3. The light-off (or ignition of temperature ramp-up) curves are reproduced for comparison in Figure 4.3A, and the corresponding light-off (extinction, or temperature ramp-down) experiment is shown in Figure 4.3B. Table 4.3 shows these results in tabular format.

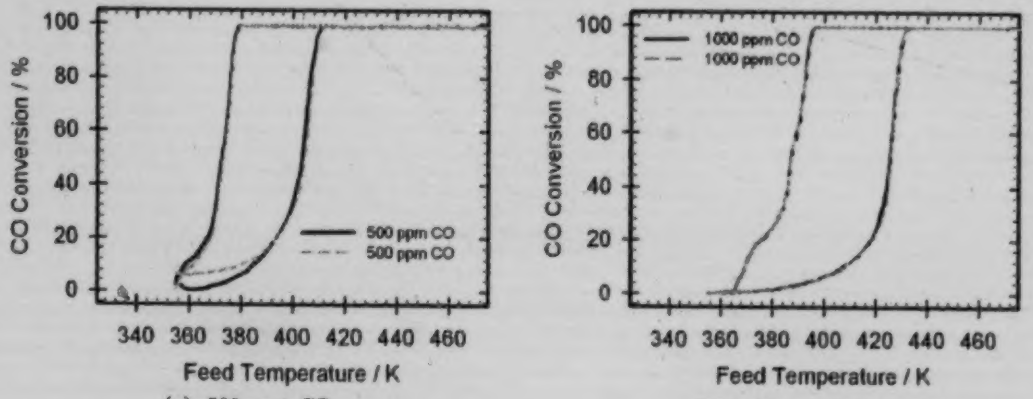

(a) 500 ppm CO

(b) 1000 ppm CO

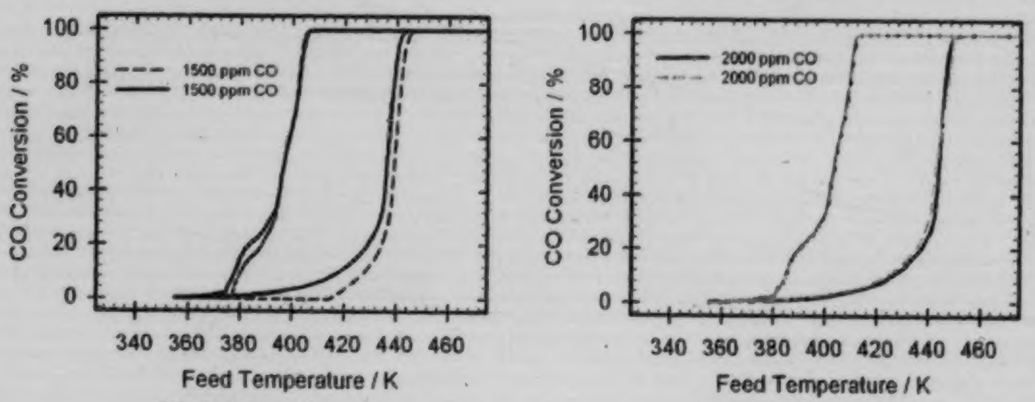

(c) 1500 ppm CO

(d) 2000 ppm CO

Figure 4.3: Light-Off Curves at various levels of CO. 6% O_2, rest N_2. SV = 25000 hr^{-1}. Multiple experimental runs are shown.

The overall surface coverage of the catalyst during light-off and light-out is well established in the literature, and typically proceeds via a LH mechanism. More details about the mechanism will be discussed later. At low temperature (approximately room temperature), CO dominates the surface sites. The sticking coefficient for CO is much higher than for oxygen. If there is a small amount of oxygen on the surface, CO may slowly consume this oxygen, but the available free sites will be dominated by adsobing CO. As CO adsorbs to the catalyst surface so readily, it blocks oxygen from adsorbing (see 4.2.2A). Without oxygen

CO Concentration (ppm)	Water Concentration (%)	Light-Off Temperature (K)	Light-Out Temperature (K)	Δ Temperature (K)
100	0	not observed	not observed	
500	0	404	373	31
500	0	404	373	31
500	0	425	380	45
500	0	397	380	17
500	0	408	—	
500	0	406	376	30
500	0	413	371	42
500	0	402	364	38
500	0	415	359	56
1000	0	426	388	38
1000	0	426	387	39
1000	0	429	376	53
1000	0	415	376	42
1000	0	447	375	72
1000	0	431	357	74
1500	0	439	397	42
1500	0	436	397	39
1500	0	445	358	87
2000	0	444	404	40
2000	0	443	404	39
2000	0	431	391	40
2000	0	441	393	48
2000	0	443	393	50
2000	0	457	395	62

Table 4.3: CO light-Off and light-Out temperatures at various CO concentrations.

on the surface sites, no reaction takes place. Thus, CO can self-poison the surface at low temperatures.

This self-poisoning effect of CO is, however, fully reversible. As the temperature of the catalyst increases, the rate of desorption of CO increases. As the rate of CO desorption increases, there is an increase in the turnover of free sites, and oxygen has more opportunities to adsorb to the surface. As the oxygen concentration on the surface increases, the rate of reaction also increases. As the rate of rate of reaction increases, so too does the rate of turnover of free sites, increasing the probability that oxygen will adsorb to the surface. This cycle accelerates as the reaction "lights-off" (ignites) and approached complete conversion. Once complete conversion is attained, the reaction is limited by the inlet flow rates of the reactants.

The light-off (ignition) curve is limited by the rate of oxygen adsorption, which is limited by the availability of free sites and hence the rate of CO desorption. The critical parameter that determines the light-off point is the rate of CO desorption. This is often referred to as the low-rate branch.

As the concentration of CO in the inlet gas increases, the light-off temperature also increases. When more CO is present in the feed gas, more CO is present in the bulk ready to adsorb to the catalyst surface, reducing the relative competitiveness of oxygen adsorption and increasing the light-off temperature.

At temperatures significantly above the light-off temperature, the reaction proceeds to completion. At higher temperatures, reactions kinetics are not limiting, and molecules are reacting as fast as they can be brought into the reaction and adsorb to the catalyst surface.

After the reactor has stabilized at a high temperature, the reactor is then cooled at a relatively slow rate and the outlet gases monitored. The surface is oxygen-covered at this time. As the temperature decreases, the reaction may still proceed to completion at the light-off temperature. However, slightly below the light-off temperature the reaction begins to diminish and no longer goes to completion. As the temperature decreases, the rate of the surface reaction also decreases. At some critical temperature, the rate of surface reaction becomes slower than the rate of CO adsorption. As CO begins to adsorb to the surface faster than it is consumed, it begins to dominate the surface and the relative competitiveness of oxygen adsorption decreases. The rate of reaction decreases, and CO self-poisons the surface, extinguishing the reaction. At temperatures significantly below the light-out temperature, there is no reaction and the surface is CO covered. The critical parameter in determining the light-out temperature is the rate of surface reaction. This part of the experiment is often referred to as the high-rate branch.

The adiabatic temperature rise of reaction and the differing surface states are often cited as the causes of the differences between the light-off and light-out temperatures, however, these have not yet been successfully modelled for a complete set of experiments.

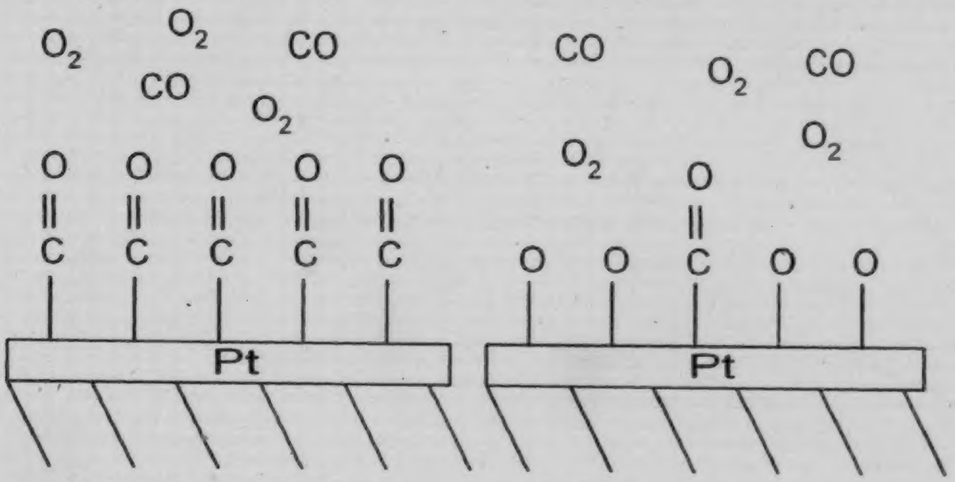

(a) CO covered surface pre-light-off (b) O covered surface Post-light-off

Figure 4.4: Surface coverages before and after light-off. (a) shows the so-called low-rate branch, where the surface is dominated by CO and the rate of reaction is very slow and limited by the rate of oxygen adsorption (which is inhibited by CO adsorption). (b) shows the high-rate branch, where the reaction rate and conversion are both high, and the surface is dominated by adsorbed oxygen. On the high-rate branch, the turnover of free sites is high enough that CO adsorption to the surface does not limit the overall rate of reaction significantly.

4.2.3 Moving Extinction Fronts

Ignition typically began at the back of the monolith and progressed to the front. This was most likely due to the reaction exotherm slightly increasing the reactor temperature in the rear of the monolith.

Extinction starts at the front of the monolith, where the CO gas concentration is higher. When the reaction goes to completion, all the CO may be consumed in the first portion of the monolith, with the later portions contacting a bulk phase with no significant CO. As the front portion of the reactor extinguishes, the reaction front pushes towards the back of the reactor, (relatively slowly) poisoning the catalyst surface from front to back.

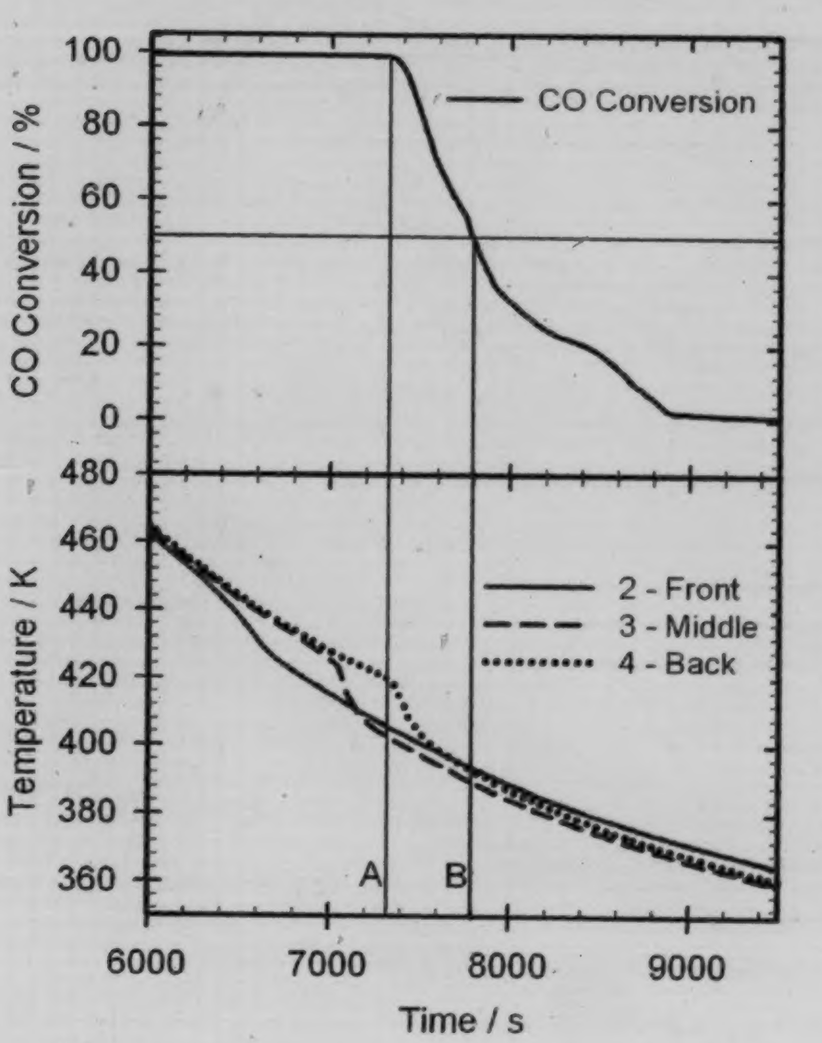

Figure 4.5: Temperature profile during the extinction of 1500 ppm CO. 6% O_2, rest N_2. SV = 25000 hr^{-1}.

Moving extinction fronts have been observed in a typical light-off/light-out experiment. In Figure 4.5, the measured temperature along the monolith centreline and CO conversion at the reactor exit are shown in parallel. At each thermocouple there is a point at which the temperature drops This point is more obvious for the middle and back thermocouples. When an extinction front moves past a thermocouple, the heat of reaction is no longer contributing to the temperature measurement as no (or only minor) conversion is taking place up to that point in the monolith. Over time, this extinction front moves towards the rear of the monolith, being pushed partly by convective heat transfer from the cooling inlet gas. However, no change in the outlet conversion is observed until the extinction front reaches the thermocouple at the rear of the monolith (at point A). The decrease in conversion and the temperature drop at the rear of the monolith coincide, and at all temperatures lower than this point, the reaction is incomplete.

An extinction front does not imply that there is zero conversion on one side, but rather that on one side of the extinction front the reaction is on the high-rate branch and on the other side, the reaction is on the low-rate branch. Minor contributions to conversion may still be made by sections of the monolith on the low-rate branch, as shown by the slow extinction of the entire monolith after "light-out" is achieved (i.e. all points after (B)).

7

4.3 CO Step Functions

Step change experiments in CO concentration at constant temperature and in an oxygen-rich environment yield information regarding the transition of the surface between a CO and an oxygen covered surface, and back again. Using these step experiments, details regarding the kinetics and reaction pathways may be obtained. As well, since the rate of oxidation depends upon the surface concentrations, during these transitions, this rate varies strongly. Experimentally, these transitions from an oxygen covered surface to a CO covered surface have been observed before on Pd and Pt [130]. However, to the knowledge of the author, these concentration steps in CO have never before been modelled.

An accurate model of concentration steps is very important when establishing a control system for a catalytic converter that considers the changes in catalytic performance when significant changes in the inlet composition occur (perhaps due to sudden variations in driving conditions such as acceleration and deceleration).

4.3.1 Reproducibility of Results for CO Step Functions

The CO concentration step experiments were reproducible. Figure 4.6 shows 4 CO step functions, all of which are 0-1000-0 ppm CO at 391 K with 10 minutes between each step up or down. Not only is the shape of each curve similar, but the steady-state conversion as well. Based on these results, it may be assumed that these experiments are reproducible. The step-up for each stop shown in Figure 4.6 is shown in Figure 4.7, where the shape of the step may be inspected more closely, and can be seen to be reproducible.

4.3.2 Experimental Results - CO Steps

During a step down in concentration, such as in Figure 4.9, the system moves from a state of high CO surface coverage to a state of high oxygen coverage. When CO is removed from the inlet gas, no more CO adsorption occurs. CO desorption occurs, but only oxygen is available to adsorb to the available free sites. During the brief transition period, the surface has significant coverages of both adsorbed CO and oxygen, and the rate of CO oxidation is relatively high. However, as this progresses, all CO in the system either desorbs and leaves or is oxidized and not replaced. As the CO supply diminishes, the rate of oxidation decreases to zero.

Nett-Carrington and Herz [136] also looked at CO concentration steps, and found similar peaks in CO_2 production during steps down in concentration. Their studies reported that the surface reaction between adsorbed CO and oxygen was the rate-determining step during the step down in CO concentration.

Figure 4.10 shows a typical increasing concentration step in CO concentration. The system begins with an oxygen covered surface (with no adsorbed CO). As CO was introduced into the system, the surface underwent a transition from being oxygen dominated to being CO dominated. Briefly during the transition, both CO and oxygen cover the surface in significant quantities, and the rate of oxidation (Equation 3.10a) may proceed very quickly. However, the supply of adsorbed oxygen on the surface is quickly exhausted, and the reaction then becomes limited by the rate of oxygen adsorption.

As the rate of oxygen adsorption is inhibited by CO, increasing the quantity of CO introduced into the system further inhibits oxygen adsorption, and hence increasing CO decreases the rate of CO oxidation. CO is self-inhibiting.

These peaks in CO_2 production lasted on the order of 60 to 100 seconds from the initial change in inlet to finally settling at an intermediate steady-state value. During experiments with fast switches and concentration pulses, on the order of 5-10 seconds, the settling of the peak would never be observed as the system would never have time to reach that point in the process.

Moving Reaction Front During Concentration Steps

Figure 4.11 shows the temperature profile during a step up from 0 to 1000 ppm CO (the outlet concentration profile is shown in Figure 4.7 and Figure 4.8). Shown here are thermocouples 1-5, placed along the centreline, with #1 immediately in front of the monolith, #2, #3 and #4 along the centreline inside the monolith, and #5 immediately following the monolith. Detailed thermocouple locations are described in Figure 2.6 and Table 2.2.

The thermocouple immediately preceding the monolith is not affected by the exotherm during the experiment. The temperature profile presented in Figure 4.11 is similar for all four steps shown in Figure 4.7 and Figure 4.8.

In this temperature profile, we see that the first point to experience a slight temperature increase is at the front of the catalyst. However, as the adsorbed oxygen on the surface is quickly consumed and the exothermic temperature rise quickly removed by convective thermal energy transfer, this temperature peak is short lived. The thermocouple in the middle of the monolith registers a temperature rise larger in magnitude but slightly later than the first. The slight delay may be due to mass transport and the oxygen covered surface in the front half of the monolith reacting being consumed first, and the reaction front moving towards the exit of the monolith as oxygen is consumed. As this reaction front moves towards the reactor exit, it carries thermal energy from preceding reactions along with it, and thus the later thermocouples register a much larger temperature rise than the former.

Also of interest is that the peak temperature measured by thermocouple #4 is approximately 14 K higher than the steady-state temperature before the introduction of CO. The adiabatic temperature rise for 1000 ppm CO is 10 K. As CO conversion briefly peaks near complete conversion, but then settles to a lower steady-state value, this difference is attributed to localized hot spots appearing in the reactor, producing localized super-adiabatic temperature rises.

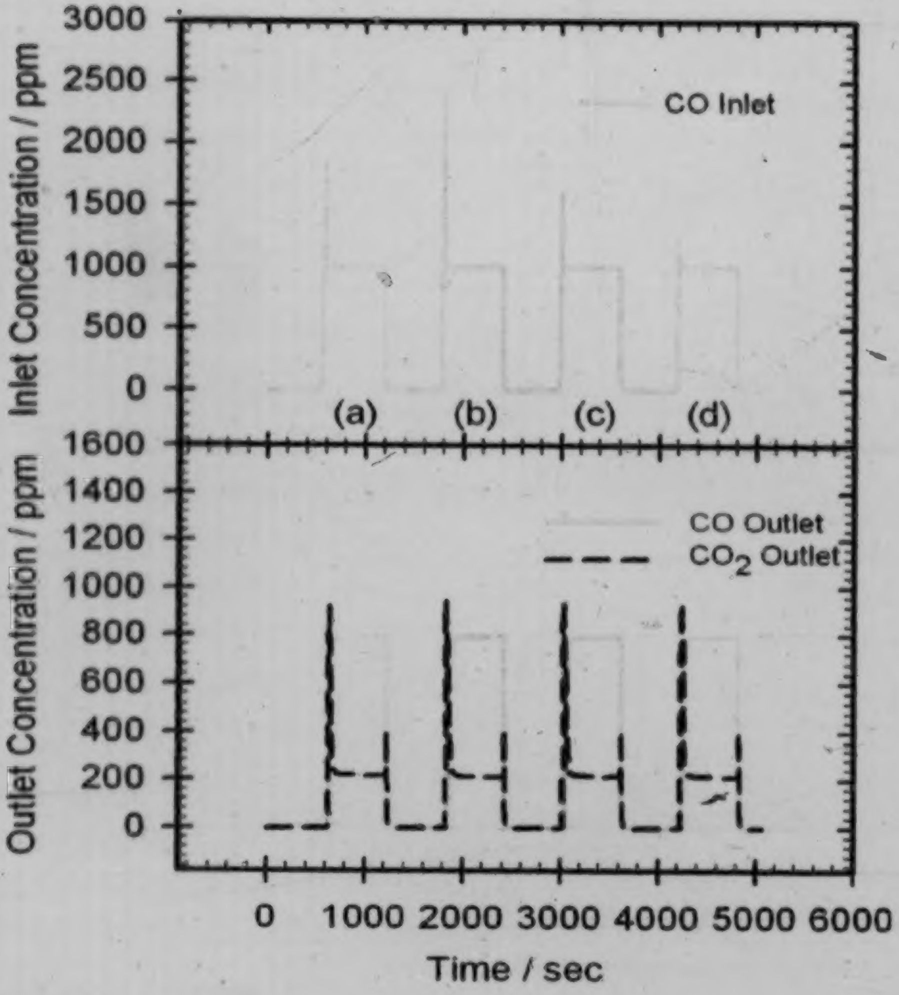

Figure 4.6: 4 steps from 0 ppm to 1000 ppm to 0 ppm CO, showing the reproducibility of experiments. 6 % O_2, rest N_2. SV = 25000 h^{-1}. Constant temperature at 391 K. The instantaneous spikes in CO inlet during step up are part of the mass flow controller response. Individual steps are shown in more detail in Figure 4.7

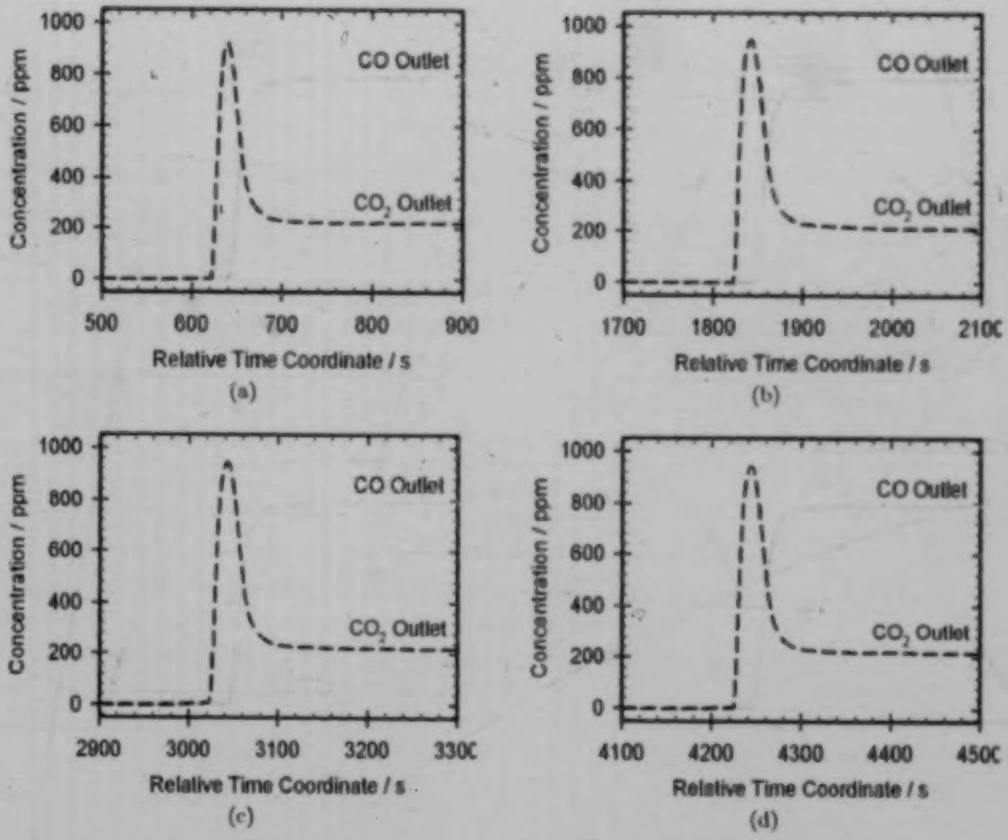

Figure 4.7: Four CO step-up functions performed under identical inlet conditions to show experimental reproducibility. CO concentration was increased from 0-1000 ppm CO at 391 K. The step up was sustained for 10 minutes, then CO stepped down to 0 ppm and the system relaxed for 10 minutes, and then the cycle was repeated.

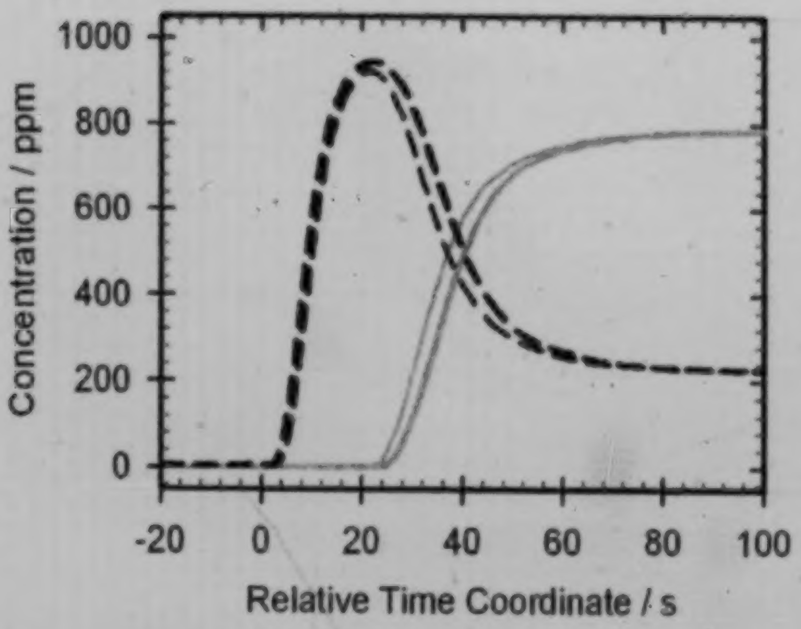

Figure 4.8: Reproducibility of step functions for 0-1000 ppm CO at 391 K. Shown are four different step-up functions, adjusted such that the step-up time point coincides for each step.

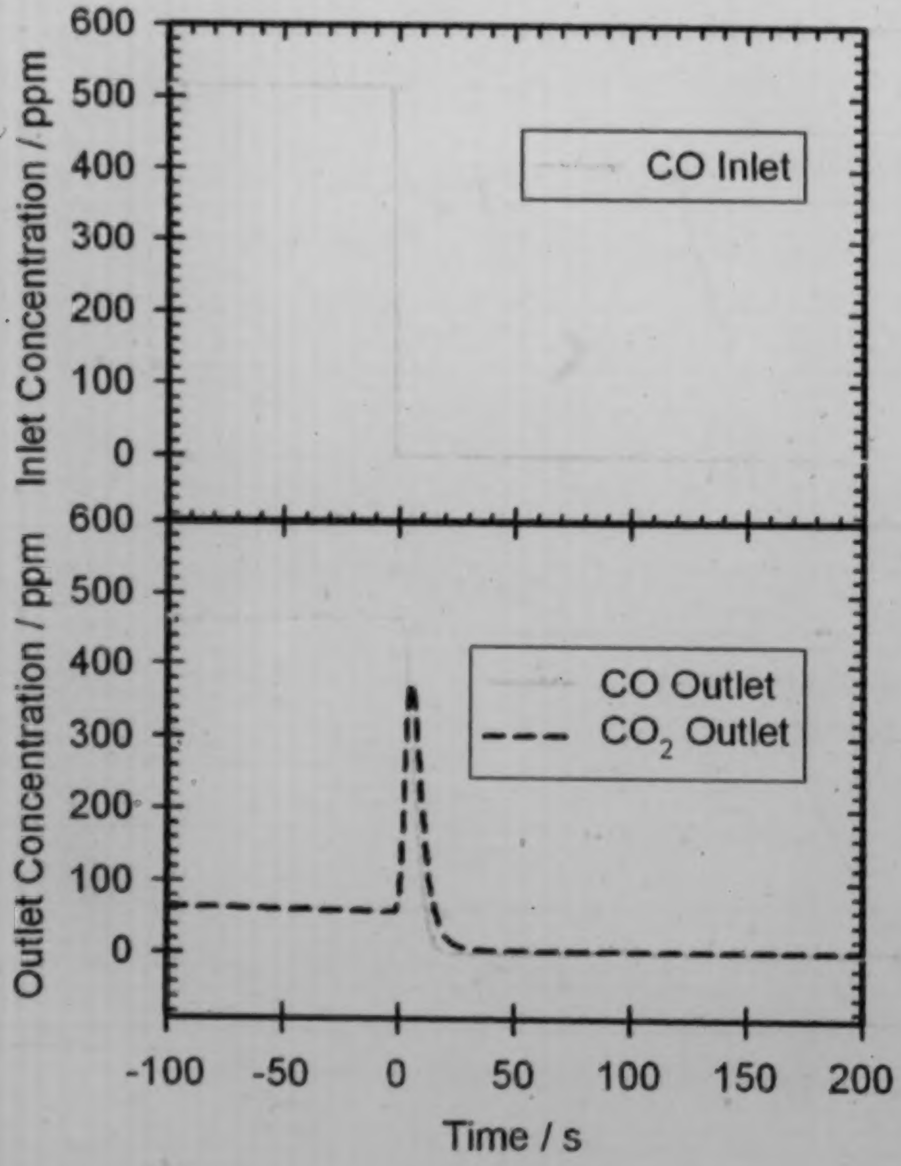

Figure 4.9: Step down from 500 ppm to 0 ppm CO. 6% O_2, rest N_2. SV = 25000 h^{-1}. Temperature constant at 373 K.

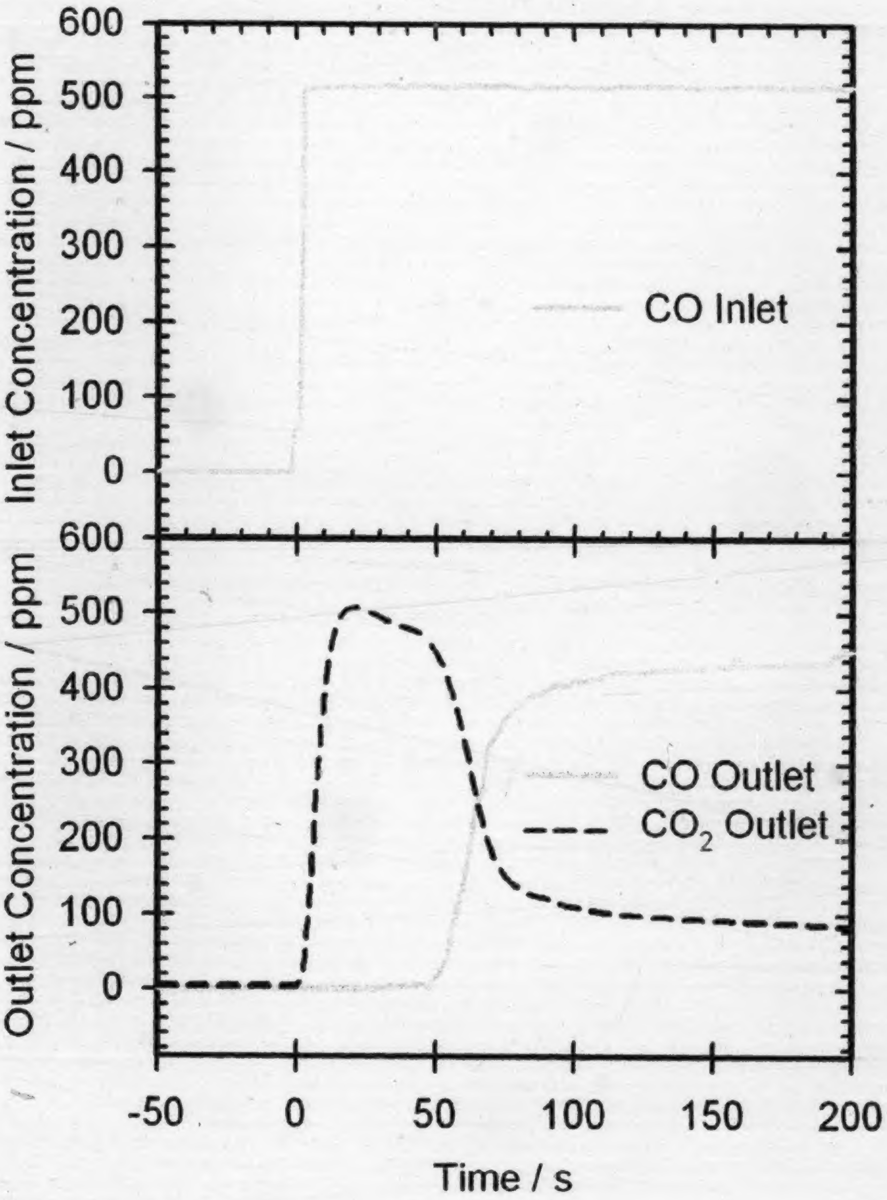

Figure 4.10: Step up from 0 ppm to 500 ppm CO. 6 % O_2, rest N_2. SV = 25000 h^{-1}. Temperature constant at 373 K.

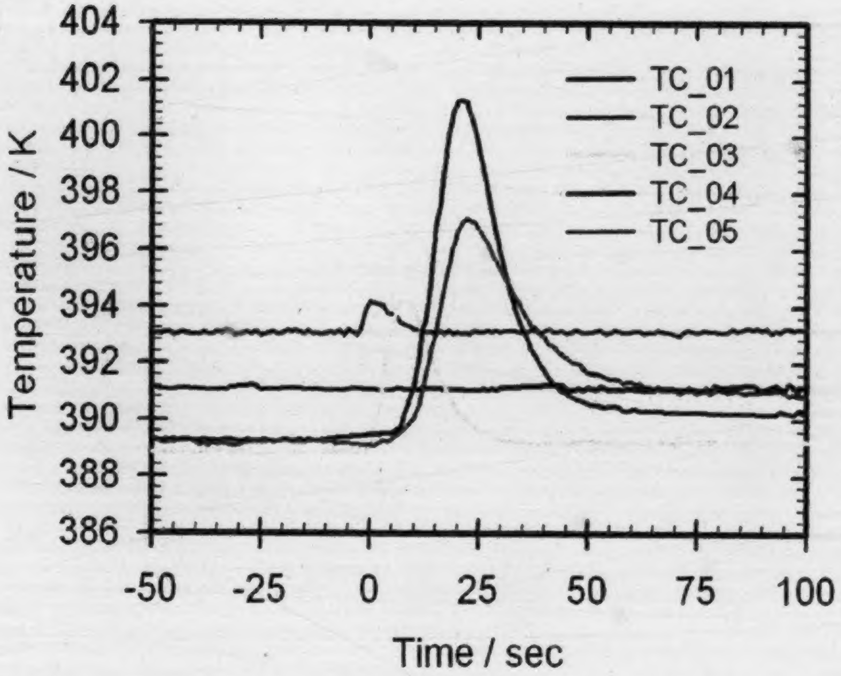

Figure 4.11: Temperature profile for a step up from 0 ppm to 1000 ppm CO. 6 % O_2, rest N_2. SV = 25000 h^{-1}. Constant temperature at 391 K. The corresponding concentration profiles are shown in Figure 4.8.

4.4 Comparison of Experimental and Simulation Results for CO Light-off

With experimental data on CO oxidation, simulations under similar conditions may begin. The simulations were compared to the experimental results to test the models to determine the strengths and weaknesses of each model. The experimentally measured inlet conditions (gas temperature and composition) to the reactor were used as the inlet conditions in the simulations. Then, the outlet conditions from the simulator were compared to the measured outlet conditions from the experiments.

The catalyst loading for each model was determined by varying the value until there was good agreement on the light-off temperature between experimental and simulation results.

4.4.1 Optimization of the Loading Factor

Due to the strong chemisorption of CO on noble catalysts, CO is often used to determine relative amounts of active catalyst present [40]. The platinum loading factor represents this relative amount of active catalyst, and may be adjusted to achieve good agreement between experimental and simulation results. Variations in the catalyst preparations may influence this value, as can the catalyst history, including sintering and ageing processes. This platinum loading factor is the first parameter that is modified from the literature values.

To determine the best fit between experimental and simulation data, four different methods of comparison were used. The first method involved the direct comparison of the resulting light-off and light-out temperatures. In rudimentary simulations, the platinum loading factor was adjusted such that simulation predicted the same light-off temperature that was observed in the experiments at a single CO concentration. This loading factor was then used for subsequent simulations.

This method was then expanded to considered both the light-off and light-out temperatures at four different CO concentrations for the LH model, which proved to be the model most suitable for simulating these experiments and used in subsequent simulations. The square of the temperature differences could be calculated and summed, as shown in Equation 4.12. This sum is shown in Figure 4.12 at various loading factors. From this graph, the best range appears to be between 0.75 and 0.87. The jump in residual that occurs at a loading factor of 3 is due to the 500 ppm CO simulation not extinguishing during the typical light-out phase. Oscillations in the residuals above a loading factor of 3.5 stem from simulations at 1000 ppm CO, where the system jumps between two steady-states under higher loading factors. Although higher loading factors were not tested, it is expected that similar behaviour would be observed with simulations at 1500 ppm and 2000 ppm.

$$Sum\ of\ \Delta\,T\ Residuals = \sum_{COConc}\left((T_{exp} - T_{sim})^2_{light-off} + (T_{exp} - T_{sim})^2_{light-out}\right) \quad (4.12)$$

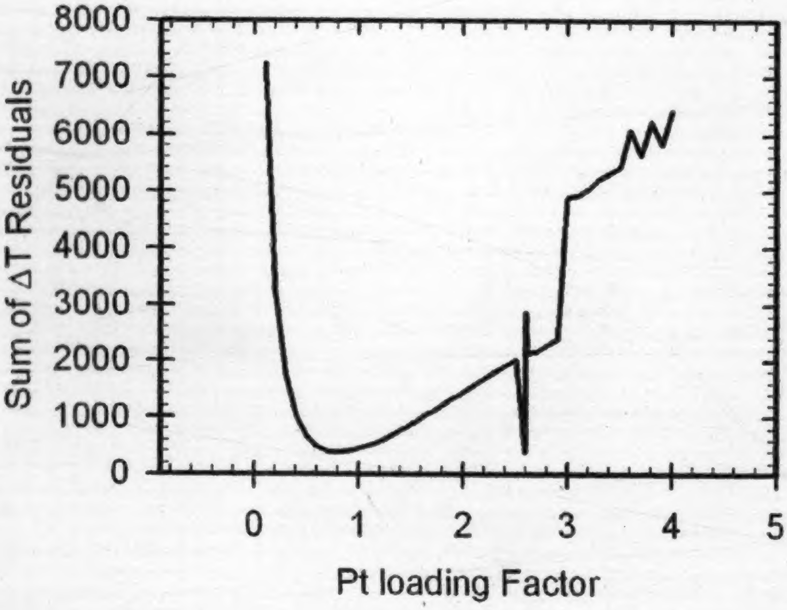

Figure 4.12: Combined sum of residuals between experimental and simulation light-off and light-out temperatures at various platinum loading concentrations using the LH model.

The third method used to determine the fitness of a simulation to an experiment was to perform a least-squares analysis on the data. First, the experimental and simulation data were reinterpolated to a common time series, and then a least-squares analysis was performed on the data sets. The sum of the residuals for one platinum loading factor and all four CO concentrations was calculated and plotted in Figure 4.13. The optimal range for a platinum loading factor, according to this method, is between 0.82 and 1.09. These results are in line with those predicted by other methods, however the range presented here is overly broad. This may be due to a large influence of data points where the system is stationary and relatively uninteresting, i.e. where conversion is 0 % or 100 %.

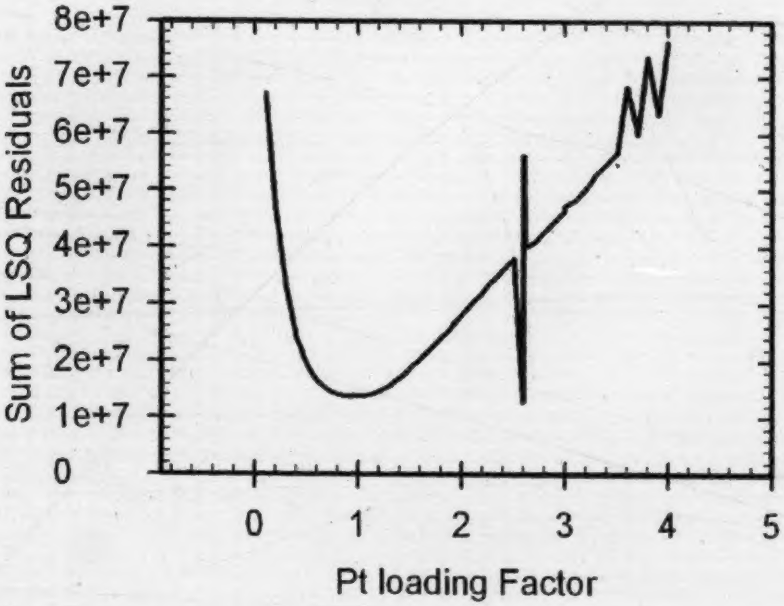

Figure 4.13: Combined sum of least-square residuals for all four CO concentrations while optimizing the platinum loading factor for the LH model.

To combat the influence of stationary datapoints, and to increase the importance of transition phases during the cycle, the least-squares residuals were then multiplied by a factor before summation, as shown in Equation 4.13. The factor was determined at every datapoint, and corresponded to the absolute value of the slope of the experimental data. Thus, stationary datapoints would become less significant due to a small derivative, and the transition phases, especially light-off and light-out, were emphasized. This method (results shown in Figure 4.14) had better agreement with the first two methods for determination of the fitness of the simulation data.

$$Sum\ of\ wLSQ = \sum_{COConc.} \sum_{T} \left((X_{exp,CO,T} - X_{sim,CO,T})^2 \cdot \frac{dT_{exp}}{dt} \right) \tag{4.13}$$

Figure 4.14 shows the combined sum of the weighted least-squares residuals for all four concentrations over a range of Pt loading factors. Here, we can see that the best value is approximate 0.84, within an acceptable range of 0.80 to 0.88, and that this value does appear to be not just a local minimum but a global minimum, (over a range of reasonable loading factors). The value is in agreement with the best range found using the first two

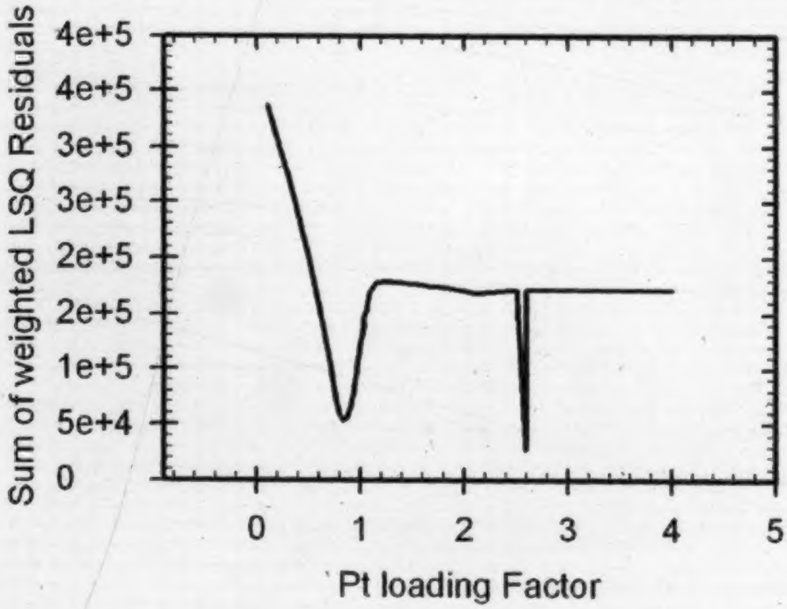

Figure 4.14: Combined sum of weighted least-square residuals for all four CO concentrations.

methods.

The influence of Pt loading factor on the predicted light-off and light-out temperatures is shown in Figure 4.15, where the influence may be see to be relatively similar at all four concentrations. The sudden drop in light-out temperature for 500 ppm CO at a loading factor of 3.0 is due to sufficient catalyst being present for CO to react at lower temperatures.

Based on results from these four methods of determining the optimal Pt loading factor, a value of 0.85 appears to agree best with three of the four methods. This value is the platinum loading factor that is used for all following LH simulations.

4.4.2 CO Light Offs

As an initial test, to determine the suitability of the literature parameters, to determine an optimal platinum loading factor for use in all later simulations, and to yield basic insight into the suitability of the models compared to other studies in literature, the three major models are used to simulate light-off behaviour. This behaviour is then compared to the experimentally observed results under the same conditions and discussed.

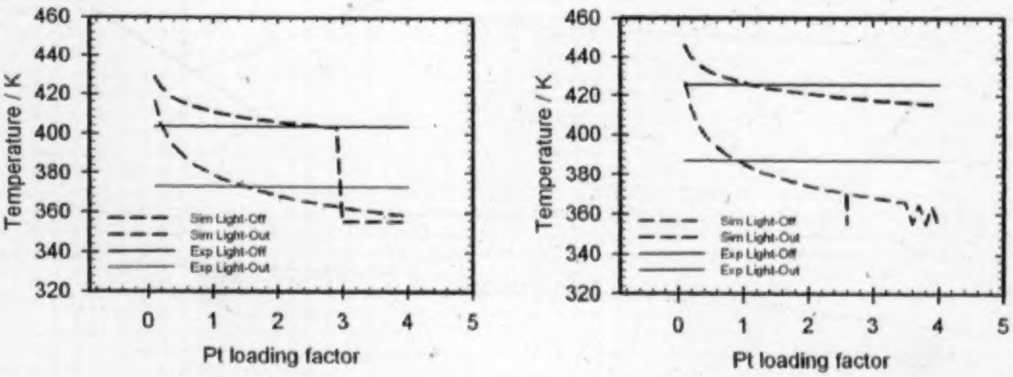

(a) 500 ppm CO (b) 1000 ppm CO

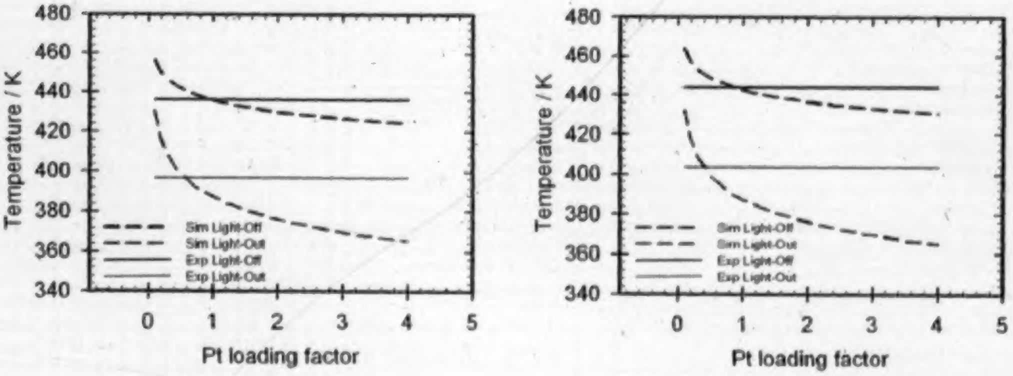

(c) 1500 ppm CO (d) 2000 ppm CO

Figure 4.15: Effect of Pt loading factor on the predicted light-off and light-out temperatures at various CO concentrations.

Simulations Using the Global Model

The global (Voltz) model was used to simulate CO light-off curves at four CO concentrations. The platinum loading factor was chosen such that the light-off temperature at 1500 ppm CO was similar for both simulation and experiment. A comparison of the simulation and experiment for each CO concentration is shown in Figure 4.16.

Both Figure 4.16 and Figure 4.17 both show that this model is very insensitive to CO concentration, compared to other models. This may be due to the model not considering CO self-poisoning on the catalyst surface (inhibition by gas-phase CO is considered in the Voltz model), as this model does not consider the rates of CO adsorption and desorption, nor the rate of O_2 adsorption. These rates have been lumped together, and their effect at various conditions has been nullified.

In addition, this global model does not correctly predict hysteresis behaviour. The difference between light-off and light-out temperature was always small (approximately equal to the adiabatic temperature rise). No surface behaviour is considered in this model, and this is the basis for the hysteresis behaviour and CO insensitivity not agreeing with the experimental result.

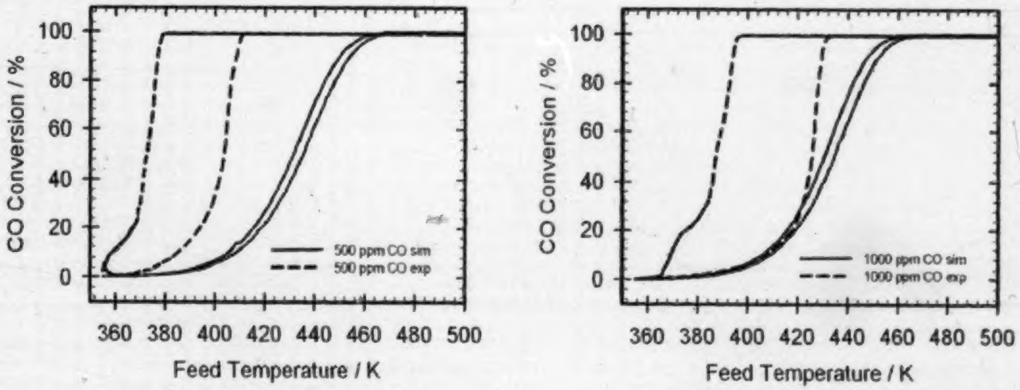

(a) 500 ppm CO

(b) 1000 ppm CO

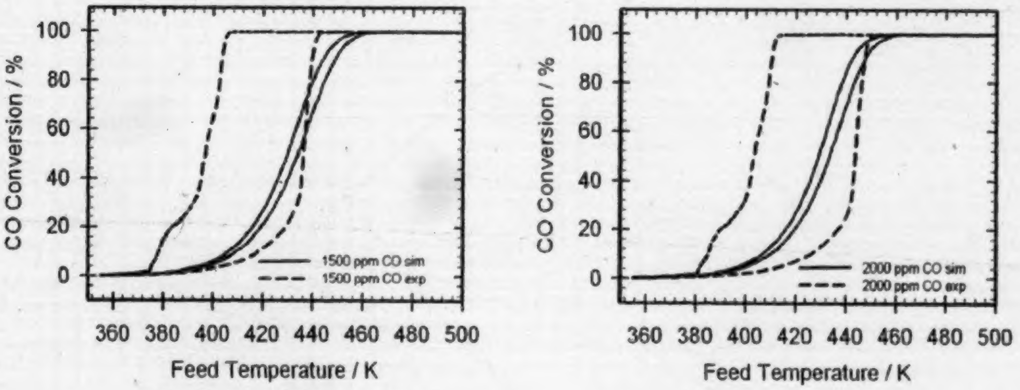

(c) 1500 ppm CO

(d) 2000 ppm CO

Figure 4.16: Light-Off Curves at various levels of CO. Shown are both the experimental result and the simulation, using the global (Voltz) model. 6% O_2, rest N_2. SV = 25000 hr^{-1}.

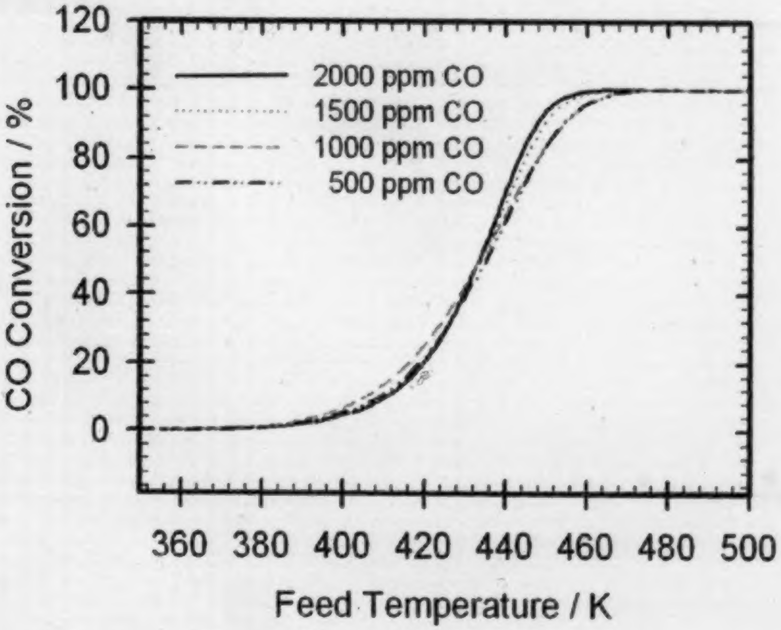

Figure 4.17: Simulations of light-off curves for 500, 1000, 1500 and 2000 ppm CO, 6% O_2, rest N_2. SV = 25000 hr^{-1}. The global (Voltz) model was applied.

Simulations Using the Eley-Rideal Model

The light-off curve predicted using the LH+ER (Eley-Rideal) model and literature parameters (section 3.5) were entirely too broad. Reaction started at room temperature, and complete conversion was not attained until above 550 K. This is shown in Figure 4.18. The curve did have a slight hysteresis to it, however, this was much smaller than was experimentally observed. The broadness of the light-off is a consequence of the oxygen adsorption step proceeding via an adsorbed molecular intermediate, even though the dissociation on the surface is assumed to be rapid. The key factor becomes the order of reaction of the oxygen adsorption. Indeed, disregarding the Eley-Rideal step, which is not important for light-off, the order of the oxygen adsorption reaction is the only mechanistic difference between the LH (section C.2) and LH+ER (section 3.5) models. The main conclusion to be drawn at this point is that with this LH type model, it is necessary to model the oxygen adsorption as dissociative chemisorption involving two surface sites to achieve the necessary steepness of the light-off curve, although it remains possible that one can achieve the effect by tuning the rate parameters.

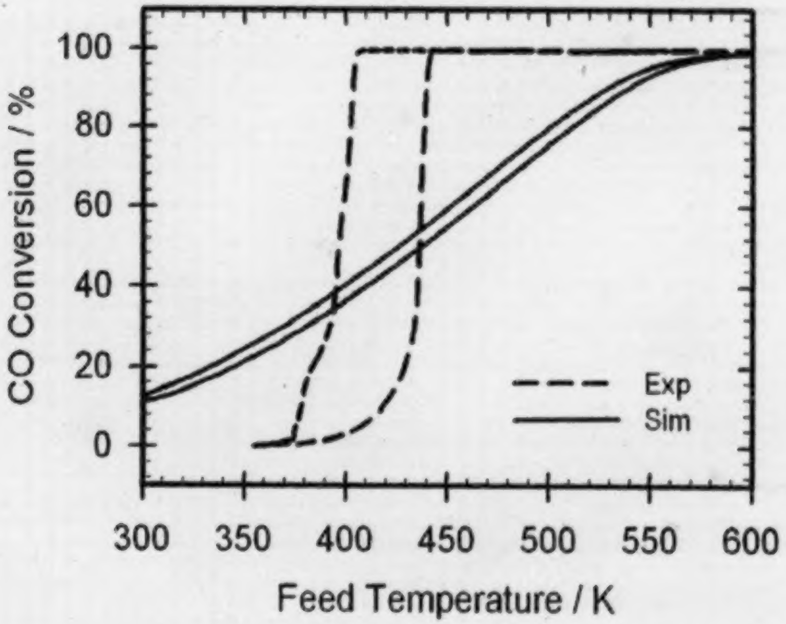

Figure 4.18: Simulations of light-off curve for 1500 ppm CO, 6% O_2, rest N_2. SV = 25000 hr^{-1}. Both experimental and simulation results are shown. The LH+ER elementary model was used for the simulation.

Further discrimination between models is discussed in later chapters, where the models can be tested under more rigorous conditions.

Simulations Using the Classical LH Model

After adjusting the platinum loading factor (as detailed in subsection 4.4.1), the agreement between experimental and simulation results for the LH model was found to be relatively good, much better than results from the other models, and especially considering that the only value that it not a literature value at this time is the platinum loading factor. The trends regarding light-off temperature with changing CO concentration agree well with experimental results, as shown in Figure 4.19. The light-off temperature is not so well predicted, with the simulation predicting a very sudden extinction of the reaction, whereas it was experimentally observed that the reaction very slowly dies out.

As the LH model does consider surface reactions, the temperature difference between the light-off and light-out temperatures was not purely comprised of the adiabatic temperature rise, but also included some surface effects as well. These surface effects are explored in more depth later.

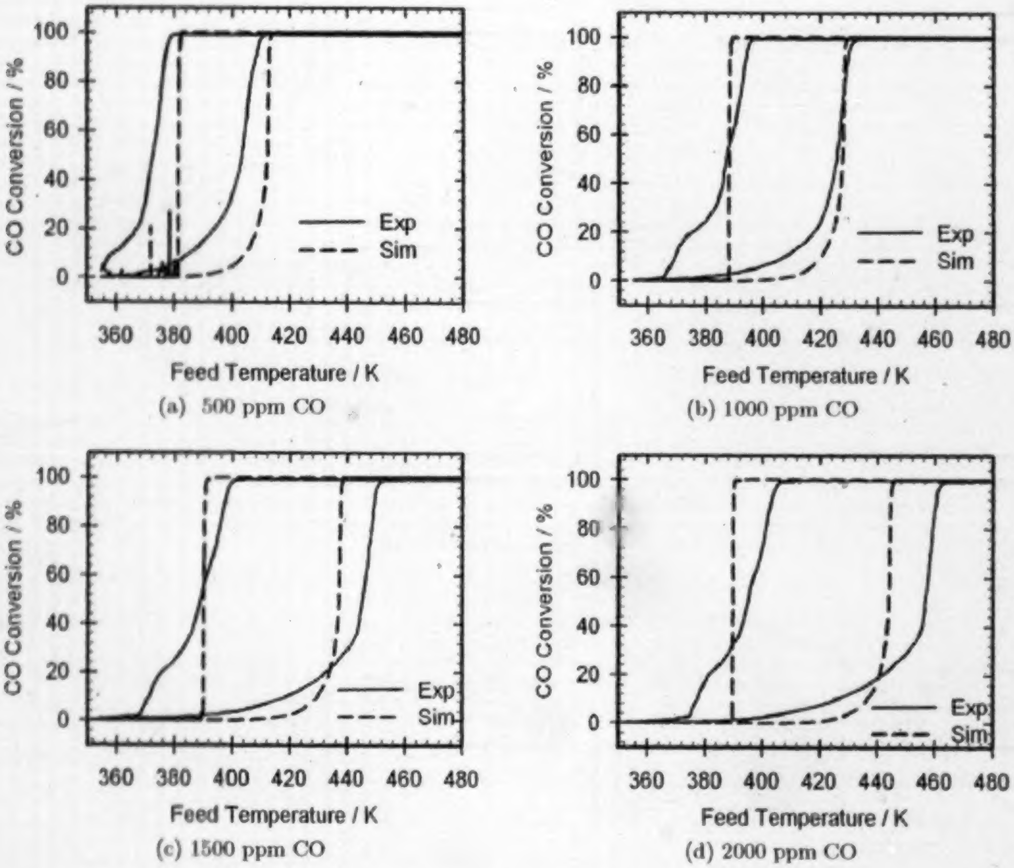

(a) 500 ppm CO

(b) 1000 ppm CO

(c) 1500 ppm CO

(d) 2000 ppm CO

Figure 4.19: Light-Off/Light-Out Curves at various levels of CO. Shown are both the experimental result and the simulation, using the LH model and a platinum loading factor of 0.85. 6% O_2, rest N_2. SV = 25000 hr^{-1}.

Further comparisons between the global and elementary models are presented and discussed with regards to concentration step experiments in section 4.5.

4.4.3 Effect of the Sticking Coefficients

When the competitiveness of oxygen adsorption, relative to CO adsorption, is increased, the light-off temperature decreases. By affording oxygen more opportunities to adsorb, the

CO Concentration (ppm)	Light-Off Temperature (K)	Light-Out Temperature (K)	Δ Temperature (K)
500	412	382	30
1000	428	388	40
1500	437	390	47
2000	444	390	54

Table 4.4: CO Light-Off and Light-Out Temperatures at various CO concentrations, using the classical LH Simulation

CO S^0	O_2 S^0	Light-Off Temperature (K)	Light-Out Temperature (K)	Δ Temperature (K)
0.84	0.07	439	400	39
0.42	0.07	428	400	42
0.84	0.14	433	400	33

Table 4.5: Effect of Oxygen and CO Sticking Coefficients on Light-off and Light-Out temperatures, using the fully reversible LH model and a light-off curve with 1500 ppm CO.

oxygen may adsorb in significant amounts at lower temperatures, allowing light-off to be achieved at lower temperatures.

Also interesting, is the observation that the sticking coefficients (3.9.2) do not appear to have an effect on the extinction temperature. This would suggest that the reaction is not limited by mass transfer to the surface during this phase, and may be used to our advantage when optimizing parameters to better match experimental data. A basic method may be proposed to adjust kinetic parameters.

As the parameters used in this study have origins in the literature from studies on other catalysts that may have different dispersion characteristics, particles sizes or ageing histories than the catalyst used in this study. The objective of the following parameter optimization is not to obtain ideal parameters, but to establish a method by which kinetic parameters for a catalyst may be fitted to a model. Obviously, kinetic parameters measured experimentally under tightly controlled conditions are preferred, however these parameters are not always easily obtained.

CO feed (ppm)	Washcoat Elements	Light-Off Temperature (K)	Light-Out Temperature (K)	Δ Temperature (K)
500	Exp	404	373	31
1000	Exp	426	387	39
1500	Exp	436	397	37
2000	Exp	444	404	40
500	1	412	382	30
1000	1	428	388	40
1500	1	437	390	47
2000	1	444	390	54
500	10	411	390	21
1000	10	426	401	25
1500	10	436	406	30
2000	10	443	410	33

Table 4.6: Effect of the washcoat on light-off and light-out temperatures, using the LH model and a platinum loading factor of 0.85.

4.4.4 Effect of Modelling the Washcoat

The additional washcoat elements did add accuracy to the simulation, but required an order of magnitude more simulation time to complete. While it would be better to perform all simulations with a washcoat of at least 10 elements, this may not be practical in all cases at this time. As computers become faster and more efficient, the addition of washcoat elements becomes a trivial decision. For the current work, the washcoat will not be used and this is not expected to significantly alter the discussion of observed trends. For future works and more detailed discussions of targeted results for specific catalysts, the washcoat may need to be considered more carefully.

4.4.5 Initial Parameter Optimization

A basic method for parameter optimization would entail the following steps.

1. the platinum loading factor is adjusted to match the light-off temperature, either for a specific CO concentration or to minimize the sum of least squares for a series of CO concentrations

CO (ppm)	Light-Off (K)	Light-Out (K)	Δ (K)	Pt loading	$k_{CO\_Pt+O\_Pt}$	S^0_{O2}
1500	436	397	39	Experimental		
1500	435.9	387.7	48.2	1.00	1.006×10^{12}	0.07
1500	436.2	397.2	39	1.00	5.8×10^{11}	0.07

Table 4.7: Optimizing the kinetic parameters such to obtain a better match between experimental and simulation results. The experimental result was shown above in Figure 4.3(d). 1.006×10^{12} is the literature value [66].

2. the pre-exponential factor for the rate of CO oxidation (Equation 3.9a) on the surface ($k_{CO_{Pt}+O_{Pt}}$) is adjusted such that the light-out temperature matches the experimental value

3. as adjusting the pre-exponential value in step 2 will affect the light-off temperature, steps 1 and 2 may be performed iteratively with a solver, or fine tuned with step 4

4. as the sticking coefficients for CO and O_2 and the pre-exponential factor for CO desorption influence the light-off temperature, but not the light-out temperature, one of these parameters may be adjusted such that the light-off temperature predicted by the simulator matches that which was experimentally measured

As the values used for sticking coefficient and rate of CO desorption were calculated to be thermodynamically consistent [66], and as oxygen adsorption is assumed to be irreversible, the best value to adjust is the sticking coefficient for oxygen.

This method was used to obtain the result shown in Figure 4.20 and in Table 4.7. Figure 4.20 shows the effect of modifying the value of $k_{CO\_Pt+O\_Pt}$ on the light-out temperature. Here, the value was modified until the light-out temperature predicted by the simulator was the same as experimentally measured. Decreasing the rate of CO oxidation increases the temperature at which light-out occurs. Note that modifying this value does not affect the light-off curve in a significant manner, nor does this value appear to influence the shape or steepness of the curves. The steepness of the light-out curve in the simulator compared to the experiment may be due to temperature gradients which are slightly larger in the experiments than in simulations or due to travelling extinction fronts moving faster in the simulation than in the experiment.

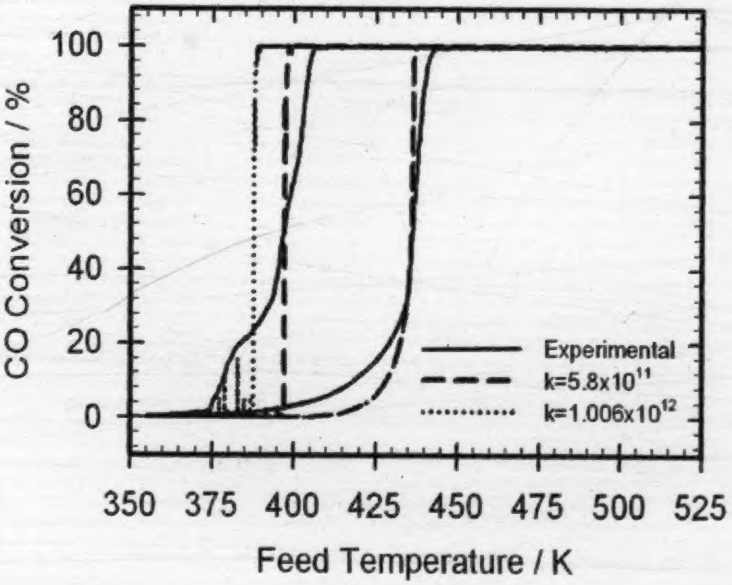

Figure 4.20: The effect of $k_{CO\_Pt+O\_Pt}$ on 1500 ppm CO light-off curve. 6% O_2, rest N_2. SV = 25000 hr^{-1}.

4.5 Modelling CO Concentration Steps

Modelling CO Concentration Steps with Voltz Model

Attempts to model concentration steps using the Voltz model (section 3.3) were unsuccessful. As this model is a global mechanism, and does not consider surface coverages, several behavioural traits were not predicted by this model.

For all simulations performed with Voltz kinetics, transient behaviour was not observed. The initial peak in CO_2 production was never seen, nor transitions from oxygen-covered to CO-covered surfaces. Only steady-state results were predicted, as shown in Figure 4.21. Variation of the parameters only affects the steady-state values predicted, and does not reveal additional information. As a global mechanism, this model cannot be used to predict transient phenomena, as surface coverages and reactor history are never considered in the model. As well, as a contributing factor of the difference between reactions along the high-rate branch and reactions along the low-rate branch is the surface composition, any mechanism (e.g. global mechanisms) that does not consider surface composition will similarly not adequately predict differences between these two branches. In the present work, the Voltz model is not used for any further investigations.

Eley-Rideal

There has been much discussion regarding the mechanism of CO oxidation on a platinum surface in the literature (see subsection 4.1.8). Both ER and LH models have been explored in both the literature and in the present work. While the ER model was considered an early favourite, the current general consensus in the literature is that the reaction proceeds via the LH model. However, the reaction deviates from simple LH behaviour due to surface coverage dependencies [62]. These deviations are significant, and must be considered when modelling the behaviour of these systems.

Nibbelke observed that when switching from oxygen to CO inlet gases, that CO_2 production began almost immediately and there was no inhibition of CO oxidation by preadsorbed O_2 [150]. As instantaneous reaction of CO on an oxygen covered surface was not predicted by the classical LH model, this was explained by the addition of an OCO* step, whereby CO adsorbs onto a site that is already in use by an oxygen atom. This is represented by Equation 3.20a in the ER model used here. As oxygen absorption on Pt at moderate temperatures (below 1000K) is considered to be irreversible, adsorbed oxygen will not desorb. So long as oxygen is allowed to cover the entire surface, there must a mechanism by which other components, specifically CO, may adsorb.

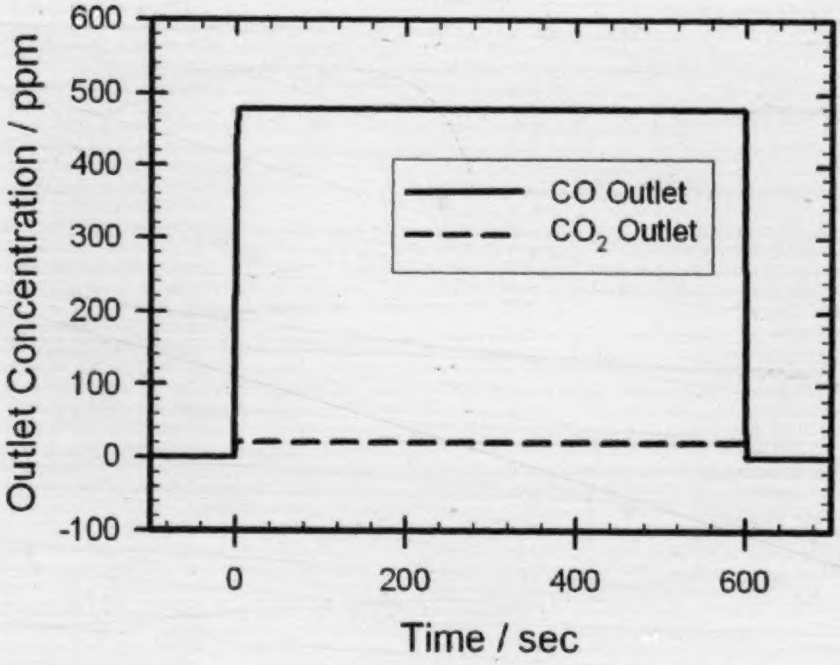

Figure 4.21: Step up and down from 0-500-0 ppm CO, simulated using Voltz kinetics. 6 % O_2, rest N_2. SV = 25000 h^{-1}. Constant temperature at 373 K.

Step Functions with Classical LH Model

Before the step in CO concentration, the only present gases in the bulk phase were nitrogen and oxygen. The surface was covered by adsorbed oxygen. In the classical LH model, the only available path for CO and O_2 to react is on the surface via adsorbed components. Therefore, for the reaction to take place, CO must first adsorb. However, on an oxygen covered surface, the only way for CO to adsorb is if some oxygen first leaves the surface to free up some sites. Other than through reaction, the only other means for oxygen to leave the surface is through desorption, however, associative desorption of oxygen generally does not occur at temperatures less than 800 K [89, 90].

The pre-exponential factor for the oxygen desoption step was set to zero in these simulations to account for irreversible oxygen adsorption. There was no reaction, as seen in Figure 4.22, as there was no means for oxygen to leave the surface through this mechanism. There were no free sites available for CO to bind to, and no mechanism step to react adsorbed oxygen with gas-phase CO. The calculated fractional surface coverage of the system over time was 1 for adsorbed oxygen over the entirety of the simulation.

The simulations were repeated, with regular desorption allowed. Oxygen could leave the surface through desorption in this case, and slowly, as oxygen left the surface, CO bound itself to the free sites. Over time, the surface coverage of CO increased. Once CO coverage reached a critical coverage, the reaction ignited. As oxygen on the surface reacted and the product left, active sites were freed up. CO dominated the coverage of these free sites, and the coverage of the overall surface became predominately CO. Reaching a critical coverage took time, and the required time was larger with decreasing temperature. In the simulation shown in Figure 4.23, the time required before the reaction ignited was on the order of 450 seconds. After ignition occurred in this simulation, there was no decay of the reaction and no subsequent CO poisoning.

This behaviour is inconsistent with the experimentally observed results. Experimentally, the reaction began immediately upon CO entering the monolith, and CO did self-poison after a brief period of high reaction rate while the surface oxygen was consumed.

The classical LH model has no provision for the immediate reaction of CO with an oxygen covered surface, contradicting experimental observations and literature discussions. Preadsorbed oxygen was reported to have no inhibiting effect on CO adsorption [181].

When the surface was initially oxygen covered, and the oxygen adsorption made to be irreversible (pre-exponential factor was set to zero), a light-off curve (1500 ppm CO, 6% O_2, rest N_2) was simulated using the classical LH model. The simulator predicted no reaction over the normal temperature range. This is expected from the model, as there is no way to get CO onto the surface with an initially oxygen covered surface and no oxygen desorption. This is, however, not what is experimentally seen. The experimental light-off curve was not influenced by the order of addition of CO and oxygen to the inlet gas before heating.

There needs to be a step to react CO with an oxygen-covered surface, which may be provided by the Eley-Rideal step or by another step (discussed later).

Problems with the Traditional Models

Due to the nature of global models, the Voltz model was unable to predict any transient phenomena during concentration step studies. Surface studies [130, 50] and modelling studies [196, 167] have shown that the Eley-Rideal step is not possible. However, simulations using a simple LH model do not predict CO concentration steps when the initial condition is an oxygen covered surface. Oxygen adsorption is irreversibly dissociative below 700K, and therefore a means for immediately reacting CO on introduction to an oxygen covered surface must be found. When oxygen was introduced to a CO covered surface, CO desorption occurred, affording opportunities for oxygen to adsorb and react with the adsorbed layer [166].

Other pathways have been proposed in the literature. A CO_2 precursor [91] has been suggested and refuted [62]. Subsurface oxygen formation [190] has also been proposed. Asymmetric inhibition (CO inhibits O but O does not inhibit CO) and a short co-existence were used by Eiwerth et al. to use a pseudo-reaction for the CO adsorption step on an oxygen covered surface [197]. These alternate models and others are discussed below.

4.5.1 Simulating Step Functions with the Subsurface Oxygen Model

The subsurface oxygen [198, 190] model (section C.6) describes a means by which oxygen can be stored below the catalyst surface for later use. Oertzen et al. state that subsurface oxygen's role during propagating reaction waves on the surface it in providing temporary storage capacity [190]. Oxygen is temporarily stored below the surface, only to return to influence the propagation of reaction fronts on the surface.

This model was added to the LH model already discussed to test its applicability.

This model was tested, and the results did not show significantly different behaviour compared to the traditional LH model. During a step up of 0-500 ppm CO at 393K (see Figure 4.24), there was a delay of approximately 400 seconds, and then ignition occurred. This is similar to the results for the LH model on its own, as shown in Figure 4.23 and discussed in 4.5. The trend was the same at slightly higher temperatures (Figure 4.26) and at 1000 ppm CO (see Figure 4.25 and Figure 4.27).

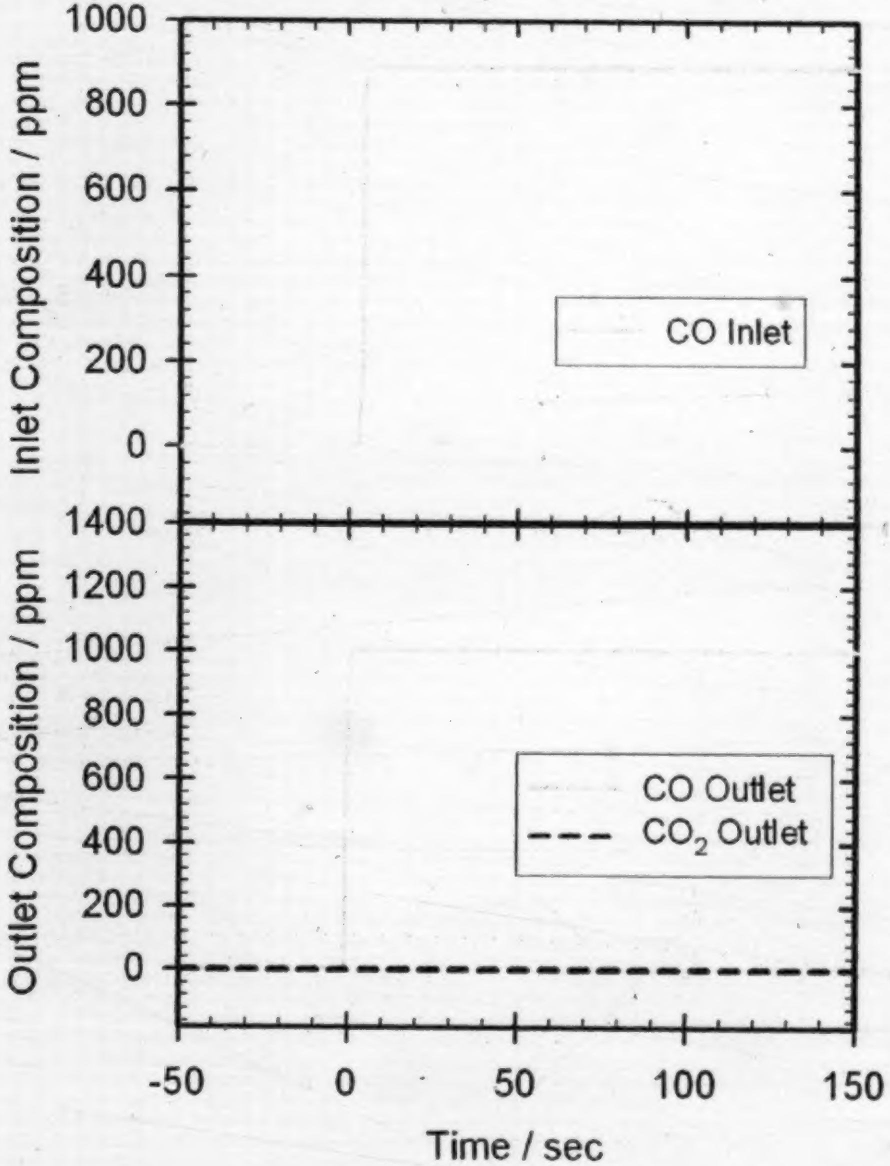

Figure 4.22: Simulation of 1000 ppm CO step using LH model and irreversible oxygen adsorption. 6% O_2, rest N_2. SV = 25000 hr^{-1}, T = 420 K.

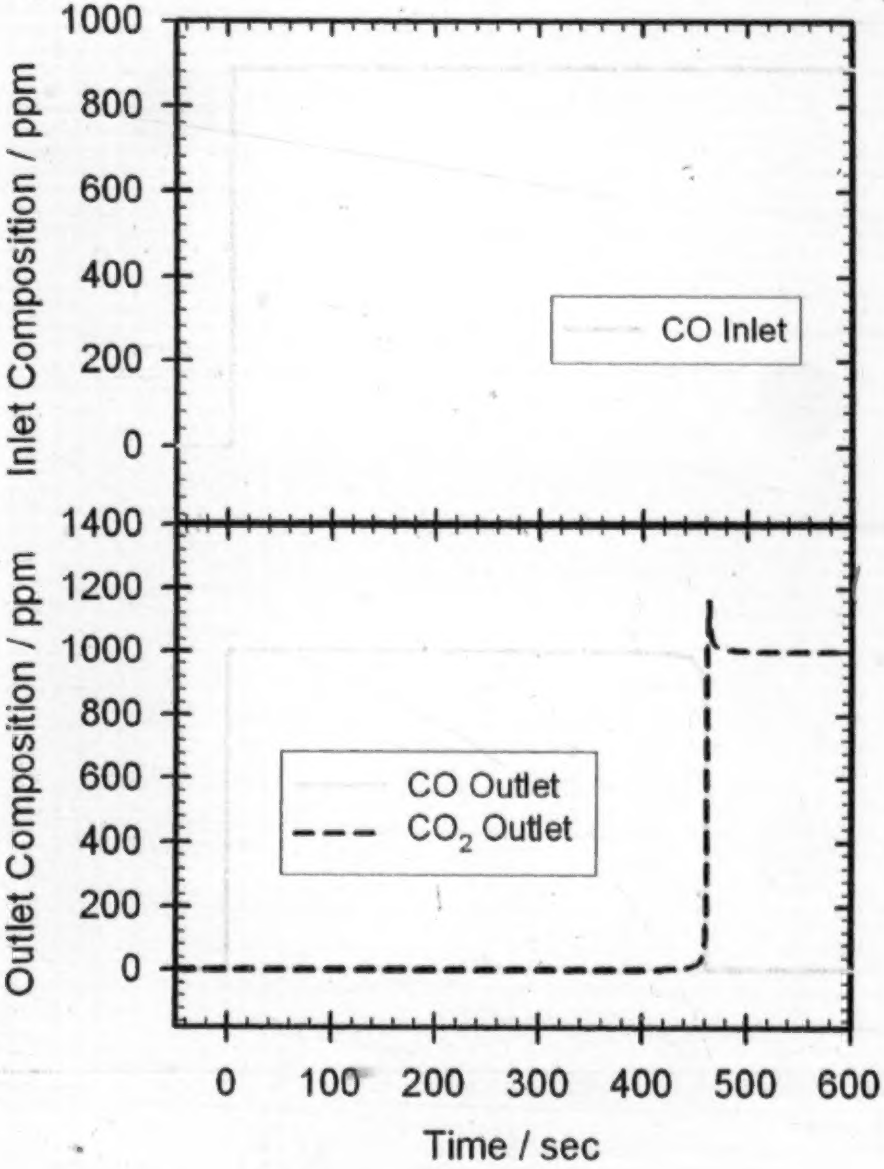

Figure 4.23: Simulation of 1000 ppm CO step using LH model with reversible oxygen adsorption. 6% O_2, rest N_2. SV = 25000 hr^{-1}, T = 420 K.

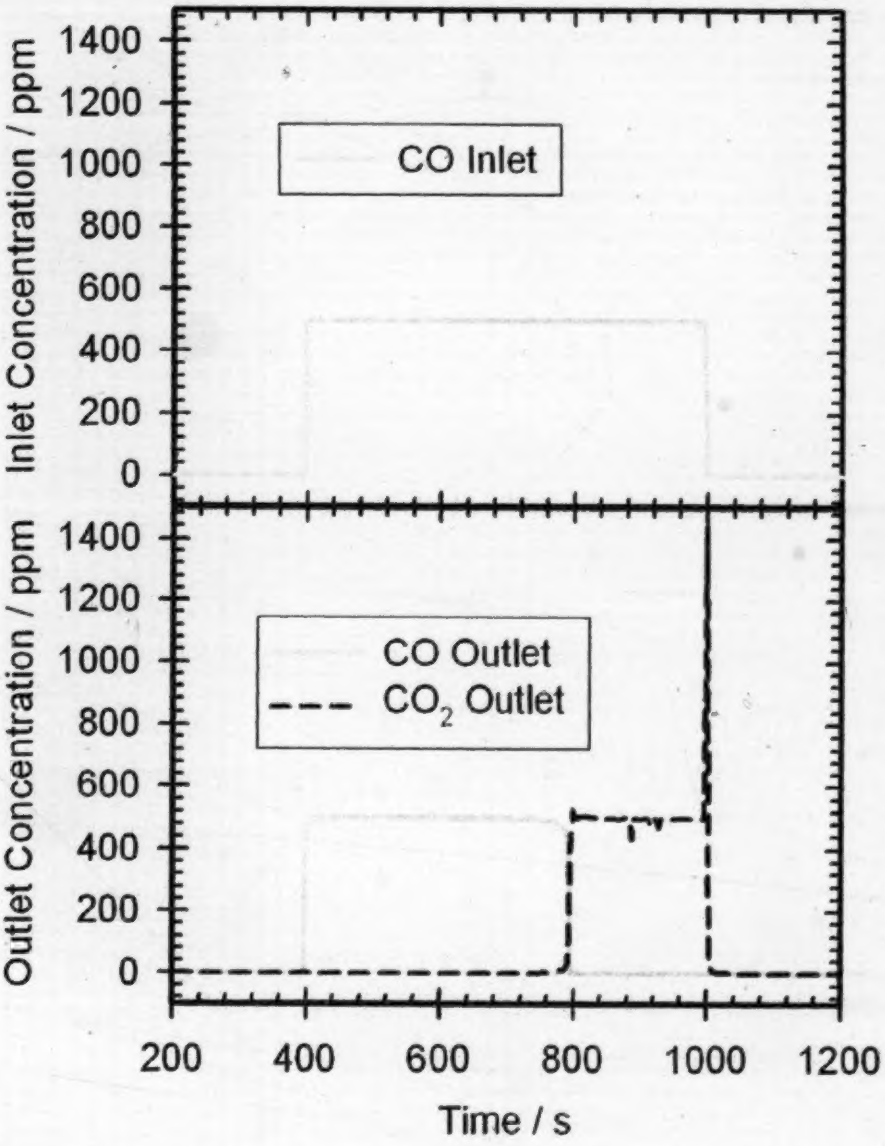

Figure 4.24: 500 ppm CO step, 6% O_2, rest N_2. SV = 25000 hr^{-1}. Temperature constant at 393 K. The subsurface oxygen model was used.

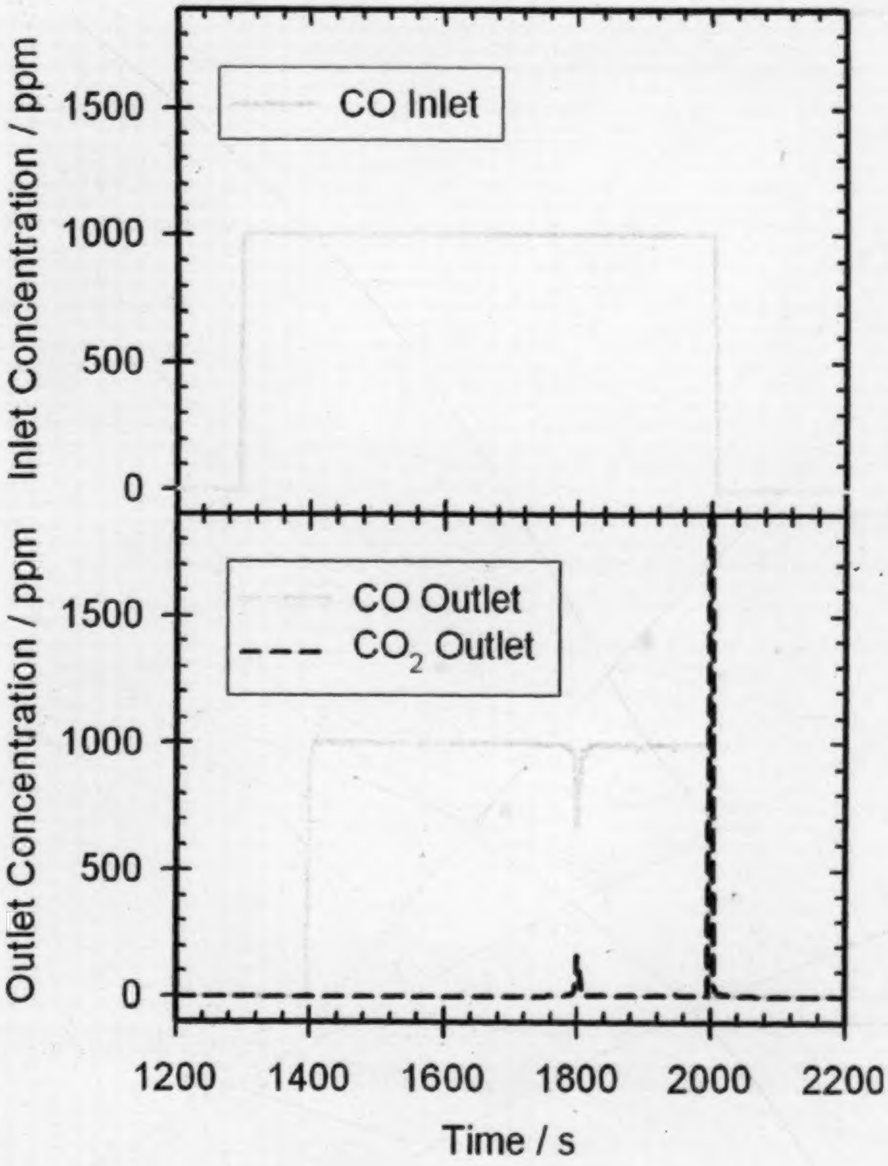

Figure 4.25: 1000 ppm CO step, 6% O_2, rest N_2. SV = 25000 hr^{-1}. Temperature constant at 393 K. The subsurface oxygen model was used.

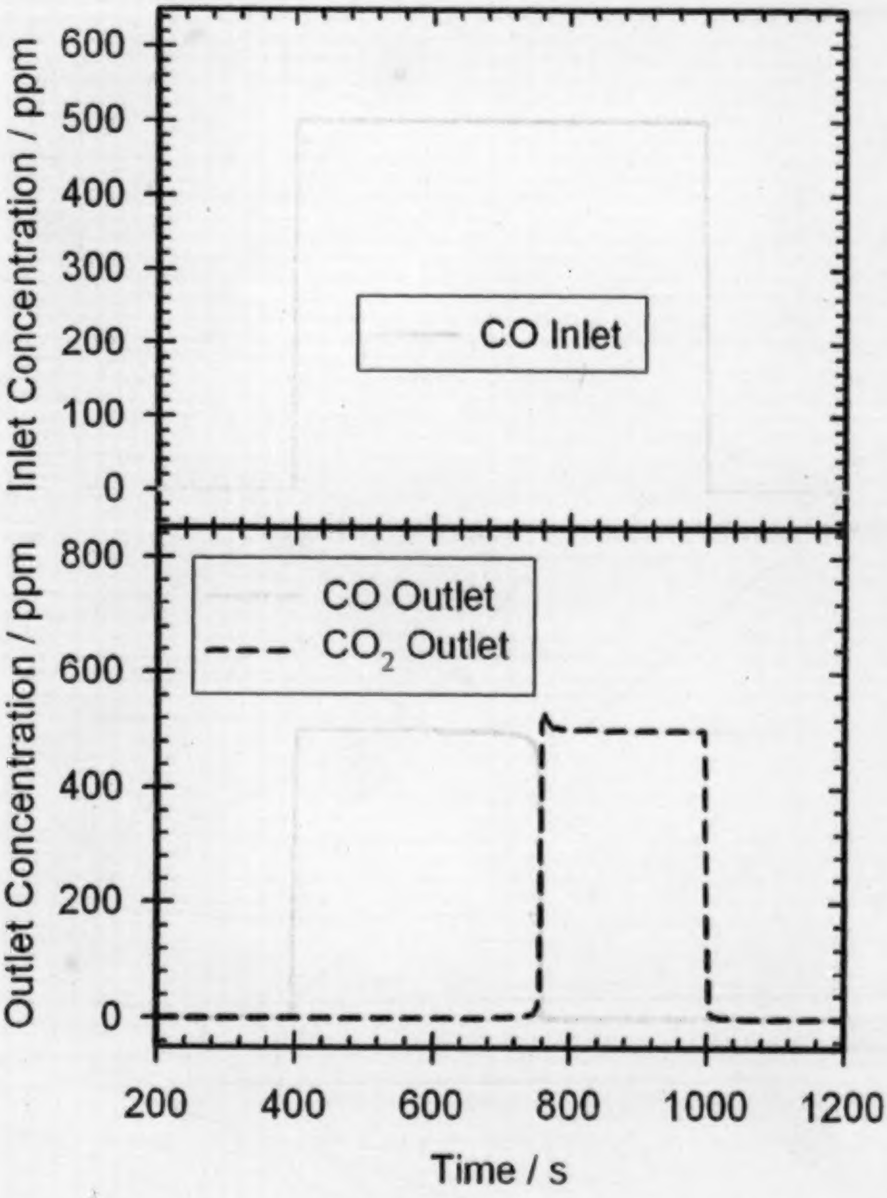

Figure 4.26: 500 ppm CO step, 6% O_2, rest N_2. SV = 25000 hr^{-1}. Temperature constant at 403 K. The subsurface oxygen model was used.

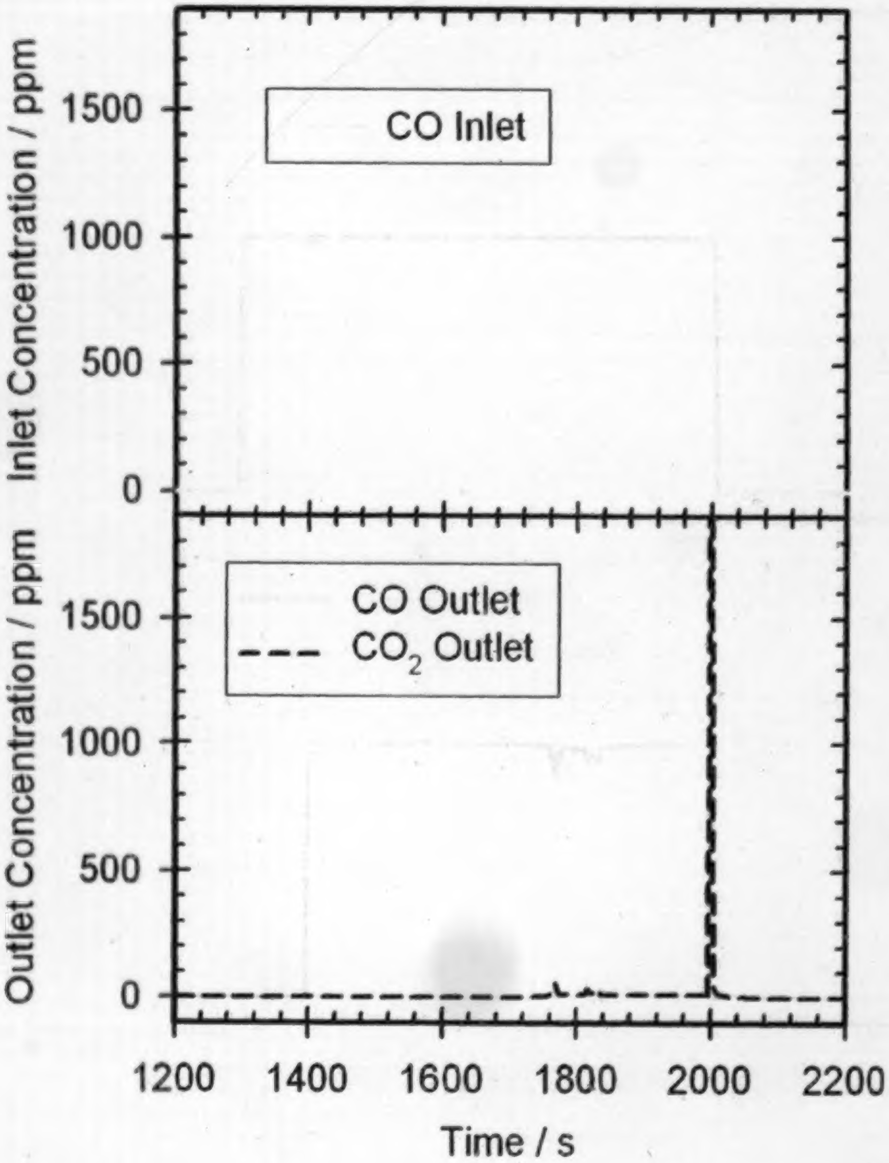

Figure 4.27: 1000 ppm CO step, 6% O_2, rest N_2. SV = 25000 hr^{-1}. Temperature constant at 403 K. The subsurface oxygen model was used.

The additional steps allowing oxygen storage with the parameters used did not appear to significantly change the concentration step behaviour. This may be due to the subsurface mechanism influencing the reaction on a microscopic scale, whereas the experiments performed were observing the catalyst as a whole, and differing microscopic changes were averaged out when considered as a whole.

4.5.2 Simulating Step Functions with the AB Model

The "AB" model, as stated by Kissel-Ostrangler et al. [199] and described in more detail in section C.5, shows a different behaviour during CO steps compared to the classical LH and the LH+ER models.

The AB model is essentially a LH model, but in a system with two slightly different types of surface sites. This model is predicated on the assumption of two different surface sites (type A and B) have differing activities towards the respective components. The sites are assumed to be equally dispersed throughout the catalyst, and adsorbed species on one site can react with adsorbed species on the other. Of special note, one type of site is much more active towards oxygen adsorption than the other.

In Figure 4.28, the predicted behaviour is closer to what has been observed experimentally. After a long delay (100-400 seconds, the delay is CO concentration and temperature dependent), the reaction begins. There is an initial period of high conversion, followed by poisoning of the surface by CO, leading to a diminishment in the reaction rate and settling to an intermediate steady-state rate. The delay before reaction was not observed in previous experiments nor reported in literature sources, where CO concentration steps were reported to be immediately followed by the initial CO_2 production peak.

The width of the peak in CO_2 production was very short-lived, having peaked and resettled within 8 seconds. Experimentally, the peak and subsequent relaxation required 60-80 seconds, both in the present work and in similar studies [136] into CO concentration steps. This discrepancy cannot be fully accounted for at this time.

4.5.3 Simulating Step Functions with the classical LH Model and Irreversible Oxygen

Figure 4.30 shows a simulation of a CO concentration step using the classical LH model and assuming irreversible oxygen. In this case, the surface was assumed to initially have no adsorbed components, and the simulation ran for 400 seconds. As oxygen was the only component in the feed stream available to adsorb to the surface, the surface became covered

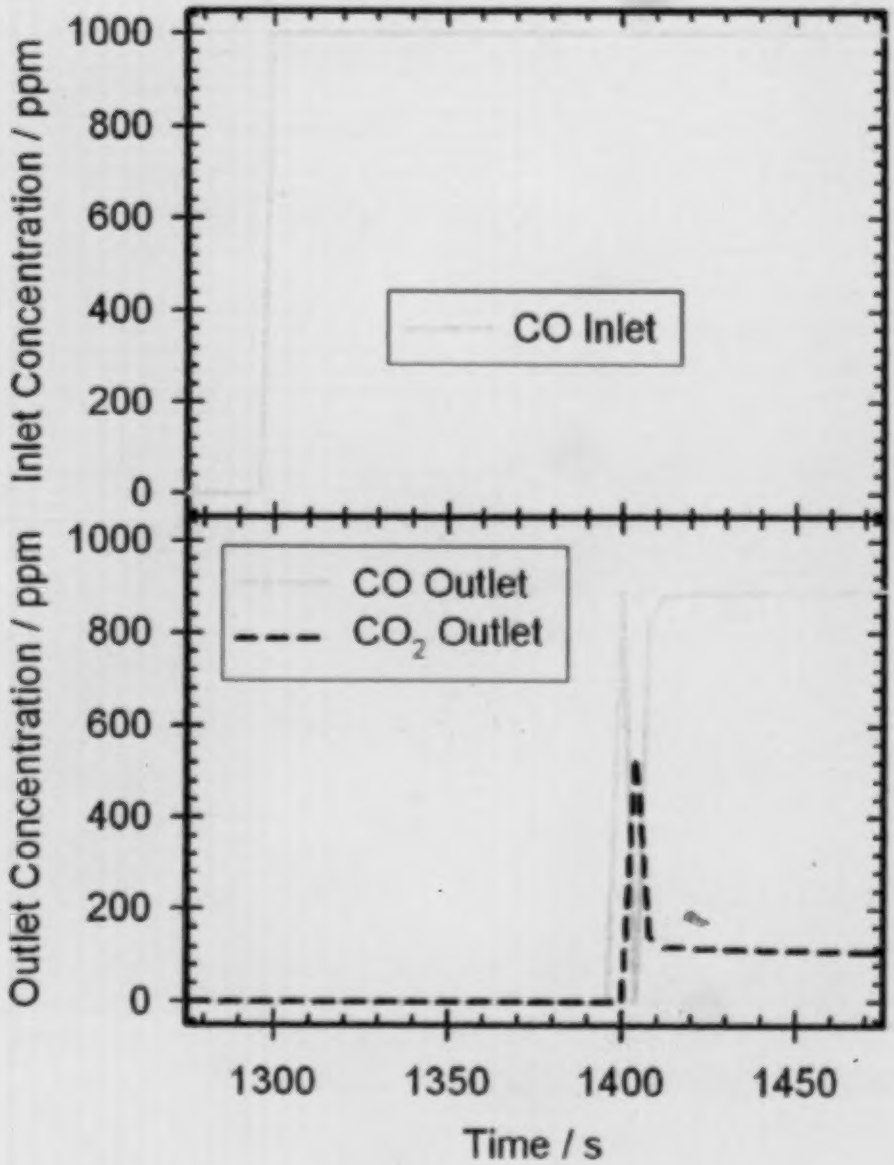

Figure 4.28: Step up from 0 ppm to 1000 ppm CO. 6 % O_2, rest N_2. SV = 25000 h^{-1}. Constant temperature at 383 K. The AB model was applied.

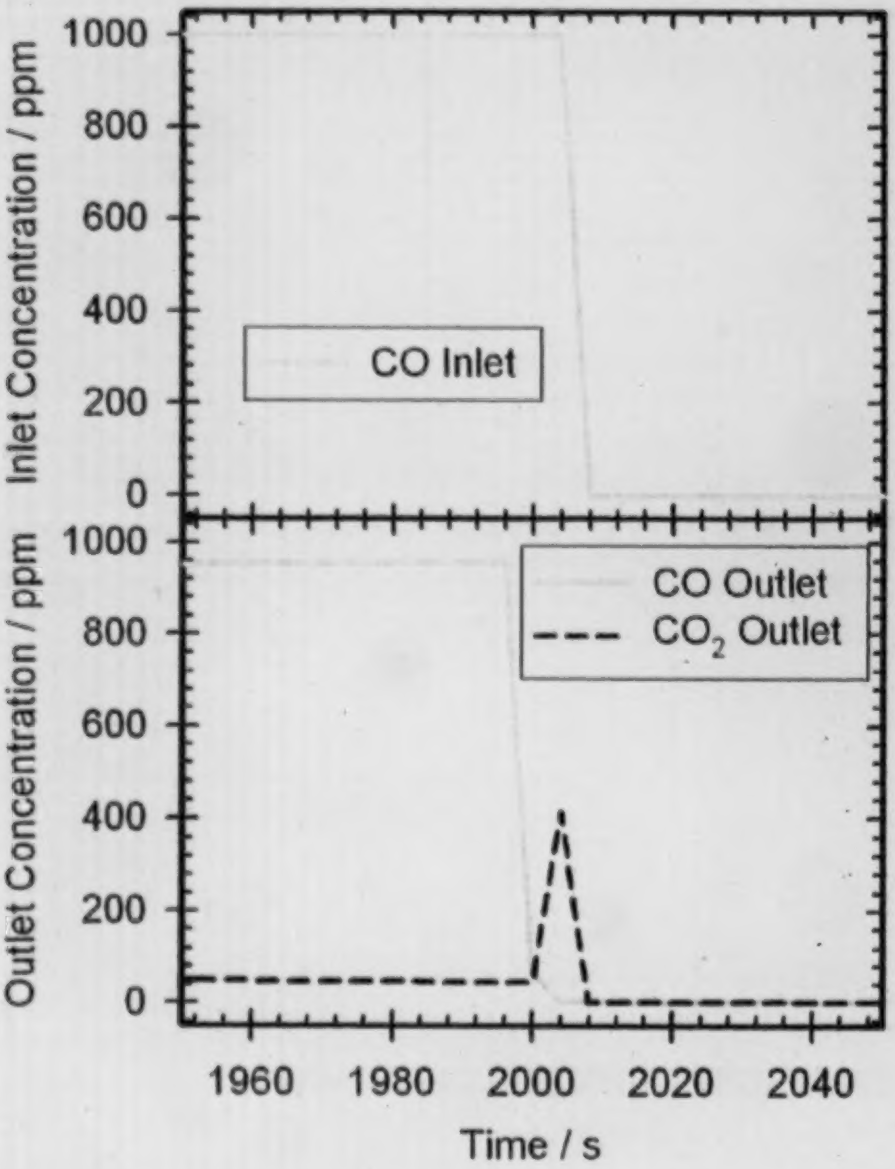

Figure 4.29: Step down from 1000 ppm to 0 ppm CO. 6 % O_2, rest N_2. SV = 25000 h^{-1}. Constant temperature at 383 K. The AB model was applied.

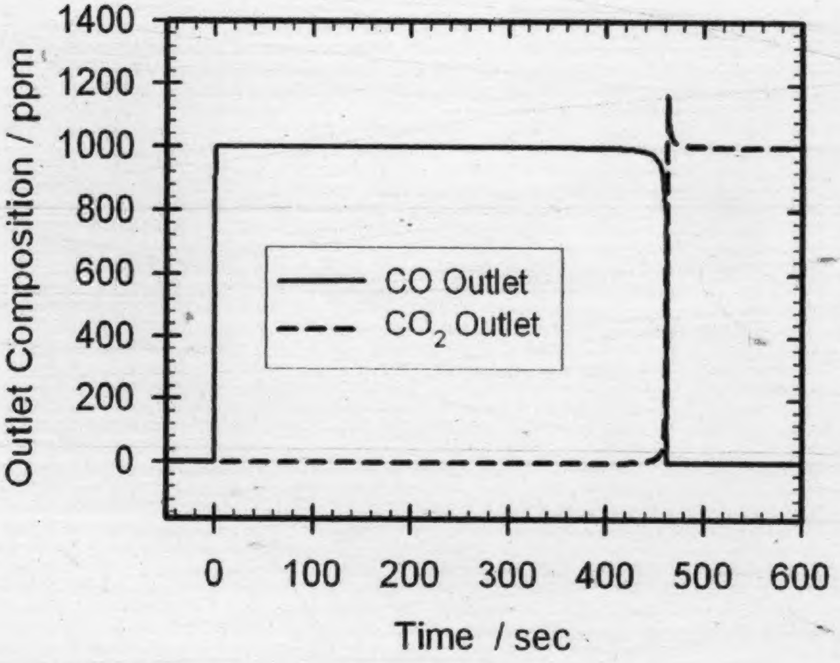

Figure 4.30: Simulation of a CO step of 0-1000 ppm CO using the classical LH model. 6 % O_2, rest N_2. SV = 25000 h^{-1}.

by adsorbed oxygen. However, the surface was not 100% covered by oxygen at the time of the step increase. Upon the initial step increase, the majority of sites were occupied by oxygen, and no significant CO conversion occurred. However, as a small number of sites were available to CO for adsorption, small amounts of CO were able to adsorb and react. As CO reacted, the turnover of free sites increased, and more sites became available for CO adsorption. The quantity of free sites available to CO did not become significant until approximately 450 seconds after the step increase, at which point the reaction ignited and CO conversion jumped to 100%. However, this phenomena was not observed experimentally, and is attributed to the the simulator not correctly modelling the coverage of oxygen on the surface.

If the surface is assumed to be initially completely covered by adsorbed oxygen, and oxygen adsorption is irreversible, there is no means by which CO may adsorb to the surface and react, and no conversion is ever seen.

Thus, an alternate model must be found that adequately describes the adsorption of CO onto an oxygen-covered surface and shows instantaneous reaction, as well as models the behaviour of the peak and relaxation.

4.5.4 Simulating Step Functions with the Compressed Oxygen Model

Another possible model includes the classical LH model, but with the addition of the possibility for the adsorption of CO to force adsobed oxygen adatoms to form "compressed islands", where the number of sites occupied is less than the number of adatoms in the island. The crux of this model are three steps allowing two oxygens to share a single catalyst surface site. More details of this model are shown in section C.7.

The adsorption of CO (Equation 4.14) is the only step that can produced compressed oxygen (OO). Simply adsorbing more oxygen does not form the compressed oxygen species.

$$CO + 2O^* \rightarrow CO^* + OO^* \tag{4.14}$$

$$CO^* + O^* \rightarrow CO_2^* + 2^* \tag{4.15}$$

Equation 4.15 is the same as the surface reaction shown in the classical LH model in Equation 3.9a.

$$CO^* + OO^* \rightarrow CO_2 + O^* +^* \tag{4.16}$$

Equation 4.16 is the surface reaction between compressed oxygen and adsorbed CO. A reasonable assumption is that this reaction proceeds at the same rate as the surface reaction between a typically adsorbed oxygen and CO. This assumption, however, does give the equation a good order-of-magnitude approximation.

$$OO^{*} + {}^{*} \rightarrow 2O^{*} \tag{4.17}$$

Equation 4.17 allows the compressed oxygen to "dissociate" such that it occupies two separate sites instead of one. This step prevents excessive buildup of the compressed oxygen.

The behaviour observed when using this mechanism to model a step in CO concentration resembles that which was experimentally observed quite well. The step up function is shown in Figure 4.31, and a comparison between this step (at 403 K) and the experimentally observed step (at 373 K) are shown in Figure 4.10. Although the temperatures at which these results are obtained are slightly different, the shape of the simulation closely resembles that of the experimental result. The step up behaviour exhibited the initial high conversion to CO_2. As CO_2 formed and left free sites available on the surface, these newly available free sites were dominated by CO. When the adsorbed oxygen diminished, so did the reaction rate. A slight dip in the outlet conversion may also be observed at the point where CO_2 production began to drop.

Figure 4.32 shows another simulation of a CO step in concentration. This time, a step change of 0 to 1000 ppm CO at 420 K is shown. Again, there is an initial peak in the reaction, followed by a diminishing rate of CO_2 production as CO dominates the surface. However, in this simulation, CO does not completely extinguish the reaction. The temperature was high enough that some CO desorption was able to occur and significant oxygen adsorption did occur. The reaction was not extinguished, but persisted at a low ($\tilde{1}0\%$) conversion. Such behaviour was also experimentally observed, whereby there was an intermediate CO concentration where the system settled to an intermediate conversion (i.e. not complete conversion and not complete extinction).

The compressed oxygen model predicts the same result regardless of whether the initial conditions on the surface are CO covered, oxygen covered, or empty sites. In the case of CO covered and empty sites, after a few seconds in an atmosphere with only nitrogen and oxygen, any CO present desorbs and leaves, and oxygen adsorbs to fill the sites. Immediately before the step in CO concentration, oxygen covers all sites with the exception of a small amount. Regardless of whether the initial condition of the surface is that of completely covered by adsorbed oxygen, or to within numerical error, with the compressed oxygen submechanism, steps exist by which CO may adsorb onto an oxygen covered surface and react quickly.

When comparing the predicted step function to an experimental step in concentration, it is clear that the simulation is reaching a steady-state much sooner than the experiment. Figure 4.7 shows the experimental result of a 1000 ppm step up in CO concentration at 391 K, where the system requires approximately 20 seconds to reach peak CO_2 production and an additional 60 seconds to relax to the steady-state. Figure 4.32 shows the simulation result for a 1000 ppm CO step up in CO concentration at 420 K, requiring 4 seconds to reach peak CO_2 production and an additional 4 seconds to relax to steady-state.

These results for the compressed oxygen model appear to be promising, however these parameters also have an effect on the light-off curve. Figure 4.33 shows the effect of the addition of the compressed-oxygen submechanism on the prediction of a 1500 ppm CO light-off curve. While the ignition curve remains the same for both the classical LH and compressed oxygen models (both predict a light-off temperature of 439 K), the extinction point for the compressed oxygen model is at a much higher temperature. The experimental extinction point was 397 K (see Table 4.3), an extinction point of 390 K was predicted by the classical LH mechanism, and the compressed oxygen model predicted 432 K.

The additional steps introduced by the compressed oxygen mechanism influences the adsorption of CO on an oxygen covered surface. These steps should not be significant when oxygen surface coverage is low. As the temperature is increasing in a standard temperature programmed reactor, the surface is dominated by CO: oxygen coverage is low and the compressed oxygen mechanism is not significant. However, after ignition the catalyst surface is dominated by oxygen species. After the peak temperature has been met and the feed temperature begins to be lowered, the system approaches the extinction, or light-out, point. As the compressed oxygen mechanism assists in getting CO onto an oxygen covered surface, the transition from oxygen covered surface to CO-covered surface occurs earlier with this step than without, i.e. the shift from an oxygen covered surface to a CO-covered surface is shifted to favour the CO-covered surface. This is shown graphically in Figure 4.33.

At this point, a proper parameter optimizer is required to obtain parameters that better describe the experimentally-observed results. The reaction rate parameters may be adjusted to model the step at the same temperature as the experimental result, including the total time required for the step to arrive at steady-state, as well as the steady-state conversion.

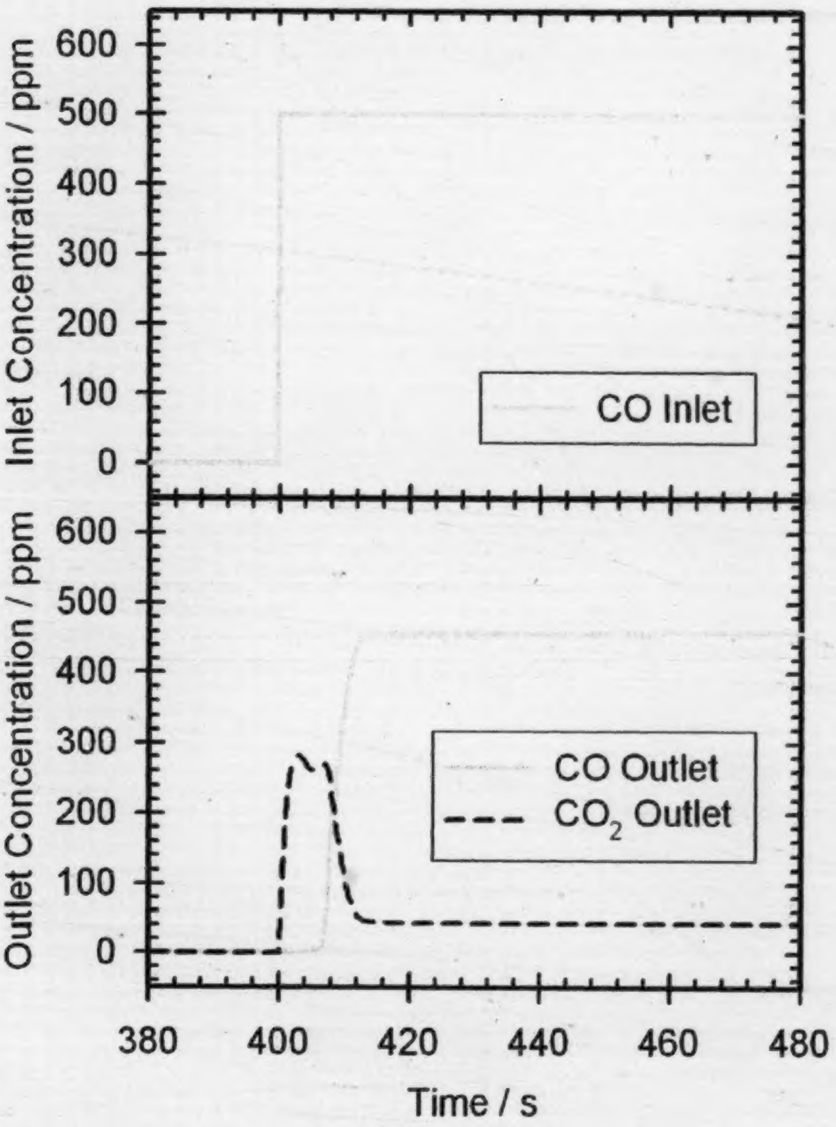

Figure 4.31: 500 ppm CO step, 6 % O_2, rest N_2. SV = 25000 hr^{-1}. Inlet temperature was constant at 403 K. The compressed oxygen model was used.

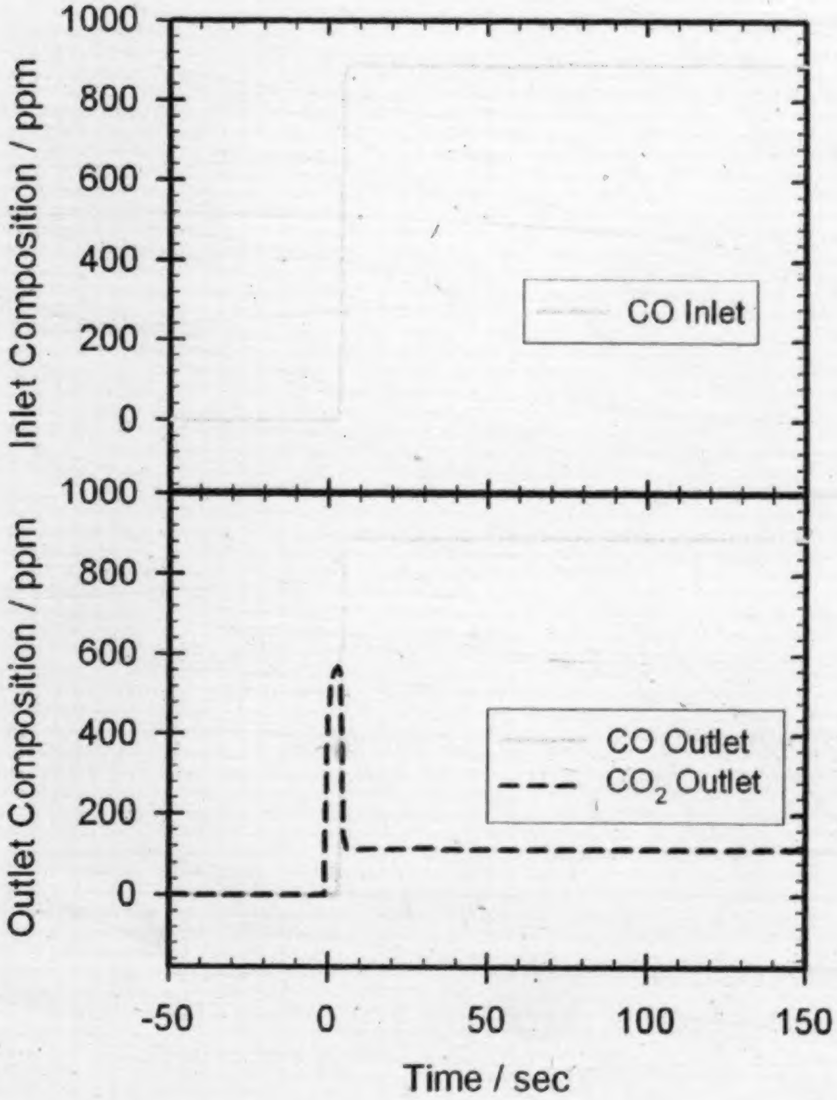

Figure 4.32: Simulation of 1000 ppm CO step. 6% O_2, rest N_2. SV = 25000 hr^{-1}, T = 420 K. The compressed oxygen model was used.

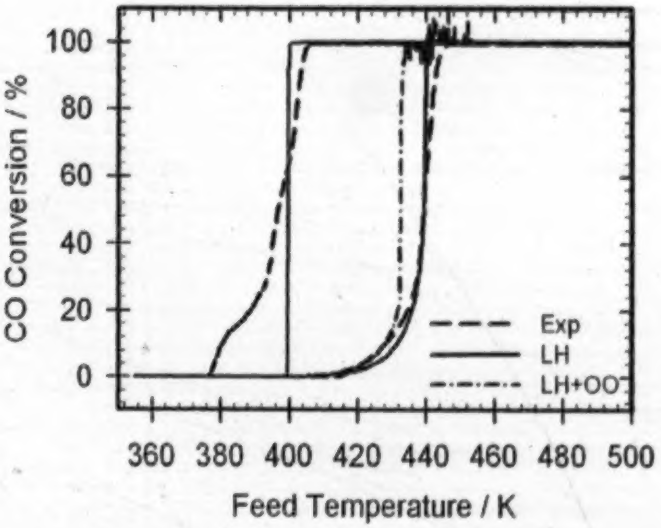

Figure 4.33: A comparison between the experimental result, the classical LH model, and the compressed oxygen model for a 1500 ppm CO temperature programmed reaction. 6 % O_2, rest N_2. SV = 25000 h^{-1}.

4.5.5 Simulating Step Functions with the Compressed Oxygen Model and Oxidized Platinum

An additional surface species representing oxidized platinum, may be added. This species is in equilibrium with adsorbed oxygen on the surface, and when the chosen parameters are accurate, could potentially alter the shape of the peak during a step in CO concentration by slowing the source of available oxygen on the surface. A rudimentary parameter set for the oxidation and reduction of platinum may be found in Table F.6.

Using activation energies of 70 kJ·mol^{-1}, the pre-exponential factors were both varied between 10^9 and 10^{16}. Within this range, no prolongment of the CO step up was observed. However, if the equilibrium was shifted too far in favour of the oxidized state, then conversion was hindered.

When the pre-exponential rate coefficients were set to $k_{f,95} = 1.006\times10^{12}$ and $k_{f,96} = 1.006\times10^{13}$, an equilibrium between adsorbed oxygen and the oxidized form of approximately $k_{f,95}$:$k_{f,96}$ = 10:1 was established. The ratio was kept constant, and the rate constants were decreased in steps of 1 order of magnitude. This ratio had no significant effect on the shape of the step response, or the length of time over which the the response occurred above $k_{f,95}=1.006\times10^{8}$. Below this value, the slow rate of exchange allowed Oox-Pt to occupy sites on the surface well above the light-off temperature, inhibiting CO oxidation. However, this did not broaden the CO_2 production peak.

4.5.6 Factors Influencing the Steady-State Conversion

After a typical step up in CO concentration, the system settles to a steady-state conversion. This steady-state is determined by the competitiveness of oxygen adsorption onto the surface, and several parameters influence this behaviour. These factors include the sticking coefficients for CO and oxygen, as well as the CO desorption rate. By increasing the competitiveness of oxygen adsorption a small quantity, the steady-state rate of CO conversion will increase. This relationship is not linear, and is sensitive to these parameters, as larger changes to these values will result in a steady-state conversion of zero or 100%.

The influence of CO desorption rate (Figure 4.34), CO sticking coefficient (Figure 4.35) and oxygen sticking coefficient (Figure 4.36) are shown, and detail the non-linear relationship between the parameters and the predicted steady-state CO conversion rate.

Figure 4.34 details the effect of CO desorption rate on CO_2 production. Smaller values decrease the turnover rate of free sites on a CO covered surface, decreasing the competitiveness of oxygen adsorption. As a result, the steady-state conversion is decreased to the point that no more conversion occurs. Increasing the CO desorption rate increases the competitiveness of oxygen, and the CO_2 production rate. At some rate of CO desorption, the reaction begins to take off. As the CO desorption rate increases, the rate of oxidation also increases. The reaction ignites at the reactor exit, and a reaction front slowly moves towards the reactor entrance. After this reaction front has progressed through the entire reactor, the steady-state will be attained. This steady-state may be a relatively high rate of CO_2 conversion, potentially as high as the initial CO_2 production peak. At the exit of the reactor, the simulator predicts the surface to be half-covered with adsorbed CO and the remaining half covered by adsorbed oxygen and compressed oxygen species. If the CO desorption rate is set even higher, then CO conversion will be complete.

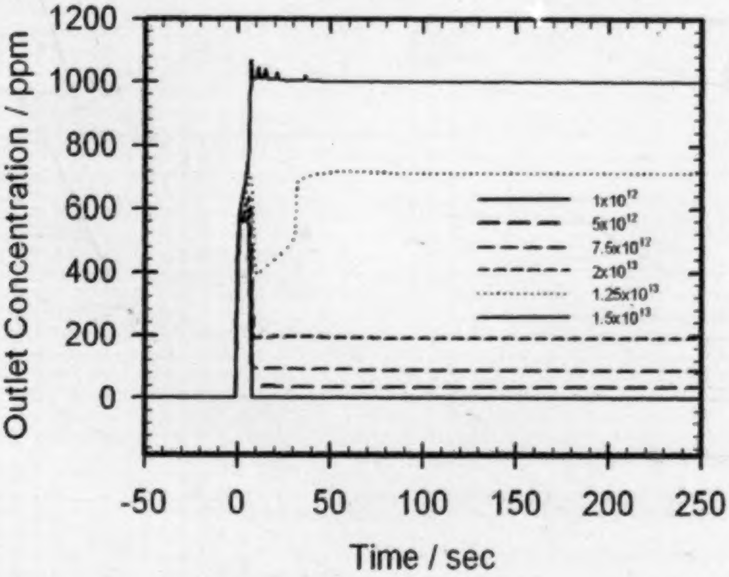

Figure 4.34: Effect of the rate of CO desorption on CO_2 production for a concentration step of 0-1000 ppm CO. Shown is the outlet concentration for CO_2 over time.

The CO sticking coefficient may be used for fine tuning of the steady-state conversion rate, within a small range, as shown in Figure 4.35. Increases in the CO sticking coefficient decrease the rate of steady-state CO oxidation by small degrees. Decreases in the sticking coefficient for CO, however, have a non-linear effect. Small decreases in the sticking coefficient slightly increase the steady-state oxidation rate, however, at some point, the oxidation rate jumps to complete conversion. At values near 0.70, there is a slight local minimum in oxidation rate immediately following the initial peak. As time progresses, a reaction front

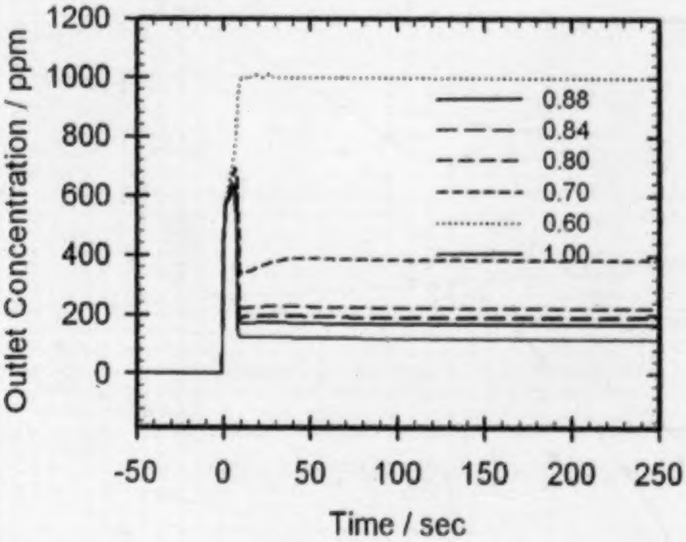

Figure 4.35: Effect of the CO sticking coefficient on CO_2 production for a concentration step of 0-1000 ppm CO. Shown is the outlet concentration for CO_2 over time.

may move through the reactor until steady-state is achieved. Such local minima were not observed experimentally, and as such, the range of validity over which this CO sticking coefficient may be adjusted to fit experimental data may be small.

Decreases in the oxygen sticking coefficient decrease the competitiveness of oxygen adsorption, and likewise decreases the steady-state rate of CO oxidation. When the sticking coefficient is increased, there is some point at which a moving reaction front is predicted before the steady-state value is attained. Care must be taken when adjusting this value, as there also appears to be a range of valid values under the reaction conditions that must be considered when adjusting the parameters. Also important to note, the steady-state oxidation rate is a function of oxygen competitiveness, and three parameters have been shown here to influence the result. As there is a balance between these values, the adjustment of two of these parameters in the associated directions may nullify the effects.

4.5.7 Factors Influencing the Peak Conversion

During a CO step increase, the rate of CO oxidation has a minor influence on the initial production peak height. However, above an increase of approximately 50%, this rate dominates and conversion becomes complete.

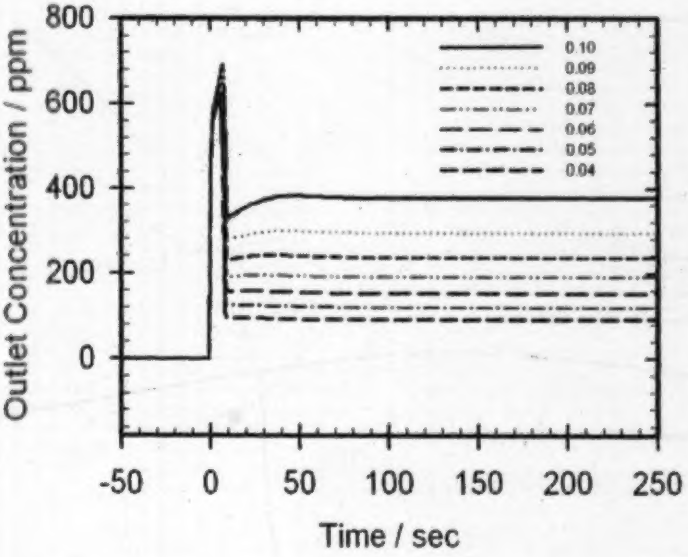

Figure 4.36: Effect of the sticking coefficient for oxygen on CO_2 production for a concentration step of 0-1000 ppm CO. Shown is the outlet concentration for CO_2 over time.

The rate of reaction between adsorbed CO and adsorbed compressed oxygen islands ($CO\_Pt + OO\_Pt \rightarrow CO_2\_Pt + O\_Pt$) influences the height of the peak CO_2 production, as shown graphically in Figure 4.37. Here, the rate constant was varied, and the non-linear relationship between the rate and the peak height explored.

For large values of k ($\geq 5 \times 10^{15}$), the reaction proceeds very quickly. CO adsorbs to the surface by displacing an adsorbed oxygen and forming a compressed oxygen species. This compressed oxygen species then reacts very quickly with the adsorbed CO, leaving a free site and an adsorbed oxygen. The free site then becomes occupied by either CO or oxygen (and when CO conversion is complete, only oxygen is available to adsorb), and the cycle begins again. As the rate of oxidation via this pathway with this parameter value is so fast, CO never stays on the surface long enough to dominate sites, and the overall surface coverage of CO under these circumstances is very low. As conversion is essentially complete as soon as CO is introduced to the system, no clear peak is observed. Adsorbed oxygen dominates the surface at essentially all points (with the exception of a short entrance region), and the reaction goes to completion in the first half of the monolith. At some value near 1.5×10^{15}, the steady-state conversion jumps to a larger value, whereby CO dominates the surface following the introduction of the reactant.

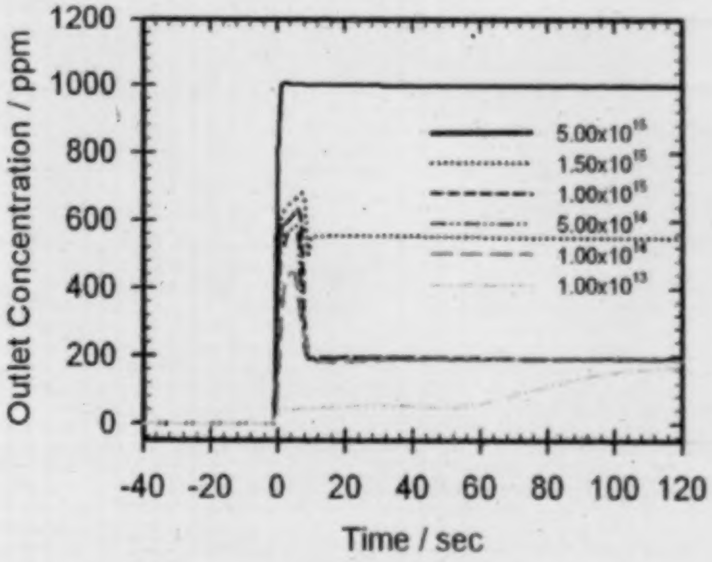

Figure 4.37: Effect of the rate of reaction for CO-Pt + OO-Pt → CO_2-Pt + O-Pt on CO_2 production for a concentration step of 0-1000 ppm CO. Shown is the outlet concentration for CO_2 over time.

Over a range of approximately 1×10^{14} to 1.5×10^{15}, increases in the k value cause an increase in the peak production height, with each peak being essentially the same width. Over this range, the rate of reaction between adsorbed CO and adsorbed compressed oxygen appears to only influence the peak height and not the peak width. In this region, the steady-state rate is controlled by the competitiveness of oxygen adsorption (see subsection 4.5.6). For smaller values of k ($\leq 1 \times 10^{13}$), the system slowly begins to react and relatively slowly proceeds to a steady state controlled by the competitiveness of oxygen adsorption.

4.5.8 Carbon Deposition

Deposition of carbon [166, 200, 81, 201, 202] onto the surface of the catalyst has been stated to lower catalytic activity during dry-reforming of methane [203], and may be a significant factor in CO oxidation. Deposition of carbon from methane sources is insignificant at low pressures (~ 1 bar), but significant at higher (~ 14 bar) pressures [204]. However, this theory is tested here to determine if this pathway is indeed significant.

Several mechanisms exist in the literature for the formation of carbon from CO on platinum catalysts. CO disproportionation may occur via either of two mechanisms: either direct disproportionation of a single CO molecule (Equation 4.18 and Equation 4.19), or via a bi-molecular reaction as shown in Equation 4.20 [204]. These pathways were both investigated.

$$CO^* + {}^* \rightarrow C^* + O^* \tag{4.18}$$

$$C^* + O^* \rightarrow CO^* + {}^* \tag{4.19}$$

Chatterjee et al. [66] have given parameters for the disproportionation of CO (Equation 4.18 and Equation 4.19). This mechanism for formation of carbon on the surface is unlikely, as not only does the equilibrium strongly favours the formation of CO (Equation 4.19), but the availability of free sites is limited in most cases.

At higher temperatures, CO_2 production may be attributed to CO disproportionation [205]. Carbon deposits from this reaction may influence the surface coverage over time. Equation 4.20 is commonly referred to as the Boudouard equation.

$$2CO^* \rightarrow C^* + CO_2^* \tag{4.20}$$

Carbon deposition is not only said to be temperature dependent, but also structure dependent as well. McCrea et al. [200] monitored CO dissociation on Pt surfaces with AES, and found that the onset of CO deposition (that is, the lowest temperature at which carbon deposition was detected in significant quantities) varies with the Pt surface. Temperatures were reported for three different surfaces: carbon deposition was detected in significant quantities at 500 K for Pt (100) surfaces, 548 K for Pt (557), and 673 K for Pt (111). As CO and/or CO+H_2 ignition occurs in the range of 400-500 K, it is questionable if carbon deposition is significant in the experiments presented here. If the light-off temperature is influenced by carbon deposition, then carbon deposits must be significant at temperatures lower than the light-off temperature. If carbon deposition influences concentration steps, then it is expected that a concentration step held for an extended period of time would slowly die away as carbon deposits build up and block active sites.

Experiments in Carbon Deposition

To confirm if carbon deposition does occur on the catalyst surface, several experiments were performed. The first experiment being a light-off curve with an inlet gas of 1000 ppm CO and the rest nitrogen. No oxygen was used in the feed gas, as it is thought that if no oxygen in present, then the typical oxidation route of CO (Equation 3.9a) is closed, and the only available reactions involved carbon deposition, Equation 4.19 Equation 4.18 and Equation 4.20.

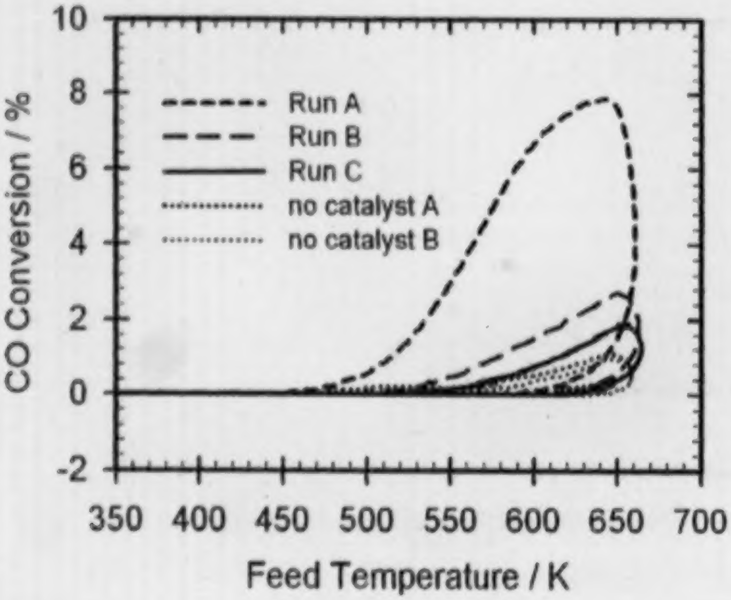

Figure 4.38: CO light-off experiments using only 1000 ppm CO and rest N_2 (no O_2 was present). SV = 25 000 h^{-1}. Three runs are with the monolith and catalyst, two are without. Note that the y-axis has been expanded to better show the effect.

During the light-off experiment with only CO and N_2 in the feed gas, the outlet CO and CO_2 concentrations were monitored and a plot of CO conversion with respect to feed temperature is given in Figure 4.38. Here, we see that a small amount of CO_2 was produced at elevated temperatures. This amounts to approximately less than 5 ppm CO_2 (0.5 % conversion) below 400 K, 10 ppm CO_2 (1 % conversion) at 500 K, and a maximum of 40 ppm CO (4 % conversion) at 600 K. Above 600 K, the rate of CO_2 production decreases, perhaps indicative of carbon deposits covering the surface.

This is a relatively small amount of CO conversion, especially at lower temperatures. The quantity of CO conversion is not expected to significantly influence the rate of CO_2 production during steps in CO concentration, such as those shown in subsection 4.3.2. The current experiment does not discriminate between oxidation via CO disproportionation (Equation 4.19) and CO self-oxidation via a Boudouard-type mechanism (Equation 4.20).

When this light-off experiment utilizing only CO and N_2 is repeated, as shown in the three successive experiments in Figure 4.38, the amount of CO_2 produced decreases with more runs. This decrease may be due to either carbon deposits covering the surface and decreasing the rate of CO self-oxidation (Equation 4.20 or Equation 4.19), or due to the CO reacting with oxygen that is held very strongly to the surface.

In the case of strongly-held oxygen at the surface, perhaps as oxidized surface sites, the oxygen may become available for reaction with CO only at elevated temperatures. As the supplies available on the surface are limited, after each successive run, less oxygen is available for reaction and the rate decreases.

This is not expected to be a significant factor during typical light-off curves, as during those experiments oxygen is always present in excess. In addition, above ~440 K, almost complete conversion of CO is observed under typical conditions via normal kinetics, whereas the conversion of CO in an oxygen-free atmosphere does not exceed 1% conversion until 500 K during the run that showed the highest conversion (run A in Figure 4.38).

The light-off curves were repeated without the monolith or catalyst present (see Figure 4.38), and very small amounts of CO_2 were observed to be produced, but not exceeding a conversion of 1% at temperatures of 650 K. This CO_2 production may be a result of either a high temperature CO+CO reaction (Equation 4.20) or very slow oxidation of CO using trace amounts of oxygen scavenged from the reactor walls. Trace oxygen impurities in the nitrogen feed amount to approximately 1 ppm of material (see Table 2.1), which does not account for all conversion. Trace amounts of oxygen may be present on oxidized sites on the reactor walls, but may only be liberated at high temperatures. This oxygen may be responsible for the small amounts of CO conversion, especially given that this oxygen supply may be finite and is slowly exhausted with each successive experiment without oxygen present.

In addition to light-off experiments in the absence of oxygen, several step functions in CO were also performed in the absence of oxygen. These experiments were performed with the intention of observing CO and CO_2 production to determine if significant amounts of CO_2 would form in an oxygen free atmosphere. Should CO_2 production be observed in the absence of oxygen, then the most likely route for this mechanism is the Boudouard equation, as discussed above and in 4.5.8.

Figure 4.39 shows three successive steps from 0 to 1000 ppm CO concentration in a nitrogen atmosphere. The inlet temperature was a constant 370 K. The initial production of CO_2 seen during the first step may be attributed to CO scavenging adsorbed oxygen still on the surface from the previous experiment involving oxygen. As this peak quickly

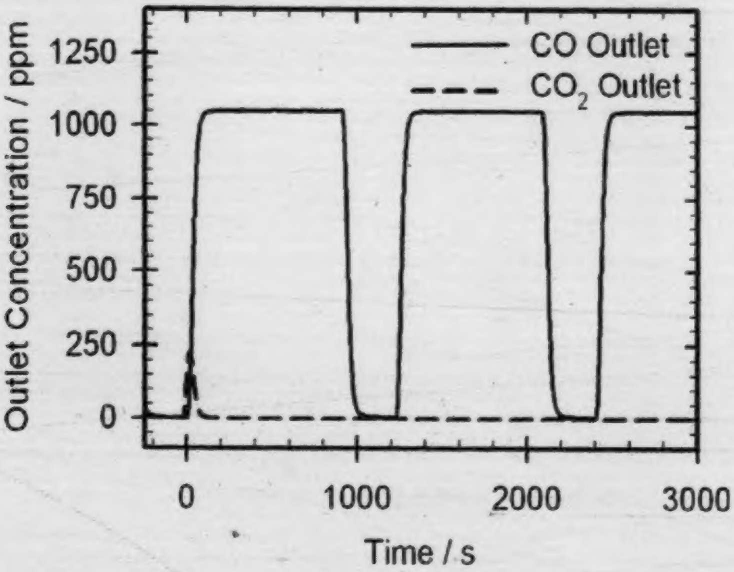

Figure 4.39: CO step functions using only 1000 ppm CO and rest N_2 at constant temperature $T_{Feed} = 370$ K. SV = 25 000 h^{-1}. The initial production of CO_2 seen during the first step is attributed to CO scavenging adsorbed oxygen still on the surface from the previous experiment.

diminished, the supply of adsorbed oxygen must have been exhausted. Successive steps in CO do not show any production of CO_2, strengthening our conclusion that Equation 4.20 is not a significant pathway under the conditions studied here.

Further evidence that CO does not self-oxidize via this step under typical catalytic converter conditions is shown in Figure 4.40. In this experiment, a step up in CO concentration (in the presence of 6 % O_2) was held for 60 minutes at constant $T_{Feed} = 390$ K. Once all available surface oxygen was consumed and a steady-state was achieved, there was no significant change in the rate of CO_2 production. If carbon deposition was occurring, then it is expected that carbon deposits would occupy active sites, blocking CO and oxygen from theses sites. As carbon deposition progresses, it is expected that the deposits would block enough active sites to influence the CO_2 production rate. As the steady-state conversion was relatively low, and would have required all available surface sites to achieve that conversion, blocking even a small number of sites was expected to produce a significant decrease in conversion. However, after an hour of CO oxidation, Figure 4.40 shows that this is not the case and that the rate of CO_2 production remains relatively constant and does not diminish

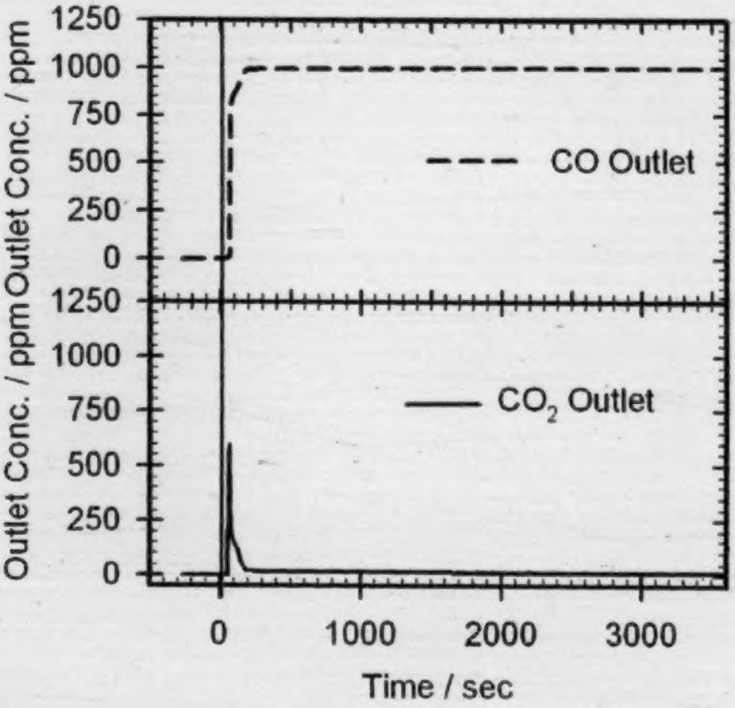

Figure 4.40: CO step functions using 1000 ppm CO, 6 % O_2 and rest N_2 at constant temperature $T_{Feed} = 370$ K. SV = 25 000 h^{-1}. The step was held for an hour to observe if there were any changes in CO_2 production.

due to carbon deposition (under these conditions).

With the above evidence, it is concluded that under the conditions of interest to automotive exhaust catalysis, carbon deposition is not a significant factor. At higher temperatures (> 500 K), minor amounts of CO conversion may occur via self-oxidation (Equation 4.20), however, this conversion may not be significant compared to the rate of oxidation using oxygen adsorbed onto the surface of the catalyst.

Effect of Boudouard Equation

Using a standard parameter set, and values show in Table 4.8, the influence of the Boudouard equation (Equation 4.20) was studied. These results are shown in Figure 4.41.

When this pathway was very small or zero, it had no influence and was identical to results that did not contain the sub-mechanism.

Reaction		A^0 $mol_i\ mol_{cat}^{-1}\ s^{-1}$	Ea $kJ \cdot mol^{-1}$
Compressed Oxygen			
Equation 4.14	$CO + 2O^* \rightarrow CO^* + OO^*$	1×10^{13}	50
Equation 4.16	$CCO^* + OO^* \rightarrow CO_2 + O^* +^*$	1×10^{15}	115
Equation 4.17	$OO^* +^* \rightarrow 2O^*$	1×10^{15}	105
Carbon Deposition			
Equation 4.18	$C^* + O^* \rightarrow CO^* +^*$	1.006×10^5	$-33\theta_{CO}$
Equation 4.19	$CO^* +^* \rightarrow C^* + O^*$	1.006×10^2	$218.5 - 45\theta_O$
Equation 4.20	$CO^* + CO^* \rightarrow C^* + CO_2^*$	varies	70

Table 4.8: Kinetic parameters used to determine the influence of the Boudouard equation.

For intermediate but not dominating values of k ($k \geq 1 \times 10^5$ and $k \leq 4 \times 10^9$), the reaction was slowly extinguished by a buildup of carbon decreasing the number of active sites.

When this pathway was very fast ($k > 10^{10}$), conversion of CO was complete. This was mostly due to CO being able to react with other CO to form CO_2 and C. When this pathway is fast, the oxidation of CO will occur irrespective of the CO desorption rate, as CO will be able to oxidize even when oxygen is not present on the surface. However, such large values of this kinetic constant appear to be unreasonable, and do not agree with experimental observations.

4.5.9 Effect of Reactor Length

The influence of reactor length on a concentration step is explored through simulations. These results are shown graphically in Figure 4.42. The parameters presented here utilize a classical LW mechanism (section C.2) plus compressed oxygen (section C.7). Compressed oxygen parameters are the same as shown in Table 4.8. Carbon deposition is not used in this set of simulations.

Below $1.6 \times L$, the effect of reactor length is fairly clear. The total number of active sites varies directly with the reactor length, and as the total number of active sites increases, so too does the overall conversion. The initial peak is broadened by increasing the reactor length, as initially the surface is covered by adsorbed oxygen. The integrated size of this peak will be influenced by the amount of pre-adsobed oxygen available for reaction. As well, the steady-state conversion at a specific inlet temperature and inlet gas composition will tend to be higher in a longer reactor.

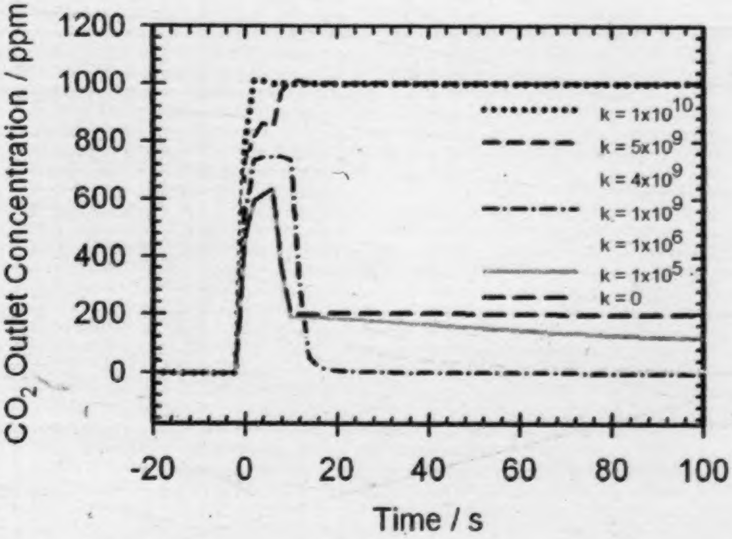

Figure 4.41: Effect of the rate of reaction for the Boudouard reaction on CO_2 production for a concentration step of 0-1000 ppm CO.

At 1.6 × L and above, the effect becomes unclear. It is possible in longer reactors, that temperature gradients and moving reactor fronts play a more significant role. As the reactor exit is heated by the heat of reaction, a slow transfer of thermal energy towards to front of the reactor may begin. As this front proceeds towards the front of the reactor, a critical point may be attained at which the reaction goes to completion at a hot spot within the reactor. This may lead to the sharp jump in conversion. As the thermal energy is distributed, and conversion becomes less localized, the steady-state is attained.

4.5.10 Limited Surface Coverage

A modification to the model has been made, such that the sticking coefficient may be made dependent upon several different properties, including surface defects and repulsion components. With elementary reactions on the surface, these modifications may be made by defining variations in the activation energy based on surface conditions. This modification is targeted toward modifying the sticking coefficient based on surface conditions, and may be used to implement the self-exclusion mode (4.1.9). The sticking coefficient is multiplied by a factor which is dependent upon the surface coverage of a selected component, as shown in Equation 4.21. The function used to calculate the factor is shown is Equation 4.22.

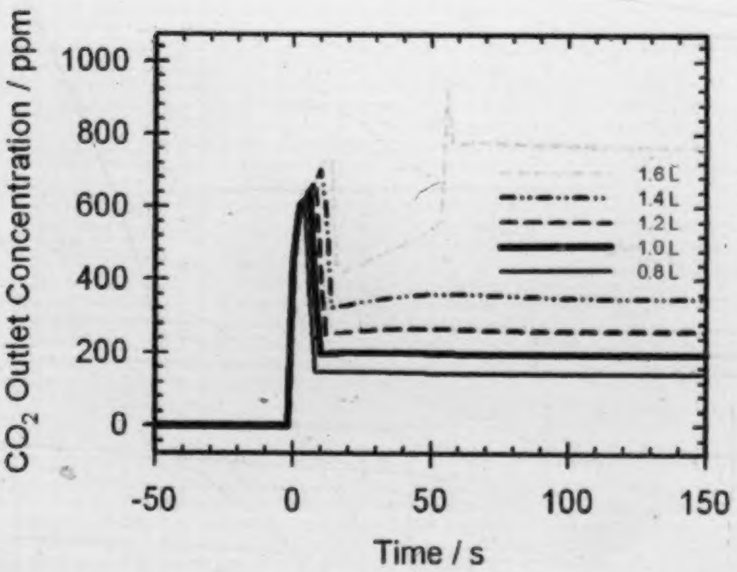

Figure 4.42: Effect of reactor length (where L = 76.2 mm) on CO_2 production for a concentration step of 0-1000 ppm CO.

$$S^0_{modified} = S^0_{standard} \times Factor(\theta_X) \tag{4.21}$$

$$Factor = (B_{highcoverage} - A_{lowcoverage}) \cdot \left(\frac{1}{1 + e^{C_{steep}\cdot(\theta_X - D_{inflectionpoint})}}\right) + A_{lowcoverage} \tag{4.22}$$

Where A is the value of the factor under conditions of low coverage, B is the value of the rate factor at high coverage, C describes the steepness of the transition between A and B, and D describes the transition point (or inflection point) where the transition occurs. Under standard conditions, and all conditions where this factor is not explicitly stated to be in use, this rate factor is equal to 1.

To implement this function to limit the surface coverage of a selected component to a stated value, the high coverage limit is set to zero, and the inflection point may be set to the adsorption limit ($D_{inflectionpoint} = \theta_O^{sat}$). This may be used, for example, to describe the repulsive forces between components that are highly electronegative.

Two sample functions that may be applied are shown in Figure 4.43. The poisoned curve shows a sample curve whereby the rate of coverage of a component is limited by increasing coverage of the component of interest. Here, an inflection point of 0.8 was defined. This may be useful for describing such phenomena as the saturation limits of a component on a surface, or the repulsive interactions between components that make adsorption beyond specific limits difficult (but not impossible) to attain.

The promoted adsorption function may be useful to describe other phenomena, such as variations in the oxygen sticking coefficient that cause changes in the surface phase in the presence of larger coverages of CO. Lynch et al. described transitions between the (1x1) and (5x20) phase on platinum that were dependent upon, among other factors, the surface coverage of CO [182]. The sticking coefficient for oxygen varied strongly between the two phases, with the sticking coefficient being higher under higher CO coverage (the (1x1) phase). Although the original reference [182] describes a hysteresis effect, however, this effect is not reproduced here at this time.

This function is expected to allow CO to adsorb onto an oxygen saturated surface, as even when oxygen adsorption is irreversible, not every site is occupied.

When these limits are properly defined, then several aspects of an experiment may be better modelled.

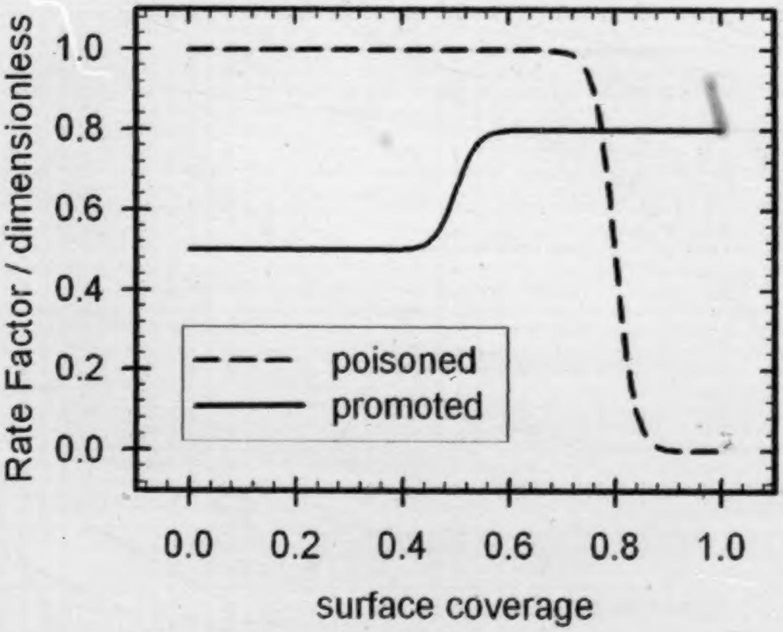

Figure 4.43: Functions used to modify sticking coefficients to reflect surface dependent behaviour. The equation may be found in Equation 4.22.

The possibility of having small fractions of adsorbed oxygen on the surface at temperatures well below light-off may assist in predicting smoother light-off curves, as small amounts of oxygen may adsorb at lower temperatures and react, albeit slowly.

As well, the potential for having other adsorbed species, such as hydrogen and oxygen, on the surface well below the light-off temperature improves the significance of H/O/CO/OH surface reactions and the promotion of CO via an OH species.

	Value	Comments	Reference
CO	$\theta_{CO}^{sat} = 1$	PrOx conditions	[140]
	$\theta_{CO}^{sat} = 1$	Pt(110)	[89]
	$\theta_{CO}^{sat} = 1ML$	Pt(110), 160 K	[141]
	$\theta_{CO}^{sat} = 1ML$		[140]
	$\theta_{CO} > 0.9\theta_{sat}$	Pt	[139]
	$\theta_{CO}^{sat} = 0.79ML$	Pt(112)	[134]
	$\theta_{CO}^{sat} = 0.77ML$	Pt(100), 190 K	[141]
	$\theta_{CO}^{sat} = 0.64ML$	Pt(111), 160 K	[141]
	$\theta_{CO}^{sat} = 0.44 - 0.49ML$	Pt(111), 300-300 K	[141]
	$\theta_{CO}^{sat} = 0.88ML$	Pt(110)	[142] [a]
	$\theta_{CO}^{sat} = 0.49ML$	Pt(111)	[142] [a]
	$\theta_{CO}^{sat} = 0.77ML$	Pt(100)	[142] [a]
O	$\theta_{O}^{sat} = 0.82\theta_{CO}^{sat}$		[89]
	$\theta_{O}^{sat} = 0.75ML$	Pt(111), UHV, 400 K, NO_2 Exposure	[54]
	$\theta_{O}^{sat} = 0.26ML$	Pt(111)	[141]
	$\theta_{O}^{sat} = 0.25ML$	Pt(111)	[156]
	$\theta_{O}^{sat} = 0.25ML$	Pt(111)	[206]
H	$\theta_{H}^{sat} = 1ML$	Pt(111)	[156]
	$\theta_{H}^{sat} = 0.75\theta_{CO}^{sat}$	zero pressure	[89]

---

[a] and references therein.

Table 4.9: Surface coverage saturation values from literature. Values are fractions of one monolayer (ML) of coverage.

4.6 Summary

4.6.1 CO Light-Off Curves

Along the high-rate branch, the reaction is kinetically limited and adjustment of the rate of CO oxidation on the surface with influence the light-out temperature. Along the low-rate branch, the reaction is limited by mass transfer, and specifically transfer of oxygen onto the surface. By increasing the rate at which oxygen adsorbs to the surface, the light-off temperature may be lowered in the simulations. The rate of oxygen adsorption may be increased by increasing the sticking coefficient for oxygen, or by allowing oxygen to have more opportunities to adsorb to the surface. This may be accomplished by decreasing the sticking coefficient for CO or increasing the rate of CO desorption.

4.6.2 CO Concentration Steps

During a step up in CO concentration on a system pre-covered in oxygen, there is an initial high rate of production of CO_2 while the surface concentration of adsorbed oxygen is high. However, once the supply of adsorbed oxygen is diminished, the rate of CO_2 production settles to a steady-state.

In the CO concentration steps studied, none of the traditional models (global kinetics, ER and LH) were able to predict the transient behaviour. As the global mechanism does not consider surface composition, this mechanism will never be able to predict transient phenomena. The ER model was able to predict transitions. However, the shape of the resultant prediction and the time-scale on which this was seen were not in agreement with the experimental result.

With the assumption of irreversible oxygen adsorption, the LH model was unable to predict any reactions on an oxyxgen covered surface, as there was no step to remove oxygen from the surface. When such a step was added, via the compressed oxygen mechanism, the behaviour was predicted. However, a proper parameter optimization must be performed such that better parameters may be obtained and the issue of time-scale of the process may be resolved.

4.7 Requirements for an Acceptable Model

An acceptable model for prediction of CO oxidation on a Pt surface must account for the following observations:

- Below the ignition temperature, the steady-state surface coverage should be dominated by CO
- Above the ignition temperature, the steady-state surface coverage should be dominated by O
- Correct prediction of the shape of the light-off curve, and the sharpness at the ignition point
- Correct prediction of the light-off temperature
- Correctly prediction whether ignition begins at the front or end of the monolith
- Correctly predict the progression of the reaction front through the monolith
- Prediction of the correct ΔT trend (or constant value) with increasing CO concentration during light-off curves
- Prediction of the shape of a step function, especially the initial conversion followed by poisoning during a step up in CO concentration, as well as the initial high conversion/desorption curve observed during the step down in CO concentration
- A step for reacting CO on an oxygen covered surface. This may be satisfied by a compressed oxygen step
- A step for reacting oxygen on a CO covered surface. This is satisfied by CO desorption in the standard models

4.8 Future Work

A better match to the experimental data may arise with an optimized parameter set. Although the kinetic parameters used were from the literature and derived from thermodynamic data, it is very difficult for two catalysts prepared in separate locations using separate methods to have matching kinetic parameters. The metal loading factor attempts to compensate for this, but as shown by Arnby et al. [122], the catalyst properties (especially dispersion and metal loading) significantly and non-linearly affect the shape of the light-off curve and light-off temperature.

As discussed before, the parameters used for the compressed oxygen steps must be optimized and better values found. Idealy, these values would be experimentally obtained, however such values do not currently exist in the literature.

Agreement between the experimental and simulation CO light-out curves has not yet been attained. The parameter or modification that allows the system to predict a long, smooth CO light-out (instead of the abrupt one currently predicted) is expected to be the same as that which allows a much longer peak and relaxation time during the steps in CO concentration. This factor may be related to moving reaction fronts along the catalyst surface, proceeding from the front end to the back (or vice versa) over time.

5

CO+H_2 Oxidation[*]

5.1 CO+H_2 Literature Review

In 1823, Döbereiner [209, 210] reported to Göthe that hydrogen reacts with oxygen to form water at room temperature when the gas contacts Pt. Since this time, much work has been done with respect to the reaction of H_2 on Pt. As hydrogen is present in the exhaust gas of diesel engines, the interactions between CO oxidation and hydrogen oxidation are important to understand when attempting to improve the overall efficiency of a catalystic converter. As will be shown, these components do not oxidize independent of one another, but interact quite closely.

Hydrogen is considered to be a clean fuel, as water is the product of hydrogen combustion, and a concentrated source of energy. As such, research in hydrogen and platinum has as of late been reinvigorated with the promise of hydrogen fuel cells and the potential of a hydrogen economy [211, 10]. Long-term political plans include hydrogen as a carbon-free means of energy storage, with the local combustion/usage of hydrogen not affecting the global carbon cycle.

5.1.1 Hydrogen on the Pt Surface

Hydrogen is modelled in a similar manner as CO oxidation, with the reaction occuring on the catalyst surface. The difference is that hydrogen adsorbs dissociatively onto the surface and then oxidizes in two steps. Hydrogen oxidation typically uses similar parameters for

---

[*] a portion of this chapter has been published [207] in *Catalysis Today*, presented [208] at IWCC6, the 6th International Workshop on Catalytic Combustion in Ischia, Italy, September 2005, or is in preparation for publication.

Reference	H_2	CO	O_2
Chatterjee et al. [66]	0.046	0.84	0.07
Kasemo and Törnqvist [89]	0.62	0.54	0.38
Zafiris and Gorte [143]		0.5	0.01
Nett-Carrington and Herz [136]		1.0	0.00056
Schubert et al. [139]		0.5-0.8	

Table 5.1: Sticking Coefficients from literature sources.

the many common steps that have already been described for CO oxidation, such as those steps involving oxygen adsorption.

Dissociative Adsorption

Hydrogen adsorbs dissociatively onto Pt [212, 94, 95, 61] and Pd [213] surfaces at temperatures in the range studied here. When oxygen coverage was greater than 10% of the saturation coverage, Verheij and Hugenschmidt found that hydrogen adsorption was the limiting factor towards hydrogen oxidation within a temperature range of 300-600 K [95].

A reaction order of -1 with respect to hydrogen adsorption on empty sites is used in the simulations [66]. This value is critical in achieving accurate results. Without this term, hydrogen does not appear to satisfy the most basic of conditions and react at room temperature.

Sticking Coefficients

Kasemo and Törnqvist [89] state the sticking coefficients at zero-coverage for H_2, CO and O_2 on a Pt surface are 0.62, 0.54, and 0.38 respectively. As the sticking coefficient for H_2 is slightly higher, CO should not be able to poison the surface against H_2, however this will also depend on the rates of desorption as well as the dependence of the sticking coefficients on the surface coverage. In the Chatterjee parameter set, the activation energy for hydrogen desorption is half that of CO, enabling hydrogen to desorb at a much higher rate.

The sticking coefficients reported by Kasemo and Törnqvist [89] differ from those reported and used by Chatterjee et al. [66], as shown in Table 5.1. The order of adsorption of CO and H_2 is very different between the two sources, perhaps due to differing test conditions.

Desorption

Hydrogen can be easily removed from a Pt surface by mild heating [214], and is modelled as such. The limiting factor for this reaction in the system that was studied was the relatively low surface concentration of hydrogen.

Desorption of CO, CO_2, and oxygen are the same as previously discussed. Desorption of OH, an intermediate species formed during hydrogen oxidation has a high activation energy (on the order of 200 kJ·mol^{-1}) [215, 216, 217], and typically only occurs at high temperatures. OH desorption is thus considered to be negligible.

Diffusion on the Surface and through the Washcoat

The rate of diffusion of H_2 through the washcoat is very high, and the solid temperature has been seen to exceed the adiabatic temperature rise [41] under some conditions.

Seyed-Reihani and Jackson evaluated the surface chemistry of hydrogen oxidation on a Pd catalyst [218], reporting that the effectiveness factor of washcoats (even thin washcoats) can be < 1.0 and may also be influenced by such factors as H_2O and H_2 concentrations.

5.1.2 CO and Hydrogen on the Pt Surface (no reaction)

Dawoody et al. performed CO-TPD experiments and observed [219] hydrogen from the previous experimental step (reduction) desorbing at various temperatures. Three hydrogen desorption peaks were reported; the first being at 4°C and attributed to CO adsorbing to the surface and weakly-adsorbed hydrogen desorbing. At approximately 100°C, a second peak of hydrogen desorption appeared, corresponding to the point where significant CO desorption also begins. The third peak was not observed until 400°C, and would not be significant under the conditions of interest in the present study.

5.1.3 Oxidation of Hydrogen

Hydrogen alone

Under the conditions of interest for a diesel oxidation catalyst, hydrogen oxidation alone is not very interesting. Oxidation of hydrogen on a Pt surface has been known to proceed at temperatures as low as 120 K [94], and hydrogen oxidation was observed to go to completion at the lower temperature of the experimental apparatus at $\varpi \sim 308$ K (35°C). When the surface is oxygen covered, the reaction is limited by the rate of adsorption of hydrogen [95].

The reaction between H_2 and O_2 is generally agreed to proceed upon the surface between adsorbed components [89]. Surface studies [220] show that the only species present on the surface during hydrogen oxidation were O^*, OH^*, and H_2O^*. Adsorbed hydrogen (H^*) was not found on the surface in the forementioned study as it cannot be detected by High Resolution Electron Energy Loss Spectroscopy.

Eisert and Rosén [156] show a dual-path mechanism for the oxidation of H_2 on Pt. The mechanism that they have developed is shown here:

$$H_{2(g)} + 2* \rightleftharpoons 2H^* \tag{5.1a}$$

$$O_{2(g)} + 2* \rightleftharpoons 2O^* \tag{5.1b}$$

$$H^* + O^* \rightleftharpoons OH^* + {}^* \tag{5.1c}$$

$$OH^* + H^* \rightleftharpoons H_2O^* + {}^* \tag{5.1d}$$

$$OH^* + OH^* \rightleftharpoons H_2O^* + O^* \tag{5.1e}$$

$$H_2O^* \rightleftharpoons H_2O_{(g)} + {}^* \tag{5.1f}$$

Equation 5.1a shows the dissociative adsorption of H_2 on the surface, proceeding up to $\theta_{H,max} = 1$ (θ represents the surface coverage of the component as a fraction of a monolayer). For $T > 150$ K, O_2 adsorbs dissociatively (Equation 5.1b) on the Pt surface with $\theta_{O,max} = 0.25$. Adsorbed H and O can form the hydroxyl as in Equation 5.1c. At this point, Eisen and Rosén state that two reaction pathways are now possible at $T > 120$ K. Hydrogen addition (Equation 5.1d) can occur, forming adsorbed water. Also possible is the hydroxyl disproportionation step (Equation 5.1e). Both pathways use OH^* as an intermediate species. In the end, water may desorb from the catalyst surface, as shown in 5.1f.

Eisen and Rosén stated that the hydrogen addition pathway (Equation 5.1d) is more important under conditions of high temperature and high pressure (>10 mtorr), whereas the hydroxyl disproportionation step (Equation 5.1e) is favored at lower temperatures due to the lower activation energy of this pathway. This is echoed by Zhdanov and Kasemo [92], with hydroxyl disproportionation being significant under conditions of low temperature or large oxygen excess. In the simulations to be presented in this work, it will be shown that under diesel exhaust gas conditions, the dominant pathway is via the hydrogen addition steps (Equation 5.1c and Equation 5.1d) and not hydroxyl disproportionation (Equation 5.1f). Snytnikov et al. also considered the hydroxyl disproportionation step to be insignificant under automotive exhaust conditions [221].

Völklinger et al. stated that below the water desorption temperature (~ 170 K under UHV), adsorbed water and oxygen would react to form adsorbed OH (the reverse reaction of Equation 5.1e) in an autocatalytic manner, but above this temperature, the reaction would proceed through hydrogen addition.

Harris et al. [222] published an early model, that, although it does not include the hydroxyl disproportionation step, claims that the OH* formation step Equation 5.1c) is rate-limiting. Pedrero et al. [223] also neglected the hydroxy disproportionation step. Based on these literature results, and several simulations where the various pathways were isolated and this step did not show an influence, the hydroxy disproportionation step is not considered to be significant under the conditions in the present study.

Superadiabatic Combustion and Hotspots

Travelling reaction fronts of adsorbed H, OH and H_2O have been observed to be 10-100 nm wide at 170 K [224, 225, 226]. At such small sizes, these fronts would most likely not be observed on the scale of a monolith catalyst, and many thousands of small reaction fronts moving in random on a micro scale would average out to a steady value on a macro scale.

Yakhnin and Menzinger have observed larger travelling reaction fronts in the catalytic combustion of hydrogen [227] for concentrations of 1-5% H_2. At these concentrations, hot spots were observed, and the origin of these hotspots attributed to the fast diffusion of the fuel relative to the slower diffusion of thermal energy. The propegation rate and direction of these hot spots was reported to vary with the flow velocity. The movement of the hotspots along the axial co-ordinate of the reactor depended upon the relative rates of conduction (moving the hotspot upstream) and convective energy transfer (shifting the hotspot downstream). This typically results in the hotspot shifting downstream while at low flow velocities and upstream at high flow velocities.

The magnitude of the hotspot was also reported to be flowrate dependent, becoming superadiabatic at high flow rates due to the decreased residence time of the gas, decreasing the efficiency of thermal energy removal [227].

5.1.4 Water Gas Shift

The concentration of H_2 in the exhaust gas is usually determined by the water-gas shift reaction occuring during combustion in the engine, yielding a molar ratio of approximately CO:H_2 3:1 [41, 228]. This reaction (Equation 5.2) has been stated to occur on the platinum surface [229, 230].

$$CO + H_2O \rightleftharpoons CO_2 + H_2 \tag{5.2}$$

Equation 5.3 is a variation of this reaction that appears in the literature for homogeneous combustion of CO in the presence of hydrogen [231].

$$CO + HO \rightleftharpoons CO_2 + H \tag{5.3}$$

It is generally accepted that the water-gas shift reaction does not occur in the gas phase under the conditions of typical operation of a diesel oxidation catalyst, as the temperature of the catalyst is too low (as compared to the temperature in the engine, which can be 700-900°C). This reaction is slow compared to oxidation and its influence is negligable [140, 232]. Some simulations were performed in this study, and it was found that the water-gas shift reaction on the platinum surface was not significant under the conditions studied here. As such, the water-gas shift was not used for simulations in the present work.

5.2 CO+H$_2$ - Selectivity

5.2.1 Selectivity of Pt Catalysts Towards Oxidation of Carbon Monoxide

Due to industrial interest in steam reforming, much has been written in the literature regarding the preferrential oxidation of carbon monoxide in the presence of hydrogen. The PROX literature shows us that platinum catalysts will typically be selective towards CO oxidation [139, 233, 142, 234, 235, 236, 237, 238, 140, 232, 239, 240, 241, 242, 243] despite the presence of large concentrations of hydrogen (from 1% to 75% H$_2$ compared to 50-5000 ppm CO).

Kahlich et al. observed a decrease in CO conversion at temperatures $\geq$ 250°C, and attributed this to loss in selectivity [142]. This, however, was not observed in the experiments presented here, as at elevated temperatures the catalyst was observed to completely oxidize all CO and all H$_2$. The reason for not observing the effect may be due to the component concentrations; Kahlich et al. used an inlet gas composed of 75% H$_2$ and 0.02-1.5% CO, compared to the much lower concentrations in this work. As well, the contact time between the gas and the monolith may be sufficiently high in these studies to allow complete combustion.

The production of hydrogen fuel for fuel cells demands a very clean source of hydrogen. The presence of significant amounts of CO in the fuel can poison the catalyst, decreasing the effectiveness of the fuel cell. Thus, the fuel to be used in a fuel cell is to have as low a concentration of CO as possible. Pt catalysts are useful in this regard, and several recent studies have shown this.

Zhou et al. [244] tested a number of catalysts for producing clean hydrogen for fuel cell applications. Pt was found to perform better at selective CO oxidation than the other nobel metal catalysts (Pd, Ru and Rh) tested under methanol reforming conditions in the study. This catalyst achieved as much as 99.3% conversion of CO, with outlet gas composition of CO being on the order of 70 ppm. Water was also found to enhance the preferential oxidation of CO slightly, compared to the presence of CO_2, which slightly inhibited the reaction.

İnce et al. [239] also studied selective CO oxidation with Pt-Ce/Al_2O_3 for fuel processing for hydrogen fuel cells. In their study, İnce et al. were able to achieve 100% CO conversion using a 1.4 wt% Pt-1.25 wt% Co-1.25 wt% Ce/Al_2O_3 with significantly high selectivity at a reaction temperature of 90°C. While this result could be achieved at oxygen concentrations approaching 0.5% (CO inlet was 1%), this was in the absence of carbon dioxide and water. The effect of water was also studied, conferring with the study of Zhou et al. [244], showing that the presence of water enabled the reaction to be sustained for a longer time. With 10% water in the feed gas, 100% conversion of CO could be acheived at 110°C even after 300 minutes. In similar tests without water, the conversion would diminish after 150 minutes on-stream. This has been attributed to two possible explanations. The presence of water is supposedly allowing the water-gas shift reaction to remove some CO from the system, at the same time produce small amounts of H_2. The second explanation is that OH is forming at the surface, allowing CO oxidation to proceed in an alternate pathway [245].

Several groups have reported that the addition of Fe to a Pt catalyst may alter the selectivity and activity of a catalyst, and potentially increase CO oxidation by introducing a non-competitive adsorption site for oxygen [235, 246, 247]. Oxygen can adsorb onto the Fe sites, whereas CO does not. However, oxygen adsorbed onto the Fe sites can react with neighbouring CO adsorbed onto Pt sites. Therefore, even if CO saturates the Pt surface, small quantities of oxygen may adsorb onto the Fe surface and react with neighbouring CO-Pt. Although this introduces non-competitive adsorption, the particles must be sufficiently disperse such that the active sites are directly next to one another.

5.3 Experimental Light-Off Curve

Light-off experiments were performed using various mixtures of CO and H_2 to observe the relationship between these two components. Light-off temperature results are in Table 5.2,

Concentration		CO		H_2	
CO (ppm)	H_2 (ppm)	Light-Off (K)	Light-Out (K)	Light-Off (K)	Light-Out (K)
1000	0	426	388	—	—
1000	500	403	365	403	365
1000	2000	400	352	400	352
2000	0	444	404	—	—
2000	225	426	388	426	386
2000	300	427	386	427	384
2000	500	422	381	422	381
2000	1000	423	377	423	375
2000	2000	419	367	420	367

Table 5.2: Experimental CO Light-Off and Light-Out Temperatures in the presence of Hydrogen. 6% O_2, rest N_2. SV = 25000 hr^{-1}.

Figure 5.1, and Figure 5.2, and are discussed in the following sections.

The presence of hydrogen is promoting the ignition of CO. Several theories are present in the literature that attempt to explain the cause of this promotion effect. This will be explored later in section 5.9.

5.3.1 1000 ppm CO and 500 ppm H_2

A mixture of 1000 ppm CO and 500 ppm H_2 was used to perform the light-off experiment shown in Figure 5.3. The CO ignition follows a similar shape as before, with a gradual increase in conversion, accelerating with increasing temperature. After reaching 50% conversion (light-off temperature), complete conversion of CO is quickly attained.

The hydrogen light-off curve is somewhat different, with approximately 0% conversion being observed until CO reaches the light-off temperature. As CO ignites and sufficient CO conversion takes place, hydrogen ignition is swift, reaching almost complete conversion in a very short time period. The catalyst appears to be quite selective towards CO oxidation, despite the fast rate at which hydrogen oxidation proceeds, even at low (room) temperatures.

The light-off temperature of a mixture of 1000 ppm CO and 500 ppm H_2 was 403 K, compared to 426 K without H_2. The influence of the presence of hydrogen on CO light-off temperature will be discussed in section 5.6.

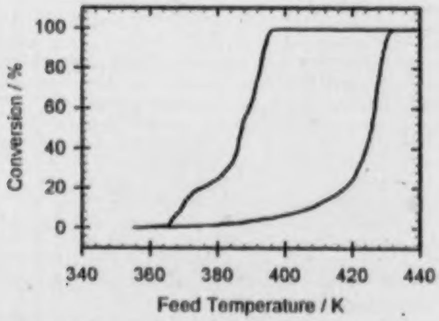

(a) 1000 ppm CO + no H_2 Light-Off Curve

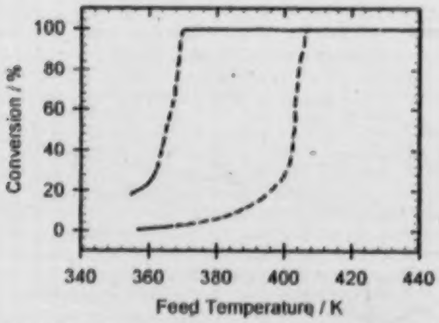

(b) 1000 ppm CO + 500 ppm H_2 Light-Off Curve

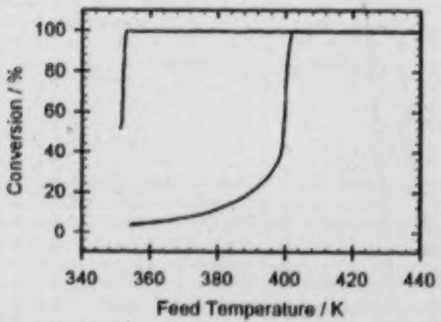

(c) 1000 ppm CO + 2000 ppm H_2 Light-Off Curve

Figure 5.1: CO Light-Off Curves for 1000 ppm CO and various levels of H_2. 6% O_2, rest N_2. SV = 25000 hr^{-1}.

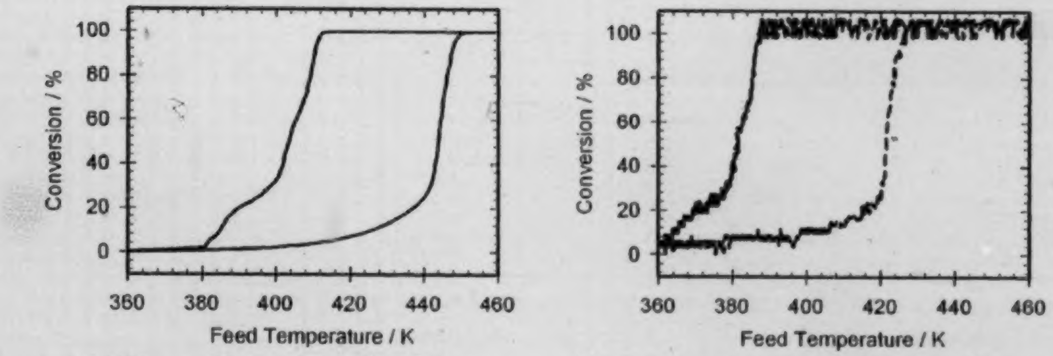

(a) 2000 ppm CO + no H_2 Light-Off Curve (b) 2000 ppm CO + 500 ppm H_2 Light-Off Curve

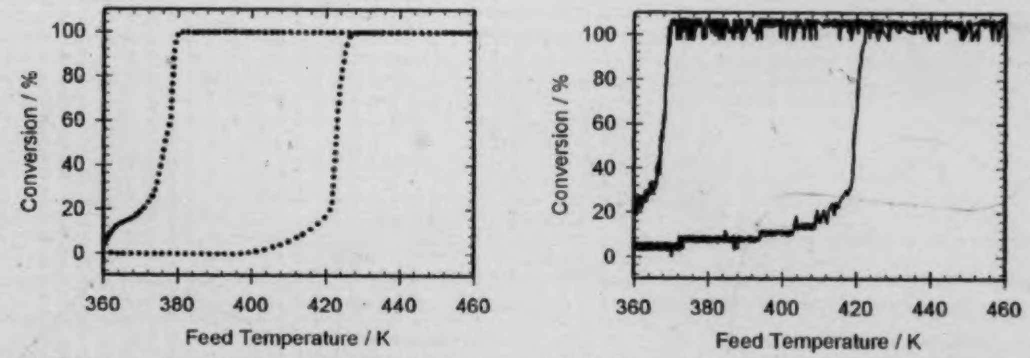

(c) 2000 ppm CO + 1000 ppm H_2 Light-Off Curve (d) 2000 ppm CO + 2000 ppm H_2 Light-Off Curve

Figure 5.2: CO Light-Off Curves for 2000 ppm CO and various levels of H_2. 6% O_2, rest N_2. SV = 25000 hr^{-1}.

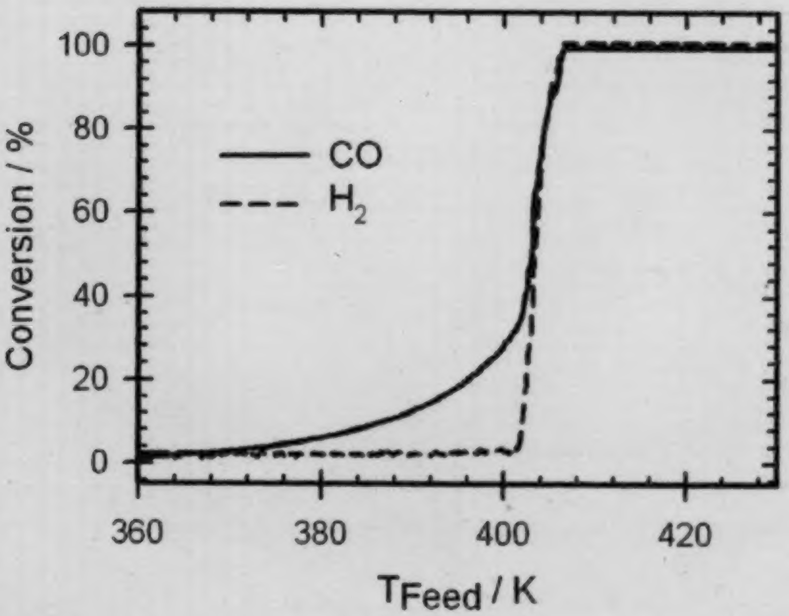

Figure 5.3: Experimental CO+H_2 Light-Off curves for CO and H_2 conversion. 1000 ppm CO and 500 ppm H_2, 6% O_2, rest N_2. SV = 25000 hr^{-1}.

5.4 Selectivity and Order of Ignition

As mentioned previously (subsection 5.2.1), the PROX literature shows that platinum catalysts will typically be selective towards CO oxidation despite the presence of large concentrations of hydrogen (typically between 1% and 75%). This selectivity is stated to be due to the increased preference for CO to adsorb to the catalyst surface, with the inhibition of hydrogen oxidation by CO being attributed to competitive adsorption [41].

Selectivity is defined in subsection A.3.2, and shown in Equation 5.4.

$$Selectivity = \frac{C_{CO} \cdot X_{CO}}{C_{CO} \cdot X_{CO} + C_{H_2} \cdot X_{H_2}} \tag{5.4}$$

$$Selectivity = \frac{1000 \cdot X_{CO}}{1000 \cdot X_{CO} + 500 \cdot X_{H_2}} \tag{5.5}$$

For a system of 1000 ppm CO and 500 ppm H_2, above light-off when both components are oxidized to completion, the selectivity will be 0.667. Below light-off, the value here will reflect either a preference for CO oxidation ($S > 0.667$) or a preference for H_2 oxidation ($S < 0.667$). Experimentally, the selectivity is clear: CO is preferentially oxidized (Figure 5.3) so long as it is not dominating all available free sites and blocking oxygen adsorption. At low temperatures, the rates of CO desorption and CO oxidation are low, and CO adsorption blocks all accessible sites. As the temperature increases, the rate of CO desorption increases such that other components are afforded more opportunities to adsorb. As oxygen adsobs and the surface concentration of oxygen increases, the rate of CO oxidation also increases. While hydrogen may be able to adsorb at temperatures several degrees below light-off (e.g. 20 K below light-off while CO conversion is still below 10%), the surface concentrations of oxygen and hydrogen will both be relatively small, in comparison to CO dominance (~99%) of the sites, ensuring hydrogen conversion is low.

At some critical temperature, the rates of CO desorption and oxidation are high and the turnover of free sites is high enough that hydrogen and oxygen may both adsorb in significant quantities. This point occurs near the CO light-off point, and is the point where hydrogen conversion becomes signifiant. At this point, oxygen adsorption and free site turnover are high enough that the catalyst is no longer kinetically limited, and both CO and hydrogen react to completion.

Hydrogen reacts to completion, even at room temperature, when sufficient oxygen is available but no CO is present. This is shown in step experiments such as Figure 5.4, performed at room temperature an in an excess of oxygen. Initially in this step experiment, the system has oxygen (6%) and hydrogen (100 ppm) present in the feed gas, and the hydrogen oxidizes to completion. Upon introduction of CO (250 ppm), the oxidation of hydrogen is halted. CO adsorbs to the surface sites. However, as this experiment was performed near room temperature (35°C), the surface reaction rate and the rate of CO desorption will be quite slow, allowing CO to occupy surface sites and block other components from adsorbing. Upon removal of CO from the inlet gas, adsorbed CO may desorb or react, freeing surface sites for hydrogen and oxygen to adsorb to and react upon. Hydrogen oxidation proceeds to completion in the absence of CO and at room temperature. This is consistent with the results reported in the early days of catalysis [209, 210].

5.4.1 Rate of Reaction of First Hydrogen Oxidation Step: O^*+H^*

With the lower pre-exponential factor, the ignition of hydrogen occurs at approximately the same time as the ignition of CO. However, the presence or absence of hydrogen has a very minor effect on the CO ignition temperature in these simulations, as shown in Figure 5.7, but the effect predicted by the classical LH model in the current state is a trend in the *wrong* direction. In the presence of 2000 ppm H_2, the light-off temperature of 1000 ppm CO was 430 K. The light-off temperature of 1000 ppm CO was 429 K in the simulation in 500 ppm H_2. In the absence of hydrogen, the light-off temperature was 428 K, slightly lower than in the presence of hydrogen. These results suggest that the simulator is predicting CO and H_2 compete for active sites and oxygen, as the presence of more hydrogen appears to be increasing the light-off temperature slightly.

There is some debate in the literature with respect to the value of the activation energy for hydrogen oxidation on platinum. Several literature values are summarized in Table 5.3. The activation energy for the hydrogen oxidation steps (Equation 5.1c and Equation 5.1d) was varied and several simulations were performed, the most significant of which are shown in Figure 5.4.

As a simple check, values for an activation energy below $E_{a,H*+O*} = 90\ \mathrm{kJ \cdot mol^{-1}}$ do correctly predict hydrogen oxidation going to completion at low temperatures.

When the simulation results in Figure 5.4 are compared with the experimental results Figure 5.3, it is clear that an optimized value for the rate of this step will be closer to Figure 5.4D, based on the shapes of the curves. This could, however, depend on other factors that allow us to predict the promotion effect.

At $E_{a,H*+O*} = 65\ \mathrm{kJ\ mol^{-1}}$, H_2 is still preferentially oxidized, however, above $E_{a,H*+O*} = 70\ \mathrm{kJ\ mol^{-1}}$ the correct order of ignition is predicted. Völkening et al. [220] stated that above 300 K, the activation energy for hydrogen oxidation was higher, on the order

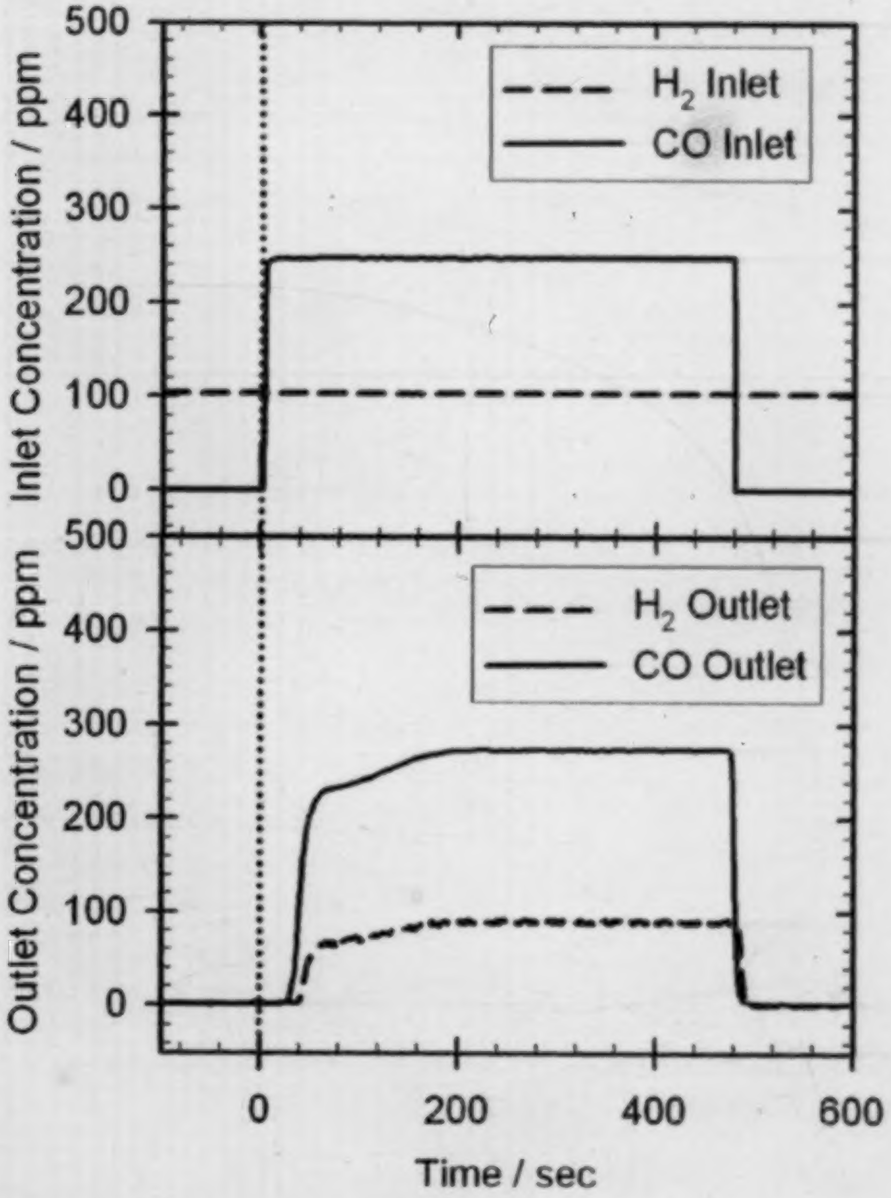

Figure 5.4: Step change in inlet concentration of 250 ppm CO in a stream of 100 ppm H_2. 6% O_2, remainder N_2. SV = 25000 hr^{-1}. Experiment performed at 35°C.

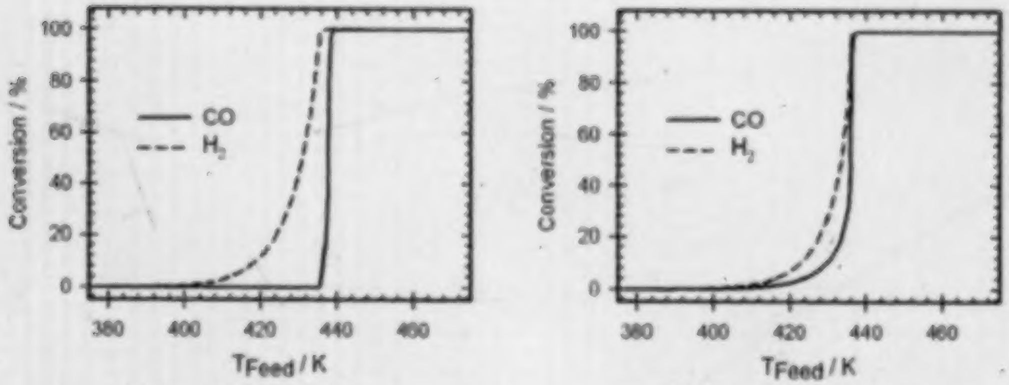

(a) Ea = 10.5 kJ· mol^{-1} (b) Ea = 65 kJ· mol^{-1}

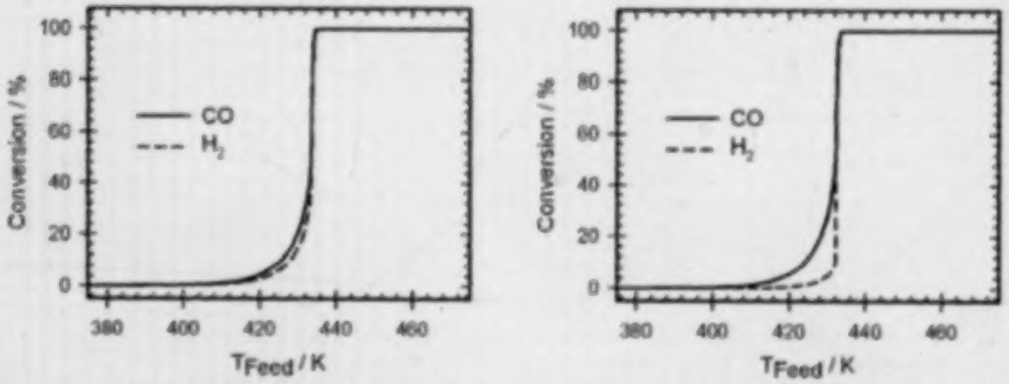

(c) Ea = 70 kJ· mol^{-1} (d) Ea = 75 kJ· mol^{-1}

Figure 5.4: Effect of the value of E_a for the first oxidation step of H ($H^* + O^* \rightarrow OH^* + {}^*$, Equation 3.13a) on selectivity and order of ignition. 1000 ppm CO and 500 ppm H_2.

of 0.52 to 0.69 eV (50 to 67 kJ·mol^{-1}) compared to a value of 0.13 eV (12.5 kJ·mol^{-1}) at temperatures below 170 K. Völkening et al. did not state which reaction step was limiting. Anton and Cadogan claimed that the adsorption steps (Equation 5.1a and Equation 5.1b) and the first oxidation step (Equation 5.1c) were very fast and the second oxidation step (Equation 5.1d) was rate-determining [206]. However, the experiments used to report this limitation were performed in the absence of CO and at low surface coverages, in a region where the rate parameters were assumed to be independent from surface coverage.

In the absence of other components on the platinum surface, the rate of surface diffusion (or surface mobility) of hydrogen is very high. It may be argued that, in the presence of other components, especially CO at high coverage, that the rate of surface diffusion is inhibited, and this inhibition is reflected in the increased value for activation energy.

Increasing the activation energy for the hydrogen addition reaction (Equation 5.1d) does not significantly alter the light-off temperatures or the order of ignition. Before ignition, oxygen is very scarce on the surface, whereas hydrogen is more abundant, and OH coverage, while small ($\sim 10^{-4}$), still appears to be sufficient.

When a simulation is performed with a modified activation energy for the second oxidation step (Equation 5.1d), no effect was observed for activation energy values up to $E_{A,H\bullet+OH\bullet} = 75$ kJ·mol^{-1}, as shown in Figure 5.5.

While $E_{A,O\bullet+H\bullet} = 70$ kJ·mol^{-1} is higher than then range stated by Völkening et al., this value is not unreasonable. As well, with a parameter solver, perhaps a better value can be found that also lies within the literature range and still predicts the correct selectivity.

When the selectivity of the catalyst is plotted directly, the influence of the activation energy value may be seen and compared with the experimental result. Figure 5.6 shows the selectivity for the experiment as well as for two simulations. One simulation was performed using the literature value (10.5 kJ·mol^{-1}) for the activation energy of the initial surface reaction (Equation 5.1c) and the other using a higher value (70 kJ·mol^{-1}). During the experiment, the catalyst was selective towards CO oxidation. A selectivity of 1 occurs when the CO is completely oxidized and no hydrogen is oxidized. Conversely a value of zero results from a system that selectively oxidizes all the hydrogen but no CO. Experimentally, CO oxidation was favoured. With the low activation energy, hydrogen oxidation was favoured until that oxidation was complete and CO light-off was achieved. With the higher activation energy value, the catalyst favoured CO oxidation.

Due to the stoichiometry and concentrations used, the selectivity (Equation 5.4) towards CO is 0.67 when both 1000 ppm CO and 500 ppm H_2 are completely oxidized. Noise in Figure 5.6 is a result of measurement and numerical error at very low conversions (less

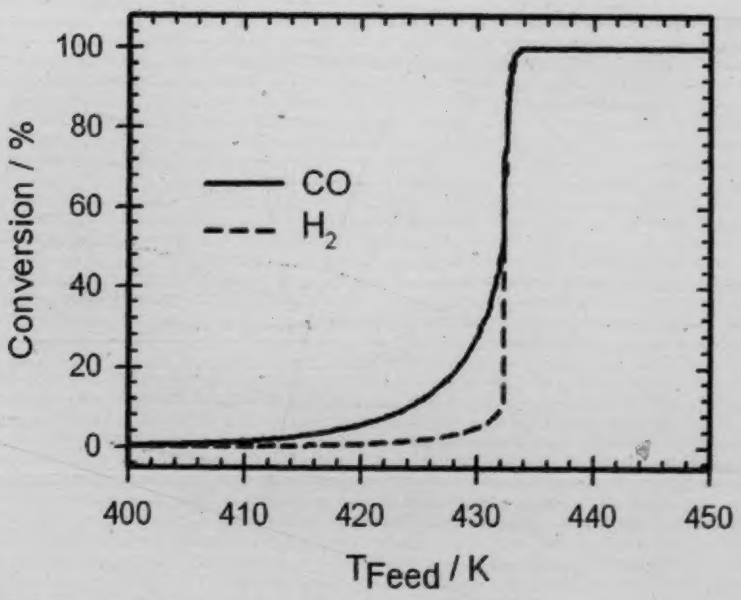

Figure 5.5: Simulation result for light-off curve with 1000 ppm CO 500 ppm H_2, 6 % O_2, rest N_2. SV = 25000 hr^{-1}. Activation energy for second hydrogen oxidation step is $E_{A,H*+OH*} = 75$ kJ·mol^{-1}.

Pre-exponential Factor (s^{-1})	β (unitless)	Activation Energy ($kJ \cdot mol^{-1}$)	Comments	Reference
1 $\times 10^{15}$ $Torr^{-1} \cdot s^{-1}$		10.5		[217]
		0.13 eV	$T < 175$ K	[220]
		12.5	$T < 175$ K	[220]
		0.52 - 0.69 eV	$T > 300$ K	[220]
		50 - 67	$T > 300$ K	[220]
		16 $kcal \cdot mol^{-1}$		[206]
		67.2 $kJ \cdot mol^{-1}$		[206]
2 $\times 10^{13}$ $mol \cdot K \cdot m^{-2} \cdot s^{-1}$		95		[248]
3.70×10^{21} $mol \cdot cm \cdot s$	0	11.5		[148, 249, 250, 66]
3.70×10^{21} $mol \cdot cm^3 \cdot s$	0	0.12 eV		[251]
5×10^{22} $mol \cdot cm \cdot s$	0	83.7	Rhodium	[252]
1.28×10^{21} $mol \cdot cm \cdot s$	0	11.2		Ch. 6 [252]
3.70×10^{21} $mol \cdot cm \cdot s$	0	11.5		Ch. 7 [252]
2.22×10^{10}	0	$34 - f(\theta)$		[253]
6.33×10^{12}	0.624	$37 - f(\theta_O, \theta_H, \theta_{H2O}, T)$		[229]
1.73×10^{10}	-0.710	$59 - f(\theta_O, \theta_H, \theta_{H2O}, \theta_{CO}, T)$		[230]
7.58×10^{10}	-0.710	$59 - f(\theta_O, \theta_H, \theta_{H2O}, \theta_{CO}, T)$		[230]
		Monte Carlo Simulation	no values stated	[140] [254]

Table 5.3: Literature Values for the Reaction "$O^* + H^* \rightarrow OH^* + {}^*$", Equation 5.1c

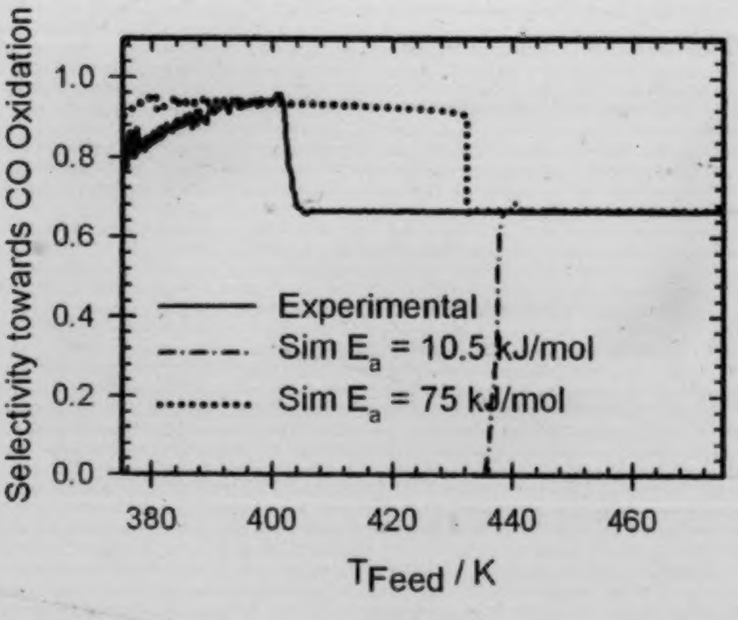

Figure 5.6: Selectivity towards CO oxidation for light-off with 1000 ppm CO with 500 ppm H_2. Shown are the experimental, simulation (literature activation energy) and simulation (modified $E_{A,O\bullet+H\bullet}$) values. Due to the stoichiometry and concentrations used, the selectivity towards CO is 0.67 when both CO and H_2 are completely oxidized.

than 1% conversion). The discrepancy between the points when complete conversion of all components occurs (a value of 0.67 here) is due to hydrogen promotion of CO oxidation, and will be discussed later.

The presence of hydrogen makes the numerical problem much stiffer, with the solver requiring up to an order of magnitude more time to be solved for the 2000 ppm H_2 case compared to the 0 ppm H_2 case. The stiffness of the problem may be seen in the numerical noise immediately following the ignition of the 2000 ppm H_2 case in Figure 5.8. Perhaps a lower error tolerance would rectify this noise.

For activation energies above 80 kJ·mol^{-1}, hydrogen ignition becomes very abrupt, igniting almost instantaneously when the critical temperature is reached. However, this sudden ignition causes very strong gradients, increasing the length of time required for the solver to converge to a solution. For example, solving the light-off curve at 80 kJ·mol^{-1} requires approximately 11 minutes computing time on a Pentium4 1.6GHz computer, compared to approximately 5 hours to solve at $\mathrm{E}_{a,O*+H*} = 85$ kJ·mol^{-1}.

The activation energy used in the simulation can be tuned to the best value when selectivity data is available, such as in Figure 5.6.

5.5 Conclusions on Catalyst Selectivity

The oxidation catalyst was experimentally observed to be selective towards CO oxidation. Although hydrogen could be oxidized in the absence of carbon monoxide and presence of oxygen at room temperature and pressure, in the presence of carbon monoxide the catalyst preferentially oxidized CO when oxygen could adsorb to the surface (i.e. when CO did no self-poison the surface).

The importance of knowing the correct selectivity when modelling the results was demonstrated. The value of activation energy for the surface reaction between adsorbed O and H (Equation 5.1c) was modified to a use a value of $E_{a,O*+H*}$=70 kJ·mol^{-1}. This value allowed for the correct prediction of the CO+H_2 light-off curve, including the light-off temperatures, order of ignition, curve shapes and catalyst selectivity. Without knowing the correct selectivity, errors could be made in determining the causes of other phenomena, such as the cause of hydrogen promotion of CO oxidation (which will be discussed in section 5.6).

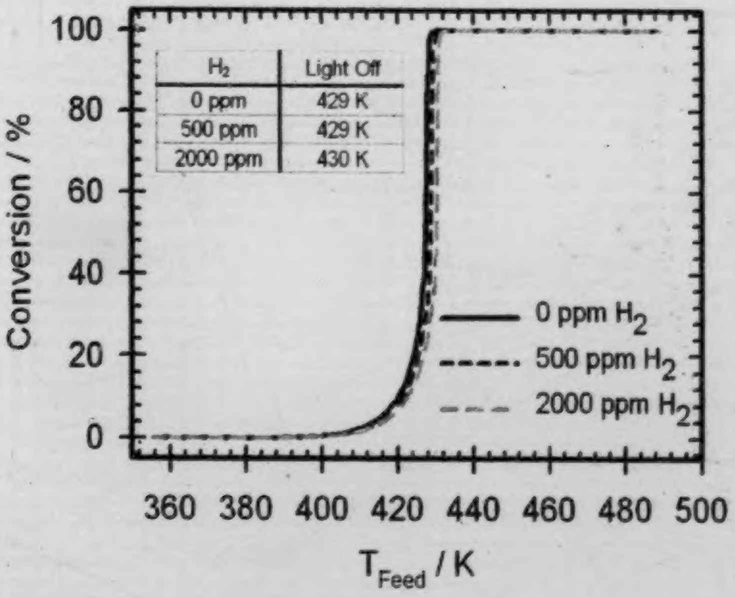

Figure 5.7: Conversion of 1000 ppm CO for simulated light-off with 0, 500 and 1000 ppm H_2. 6% O_2, remainder N_2. SV = 25000 hr^{-1}. Simulations with pre-exponential factor of 1.006×10^4 s^{-1} for the reaction of $O^* + H^* \rightarrow OH^* + *$.

5.6 Hydrogen Promotion of CO Oxidation[†]

Hydrogen has been reported in the literature to promote CO oxidation, however, the cause of this promotion effect is still under debate. To the knowledge of the author, the effect has not yet been modelled.

5.7 The Oxidation of Carbon Monoxide and Hydrogen

Given the recent interest in fuel cells and the need for a source of hydrogen with very low CO concentrations, the discussion in the literature of CO and H_2 oxidation over Pt catalysts has been dominated by the study of preferential oxidation of CO (PROX) [233, 142, 237, 232], where typical platinum catalysts have been shown to oxidize carbon monoxide selectively despite the high concentrations of hydrogen present. While many low-temperature, low-pressure [255], and single-crystal [256] studies have been performed closely studying the catalyst surface, less is known about the system at atmospheric pressure and low hydrogen

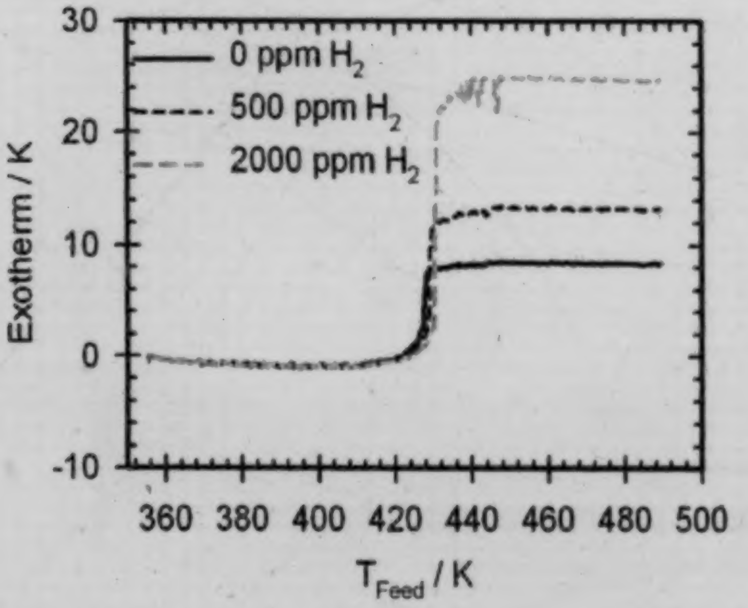

Figure 5.8: Exotherm predicted for simulations presented in Figure 5.7.

concentrations. It has been reported that CO inhibits the ignition of H_2, and H_2 promotes the ignition of CO [67, 257, 258]. The inhibition of hydrogen oxidation by CO has been attributed to competitive adsorption [41], while hydrogen promotion of CO oxidation has been attributed to various effects. Different proposals exist in the literature, and the debate remains open.

Sun et al. measured the temperature response of a monolith to CO and hydrogen concentration steps [67]. The monolith had a Pt/Al_2O_3 washcoat, and axial temperatures were measured along the centreline. Their experiments showed that, at a constant temperature, increasing the CO concentration would lead to self-inhibition and extinction of CO oxidation at a critical concentration. In the presence of hydrogen, the critical CO extinction concentration was shifted to a higher CO concentration, allowing higher concentrations of CO to ignite when they would otherwise (in the absence of hydrogen) not react. These observations were attributed to the exotherm from hydrogen combustion increasing the temperature at the catalyst, shifting the CO adsorption-desorption equilibrium. The concentrations of hydrogen used in their study ranged from 0-2.5%, and exotherms were reported to be on the order of 150°C, much higher than observed in this work.

Other groups [259, 260, 257, 233] have attributed this promotion effect to hydrogen in the gas influencing the desorption rate of CO. By increasing the rate of CO desorption, the turnover of surface sites increases, affording other components more opportunites to adsorb. However, the reactions are said to proceed via Langmuir-Hinshelwood type reactions instead of via an Eley-Rideal mechanism (between gas-phase and surface components) . To the knowledge of the present author, little experimental evidence of this influence on CO desorption has been reported in the literature. Kahlich et al. were also inconclusive as to whether the effect is due to hydrogen increasing the rate of CO desorption, and also suggested that there may be an interaction between CO on Pt and the hydroxylated alumina support [142].

Atalik and Uner [261] reported observing no hydrogen promotion effect on catalysts with 69 and 83% dispersions, however catalysts with higher dispersions exhibited lower light-off temperatures in the presence of hydrogen. This was attributed to the hydrogen oxidation reaction being enhanced on catalysts with more defect sites, but this could also be due to an increase in hydrogen promoted CO desorption at defect sites.

The discussion of surface reactions between adsorbed CO and hydrogen is relatively new, and holds more promise for a solution. Coupled reactions (on the surface) [229, 230] have been proposed, but as yet none have definitively shown the surface mechanism to be the cause of the hydrogen promotion effect. Heterogeneous and homogeneous oxidation pathways were said to be coupled above 500 K [258], however, as the interactions of interest to the present work typically occured between 373 K and 473 K, homogeneous pathways are not considered to be significant.

Dynamics in Oxidation of CO and H_2 Mixtures

Oh and Sinkevitch [233] stated that the presence of H_2 will cause an interaction between adsorbed CO, forming a H-CO complex. This complex is said to desorb more readily, increasing the turnover rate of free sites and allowing oxygen more opportunities to adsorb, enhancing the rate of CO oxidation [257].

Four simulations using the LH model were performed with 1000 ppm CO; with and without 500 ppm H_2, and with three different CO desorption pre-exponential factors. The results of these simulations is shown in Figure 5.9.

In Figure 5.9, the normal desorption rate pre-exponential factor for CO desorption is $A = 1 \times 10^{13}\ mol \cdot cm^{-1} \cdot s^{-1}$. The value used for fast desorption is 10 times larger than the normal value: $A = 1 \times 10^{14}\ mol \cdot cm^{-1} \cdot s^{-1}$, and the value used for slow desorption is 10 times smaller: $A = 1 \times 10^{12}\ mol \cdot cm^{-1} \cdot s^{-1}$. The faster CO desorption rate shifts the

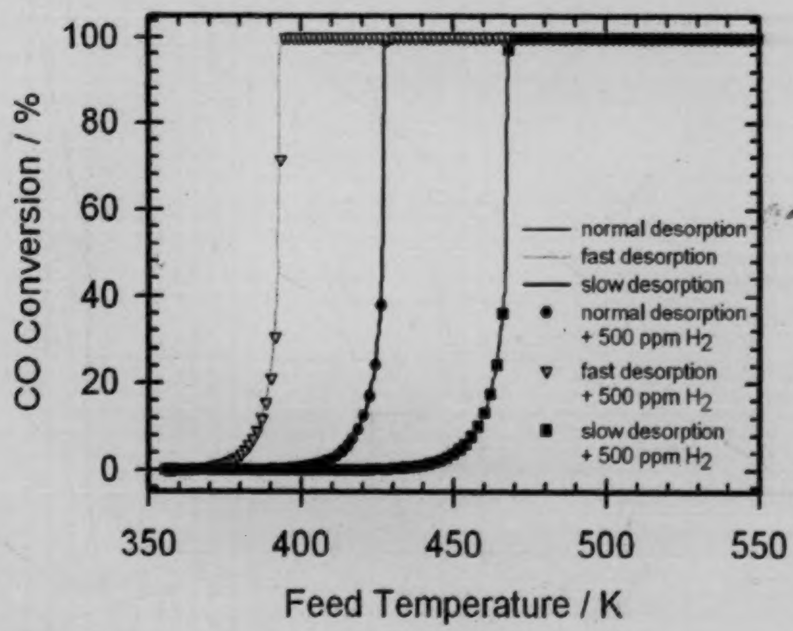

Figure 5.9: Effect of rate of CO desorption and H_2 in gas on CO ignition. The LH model was applied to the simulations.

entire light-off curve towards lower temperatures. Decreasing the desorption rate has the opposite effect within this range. This may be due to the increased turnover of sites and the increased availability of free sites to which oxygen may adsorb.

The addition of hydrogen directly has no influence in this model. This may be due to the CO-hydrogen interaction not being considered in the current model. If hydrogen promotion of CO oxidation were to be caused by a bond between gaseous hydrogen and adsorbed CO, then a non-linear relationship would need to be defined. However, this route does appear to be the dominant route through which the promotion effect is realized.

5.8 CO + H_2 Experimental Light-Off Curves

Light-off experiments have been performed over several different inlet CO and hydrogen concentrations to explore any possible relationship between hydrogen and the light-off temperature of CO and to describe the observed promotion effect. These light-off experiments were originally presented and analyzed in previous publications [207, 108], where it was found that CO achieves light-off before H_2.

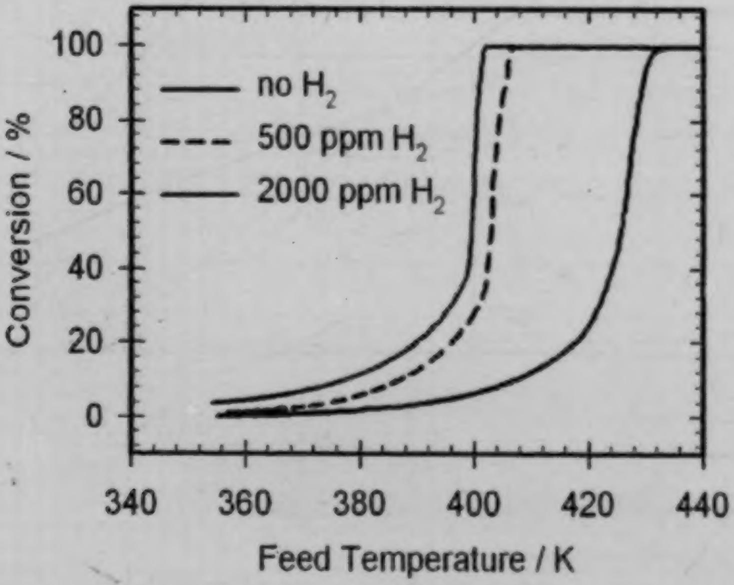

Figure 5.10: Experimental CO light-off curves for 1000 ppm CO and 0, 500 and 2000 ppm H_2. All mixtures include 6% O_2 and the remainder as N_2.

The light-off curves for 1000 ppm CO and 2000 ppm CO with various concentrations of H_2 are shown in Figure 5.10 and Figure 5.11, respectively. These experimental CO light-off temperatures are summarized in Figure 5.12 and the data shown in Table 5.7 and Table 5.8. Both experimental datasets show a promotion effect, whereby CO lights-off at a lower temperature in the presence of hydrogen. This effect appears to have diminishing marginal returns, whereby the influence of additional H_2 does not have a correspondingly large effect as the initial hydrogen. The first 1000 ppm H_2 has a greater marginal impact than an additional 1000 ppm H_2.

5.8.1 CO + H_2 Steps

As stated earlier, CO inhibits the ignition of H_2, and H_2 promotes the ignition of CO [67], however the interactions between kinetics, mass and energy transfer in a monolith are not well understood, especially under transient conditions. No models in the literature have

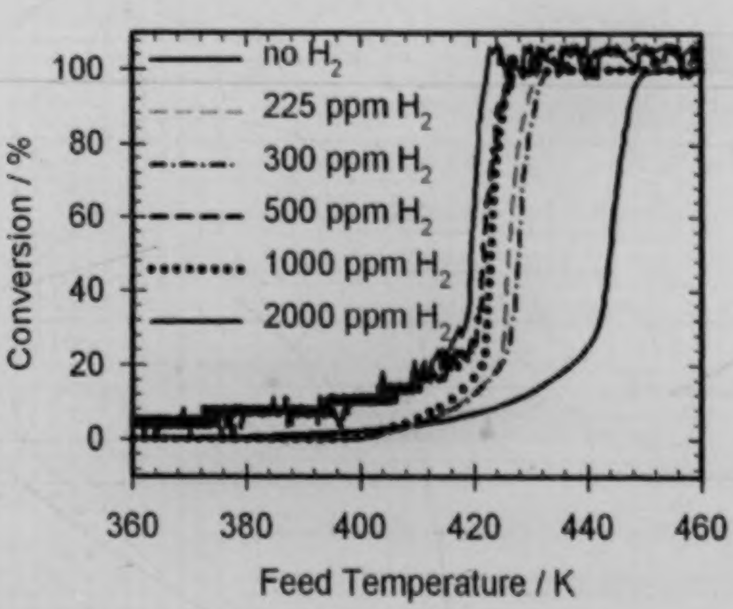

Figure 5.11: Experimental CO light-off curves for 2000 ppm CO and 0, 500 and 2000 ppm H_2. All mixtures include 6% O_2 and the remainder as N_2.

been presented as yet that predict the behaviour of a concentration step with both CO and hydrogen in the feed gas.

Step changes in hydrogen inlet concentration at constant CO and O_2 flowrates confirm the influence of hydrogen on the rate of CO oxidation, as shown in Figure 5.13. Under the experimental conditions and in the absence of hydrogen, CO conversion is roughly 14 %. In the presence of 500 ppm H_2, CO conversion rises to approximately 18 %. With 2000 ppm H_2 in the inlet feed, CO conversion is 25 %. Hydrogen in the feed is increasing the rate of CO oxidation and the overall rate of CO conversion. Due to a lack of availability of the required mass spectrometer, H_2 outlet concentrations are not available for all experiments.

In a series of step experiments at relatively moderate temperatures (~ 100-130°C), in the presence of O_2 and absence of CO, H_2 conversion was essentially 100%. Despite measuring an inlet flow of H_2, no exit H_2 was measured. As the thermocouples within the monolith recorded temperature increases during step increases in H_2, and the recorded temperatures dropped immediately following a step down to zero inlet H_2, a valid conclusion is that these temperature increases are due to the H_2 exotherm. This is evidence of 100 % conversion of H_2 occuring at these temperatures under flow conditions of a space velocity of 25000 hr^{-1}.

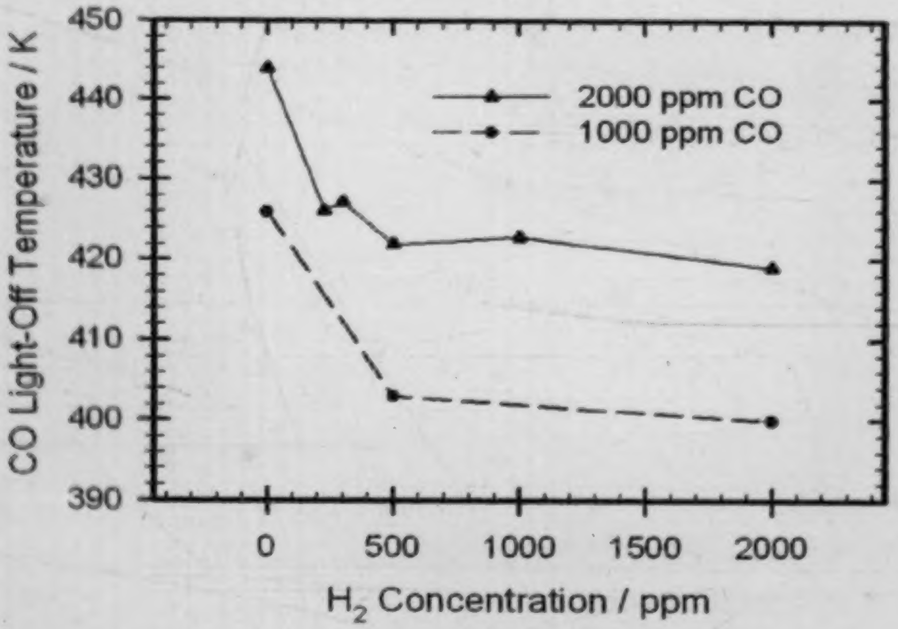

Figure 5.12: Effect of H_2 on CO Light-Off for 1000 and 2000 ppm CO. All mixtures include 6% O_2 and the remainder as N_2. Experimental results.

This is consistent with other studies of a H_2-O_2 system on platinum.

Figure 5.14 shows several phases during a step up in CO concentration in a constant hydrogen atmosphere. Initially (A), no CO is present, the surface is dominated by oxygen, and hydrogen conversion is complete. Upon introduction of CO to the system (B), CO_2 production increases strongly as the availability of adsorbed oxygen with which to react is quite high. During this phase, hydrogen conversion is unaffected as oxygen on the surface is plentiful. However, adsorbed oxygen is not refreshed at the same rate that it reacts, and the surface becomes CO dominated. In (C), the dominant surface species is CO, but others are still significant. The catalyst is selective towards CO oxidation at this time. With time, CO displaces all other species on the surface (D), poisoning the surface and preventing oxidation of all species. At higher temperatures or lower CO concentrations, the rate of CO desorption may be large enough that CO does not completely poison all oxidation reactions. Figure 5.16 shows CO concentration steps of varying magnitude but at the same inlet tempeerature. From Figure 5.16, we can see that increasing the amount of CO added to the system will increase the degree of poisoning that occurs. Steady-state hydrogen conversion only occurs at lower CO concentrations.

Similarily, during a step down in CO concentration, the surface also changes dramatically. The system begins in Figure 5.15 in state A (the same state as D in Figure 5.14), where the surface is dominated by CO and CO oxidation is limited by the rate of oxygen adsorption. Hydrogen oxidation is blocked. Upon removal of CO from the system (B), no new CO will adsorb to the surface, the CO will either desorb or react, leaving free sites for oxygen and hydrogen to bind to. During this phase, the oxygen coverage on the surface increases, such that the rate of CO oxidation also increases. Most of the CO conversion observed here is the consumption of surface adsorbed CO. However, once the supply of CO on the surface becomes exhausted (C), the CO oxidation rate also decreases. Due to the selectivity of the catalyst, hydrogen oxidation begins. Once all CO has been purged from the system and the surface becomes once again oxygen dominated, hydrogen oxidation proceeds to completion, being only limited by the rate of hydrogen flowing into the system.

Figure 5.16 shows the influence of increasing CO concentrations on the CO and H_2 conversions during a step increase in CO. At 250 ppm CO (Figure 5.16A), CO does not completely poison the surface, as the steady-state conversions of both CO and H_2 are still significant. With 500 ppm CO (Figure 5.16B), CO poisons the surface, bringing the steady-state conversions to 0 %. At higher CO concentrations, such as 1000 ppm (Figure 5.16C) and 2000 ppm (Figure 5.16D), the poisoning effect is also complete and accelerated by higher CO concentrations.

For a step up and down of 1000 ppm CO in 100 ppm H_2 (Figure 5.16C) the curves may be integrated to determine the total amount of CO_2 produced during the transition. 0.00024 mol CO_2 was produced during the step up and 0.00004 mol CO_2 was produced during the step down (see Table 5.4). During the step up, there is the initial peak of CO_2 formation, and this peak extinguishes, but not as fast as it ignited. The reaction fades out as oxygen and hydrogen are present on the surface and attempt to maintain a steady state reaction. However, CO manages to slowly dominate all the surface sites. The transition to a CO dominated surface (extinction) is slower than the transition to a oxygen dominated surface (ignition), and therefore the integral under the step up curve is larger than the integral under the step down. The difference is the residual CO_2 produced during the slow extinction.

For a step up and down of 500 ppm CO in 100 ppm H_2 (Figure 5.16B), the integrated area of the step up shows 0.00027 mol CO_2 and the step down 0.00004 mol CO_2. As the slow decay will be dependent upon the inlet CO concentration (with higher CO concentrations extinguishing faster, and therefore having less overall CO_2 produced during the step up).

CO Concentration (ppm)	H_2 Concentration (ppm)	CO_2 Production step-up (mol)	CO_2 Production step-down (mol)
500	100	0.00027	0.00004
1000	100	0.00024	0.00004
2000	100	0.00013	0.00004
2000	100	0.00013	0.00004

Table 5.4: Integrated CO_2 production over a step-up or step-down in CO concentration at 347K.

With a step down in concentration, the amount of CO_2 measured in the integral should be equivalent to the amount of CO adsorbed to the surface at the moment the CO_2 inlet gas was removed form the feed stream. As the reaction was extinguished due to CO occupying all the available free sites, this is a simple measure of the capacity of the catalyst surface, or the total number of available free sites. The integrated peaks for both 500 and 1000 ppm were quite similar, as the steady-state reaction and extinction was eliminated and only the adsorbed CO was available for reaction.

5.8.2 Mechanism

The details for the oxidation of CO were given in chapter 4, and are repeated here for completeness.

$$O_2 + 2^* \rightarrow 2O^* \tag{5.6}$$

Oxygen adsorption considered to be dissociative above 300 K [89, 130], while desorption is associative above approximately 800 K [89, 90]. In the range of interest for automotive catalysis, oxygen adsorption is generally considered to be irreversible.

$$CO_2 + ^* \rightleftharpoons CO_2^* \tag{5.7}$$

The general consensus in the literature is that CO_2 desorption is practically instantaneous after the surface reaction at temperatures above 300K.

$$CO + ^* \rightleftharpoons CO^* \tag{5.8}$$

$$CO^* + O^* \rightleftharpoons CO_2^* + ^* \tag{5.9}$$

$$C^* + O^* \rightleftharpoons CO^* + ^* \tag{5.10}$$

A compressed oxygen step was added [108] to correct a shortcoming of the standard Langmuir-Hinshelwood mechanism: namely the inability of the LH mechanism to model reactions on an oxygen covered surface. This compressed oxygen mechanism does not significantly influence the specific simulations presented in the present work, but is presented here for completion.

$$CO + 2O^* \rightarrow CO^* + OO^* \tag{5.11}$$

$$CO^* + O^* \rightarrow CO_2^* + 2^* \tag{5.12}$$

$$CO^* + OO^* \rightarrow CO_2 + O^* + ^* \tag{5.13}$$

$$OO^* + ^* \rightarrow 2O^* \tag{5.14}$$

Hydrogen also adsorbs onto the catalyst surface, competing with CO and oxygen for surface sites.

$$H_2 + ^* + ^* \rightleftharpoons H^* + H^* \tag{5.15}$$

$$H^* + O^* \rightleftharpoons OH^* + ^* \tag{5.16}$$

$$H^* + OH^* \rightleftharpoons H_2O^* + ^* \tag{5.17}$$

$$H_2O^* \rightleftharpoons H_2O + ^* \tag{5.18}$$

Although these equations are shown as fully reversible, the surface equations (Equation 5.16, Equation 5.17 and Equation 5.18) are essentially irreversible under the conditions studied. Hydrogen desorption is significant, but all other equilibrium with surface hydrogen are essentially irreversible.

5.8.3 Modelling CO+H_2 Light-Off

We know from the literature that platinum catalysts are selective towards CO oxidation [233, 142, 139, 234, 235, 236, 237, 238, 140, 232, 239, 240, 241, 244, 243] and experimentally, we have seen that CO ignites before H_2 [208, 207]). The experimental observation of order of ignition has been successfully modelled with a modification of the activation energy for the surface oxidation of adsorbed hydrogen species [207]. However, this modification alone does not predict the promotion of CO oxidation by the presence of H_2 that has been experimentally observed, as shown by the results for $\frac{dEa_{CO-H}}{dPt_B} = 0$ in Figure 5.12, Table 5.7 and Table 5.8). Another step in the mechanism is not yet modelled, and the current work will attempt to describe that step and model the effect.

5.9 Hydrogen Promotion Of CO Oxidation

There are other possible explanations for the promotion effect that hydrogen has on CO oxidation. Sun et al. [67] have performed studies of CO and H_2 oxidation on a monolith, whereby they studied the temperature response of the reactor to stepwise changes in the inlet concentration. It has been reported that CO inhibits the ignition of H_2, and H_2 promotes the ignition of CO [67, 257, 258]. The inhibition of hydrogen oxidation by CO has been attributed to competitive adsorption [41], while hydrogen promotion of CO oxidation has been attributed to various effects. Sun et al. [67] ascribed the promotion effect to thermal effects, with the heat of reaction from hydrogen oxidation shifting the adsorption-desorption equilibrium of CO towards desorption. Oh and Cavendish [41] attributed the hydrogen-promotion of CO to hydrogen influencing the desorption rate of CO. Kahlich et al. attributed this effect to be due to either hydrogen-induced CO desorption or an interaction between CO on Pt and the hydroxylated alumina support [142].

Others [229, 230] have proposed a mechanism that utilizes a parallel path for CO oxidation with a hydroxyl (OH*) species. Our simulations involving parallel reactions via the OH* species showed that there was insufficient H and O adsorbed on the surface pre-light-off to allow this step to be significant under the conditions studied, which were much lower concentration that the referenced paper.

5.9.1 Role of Adiabatic Temperature Rise

Several literature sources have attributed the promotion of CO oxidation to the exotherm produced by H_2 oxidation [67]. However, as we know the order of ignition [207] during light-off experiments, this cannot be the predominant factor in promoting CO oxidation. In addition, additional increases in hydrogen inlet concentration did not show a corresponding decrease in CO light-off temperature.

Sun et al. [67] claim that H_2 assists the ignition of CO. In the experiments performed by Sun et al., the inlet H_2 concentration is on the order of 1%, and inlet CO is on the order of 0.7%. The adiabatic temperature rise is approximately $\sim$ 75 K for 1% H_2 and 100 K for 1% CO. Thus, the adiabatic temperature rise is the Sun et al. systems is on the order of up to 175 K. In comparison, the systems studied in this work involve much lower concentrations. The range of H_2 used in the system is 0-2000 ppm ($\Delta T_{abiabatic} = 0\text{-}16$ K), and 0-2000 ppm CO ($\Delta T_{abiabatic} = 0\text{-}19$ K). Thus, the adiabatic temperature rise associated with the experiments here is on the order of 5-35 K, much lower than the Sun et al. systems, and much less likely to influence the light-off.

At higher concentrations of hydrogen, the adiabatic temperature rise also appears to influence the simulated ignition, but in a lesser role. When a simulation with hydrogen is run in a "nonexothermic" mode, where the heat of reaction is set to zero, then the effect is relatively small for 5000 ppm H_2, but has a significant influence on CO.

Hydrogen begins to react at a similar temperature in both the exothermic and non-exothermic cases, but at approximately 15% the curves diverge, with the exothermic case increasing more sharply. When the exotherm is present (non-zero), the simulation with 5000 ppm H_2 including the exotherm reaches hydrogen light-off ($\geq$ 50% conversion) at 447 K, compared to 454 K when the exotherm is not present. However, in the exothermic case, the CO light-off point is 449 K, compared to 460 K for the non-exothermic case.

The current model is predicting a shift to higher light-off temperatures due to the presence of hydrogen in the system, which is consuming adsorbed oxygen before CO reacts, as well as a lesser shift to lower light-off temperatures due to the adiabatic temperature rise from the reacted hydrogen. The shift to higher light-off temperatures does not follow the experimental results.

In addition to the exothermicity of reaction not being sufficient to describe the promotion effect, we know from previous publications that the catalyst is selective towards CO, and that, at the relatively low concentrations studied here, hydrogen oxidation occurs after CO oxidation [207]. The fractional conversion of hydrogen trails that of CO, and thus the heat of reaction from hydrogen combustion cannot be significantly promoting CO oxidation.

CO Conc. (ppm)	H_2 Conc. (ppm)	exothermic	Ea_{H+OH} ($kJ \cdot mol^{-1}$)	CO Light-Off (K)	H_2 Light-Off (K)	Δ for CO (K)
1000	0	exothermic	-	429.8	-	1.5
1000	0	nonexothermic	-	431.3	-	
1000	500	exothermic	11.5	444.1	437.4	0.4
1000	500	nonexothermic	11.5	444.5	437.5	
1000	500	exothermic	70	434.0	434.3	1.6
1000	500	nonexothermic	70	435.6	436.2	
1000	5000	exothermic	11.5	466.4	460.7	0.8
1000	5000	nonexothermic	11.5	467.2	461.1	
1000	5000	exothermic	70	442.0	442.7	1.7
1000	5000	nonexothermic	70	443.7	444.8	

Table 5.5: Effect of H_2 concentration and exothermicity on light-off temperature. $\Delta T_{adiabatic} = 4.04$ K for 500 ppm H_2 and 40.4 K for 5000 ppm H_2.

5.9.2 CO Desorption Dependence on Gas-Phase Hydrogen

Stetter and Blurton [257] and Oh and Sinkevitch [233] postulated that the rate of CO desorption depends on the presence of hydrogen in the system [260, 259]. A complex was said to form between adsorbed CO and hydrogen in the gas phase, and this H-CO complex would more easily desorb, removing CO from the surface. When the rate of CO desorption increases, then the turnover of free sites also increases, and the opportunity for oxygen to adsorb also increases. Thus, the surface coverage of oxygen increases and so also the surface reaction rate for CO oxidation.

Preliminary simulations were performed, adapting this principle by adding a dependency on the hydrogen coverage to the activation energy for CO desorption (the reverse reaction in Equation 3.8a). When this activation energy was varied, the light-off temperature was affected, as seen in Figure 5.9.

The literature is not clear on whether this effect originates from hydrogen in the gas phase or hydrogen adsorbed onto some surface.

As we know from previous studies [108], the Eley-Rideal model is generally considered to not be significant for CO-O_2 reactions, perhaps the same may be assumed to be true for systems that also include hydrogen. In this case, it would be surface hydrogen that would be postulated to be promoting the desorption of CO. To properly test this potential route, a model must be proposed and simulated. The crux of this sub-model involves the adsorption of hydrogen to a pseudo-surface, and the subsequent influence of the surface

E_a (kJ·mol^{-1})	$\frac{dE_a}{d\theta_H}$ (kJ·mol^{-1})	$\frac{dE_a}{d\theta_{CO}}$ (kJ·mol^{-1})	CO Light-Off (K)	H_2 Light-Off (K)
126.4	-40	33	431.3	431.6
126.4	0	33	430.0	430.1
126.4	40	33	428.4	428.8
126.4	80	33	426.9	427.2
126.4	120	33	425.4	425.4
126.4	200	33	421.6	421.6

Table 5.6: The effect of $\frac{dE_a}{d\theta_{H_{(g)}}}$ for CO desorption on CO and H_2 Light-Off. The traditional value of $\frac{dE_a}{d\theta_H}$ is 0.

coverage of this hydrogen on the CO desorption rate via a $\frac{dEa_{CO-H}}{d\theta_{H\_PtB}}$ term. As hydrogen has few sterric hindrances, it is possible that some surface sites are accessible to hydrogen and no other species. This surface could be part of either the platinum surface, or the alumina surface [142]. If the alumina support is the location of the adsorption, then a study of the influence of the support material on the hydrogen promotion effect would shed light on this topic. In the current study, we will refer to this surface type as PtB.

As we know from previous studies [207] that in the presence of CO the quantity of hydrogen adsorbed on the platinum surface below the light-off temperature is quite small, we will ignore for the present the influence of hydrogen adsorbed onto the typical platinum surface sites.

If there is no hydrogen in the system, then this sub-mechanism has no effect, true to all results previously published using this model.

The additional submechanism includes the following steps:

$$H_{2(g)} + 2\bullet \rightarrow 2H\bullet \tag{5.19}$$

Hydrogen adsorbs to a pseudo-site, PtB, represented by •. This surface may also be thought of as the CO to which hydrogen has been stated to bind to [259, 260, 257, 233, 142]. Hydrogen has a very high mobility, and is the least sterrically hindered species under consideration.

$$2H\bullet \rightarrow H_{2(g)} + 2\bullet \tag{5.20}$$

Hydrogen that adsorbs to a surface may also desorb. The parameters used for Equation 5.19 and Equation 5.20 are taken from those used in Equation 3.11a. The critical addition that this mechanism makes is the addition of a dependency term, $\frac{dE_A}{d\gamma_{PtB-H}}$, to the

H_2 Conc. (ppm)	$\frac{dEa_{CO-H}}{d\theta_{PtB-H}}$	Ea_{O+H} (kJ·mol^{-1})	Ea_{H+OH}	CO Light-Off (K)	CO Light-Out (K)	H_2 Light-Off (K)	H_2 Light-Out (K)
0	experimental			426	388	—	—
500	experimental			403	365	403	365
2000	experimental			400	352	400	352
0	0	70	17.4	427.8	388.3	—	—
500	0	70	17.4	432.0	389.7	432.3	389.7
2000	0	70	17.4	435.7	471.5	436.4	351.9
0	14	70	17.4	427.8	388.2	–	—
500	14	70	17.4	402.0	388.4	402.8	388.4
2000	14	70	17.4	397.7	384.0	398.2	351.9

Table 5.7: Influence of $\frac{dEa_{CO-H}}{dPt_B}$ on CO promotion during light-off. A value of Ea_{H+OH} = 70 kJ·mol^{-1} was used to model the correct CO-H_2 selectivity. All results shown in this table are for 1000 ppm CO.

activation energy for CO desorption (Equation 5.8). The activation energy of CO desorption is now calculated as in Equation 5.21.

$$E_{A,COdes} = E_A - \frac{dE_A}{d\theta_{CO}} \times \theta_{CO} - \frac{dE_A}{d\gamma_{PtB-H}} \times \gamma_{PtB-H} \tag{5.21}$$

Simulations have been performed using this sub-mechanism. Various values of $\frac{dEa_{CO-H}}{d\theta_{H\_PtB}}$ were tested, but it was found that a value of 14 kJ·mol^{-1} produced the best agreement with experimental light-off temperatures. Simulations using 1000 ppm CO with 500 and 2000 ppm H_2 are shown in Figure 5.17 and Figure 5.18, respectively. The light-off curve (ignition curve) for simulations of 1000 ppm CO and various hydrogen concentrations is shown in Figure 5.19. The light-off and light-out temperatures are summarized in Table 5.7 and Table 5.8. Simulations of light-out curves (extinction) are not yet studied in detail or optimized.

Figure 5.17 and Figure 5.18 show much better agreement with the experimental light-off (ignition) curve than previous simulations ($\frac{dEa_{CO-H}}{dPt_B} = 0$ in Figure 5.20) that did not use the CO-H mechanism.

Figure 5.20 shows the CO light-off temperatures in the presence of hydrogen. This graph compares to the earlier version in [207]. When the value of $\frac{dEa_{CO-H}}{d\theta_{PtB-H}}$ is set to zero, the sub-mechanism has no significant influence on the model predictions, and predicts the same competitive inhibition as when the mechanism is not included. Previous attempts to model the promotion effect were unsuccessful, and only showed the competitive inhibition

H_2 Conc. (ppm)	$\frac{dEa_{CO-H}}{d\theta_{PtB-H}}$ (kJ·mol^{-1})	Ea_{H+O}	Ea_{H+OH}	CO Light-Off (K)	CO Light-Out (K)	H_2 Light-Off (K)	H_2 Light-Out (K)
0	experimental			443.8	403.5	—	—
225	experimental			426.1	387.7	426.1	385.6
300	experimental			427.2	386.2	427.2	384.3
500	experimental			421.6	381.2	421.9	380.6
1000	experimental			422.9	376.6	422.9	375.1
2000	experimental			419.3	367.1	420.0	367.0
0	0	70	17.4	444.1	389.9	–	—
225	0	70	17.4	446.2	386.0	446.7	386.0
300	0	70	17.4	446.7	382.0	447.0	381.8
500	0	70	17.4	447.4	389.4	447.8	389.4
1000	0	70	17.4	448.8	354.5	449.1	354.9
2000	0	70	17.4	435.8	393.3	436.4	393.2
0	14	70	17.4	444.1	389.9	–	—
225	14	70	17.4	432.3	388.5	432.0	354.8
300	14	70	17.4	430.5	387.9	430.4	355.0
500	14	70	17.4	426.3	386.0	447.8	389.4
1000	14	70	17.4	420.1	387.0	420.7	354.9
2000	14	70	17.4	419.3	367.1	419.9	367.0

Table 5.8: Influence of $\frac{dEa_{CO-H}}{d\theta_{PtB-H}}$ on CO promotion during light-off. All results shown in this table are for 2000 ppm CO and use a value of Ea_{H+OH} = 70 kJ·mol^{-1}.

effect, however, the present work shows that the addition of H-promoted CO desorption can predict the promotion effect.

Figure 5.21 shows the CO light-off temperatures for 2000 ppm CO at various H_2 concentrations. Here, we can clearly see the competitive adsorption between CO and H_2 for values of $\frac{dEa_{COdes}}{\theta_{Pt-B}} = 0$. As hydrogen concentration increases, the competition for free sites increases and CO oxidation is inhibited. When we include the CO-H submechanism, the model predicts the correct promotion effect, whereby the presence of hydrogen decreases the CO light-off temperature, but with diminishing marginal returns. A value of $\frac{dEa_{COdes}}{\theta_{PtB-H}} = 10$ kJ· mol^{-1} does not show enough of the promotion effect, whereas a value of $\frac{dEa_{COdes}}{\theta_{PtB-H}} = 20$ kJ· mol^{-1} shows too strong of an effect. A value of $\frac{dEa_{COdes}}{\theta_{PtB-H}} = 14$ kJ·mol^{-1} was determined to have the best balance for all light-off curves for both 1000 and 2000 ppm CO. The method of least squares was used to determine the degree of fitness of the model predictions over the range of $\frac{dEa_{COdes}}{\theta_{PtB-H}} = 0$ to 20 kJ · mol^{-1}.

5.9.3 The Limit of Hydrogen Promotion

As competitive adsorption between CO and H_2 still exists (but does not influence light-off as much as the promotion effect),

7

Plots for $\frac{dEa_{CO-H}}{dPt_B} = 14$ kJ·mol^{-1} at $E_{A,CO\ desorption} = 126.4$ kJ·mol^{-1} and $\frac{dEa_{CO-H}}{dPt_B} = 0$ kJ·mol^{-1} at $E_{A,CO\ desorption} = 112.4$ kJ·mol^{-1} are shown in Figure 5.22. The curve of $\frac{dEa_{CO-H}}{dPt_B} = 0$ kJ·mol^{-1} at $E_{A,CO\ desorption} = 112.4$ kJ·mol^{-1} represents what the CO light-off temperatures would be if the full impact of the hydrogen promotion was realised (126.4 - 14 = 112.4 kJ·mol^{-1}), but the competitive adsorption was still a factor.

If these curves are extrapolated to find their intersection, then the theoretical limit to which hydrogen can promote CO oxidation and the required hydrogen concentration can be estimated. Using this method, at approximately 3200-3300 ppm H_2 the promotion effect is expected to be limited by competitive adsorption, allowing a minimum CO light off temperature of ~404K, 40K below the light-off temperature in the absence of hydrogen. Above this hydrogen concentration, it is not clear which effect is the light-off determining effect, however, the hydrogen promotion effect has been observed at much higher concentrations (~75% H_2 as reported by Sun et al. [67] and others in the preferential oxidation literature).

5.9.4 Hydrogen Promotion and Selectivity

The addition of the hydrogen promotion term ($\frac{dEa_{CO-H}}{d\theta_{H\_PtB}}$) also influences the catalyst selectivity. By increasing the hydrogen promotion term, the rate of CO desorption increases (when at a constant hydrogen concentration in the gas). When the rate of CO desorption

$\frac{dEa_{CO-H}}{d\theta_{PtB-H}}$ (kJ·mol^{-1})	Ea_{H*+O*}	CO Light-Off (K)	CO Light-Out (K)	H_2 Light-Off (K)	H_2 Light-Out (K)
14	70	419.3	367.1	419.9	367.0
14	72.5	409.5	386.5	410.4	363.2
14	75	404.6	386.1	405.6	373.4
14	77.5	401.6	387.3	402.8	387.3
14	80	399.7	390.6	401.3	391.1
10	77.5	418.8	387.5	419.4	387.5

Table 5.9: Influence of Ea_{H+OH} on CO promotion and selectivity during light-off. All results shown in this table are for a mixture of 2000 ppm CO and 2000 ppm H_2.

increases, the availability of free sites for hydrogen to oxidize also increases, making hydrogen more competitive at adsorption. If the promotion of CO desorption is increased, then the rate of hydrogen oxidation may need to be decreased to retain the correct catalyst selectivity. This is done through further tuning of the value of Ea_{H*+O*}. By increasing the value for the first hydrogen oxidation step slightly, the catalyst selectivity may again be correctly modelled. Tuning of this value also influences the CO light-off temperature, as can be seen in Table 5.9 and Figure 5.24. The experimental CO and H_2 light-off curve may be seen in Figure 5.23.

While the light-off curve in Figure 5.24a has the correct light-off curve, the selectivity does not match the experimental selectivity (shown in Figure 5.23). The simulated catalyst is not selective towards CO, and the value of $E_{a,O*+H*}$ is increased.

In addition, the light-out behaviour at values of $E_{a,O*+H*} \leq 75$ kJ·mol^{-1} does not represent that seen experimentally. At higher values, such as that shown in Figure 5.24c, the hydrogen light-out behaviour is closer to the expected result. In this case, the catalyst appears to be slightly selective towards H_2 oxidation during light-out. This may be an artifact of diffusion in the washcoat under conditions of relatively higher oxygen coverage of the surface, or a result of a slowly propagating extinction wave in the catalyst. However, the result shown in Figure 5.24c more closely models this observation, with the higher value of Ea_{O*+H*} appearing to be too selective towards CO during the extinction phase.

To arrive at the optimal set of values for $\frac{dEa_{CO-H}}{d\theta_{PtB-H}}$ and Ea_{O*+H*}, an iterative process would be required. The present value of $\frac{dEa_{CO-H}}{d\theta_{PtB-H}} = 14$ kJ· mol^{-1} is too large, as light-off is occuring too soon, and the value of $Ea_{O*+H*} = 70$ kJ· mol^{-1} is too small, as the catalyst is not selective enough towards CO. These two values would need to be iteratively modified until the best agreement is reached.

Figure 5.25 shows a simulation that models both the promotion effect and the catalyst selectivity under the conditions of 2000 ppm CO and 2000 ppm H_2. Values of $\frac{dEa_{CO-H}}{dPt_B} = 10\ \mathrm{kJ{\cdot}mol^{-1}}$ and $E_{A,O\bullet+H\bullet} = 77.5\ \mathrm{kJ{\cdot}mol^{-1}}$ were used. The light-off temperature of CO under this set of parameters is 418.8 K (see Table 5.9), a match with the measured value of 419 K (see Table 5.2). The light-off temperature of H_2 was found to be 419.4 K in the simulation and experimentally to be 420 K. The selectivity matches well with the experimental values. The shape of the curve more closely matches Figure 5.24c, whereas a larger value of $E_{A,O\bullet+H\bullet}$ would have shift the shape of the curve to be closer to that of Figure 5.24d. While the shape of the curves appears to agree well with experimental data, the light-out temperatures predicted by the simulation are approximately 30 K higher than those determined experimentally. The full optimization of these parameters over the full experimental dataset is beyond the scope of the present work.

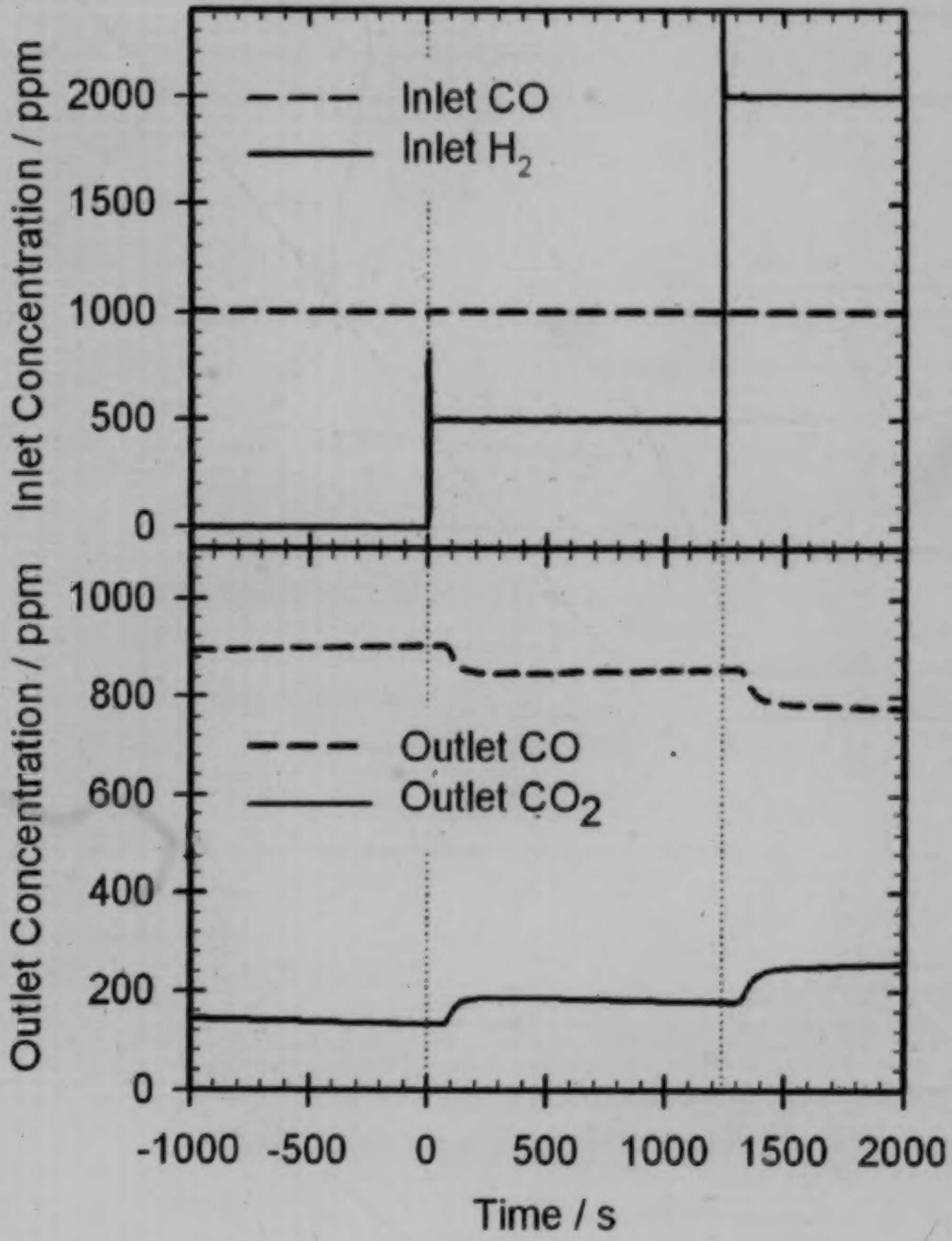

Figure 5.13: Experimental step changes in H_2 concentration, from 0-500-2000 ppm, in a stream of constant 1000 ppm CO, 6% O_2 and the remainder in N_2. SV=25000 h^{-1}, 366 K.

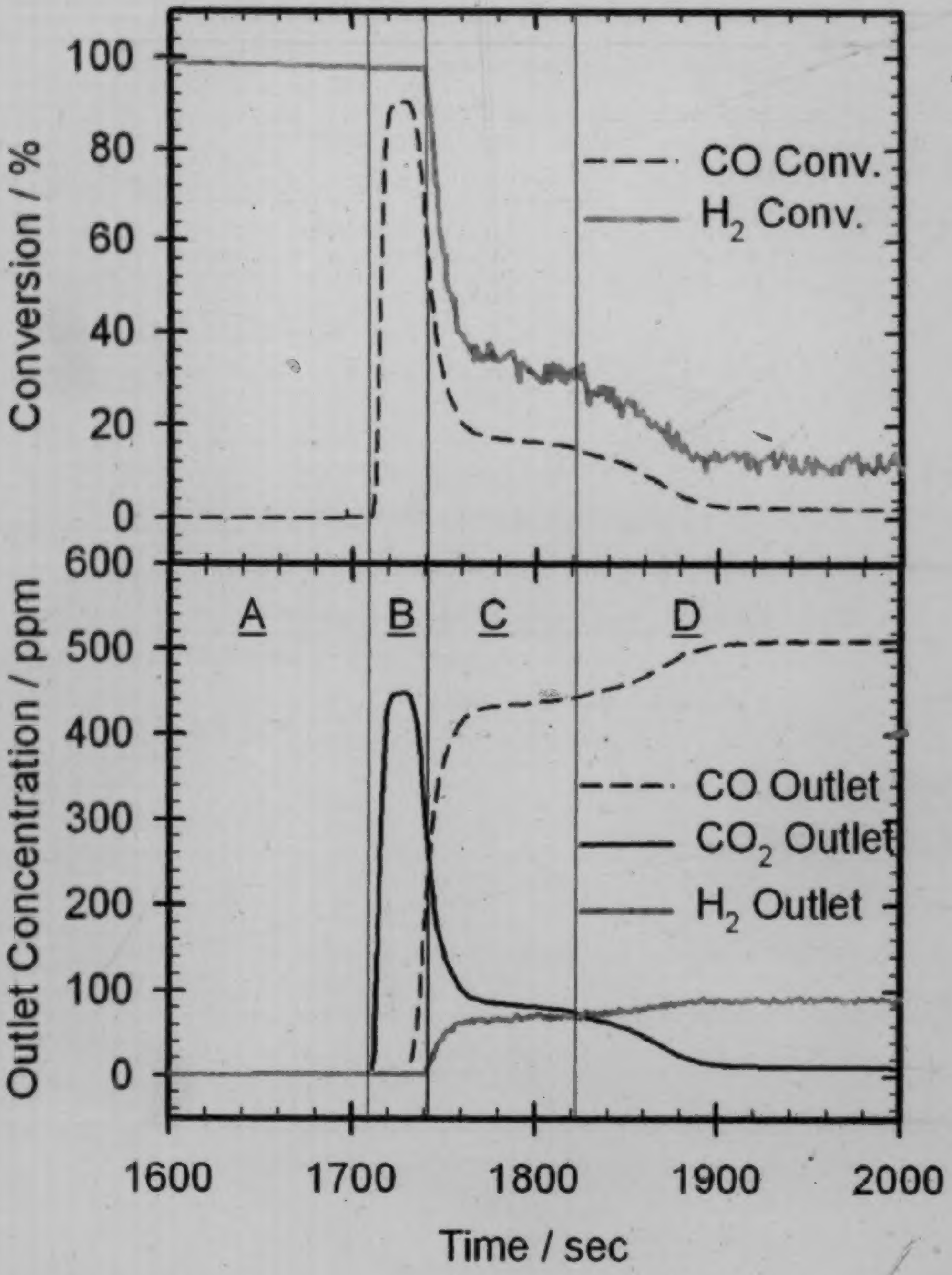

Figure 5.14: Experimental 500 ppm CO step up in 100 ppm H_2, 6% O_2 and the remainder in N_2. SV = 25000 hr^{-1}, 347 K.

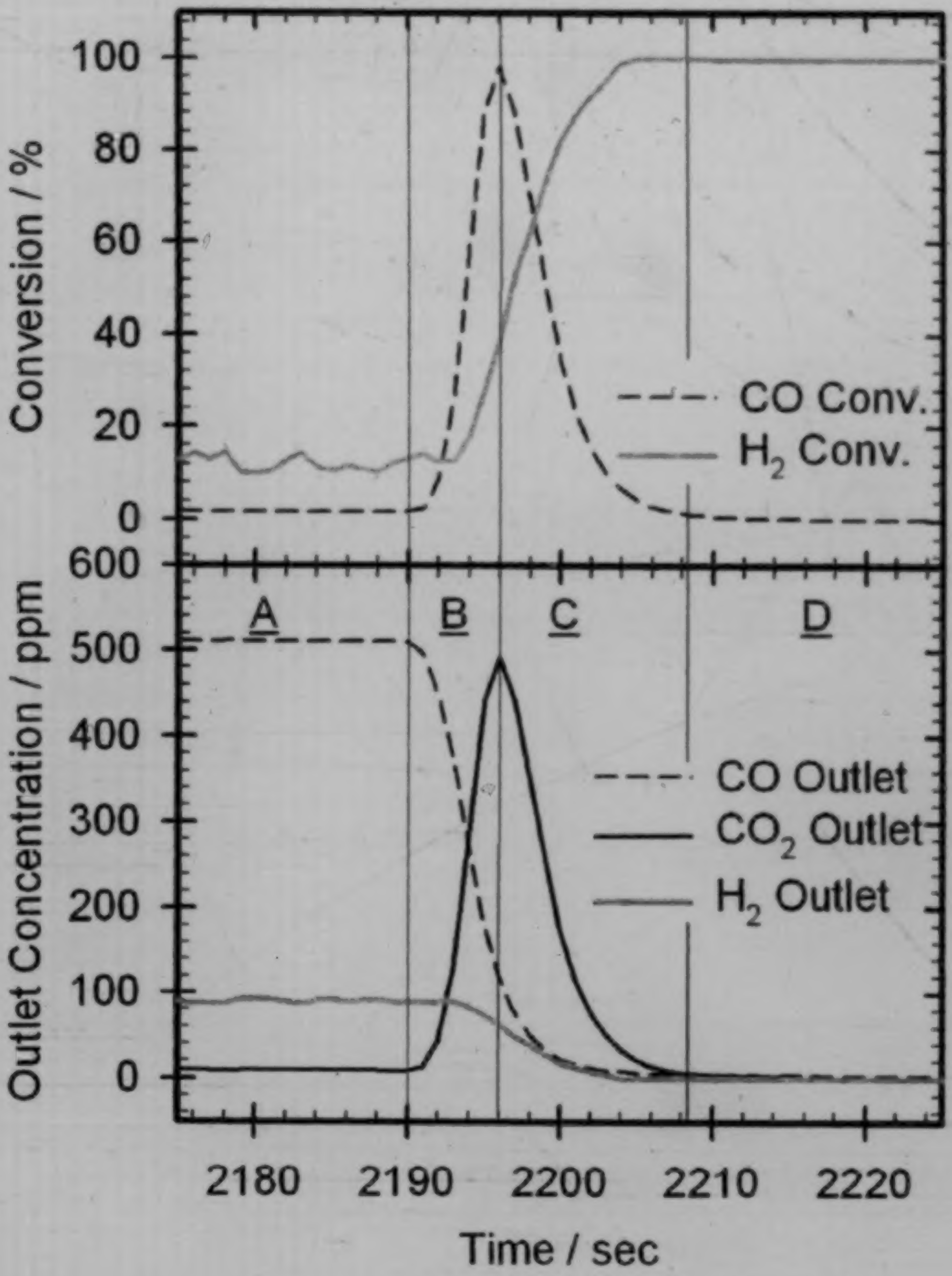

Figure 5.15: Experimental 500 ppm CO step down in 100 ppm H_2, 6% O_2 and the remainder in N_2. SV = 25000 hr^{-1}, 347 K.

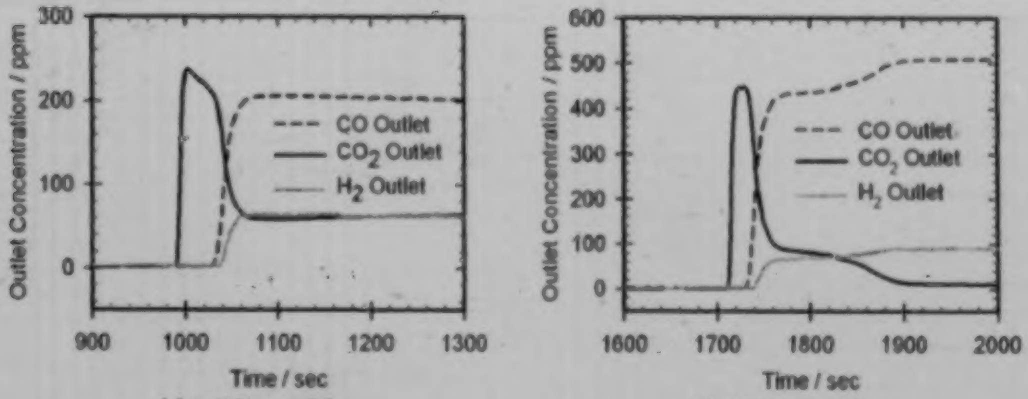

(a) 0-250 ppm CO (b) 0-500 ppm CO

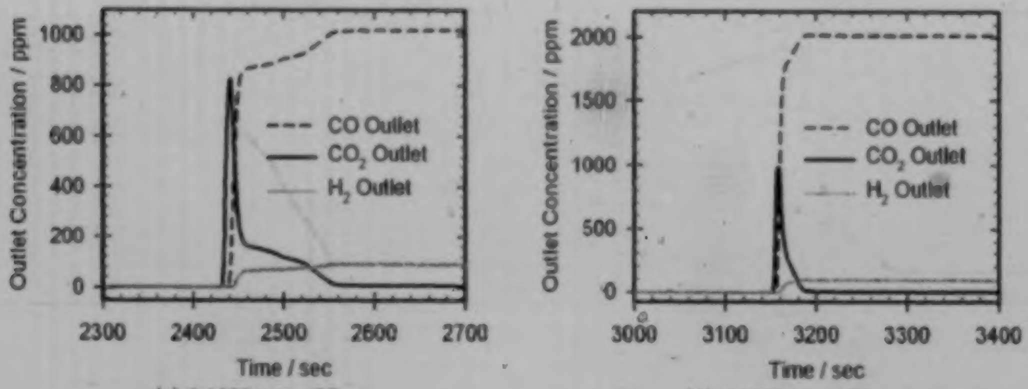

(c) 0-1000 ppm CO (d) 0-2000 ppm CO

Figure 5.16: Experimental CO concentration steps in the presence of 100 ppm H_2 at a constant temperature of 347 K.

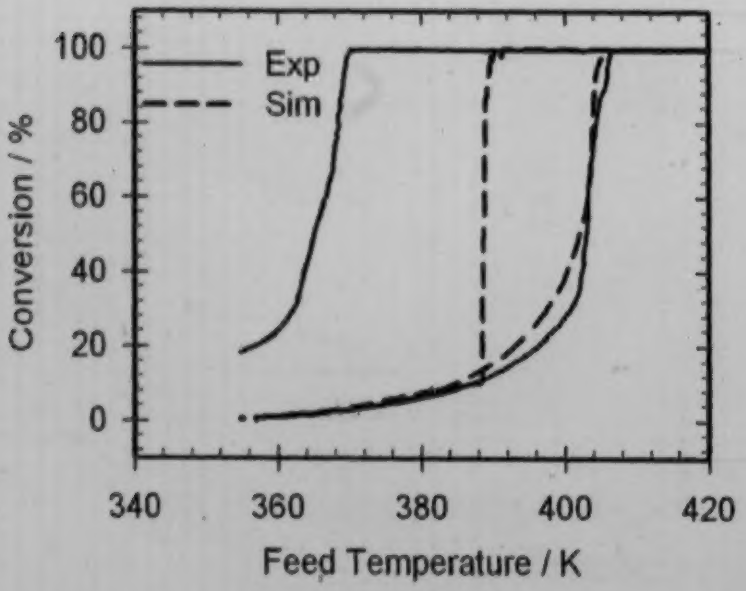

Figure 5.17: Conversion of 1000 ppm CO for simulated light-off with 500 ppm H_2. The CO-H sub-mechanism was applied, using a value of $\frac{dEa_{CO-H}}{d\theta_{H\_PtB}} = 14$ kJ·mol^{-1}. $E_{a,O\bullet+H\bullet} = 70$ kJ·mol^{-1}. 6% O_2, remainder N_2. SV = 25000 hr^{-1}.

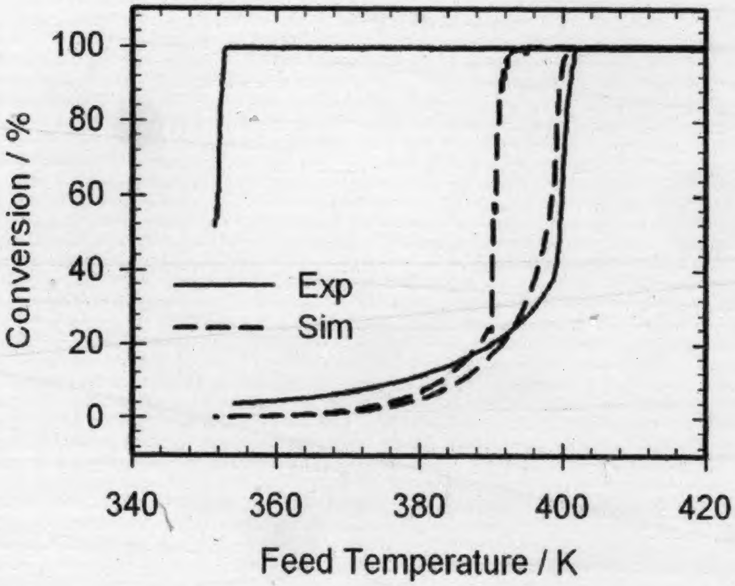

Figure 5.18: Conversion of 1000 ppm CO for simulated light-off with 2000 ppm H_2. The CO-H sub-mechanism was applied, using a value of $\frac{dEa_{CO-H}}{d\theta_{H\_PtB}} = 14$ kJ·mol^{-1}. $E_{a,O*+H*} = 70$ kJ·mol^{-1}. 6% O_2, remainder N_2. SV = 25000 hr^{-1}.

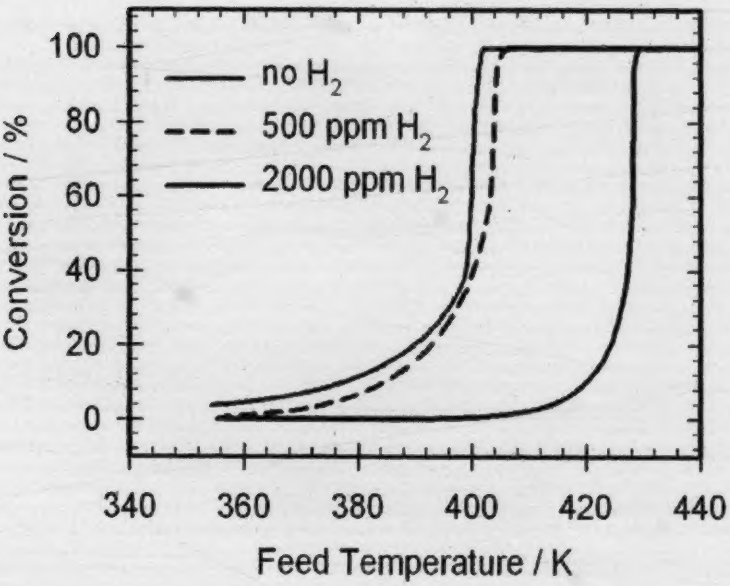

Figure 5.19: Conversion of 1000 ppm CO for simulated light-off with 0, 500 and 2000 ppm H_2. The CO-H sub-mechanism was applied with values of $\frac{dEa_{CO-H}}{d\theta_{H\_PtB}} = 14$ kJ·mol^{-1} and $E_{a,O*+H*} = 70$ kJ·mol^{-1}. 6% O_2, remainder N_2. SV = 25000 hr^{-1}.

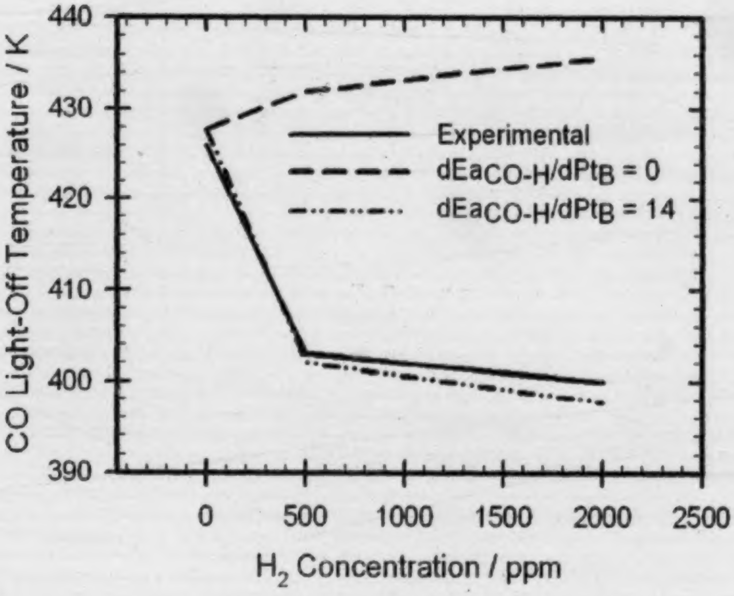

Figure 5.20: 1000 ppm CO Light-Off temperatures at various H_2 concentrations. Simulation results are shown for both with and without the CO-H submechanism. 6% O_2, remainder N_2. SV = 25000 hr^{-1}.

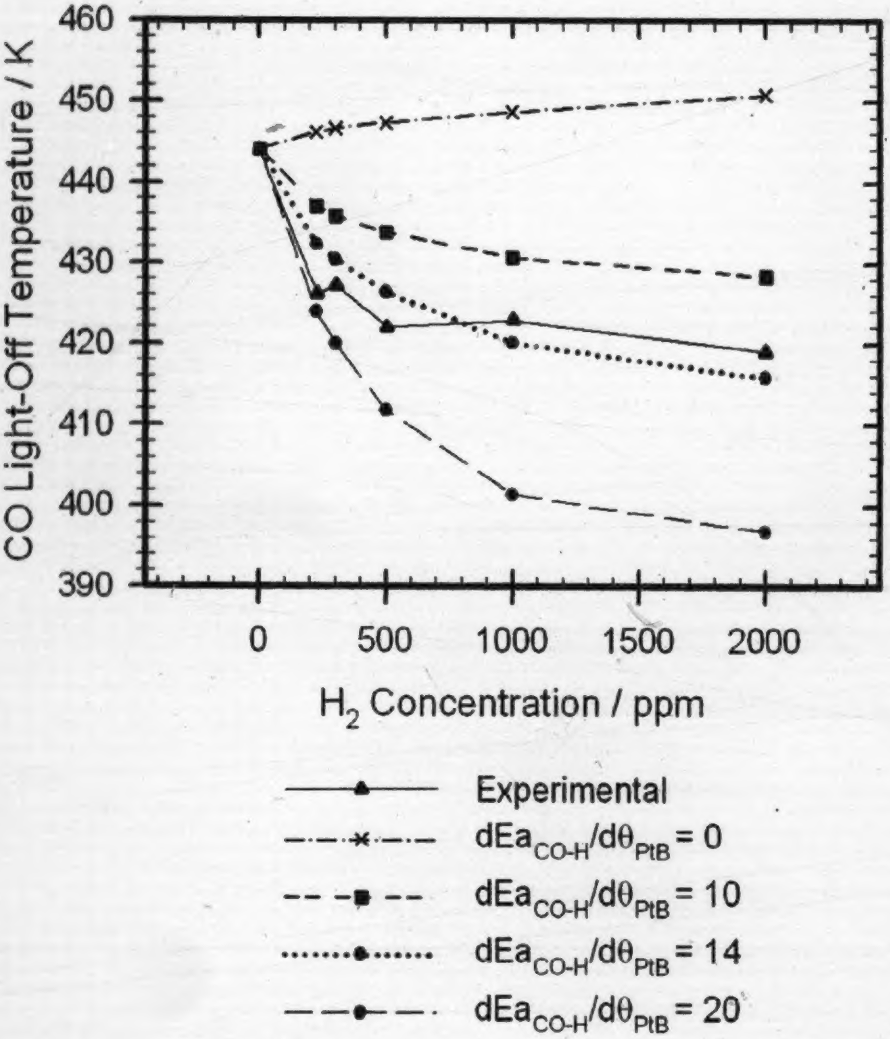

Figure 5.21: 2000 ppm CO Light-Off temperatures at various H_2 concentrations. Simulation results are shown for both with and without the CO-H submechanism, for values of $\frac{dEa_{COdes}}{\theta_{PtB-H}}$ = 0, 10, 14 and 20 kJ·mol^{-1}. 6% O_2, remainder N_2. SV = 25000 hr^{-1}.

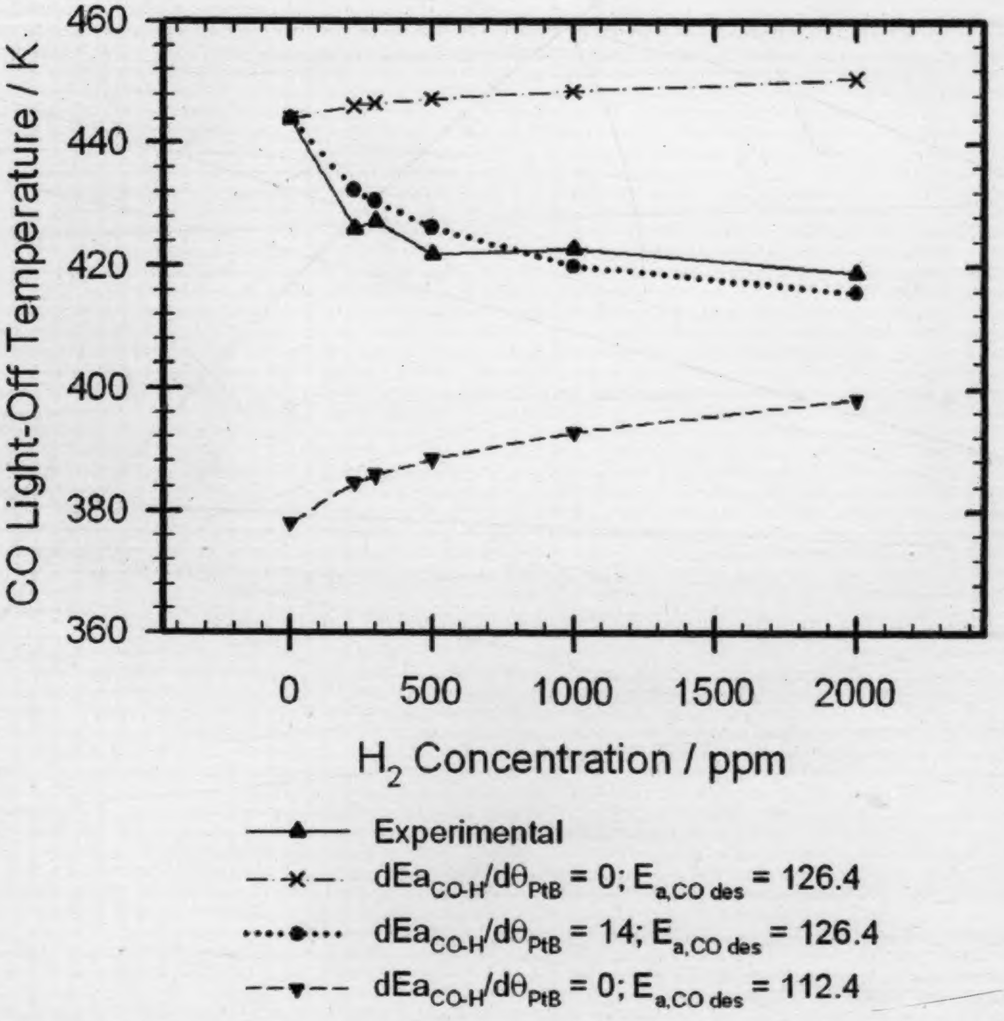

Figure 5.22: 2000 ppm CO Light-Off temperatures at various H_2 concentrations. Simulation results are shown for both with and without the CO-H submechanism, and with $E_{A,CO\ desorption} = 112.4$ kJ·mol^{-1}. 6% O_2, remainder N_2. SV = 25000 hr^{-1}. Units of $\frac{dEa_{CO-H}}{dPt_B}$ and $E_{A,CO\ desorption}$ are kJ·mol^{-1}.

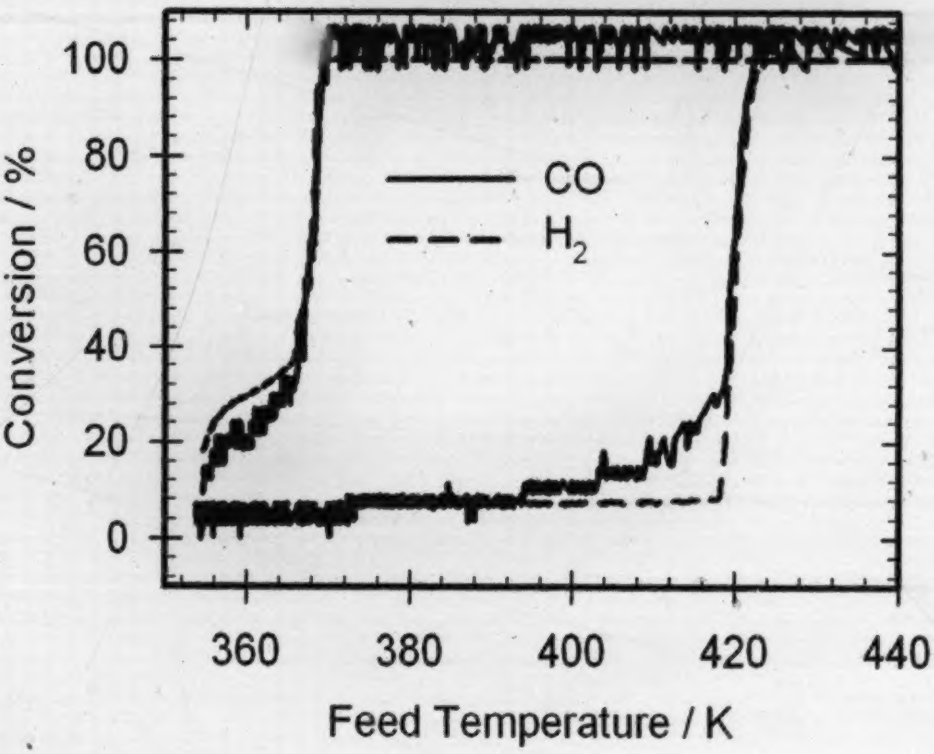

Figure 5.23: Experimental light-off curve for a mixture of 2000 ppm CO and 2000 ppm H_2. 6% O_2, remainder N_2. SV = 25000 hr^{-1}.

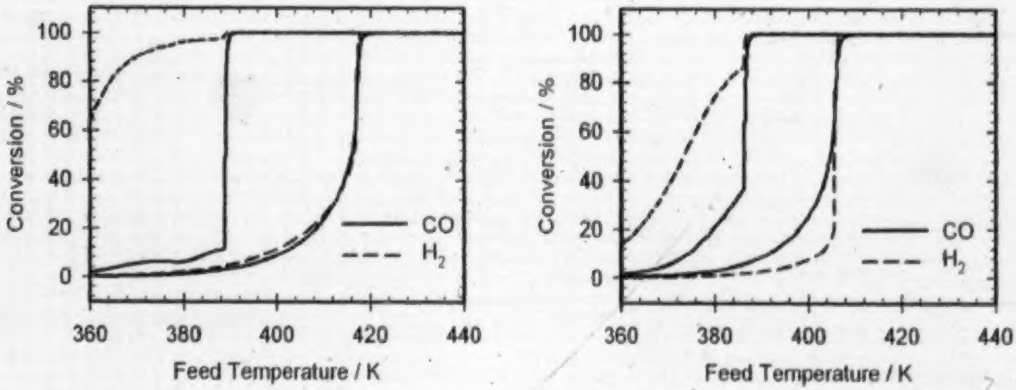

(a) Ea_{H+OH} = 70 kJ·mol^{-1}

(b) Ea_{H+OH} = 75 kJ·mol^{-1}

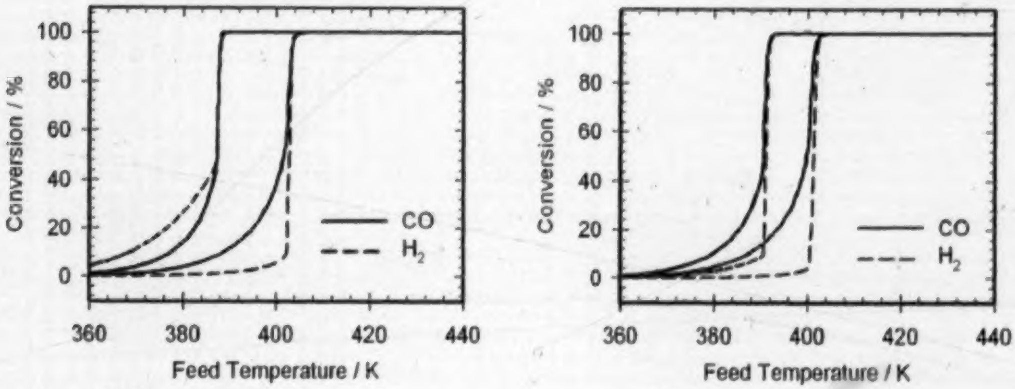

(c) Ea_{H+OH} = 77.5 kJ·mol^{-1}

(d) Ea_{H+OH} = 80 kJ·mol^{-1}

Figure 5.24: Influence of Ea_{O*+H*} on CO promotion and selectivity during light-off. A value of $\frac{dEa_{CO-H}}{d\theta_{PtB-H}} = 14$ kJ·mol^{-1} was used to model the CO-H promotion effect. All results shown in this table are for a mixture of 2000 ppm CO and 2000 ppm H_2.

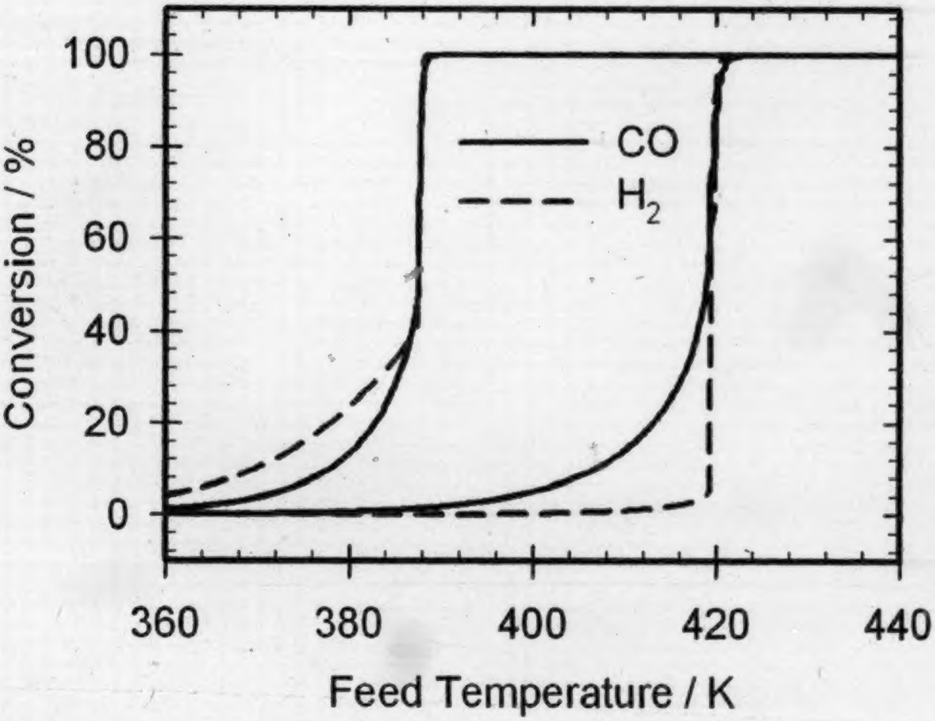

Figure 5.25: Light-off simulation for 2000 ppm CO and 2000 ppm H_2, utilizing the CO-H submechanism. $\frac{dEa_{CO-H}}{dPt_B} = 10$ kJ·mol^{-1} and $E_{A,O*+H*} = 77.5$ kJ·mol^{-1}. 6% O_2, remainder N_2. SV = 25000 hr^{-1}.

5.10 Summary of CO+H$_2$

Experimental and simulation results pertaining to mixtures of CO and H_2 (plus O_2 and N_2) have been presented and discussed.

Experimentally, it was observed that the oxidation of hydrogen did not occur until slightly after the oxidation of CO. The catalyst was selective towards CO oxidation, consistent with other results in the literature. As well, the addition of hydrogen to the bulk inlet gas decreased the temperature at which CO light-off occurred. This effect was non-linear, with increasing amounts of hydrogen having a diminishing effect.

Agreement between experimental and simulation required two factors to be correctly modelled. First, the selectivity of the catalyst towards CO oxidation had to be considered. By modifying the activation energy value of the initial reaction between H* and O* (both adsorbed onto the surface) and using a higher value of $E_{a,H*+O*} = 70$ kJ·mol^{-1}, the correct selectivity was predicted.

With the correct selectivity, it became obvious that the cause of the observed promotion effect (whereby the presence of hydrogen in the bulk gas encouraged CO oxidation and the light-off temperature was lowered) was not caused by the exothermic reaction of hydrogen. Several models were examined, however, the only model that was able to successfully model the hydrogen promotion effect involved the presence of hydrogen adsorbed onto a secondary surface site to promote the desorption of CO. This in turn increased the turnover of free sites and promoted the oxidation of CO, modelling the increase in CO oxidation in the presence of hydrogen.

This model for hydrogen promotion of CO oxidation was able to predict the light-off temperatures over the entire range of CO and H_2 concentrations studied using a value of $\frac{dEa_{CO-H}}{d\theta_{PtB-H}} = 14$ kJ·mol^{-1}.

Prediction of both the light-off temperature and the catalyst selectivity at the same time requires an iterative process to find the optimal values for both the $\frac{dEa_{CO-H}}{d\theta_{PtB-H}}$ and $E_{a,CO\ desorption}$ terms. For a simulation of a single experimental run consisting of 2000 ppm CO and 2000 ppm H_2, values of $\frac{dEa_{CO-H}}{d\theta_{PtB-H}} = 10$ kJ·mol^{-1} and $E_{a,H*+O*} = 77.5$ kJ·mol^{-1} were found to have good agreement with experimental results, in terms of light-off temperature, catalyst selectivity, and the shape of the curves. With these values, both the hydrogen promotion effect and the catalyst selectivity were modelled correctly.

6

Summary and Conclusions

6.1 Conclusions

As CO is a significant component of transportation-based emissions, classified as a primary pollutant and most prevalent component studied in the literature, this is the component that was chosen to be the first studied. Initially, a building block approach was suggested, that new components could be studied individually, and then their effects combined additively to form a more complex mixture. However, as components interacted with each other, and more complex behaviour was observed, this building block approach has proven to be insufficient.

An experimental apparatus was built to enable experiments transient in either feed gas composition or temperature. Experimental results agreed with similar results in the literature.

A simulator was used to predict experimental observations, and in some cases, the literature LH model performed fairly well. Models based on either an Eley-Rideal or global mechanism did not agree with observations as well. However, the LH literature model was found to have several shortcomings and was insufficient to fully describe the experiments involving CO, O_2 and N_2.

The rate determining step in attaining CO ignition was determined to be the adsorption of oxygen onto the surface. CO and oxygen compete for active sites on the catalyst surface. As CO dominates the surface, very little oxygen can adsorb and the surface coverage by oxygen is very low pre-ignition. As the temperature in the system rises, the desorption rate of CO and hence the turnover of free sites also increases such that oxygen can bind to the surface in significant quantities and react further with CO.

During a step increase in CO concentration, starting with a CO-free atmosphere (O_2 present in excess), the LH model provided no pathway for CO to adsorb onto an oxygen covered surface. The addition of a compressed-oxygen step (subsection 4.5.4) provided the necessary pathway to model CO step changes. Limiting oxygen coverage on the surface to slightly less than unity may also achieve this same result, however the actual value for the maximum surface coverage of the catalyst under the conditions of interest is still under debate.

Light-Off curves involving CO and hydrogen (and oxygen) were performed. Small quantities of hydrogen were observed to greatly promote the light-off of CO, whereas larger amounts of hydrogen did not proportionately increase the magnitude of the effect. The marginal benefit of additional hydrogen was diminishing. This promotion effect cannot be explained by thermal effects caused by the heat of reaction from hydrogen shifting the CO adsorption-desorption equilibrium, as the catalyst is selective towards CO, and hydrogen ignition occurs AFTER CO ignition.

The selectivity of the catalyst towards CO is very important, and the initial parameter set did not correctly account for this. As CO was observed to oxidize before hydrogen, this must be considered in the model. By increasing the activation energy for the reaction between the adsorbed species O* and H* to 70 kJ·mol^{-1} the correct selectivity was achieved (section 5.4).

Once the simulator predicts the correct selectivity, insight into the nature of promotion of CO oxidation by H_2 was gained. As we now know that the catalyst is selective toward CO, and that CO will oxidize before H_2, we can confidently state that the adiabatic temperature rise from H_2 oxidation was not the cause of the promotion effect. Current literature models are not able to model this effect. After further investigations into the nature of the promotion effect, and after several other potential mechanisms failed, a reasonable mechanism was applied that does model the hydrogen promotion effect. With the addition of a secondary adsorption site for hydrogen and making the activation energy of CO desorption dependent upon the concentration of hydrogen adsorbed on this secondary site, the promotion effect for light-off curves was modelled over a range of up to 2000 ppm CO and 2000 ppm H_2. This approach was able to model the decreasing marginal effect of increasing the inlet hydrogen concentration. This effect has not been modelled before in the literature.

With the interacting effects of catalyst selectivity and hydrogen promotion, an iterative approach is required to determine the optimal parameters to use to accurately model a given catalyst over a range of concentrations. Values of $\frac{dEa_{CO-H}}{dPt_B} = 10$ kJ·mol^{-1} and $E_{A,O*+H*} = 77.5$ kJ·mol^{-1} were used to model a mixture of 2000 ppm CO and 2000 ppm

H_2, and the result shows excellent agreement with the light-off temperature, prediction of the promotion effect and catalyst selectivity. Although the light-out temperature is predicted to be higher than was experimentally measured, the shape of the extinction curve is similar to that measured experimentally.

Traditional models of oxidation catalysis have been studied, and with the addition of the discussed steps, these mechanisms are better able to predict catalyst performance with interacting gas components.

6.2 Future Work

The light-off (ignition) curves were modelled in this study, however the light-out curves are not yet satisfactorily described. The competing kinetic and mass transfer effects are not yet properly described during extinction. We know that the adiabatic temperature rise does assist in sustaining the reaction below the light-off temperature, but have not yet modelled both the light-off and light-out curves for a set of experiments with the same set of parameters.

Although the hydrogen promotion effect was modelled through the use of hydrogen-promoted CO desorption, this effect has not yet been experimentally observed under the conditions of oxidation catalysts (i.e. room temperature to 150°C, atmospheric pressure). Until this has been experimentally verified, this mechanism remains a useful tool for modelling oxidation catalysts, but cannot be described as a proven mechanism. Other adsorption models should be explored, as the Langmuir assumptions appear to be unable to model all observations.

Other components need to be added to the models to extend the model to include the complete gas mixture. Some studies involving NO_x [262], NH_3 [263], CH_4 [264], as well as with diesel particulate filters [265, 266] have already been published. More work will be required as these studies develop. As the interactions between all components are not yet know, these will have to be studied.

The results presented here may be used to further product development for manufacturers of catalytic converters as well as for the development of on-board computer control of automotive aftertreatment systems.

A

Basic Equations

A.1 Heat and Mass Transfer

A.1.1 Gas Hourly Space Velocity

The GHSV is defined as the ratio of the volumetric flow rate of the gas to the volume of the monolith.

$$GHSV = \frac{F}{\frac{1}{4}\pi D^2 H} \tag{A.1}$$

A.1.2 Reynolds Number

The Reynolds number is the ratio of the inertia and viscous forces [267], and is defined by:

$$Re = \frac{V \times L}{\nu} \tag{A.2}$$

A.1.3 Prandtl Number

The Prandtl number is the ratio of the momentum and thermal diffusivities [267], and is defined by:

$$Pr = \frac{\nu}{\alpha} \tag{A.3}$$

A.1.4 Peclet Number

The Prandtl number is a dimensionless independent heat transfer parameter [267], and is defined by:

$$Pe = Re \times Pr \tag{A.4}$$

A.2 Mass Transfer

A.2.1 Knudson Diffusion

Knudsen Diffusion [268] is the diffusion of a component through a small pore in the washcoat layer. This describes the travel of a particle through a capillary and the collisions between the wall and the molecule.

$$D_{KA} = 97.0r\left(\frac{T}{M_A}\right)^{\frac{1}{2}} \tag{A.5}$$

A.2.2 Fuller Equation

The Fuller equation [269, 268] is used to calculate the diffusivity of a component through a gas. This equation typically works well for components of a binary mixture, where one component has a small concentration. As many of the components of interest in this study are of low concentration (CO, H_2 and hydrocarbons are all on the order of 0-3000 ppm), this equation is assumed to be valid over the conditions in this study. As the concentration of O_2 is typically very high (compared to CO and others) everywhere in the system, the diffusivity of O_2 is assumed to not be a significant factor.

$$D_{AB} = \frac{1.00 \times 10^{-7} T^{1.75} \left(\frac{1}{M_A} - \frac{1}{M_B}\right)^{\frac{1}{2}}}{P_{abs}\left[\left(\sum \nu_A\right)^{\frac{1}{3}} + \left(\sum \nu_B\right)^{\frac{1}{3}}\right]^2} \tag{A.6}$$

The diffusivity of component A through B, D_{AB}, is expressed in units of $m^2 \cdot s^{-1}$. The absolute pressure is expressed in units of atm for the purposes of this equation. The diffusion volumes for a given component (i), ν_i, is expressed in units of $cm^3 \cdot mol^{-1}$ and tabulated in the literature [269, 268].

A.2.3 Effective Diffusivity

Effective diffusivity [268] This simplifies to Knudsen diffusion at low pressures and Fuller Diffusion at high pressures. This assumes equimolar counterdiffusion.

$$D'_{NA} = \frac{1}{\frac{1}{D_{KA}} + \frac{1}{D_{AB}}} \tag{A.7}$$

A more accurate value of effective diffusivity also considers the flux factor:

$$\alpha = 1 + \frac{N_B}{N_A} \tag{A.8}$$

$$D''_{NA} = \frac{1}{\frac{(1-\alpha x_{A,av})}{D_{KA}} + \frac{1}{D_{AB}}} \tag{A.9}$$

A.2.4 Effective Diffusion

Effective diffusion [268] considers the influence of the pores in washcoat on the diffusivity, including the pore tortuosity, τ, and void fraction, ϵ. Tortuosity and void fraction are both dimensionless, and $D_{A,eff}$ and D''_{NA} are expressed in $m^2 \cdot s^{-1}$.

$$D_{A,eff} = \frac{\epsilon D''_{NA}}{\tau} \tag{A.10}$$

A.3 Selectivity and Conversion

A.3.1 Conversion

Conversion is the fraction of an inlet component (i) that has reacted to form another species. This is generally calculated on a molar or mass basis using Equation A.11.

$$X_i = \frac{n_{inlet,i} - n_{outlet,i}}{n_{inlet,i}} = \frac{m_{inlet,i} - m_{outlet,i}}{m_{inlet,i}} = \frac{\dot{m}_{inlet,i} - \dot{m}_{outlet,i}}{\dot{m}_{inlet,i}} \tag{A.11}$$

For low concentration components in a mixture that has a relatively constant molar flowrate, the change in concentration may be used to approximate conversion with minimal error.

A.3.2 Selectivity

Selectivity is defined here as the preference for CO to be oxidized despite the potential for H_2 oxidation. The general oxidation equations for CO and H_2 are shown in Equation A.12 and Equation A.13.

$$CO + \frac{1}{2}O_2 \rightarrow CO_2 \tag{A.12}$$

$$H_2 + \frac{1}{2}O_2 \rightarrow H_2O \tag{A.13}$$

For both general reactions, one half oxygen molecule is used to completely oxidize the CO or H_2 to completion.

$$\begin{aligned} Selectivity &= \frac{rateofoxygenconsumptionforCOoxidation}{rateofoverall oxygenconsumption} && \text{(A.14)} \\ &= \frac{F_{CO} \cdot C_{CO} \cdot \frac{1}{2}X_{CO}}{F_{CO} \cdot C_{CO} \cdot \frac{1}{2}X_{CO} + F_{H_2} \cdot C_{H_2} \cdot \frac{1}{2}X_{H_2}} && \text{(A.15)} \end{aligned}$$

The flowrate and the stoichiometry cancels out in this particular case.

$$Selectivity = \frac{C_{CO} \cdot X_{CO}}{C_{CO} \cdot X_{CO} + C_{H_2} \cdot X_{H_2}} \tag{A.16}$$

A.4 Dew Point

Geankoplis [268, section 9.3] describes the method for calculating the relative humidity of water in air. The humidity of a system of water vapour and air can be calculated with Equation A.17:

$$H = \frac{P_A}{P_{atm} - P_A} \times \frac{M_{H_2O}}{M_{air}} = \frac{18.02}{28.97} \times \frac{P_A}{P_{atm} - P_A} \tag{A.17}$$

Where $M_{H_2O} = 18.02$ g mol^{-1} and $M_{air} = 28.97$ g mol^{-1}. The saturation pressure is the pressure at which water vapour is at equilibrium with liquid water at the given temperature and atmospheric pressure. Above this pressure, water liquid will form. In the experimental apparatus discussed in this thesis, care is taken such that the system never crosses above saturation: this is to ensure that water droplets do not taint the experimental results and modify the surface of the catalyst.

The saturation humidity can be calculated as in Equation A.18:

$$H_S = \frac{P_{AS}}{P_{atm} - P_{AS}} \times \frac{M_{H_2O}}{M_{air}} = \frac{18.02}{28.97} \times \frac{P_{AS}}{P_{atm} - P_{AS}} \tag{A.18}$$

In this equation, atmospheric and partial pressures are expressed in units of kPa. The molar mass of water (M_{H_2O}) and air (M_{air}) are expressed in $g \cdot mol^{-1}$, and the saturation humidity has units of g H_2O g dry air^{-1}.

Steam tables state the saturation pressure of water in air under various conditions. The percent humidity may be calculated using Equation A.19. Above 100%, water droplets are likely to form.

$$H_P = 100\% \times \frac{H}{H_S} \tag{A.19}$$

$$RH = 100\% \times \frac{P_A}{P_{AS}} \tag{A.20}$$

A.4.1 Antoine Equation

The Antoine Equation is used to calculate the saturated vapour pressure over a liquid, in this case water.

$$log_{10}(P_{vap}) = A - \left(\frac{B}{T + C}\right) \tag{A.21}$$

The vapour pressure, P_{vap}, in this form of the equation is expressed in units of bar. The temperature, T, is in units of K. The coefficients (A, B and C) may be found in the NIST Webbook [270].

A.5 Adiabatic Temperature Rise

The adiabatic temperature rise is calculated by summing the total enthalpy of reaction, and using that energy to heat the fluid. If all of the energy is used to heat that fluid, the adiabatic temperature rise is the temperature gained by the fluid. This calculation assumes no phase changes, which is a valid assumption for the system in the present work.

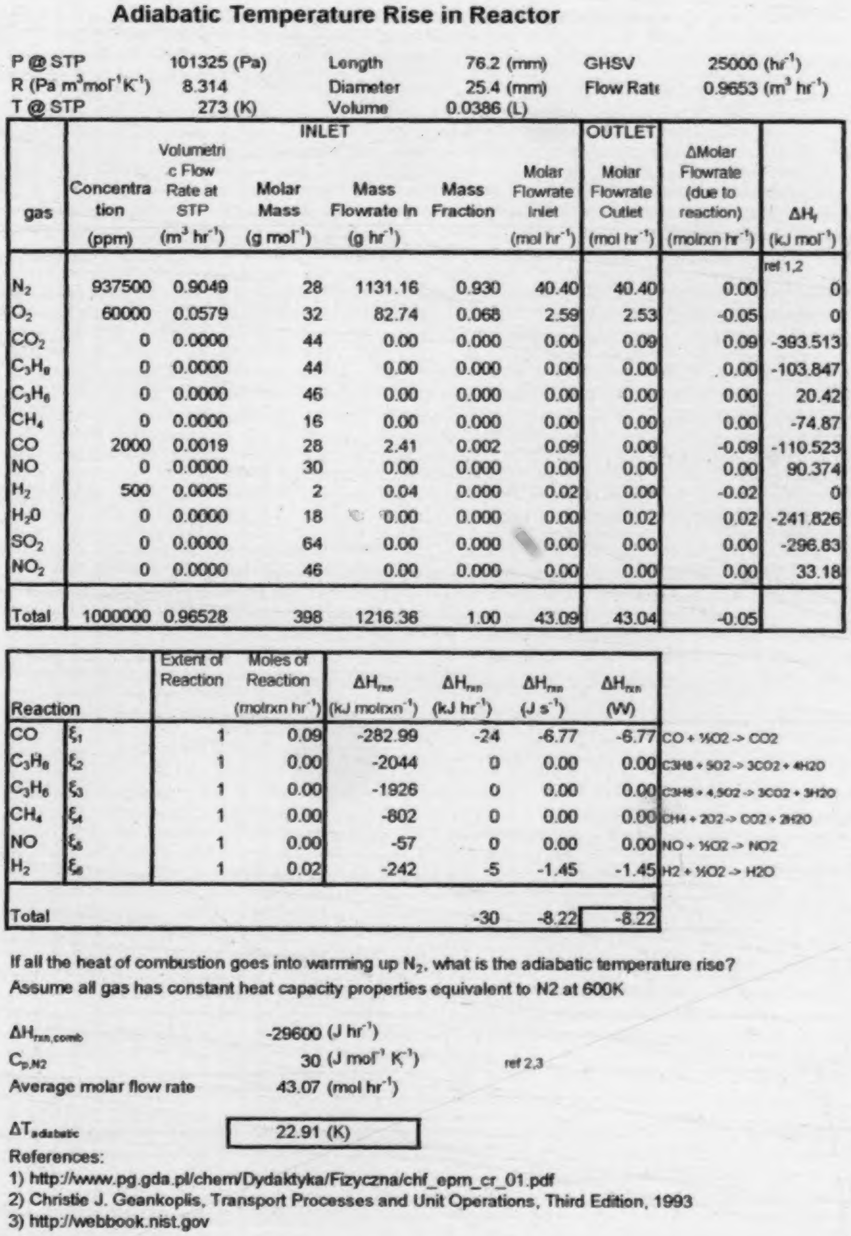

Adiabatic Temperature Rise in Reactor

P @ STP	101325 (Pa)	Length	76.2 (mm)	GHSV	25000 (hr^{-1})
R (Pa $m^3 mol^{-1} K^{-1}$)	8.314	Diameter	25.4 (mm)	Flow Rat	0.9653 ($m^3\ hr^{-1}$)
T @ STP	273 (K)	Volume	0.0386 (L)		

	INLET						OUTLET		
gas	Concentration (ppm)	Volumetric Flow Rate at STP ($m^3\ hr^{-1}$)	Molar Mass ($g\ mol^{-1}$)	Mass Flowrate In ($g\ hr^{-1}$)	Mass Fraction	Molar Flowrate Inlet ($mol\ hr^{-1}$)	Molar Flowrate Outlet ($mol\ hr^{-1}$)	ΔMolar Flowrate (due to reaction) ($molrxn\ hr^{-1}$)	ΔH_f ($kJ\ mol^{-1}$)
									ref 1,2
N_2	937500	0.9049	28	1131.16	0.930	40.40	40.40	0.00	0
O_2	60000	0.0579	32	82.74	0.068	2.59	2.53	-0.05	0
CO_2	0	0.0000	44	0.00	0.000	0.00	0.09	0.09	-393.513
C_3H_8	0	0.0000	44	0.00	0.000	0.00	0.00	0.00	-103.847
C_3H_6	0	0.0000	46	0.00	0.000	0.00	0.00	0.00	20.42
CH_4	0	0.0000	16	0.00	0.000	0.00	0.00	0.00	-74.87
CO	2000	0.0019	28	2.41	0.002	0.09	0.00	-0.09	-110.523
NO	0	0.0000	30	0.00	0.000	0.00	0.00	0.00	90.374
H_2	500	0.0005	2	0.04	0.000	0.02	0.00	-0.02	0
H_20	0	0.0000	18	0.00	0.000	0.00	0.02	0.02	-241.826
SO_2	0	0.0000	64	0.00	0.000	0.00	0.00	0.00	-296.83
NO_2	0	0.0000	46	0.00	0.000	0.00	0.00	0.00	33.18
Total	1000000	0.96528	398	1216.36	1.00	43.09	43.04	-0.05	

Reaction		Extent of Reaction	Moles of Reaction ($molrxn\ hr^{-1}$)	ΔH_{rxn} ($kJ\ molrxn^{-1}$)	ΔH_{rxn} ($kJ\ hr^{-1}$)	ΔH_{rxn} ($J\ s^{-1}$)	ΔH_{rxn} (W)	
CO	ξ_1	1	0.09	-282.99	-24	-6.77	-6.77	CO + ½O2 -> CO2
C_3H_8	ξ_2	1	0.00	-2044	0	0.00	0.00	C3H8 + 5O2 -> 3CO2 + 4H2O
C_3H_6	ξ_3	1	0.00	-1926	0	0.00	0.00	C3H6 + 4.5O2 -> 3CO2 + 3H2O
CH_4	ξ_4	1	0.00	-802	0	0.00	0.00	CH4 + 2O2 -> CO2 + 2H2O
NO	ξ_5	1	0.00	-57	0	0.00	0.00	NO + ½O2 -> NO2
H_2	ξ_6	1	0.02	-242	-5	-1.45	-1.45	H2 + ½O2 -> H2O
Total					-30	-8.22	-8.22	

If all the heat of combustion goes into warming up N_2, what is the adiabatic temperature rise?
Assume all gas has constant heat capacity properties equivalent to N2 at 600K

$\Delta H_{rxn,comb}$	-29600 ($J\ hr^{-1}$)	
$C_{p,N2}$	30 ($J\ mol^{-1}\ K^{-1}$)	ref 2,3
Average molar flow rate	43.07 ($mol\ hr^{-1}$)	
$\Delta T_{adiabatic}$	22.91 (K)	

References:
1) http://www.pg.gda.pl/chem/Dydaktyka/Fizyczna/chf_epm_cr_01.pdf
2) Christie J. Geankoplis, Transport Processes and Unit Operations, Third Edition, 1993
3) http://webbook.nist.gov

Figure A.1: Adiabatic temperature rise, under conditions stated in figure.

B

Kinetic Expressions *

The approaches of Hoebink et al. [87] and Chatterjee et al. [66] are used in this model to calculate reaction rates. These methods are described below.

B.1 Eindhoven Approach

There are different approaches to calculating the rate constants for a reaction. The first approach, detailed here, is that of the Eindhoven model [87]. In this approach, T, C_{gas}, $\theta_{surface}$, and L_A are defined, and the rate constants are to be determined.

The overall balance of a typical component in the the system will include flow rates, mass transfer, reaction, and accumulation of the species in the reactor. The rate of reaction of the compound under consideration is calculated based on the reaction stoichiometry and reaction rate parameters. For example, for the reversible reaction:

$$a_1A_1 + a_2A_2 \underset{k_{-i}}{\overset{k_i}{\rightleftharpoons}} p_1P_1 + p_2P_2 \tag{B.1}$$

Where k_{-1} is the rate constant for the reverse step. This reaction can easily be extended to many more components, but for simplicity, only two reactants and two products are shown here. The overall rate of reaction can be calculated based on the reaction rate parameters and the concentrations of the components:

$$r_i = k_i C_{A_1}^{a_1} C_{A_2}^{a_2} - k_{-i} C_{P_1}^{p_1} C_{P_2}^{p_2} \tag{B.2}$$

---

*a portion of this chapter is from Mukadi (2003) "Summary of Elementary Mechanisms" [271]

C_j here represents the concentration of the species. For the gas phase, this parameter is in units of mol per unit volume. Where surface species are concerned, this term is represented by the fractional surface coverage.

Use of the stoichiometric coefficient as the exponent is not valid unless the expressed reaction mechanism is an elementary step. For global mechanisms, the exponent may take on other values, based on the kinetics of the reaction. For an irreversible reaction, the rate constant is zero ($k_{-i} = 0$).

B.1.1 Arrhenius Equation

The rate constant is typically calculated using the Arrhenius equation. Contrary to the name, the rate constant varies with temperature:

$$k_i = A_{0,i} \cdot T^{\beta_i} \cdot e^{-\frac{E_{a,i}}{R \cdot T}} \tag{B.3}$$

Typically, $\beta = 0$, simplifying the equation.

The activation energy in the Eindhoven mechanism can be made to be linearly dependent on the surface coverage of the species.

$$E_{a,i} = E_{a,0,i} - \sum_j \alpha_j \cdot \theta_j \tag{B.4}$$

For example, for Equation 3.16b, the activation energy is dependent on CO surface coverage:

$$E_{a,i} = 113 - 8.5 \cdot \theta_{CO} \tag{B.5}$$

B.1.2 Elovich Equation

If the step is an adsorption step, then the Elovich equation (see Equation B.6) can be used to calculate the rate constant.

$$k_i = \frac{1}{L_t}\sqrt{\frac{RT}{2\pi M_i}} \tag{B.6}$$

In the Elovich equation, L_t is the density of active sites per unit surface area ($\text{mol}_{NM}\ \text{m}_{cat}^{-2}$). This is used to transform the rates into units of ($\text{mol}_A\ \text{m}_{cat}^{-3}\ \text{s}^{-1}$).

B.1.3 Source Term - Eindhoven

The source term of each species may be computed using Equation B.7.

$$s_i = L_A r_i = L_A \left(k_i C_{A_1}^{a_1} C_{A_2}^{a_2} \cdots - k_{-i} C_{P_1}^{p_1} C_{P_2}^{p_2} \cdots \right) \tag{B.7}$$

The source term may then be calculated by summing over the stoichiometric coefficients.

$$S_j = \sum_{i=1}^{N_{rxns}} \nu_{ij} s_i \tag{B.8}$$

While the surface site concentration is not directly used, the fractional surface coverage is. These term are related by Equation B.9.

$$C_{s,k} = L_A \theta_k \tag{B.9}$$

B.1.4 Steps to Calculate Eindhoven Source Terms

1. T, C_{gas}, $\theta_{surface}$ and L_A are given.
2. Calculate r_i using Equation B.2. The appropriate k value is calculated using Equation B.3 or Equation B.6.
3. The source term (s_i) for each species is calculated using Equation B.7.
4. By summing the source terms for all the species (using Equation B.8), the overall source term (S_j) may be calculated.

B.2 DETCHEM Approach

The method used by Chatterjee, Deutschmann et al. [66] in the DETCHEM model differs from that described in section B.1. There are two essential differences between the two methods as presented in Table B.1: rate units and concentration of surface species.

	Eindhoven Method	DETCHEM Method
rate	r_i $mol_A mol_{cat}^{-1} s^{-1}$	$r_i^{''}$ $mol_A m_{cat}^{-2} s^{-1}$
concentration of surface species	L_A $mol_{NM} m_{cat}^{-3}$	L_t $mol_{NM} m_{NM}^{-2}$

Table B.1: Differences between Eindhoven and DETCHEM methods

B.2.1 Species Concentration

The species concentration in the DETCHEM method is calculated using Equation B.10:

$$C_{s,k} = L_A \theta_k \tag{B.10}$$

It is important to note that the active sites concentration used in Equation B.9 is different from the active sites density in Equation B.10 ($L_A \neq L_t$). L_A is a property that not unlike density per volume. L_t relates the number of active sites per unit surface area. The symbol Γ is used to represent L_t in DETCHEM publications.

B.2.2 Thermodynamic Equilibrium

In the DETCHEM scheme, all reactions are considered to be reversible, and the thermodynamic equilibrium constant is used.

$$r_{i,forward}^{''} = k_i C_{A_1}^{a_1} C_{A_2}^{a_2} \dots \tag{B.11}$$

The units on the rate ($r_{i,forward}^{''}$) are $\text{mol}_A \cdot \text{m}_{NM}^{-2} \cdot \text{s}^{-1}$. When the thermodynamic equilibrium constant is applied, the net rate becomes:

$$r_i^{''} = k_i^{''} \left(C_{A_1}^{a_1} C_{A_2}^{a_2} \dots - \frac{1}{K_{Eq}} C_{P_1}^{p_1} C_{P_2}^{p_2} \dots \right) \tag{B.12}$$

B.2.3 Calculation of the Rate Constant

The rate constant can be calculated for both reaction (Equation B.13) and adsorption (Equation B.14) steps:

$$k_{i,}^{"} = A_{0,i} \cdot T^{\beta_i} \cdot \theta^{\mu} \cdot e^{\left(-\frac{E_i}{RT}\right)} \tag{B.13}$$

In Equation B.13, μ is a correction factor for the reaction order of θ. This is also referred to as a departure from stoichiometric power. β is a correction factor for the rate constant power dependence on temperature. However, typically $\beta = 0$.

$$k_i^{"} = \frac{1}{L_i^m}\sqrt{\frac{RT}{2\pi M_i}} \tag{B.14}$$

Where m is the number of adsorption sites involved. In the case of a reaction such as Equation B.15,

$$H_2 + ^* + ^* \rightleftharpoons H^* + H^* \tag{B.15}$$

the rate must be transformed into units of $mol_A \cdot m_{cat}^{-3} \cdot s^{-1}$, and to do this, the specific surface area of the catalyst is used. The specific surface area of the catalyst can be used to relate the concentration of active sites per unit surface area (see Equation B.9) to the density of active sites (used in Equation B.10). These two definitions of active sites intensity are directly related, as shown in Equation B.16.

$$L_A = L_t \cdot a_{cat} \tag{B.16}$$

L_t typically remains constant with a catalyst, however, L_A depends on the catalyst preparation methods and the catalyst loading. A typical value for the surface site density (L_t) for a Pt catalyst is $\sim 2.72 \times 10^{-5}\ mol_{NM} \cdot m_{NM}^{-2}$ [66]. The symbol γ is also used to represent this parameter.

B.2.4 Source Term - DETCHEM

The source term for the component can now be calculated:

$$s_i = a_{cat} r_i^{"} = a_{cat} k_i^{"} \left(C_{A_1}^{a_1} C_{A_2}^{a_2} \ldots - \frac{1}{K_{Eq}} C_{P_1}^{p_1} C_{P_2}^{p_2} \ldots \right) \tag{B.17}$$

The units of s_i are $mol_A \cdot m_{cat}^{-3} \cdot s^{-1}$. The overall source term (S_j) may be calculated using Equation B.8.

B.2.5 Steps for Calculating DETCHEM source terms

The steps to calculate the source terms using the DETCHEM method are:

1. T, C_{gas}, $\theta_{surface}$, a_{cat} and L_t are given.
2. Calculate $C_{s,k}$ using Equation B.10.
3. $r^{"}_{i,forward}$ is calculated using Equation B.11.
4. Use Equation B.12 to calculate $r^{"}_i$.
5. The source term for each species (s_i) can be calculated with Equation B.17.
6. By summing the source terms for all the species (using Equation B.8), the overall source term (S_j) may be calculated.

B.3 Bimolecular Surface Reaction Rate - Example

As an example, the rate for the oxidation of adsorbed CO with adsorbed oxygen may be calculated in the following manner. The parameters required for the calculation are shown in Table B.2.

Using Equation B.13 and the values in Table B.2, the reaction for for the oxidation of adsorbed CO, Equation 3.9a, may be calculated:

Remembering the relation between C and θ (Equation B.10), we can subsitute into Equation B.11.

$$
\begin{aligned}
r^{"}_i &= k_i C_{A_1}^{a_1} C_{A_2}^{a_2} && \text{(B.18)} \\
&= k_i \cdot (L_A \theta_{CO})^1 \cdot (L_A \theta_O)^1 && \text{(B.19)} \\
&= k_i \cdot L_A^2 \cdot \theta_{CO} \cdot \theta_O && \text{(B.20)}
\end{aligned}
$$

k_i is taken from Equation B.13, and may be simplified due to the values of β and μ:

A_0	pre-exponential factor	3.70×10^{20}	$mol \cdot cm^{2}_{NM} \cdot mol^{-2}_{NM} \cdot s^{-1}$	[66]
A_0	pre-exponential factor	3.70×10^{16}	$mol \cdot m^{2}_{NM} \cdot mol^{-2}_{NM} \cdot s^{-1}$	
θ_{CO}	surface coverage of CO	0.19	dimensionless fraction	[a]
θ_{O}	surface coverage of O	0.80	dimensionless fraction	[a]
θ_{NO}	surface coverage of NO	0.00	dimensionless fraction	[a]
μ	reaction order correction	1	dimensionless	[a]
E_A	activation energy	108.0 $+ 33.0\,\theta_{CO}$ $- 90.0\,\theta_{NO}$	$kJ \cdot mol^{-1}$	[66]
R	Ideal Gas Constant	8.314	$J \cdot mol^{-1} \cdot K^{-1}$	
T	Temperature	500	K	[a]
β	Temperature Exponent	0	dimensionless	[a]
a	site Concentration	2.0	$m^{2}_{NM}\ m^{-3}_{cat}$	[a]

---

[a] Typical Value

Table B.2: Parameters used for a sample calculation for a surface reaction. Coverages are from a typical light-off (1000 ppm CO and 500 ppm H_2), at the reactor inlet, and after ignition has occurred (T = 500 K).

$$as\ \beta = 0, \quad T^{\beta_i} \rightarrow 1 \tag{B.21}$$

$$as\ \mu = 0, \quad \theta^{\mu} \rightarrow 1 \tag{B.22}$$

$$k''_{i,} = A_{0,i} \cdot T^{\beta_i} \cdot \theta^{\mu} \cdot e^{\left(-\frac{E_i}{RT}\right)} \tag{B.23}$$

$$= A_{0,i} \cdot e^{\left(-\frac{E_i}{RT}\right)} \tag{B.24}$$

To express the rate in terms of $mol \cdot mol^{-1}_{NM} \cdot s^{-1}$, r''_i is divided by L_A. Equation B.23 can be substituted in as well.

$$r'_i = \frac{r''_i}{L_A} \tag{B.25}$$

$$= \frac{k_i}{L_A} \cdot L_A^2 \cdot \theta_{CO} \cdot \theta_O \tag{B.26}$$

$$= k_i \cdot L_A \cdot \theta_{CO} \cdot \theta_O \tag{B.27}$$

A_0 can be substituted in, and the equation may be solved using the parameters in Table B.2.

$$
\begin{aligned}
r_i' &= k_i \cdot L_A \cdot \theta_{CO} \cdot \theta_O && \text{(B.28)}\\
&= A_{0,i} \cdot L_A \cdot \theta_{CO} \cdot \theta_O \cdot e^{\left(-\frac{E_i}{RT}\right)} && \text{(B.29)}\\
&= \left(3.7 \times 10^{16}\ mol \cdot m_{NM}^{2} \cdot mol_{NM}^{-2} \cdot s^{-1}\right)\\
&\quad \times \left(2.72 \times 10^{-5}\ mol_{NM} \cdot m_{NM}^{-2}\right) \cdot (0.19) \cdot (0.80)\\
&\quad \times e^{\left(-\frac{\left(108.0 - 33.0 \times 0.19 + 90.0 \times 0\ kJ \cdot mol^{-1}\right) \times \frac{1000\ J}{1\ kJ}}{8.314\ J \cdot mol^{-1} \cdot K^{-1} \times 500\ K}\right)} && \text{(B.30)}\\
&= \mathbf{3.60\ mol \cdot mol_{NM}^{-1} \cdot s^{-1}} && \text{(B.31)}
\end{aligned}
$$

$$
\begin{aligned}
r_i &= r_i' \times a && \text{(B.32)}\\
&= 3.60\ mol \cdot mol_{NM}^{-1} \cdot s^{-1} \times 2.0 m_{NM}^{2}\ m_{cat}^{-3} && \text{(B.33)}\\
&= \mathbf{7.20\ mol \cdot mol_{NM}^{-1} \cdot s^{-1} \cdot m_{NM}^{2}\ m_{cat}^{-3}} && \text{(B.34)}
\end{aligned}
$$

The value used for A in the simulator input files is the value $A_{0,i} \times L_A$, or:

$$
\begin{aligned}
A_{sim} &= A_{0,i} \times L_A && \text{(B.35)}\\
&= 3.7 \times 10^{16}\ mol \cdot m_{NM}^{2} \cdot mol_{NM}^{-2} \cdot s^{-1} \times 2.72 \times 10^{-5}\ mol_{NM} \cdot m_{NM}^{-2} && \text{(B.36)}\\
&= 1.006 \times 10^{12} mol \cdot mol_{NM}^{-1} \cdot s^{-1} && \text{(B.37)}
\end{aligned}
$$

B.4 Unimolecular Surface Reaction Rate - Example

As the procedure is slightly different when only a single site is concerned (for example, in desorption), a second example is included here showing the calculated rate of desorption of CO_2. The parameters required for the calculation are shown in Table B.3.

Using Equation B.13 and the values in Table B.2, the reaction for $CO2_2$ desorption Equation 3.7a may be calculated:

A_0	pre-exponential factor	1.00×10^{13}	$\text{mol} \cdot \text{mol}_{NM}^{-1} \cdot \text{s}^{-1}$	[66]
θ_{CO_2}	surface coverage of CO_2	4.45×10^{-10}	dimensionless fraction	a
μ	reaction order correction	1	dimensionless	a
E_A	activation energy	27.1	$\text{kJ} \cdot \text{mol}^{-1}$	[66]
R	Ideal Gas Constant	8.314	$\text{J} \cdot \text{mol}^{-1} \cdot \text{K}^{-1}$	
T	Temperature	500	K	a
β	Temperature Exponent	0	dimensionless	a
a	site Concentration	2.0	$\text{m}_{NM}^{2}\ \text{m}_{cat}^{-3}$	a

---

[a] Typical Value

Table B.3: Parameters used for a sample calculation for a surface reaction. Coverages are from a typical light-off (1000 ppm CO and 500 ppm H_2), at the reactor inlet, and after ignition has occurred (T = 500 K).

Remembering the relation between C and θ (Equation B.10), we can subsitute into Equation B.11. Note that the exponent over L_A differs between Equation B.18 and Equation B.38.

$$\begin{aligned} r_i'' &= k_i C_{A_1}^{a_1} C_{A_2}^{a_2} && \text{(B.38)} \\ &= k_i \cdot (L_A \theta_{CO_2})^1 && \text{(B.39)} \\ &= k_i \cdot L_A \cdot \theta_{CO_2} && \text{(B.40)} \end{aligned}$$

k_i is taken from Equation B.13, and simplified as above (Equation B.21 and Equation B.23).

To express the rate in terms of $\text{mol} \cdot \text{mol}_{NM}^{-1} \cdot \text{s}^{-1}$, r_i'' from Equation B.38 is divided by L_A. k_i can be substituted in as well.

$$\begin{aligned} r_i' &= \frac{r_i''}{L_A} && \text{(B.41)} \\ &= \frac{k_i}{L_A} \cdot L_A \cdot \theta_{CO_2} && \text{(B.42)} \\ &= k_i \theta_{CO_2} && \text{(B.43)} \end{aligned}$$

A_0 can be substituted in, and the equation may be solved using the parameters in Table B.3.

$$\begin{aligned}
r_i^{'} &= k_i \theta_{CO_2} && \text{(B.44)}\\
&= A_{0,i} \cdot e^{\left(-\frac{E_i}{RT}\right)} \cdot \theta_{CO_2} && \text{(B.45)}\\
&= \left(1.00 \times 10^{13}\ mol \cdot mol_{NM}^{-1} \cdot s^{-1}\right)\\
&\quad \times e^{\left(-\frac{\left(27.1\ kJ \cdot mol^{-1}\right) \times \frac{1000\ J}{1\ kJ}}{8.314\ J \cdot mol^{-1} \cdot K^{-1} \times 500\ K}\right)}\\
&\quad \times \left(4.45 \times 10^{-10}\right) && \text{(B.46)}\\
&= \mathbf{6.56\ mol \cdot mol_{NM}^{-1} \cdot s^{-1}} && \text{(B.47)}
\end{aligned}$$

$$\begin{aligned}
r_i &= r_i^{'} \times a && \text{(B.48)}\\
&= 6.56\ mol \cdot mol_{NM}^{-1} \cdot s^{-1} \times 2\ m_{NM}^2\ m_{cat}^{-3} && \text{(B.49)}\\
&= \mathbf{13.13\ mol \cdot mol_{NM}^{-1} \cdot s^{-1} \cdot m_{NM}^2\ m_{cat}^{-3}} && \text{(B.50)}
\end{aligned}$$

As above, the equation for calculating the rate for an adsorption step in the Vlachos scheme Equation B.51 is similar to the analogous DETCHEM equation (Equation B.14), with similar exceptions.

B.5 Sticking Coefficients

Not every particle that strikes a catalyst surface will bind. The probability that this particle will bind to the surface is described as the sticking coefficient [272]. The rate of adsorption is dependent upon the probability of adsorption (sticking coefficient), temperature, particle molar mass, and active site concentration. The method used to calculate the rate of adsorption is given in section B.6.

Mhadeshwar and Vlachos [229, 230] use Equation B.51 to calculate the rate of adsorption.

$$k_i^{"} = \frac{S_0}{L_t^n} \sqrt{\frac{RT}{2\pi M_i}} \left(\frac{T}{T_0}\right)^{\beta_i} \cdot e^{\left(-\frac{E_i}{RT}\right)} \tag{B.51}$$

The temperature dependence term $\left(\left(\frac{T}{T_0}\right)^{\beta_i} \cdot e^{\left(-\frac{E_i}{RT}\right)}\right)$ is explicitly stated here, whereas the DETCHEM equation did not include it. The temperature dependence term is not used in the present work.

B.6 Unimolecular Adsorption Rate Example

When sticking coefficients are involved, the equation for calculating the rate coefficient is given by Chatterjee et al. [66] and is shown in Equation B.52.

$$k_k = S_i^0 \frac{1}{L_t^\tau} \sqrt{\frac{RT}{2\pi M_i}} \tag{B.52}$$

omenclature[gt]τoccupied adsorption sites of species

The full procedure for calculating the rate for a species adsorbing to the surface is shown in the following example.

The rate constant is calculated with Equation B.53:

$$k_k = \frac{S_i^0}{\Gamma} C_i \theta_* \sqrt{\frac{RT}{2\pi M_i}} \tag{B.53}$$

When the gas is assumed to be an ideal gas (which is a valid assumption, as N_2 comprises the majority of the gas, with the components of interest, such as CO and H_2, comprising on the order of 0.1%), the concentration of the component in the gas may be calculated as follows:

$$C_i = \frac{P}{R \cdot T} x_i \tag{B.54}$$

Where x_i is the molar fraction of the gas component. P must be in units of Pa, and a value 101325 Pa is typical. T is the gas temperature, and has units of K. R is the ideal gas constant, with a value of 8.314 $m^3\ Pa\ mol^{-1}\ K^{-1}$. Hence, the units for C_i are $mol\ m^{-3}$.

θ_* is the dimensionless fraction of free sites that are available. The full equation is now as shown in Equation B.55.

$$rate_k = \frac{S_i^0}{\Gamma} \frac{P}{R \cdot T} x_i \theta_* \sqrt{\frac{R \cdot T}{2\pi M_i}} \tag{B.55}$$

R	=	8.314	$J\ mol^{-1}\ K^{-1}$
	=	8.314	$m^3\ Pa\ mol^{-1}\ K^{-1}$
	=	8.314	$kg\ m^2\ s^{-2}\ mol^{-1}\ K^{-1}$
	=	8314	$g\ m^2\ s^{-2}\ mol^{-1}\ K^{-1}$

Table B.4: Ideal Gas Constant In Various Units

S_0	=	0.84		from Table 3.2 and [66]
Gamma	=	2.72×10^{-5}	$mol_{NM}\ m_{NM}^{-2}$	from Table 3.2 and [66]
P	=	101325	Pa	[a]
T	=	500	K	[a]
x_{CO}	=	0.001		[a]
θ_*	=	0.00272		[a]
M_{CO}	=	28	$g\ mol^{-1}$	
R	=	8.314	$m^3\ Pa\ mol^{-1}\ K^{-1}$	
R	=	8314	$g\ m^2\ s^{-2}\ mol^{-1}\ K^{-1}$	
a	=	2.0	$m_{NM}^{2}\ \ m_{cat}^{-3}$	

[a] Typical Value

Table B.5: Parameters used for Sample Adsorption Problem

When determining the units for the square root term, it is important to cast the ideal gas constant[268] in different units, as shown in Table B.4.

As an example, the rate of adsorption may be calculated for CO. In this case, the values and units used are shown in Table B.5.

These values can be placed into Equation B.55.

$$rate = \frac{S_i^0}{\Gamma}\frac{P}{R \cdot T}x_i\theta_*\sqrt{\frac{R \cdot T}{2\pi M_i}} \tag{B.56}$$

$$= \frac{0.84}{2.72 \times 10^{-5}\ mol_{NM}\ m_{NM}^{-2}} \times \frac{101325\ Pa}{8.314\ m^3\ Pa\ mol^{-1}\ K^{-1} \cdot 500\ K}$$

$$\times(0.001) \times (0.00272)\sqrt{\frac{8314\ g\ m^2\ s^{-2}\ mol^{-1}\ K^{-1} \cdot 500\ K}{2\pi \cdot 28\ g\ mol^{-1}}} \tag{B.57}$$

$$= \mathbf{315\ mol\ mol_{NM}^{-1}\ s^{-1}} \tag{B.58}$$

Using the a value and the Pt loading factor, we then obtain a final value for the rate of equation:

S_0	=	0.07		from Table 3.2 and [66]
Gamma	=	2.72×10^{-5}	mol_{NM} m_{NM}^{-2}	from Table 3.2 and [66]
P	=	101325	Pa	[a]
T	=	500	K	[a]
x_{O_2}	=	0.06		[a]
θ_*	=	0.00272		[a]
M_{O_2}	=	32	g mol^{-1}	
R	=	8.314	m^3 Pa mol^{-1} K^{-1}	
R	=	8314	g m^2 s^{-2} mol^{-1} K^{-1}	
a	=	2.0	m_{NM}^{2} m_{cat}^{-3}	

---

[a] Typical Value

Table B.6: Parameters used for Sample Adsorption Problem 2

$$rate = 315\ mol\ mol_{NM}^{-1}\ s^{-1} \times 2.0\ m_{NM}^{2}\ m_{cat}^{-3} \qquad (B.59)$$

$$= \mathbf{630\ mol\ m_{cat}^{-3}\ s^{-1}\ m_{NM}^{2}\ m_{cat}^{-3}} \qquad (B.60)$$

B.7 Bimolecular Adsorption Rate Example

When a compound adsorbs to the catalyst surface in a dissociative manner, the procedure is slightly modified.

The rate constant is calculated with Equation B.61, considering two adsorption sites:

$$k_k = 2 \cdot \frac{S_i^0}{gamma} C_i \theta_*^2 \sqrt{\frac{RT}{2\pi M_i}} \qquad (B.61)$$

C is treated as above in Equation B.54.

θ_* is the dimensionless fraction of free sites that are available. As two sites are used, this is to the second power. The full equation is now as shown in Equation B.62.

$$rate_k = 2 \cdot \frac{S_i^0}{\Gamma} \frac{P}{R \cdot T} x_i \theta_*^2 \sqrt{\frac{R \cdot T}{2\pi M_i}} \qquad (B.62)$$

The square root term is treated as before.

As an example, the rate of adsorption may be calculated for O_2. In this case, the values and units used are shown in Table B.6.

These values can be placed into Equation B.62

$$\begin{aligned} rate &= \frac{S_i^0}{\Gamma}\frac{P}{R \cdot T} x_i \theta_* \sqrt{\frac{R \cdot T}{2\pi M_i}} && \text{(B.63)} \\ &= \frac{0.07}{2.72 \times 10^{-5}\ mol_{NM}\ m_{NM}^{-2}} \times \frac{101325\ Pa}{8.314\ m^3\ Pa\ mol^{-1}\ K^{-1} \cdot 500\ K} \\ &\quad \times (0.06) \times (0.00272)^2 \sqrt{\frac{8314\ g\ m^2\ s^{-2}\ mol^{-1}\ K^{-1} \cdot 500\ K}{2\pi \cdot 32\ g\ mol^{-1}}} && \text{(B.64)} \\ &= \mathbf{4.00\ mol\ mol_{NM}^{-1}\ s^{-1}} && \text{(B.65)} \end{aligned}$$

Using the a value and the Pt loading factor, we then obtain a final value for the rate of reaction:

$$\begin{aligned} rate &= 4.00\ mol\ mol_{NM}^{-1}\ s^{-1} \times 2.0\ m_{NM}^{2}\ m_{cat}^{-3} && \text{(B.66)} \\ &= \mathbf{8.01\ mol\ mol_{NM}^{-1}\ s^{-1}\ m_{NM}^{2}\ m_{cat}^{-3}} && \text{(B.67)} \end{aligned}$$

Due to the stoichiometry, the rate of formation of adsorbed oxygen (O^*) is twice the rate of consumption of gaseous oxygen ($O_{2(g)}$).

C

Reaction Mechanisms

C.1 Classical LHHW-Type Model

Voltz et al. [40] proposed a model to describe CO oxidation in the presence of oxygen, propylene and NO. This model was based on experimental observations of a pelleted Pt-alumina catalyst using a synthetic gas mixture and a varied inlet temperature.

The original model included inhibition effects of propylene and NO. As these components are not used in the present work, these effects have been removed. This model uses a global reaction scheme, lumping parameters together and assuming that the rate-determining step is the reaction between CO and oxygen. This model does not consider surface effects, nor does it consider the catalyst history.

C.1.1 CO Oxidation

The overall reaction for the oxidation of CO can be written as shown in Equation C.1:

$$CO + \frac{1}{2}O_2 \rightleftharpoons CO_2 \tag{C.1}$$

Equation C.2 was proposed as the rate of reaction, where G1 is an inhibition term (defined in Equation C.3).

$$r_{V,CO} = \frac{k_{V,1} \cdot X_{g,CO} \cdot X_{g,O_2}}{G1} \tag{C.2}$$

Equation	Parameter	Value	Units
3.2	$A_{V,1}$	1×10^{16}	$mol_{CO}\ mol_{cat}^{-1}\ s^{-1}$
	$Ea_{V,1}$	9000	$kJ\ mol^{-1}$
	K_{a1}	65.5	$m^3\ mol^{-1}$

Table C.1: Voltz Model Parameters

$$\begin{aligned} G1 &= T\cdot(1+K_{a1}\cdot X_{g,CO}+K_{a2}\cdot X_{g,C3H6})^2 \\ &\cdot\left(1+K_{a3}\cdot X_{g,CO}^2\cdot X_{g,C3H6}^2\right) \\ &\cdot\left(1+K_{a4}\cdot X_{g,NO}^{0.7}\right) \end{aligned} \tag{C.3}$$

As NO and C_3H_6 are not used in the present work, Equation C.3 simplifies to Equation C.4.

$$G1 = T\cdot(1+K_{a1}\cdot X_{g,CO})^2 \tag{C.4}$$

The rate of CO consumption may be calculated using Equation C.5 and the parameters in Table C.1.

$$r_{V,CO} = \frac{A_{V,1}\cdot e^{\left(-Ea_{V,1}/RT\right)}\cdot X_{g,CO}\cdot X_{g,O_2}}{T\cdot(1+K_{a1}\cdot X_{g,CO})^2} \tag{C.5}$$

C.2 Mechanistic Model Based on Langmuir-Hinschelwood Assumptions

Models that attempt to account for each elementary step in the oxidation reaction have recently been presented in the literature. Chatterjee et al. presented a fully-reversible mechanism in the literature [66]. This mechanism considers CO, O_2, H_2, H_2O, C_3H_6 and other hydrocarbons. Rate parameters are derived from literature sources and thermodynamic data. The method for calculating the rate coefficients is presented in section B.2.

Other groups [88] have also published similar models, however the Chatterjee et al model is most familiar to the automotive catalysis community, and is one of the most studied. The Chatterjee et al. implementation is the implementation discussed the most in this work.

C.2.1 CO Oxidation

Before any surface reaction may take place, the respective components must first adsorb to the surface. Oxygen is considered to adsorb in a dissociative manner, as shown in Equation 3.6a. The rate equation for the chemical step (Equation 3.6a) is shown immediately below (Equation 3.6b).

$$O_2 + 2^* \underset{k^f_{cLH,8}}{\overset{k^f_{cLH,1}}{\rightleftharpoons}} 2O^* \tag{C.6a}$$

$$r_{cLH,1} = k^f_{cLH,1} C_{O_2} \theta_*^2 - k^f_{cLH,8} \theta_{O^*}^2 \tag{C.6b}$$

Although in this case oxygen adsorption is modelled as reversible, it is considered by many to be irreversible below 700 K [89, 90].

CO_2 may easily adsorb to or desorb from the surface.

$$CO_2 +^* \underset{k^f_{cLH,14}}{\overset{k^f_{cLH,6}}{\rightleftharpoons}} CO_2^* \tag{C.7a}$$

$$r_{cLH,6} = k^f_{cLH,6} C_{CO_2} \theta_* - k^f_{cLH,14} \theta_{CO_2^*} \tag{C.7b}$$

The general consensus in the literature is that CO_2 desorption is practically instantaneous after the surface reaction. However, Han et al. [91] claim to have discovered a CO_2 intermediate species that is stable up to 300 K. They state a desorption activation energy of 46±3 kJ mol^{-1}, compared to an activation energy of 75±4 kJ mol^{-1} for the direct formation of gaseous CO_2 from adsorbed CO and O. This intermediate species is not considered to be significant in the present work, as the temperatures considered here are above 300 K.

CO adsorption is fully reversible.

$$CO +^* \underset{k^f_{cLH,13}}{\overset{k^f_{cLH,7}}{\rightleftharpoons}} CO^* \tag{C.8a}$$

$$r_{cLH,7} = k^f_{cLH,7} C_{CO} \theta_* - k^f_{cLH,13} \theta_{CO^*} \tag{C.8b}$$

The surface reaction between adsorbed CO and O is:

$$CO^* + O^* \underset{k^f_{cLH,45}}{\overset{k^f_{cLH,44}}{\rightleftharpoons}} CO_2^* + {}^* \tag{C.9a}$$

$$r_{cLH,44} = k^f_{cLH,44}\theta_{CO_2^*} - k^f_{cLH,45}\theta_{CO_2^*}\theta_* \tag{C.9b}$$

If there is any carbon present on the catalyst surface, that carbon may also oxidize.

$$C^* + O^* \underset{k^f_{cLH,47}}{\overset{k^f_{cLH,46}}{\rightleftharpoons}} CO^* + {}^* \tag{C.10a}$$

$$r_{cLH,46} = k^f_{cLH,46}\theta_{C^*}\theta_{O^*} - k^f_{cLH,47}\theta_{CO^*}\theta_* \tag{C.10b}$$

The rate parameters proposed by Chatterjee et al. are given in Table C.2. Other parameter values have been reported [92, 93]. For example, Kasemo and Törnqvist [89] reported sticking coefficients of 0.62, 0.54 and 0.38 for hydrogen, CO and oxygen respectively.

C.2.2 H_2 and H_2O Adsorption and Desorption

The oxidation of hydrogen on platinum proceeds in a similar manner as that of CO, whereby the components all adsorb to the surface, react, and subsequently desorb. Oxidation of hydrogen on a Pt surface has been known to proceed at temperatures as low as 120 K [94], and when the surface is oxygen covered, the reaction is limited by the rate of adsorption of hydrogen [95].

$$H_2 + {}^* + {}^* \underset{k^f_{11}}{\overset{k^f_4}{\rightleftharpoons}} H^* + H^* \tag{C.11a}$$

$$r_4 = k^f_4 C_{H_2}\theta_*^2 - k^f_{11}\theta^2_{H^*} \tag{C.11b}$$

$$H_2O + {}^* \underset{k^f_{12}}{\overset{k^f_5}{\rightleftharpoons}} H_2O^* \tag{C.12a}$$

$$r_5 = k^f_5 C_{H_2O}\theta_* - k^f_{12}\theta_{H_2O^*} \tag{C.12b}$$

Equation	Parameter	Value	Units [a]	Source
C.6b	$k^{f}_{cLH,1}$			[66]
	S_0	0.07	unitless	
	γ	2.72×10^{-5}	$\text{mol}_{NM}\ \text{m}^{-2}_{NM}$	
	$k^{f}_{cLH,8}$			
	A_0	1.006×10^{13}	mol cm^{-1} s	
	E_A	232.2	kJ mol^{-1}	
	$\frac{dE_A}{d\theta_O}$	90	kJ mol^{-1}	
C.7b	$k^{f}_{cLH,6}$			[66]
	S_0	0.005	unitless	
	γ	2.72×10^{-5}	$\text{mol}_{NM}\ \text{m}^{-2}_{NM}$	
	$k^{f}_{cLH,14}$			
	A_0	1×10^{13}	mol cm^{-1} s	
	E_A	27.1	kJ mol^{-1}	
C.8b	$k^{f}_{cLH,6}$			[66]
	S_0	0.84	unitless	
	γ	2.72×10^{-5}	$\text{mol}_{NM}\ \text{m}^{-2}_{NM}$	
	k^{f}_{14}			
	A_0	1×10^{13}	mol cm^{-1} s	
	E_A	126.4 [c]	kJ mol^{-1}	
	$\frac{dE_A}{d\theta_{CO}}$	33	kJ mol^{-1}	
C.9b	$k^{f}_{cLH,44}$			[66]
	A_0	1.006×10^{12}	mol cm^{-1} s	
	E_A	108	kJ mol^{-1}	
	$\frac{dE_A}{d\theta_{CO}}$	33	kJ mol^{-1}	
	$\frac{dE_A}{d\theta_{NO}}$	-90	kJ mol^{-1}	
	k^{f}_{45}			
	A_0	1.006×10^{13}	mol cm^{-1} s	
	E_A	165.1	kJ mol^{-1}	
	$\frac{dE_A}{d\theta_O}$	-45	kJ mol^{-1}	
C.47b	$k^{f}_{cLH,46}$			[66]
	A_0	1.006×10^{12}	mol cm^{-1} s	
	E_A	0	kJ mol^{-1}	
	$\frac{dE_A}{d\theta_{CO}}$	-33	kJ mol^{-1}	
	k^{f}_{47}			
	A_0	1.006×10^{13}	mol cm^{-1} s	
	E_A	218.5	kJ mol^{-1}	
	$\frac{dE_A}{d\theta_O}$	-45	kJ mol^{-1}	

---

[a] units converted from literature source. For example, 3.70×10^{21} mol cm s $\times$ 2.72×10^{-9} mol cm^{-2} = 1.006×10^{13} mol s cm^{-2}. In the original literature source, surface site density $\Gamma = 2.72\times 10^{-9}\ \text{mol}_{NM}\ \text{cm}^{-2}_{NM}$.

[c] Literature values for activation energy for CO desorption vary as shown in Table 4.1. All these equations do have general agreement that the activation energy is 104 kJ mol^{-1} on a CO saturated surface.

Table C.2: LH Mechanism Parameters for CO Oxidation

C.2.3 H_2 and H_2O Reactions

The surface reactions involving adsorbed hydrogen are given as:

$$H^* + O^* \underset{k^f_{39}}{\overset{k^f_{38}}{\rightleftharpoons}} OH^* + ^* \tag{C.13a}$$

$$r_{38} = k^f_{38}\theta_{H^*}\theta_{O^*} - k^f_{39}\theta_{OH^*}\theta_{^*} \tag{C.13b}$$

$$H^* + OH^* \underset{k^f_{41}}{\overset{k^f_{40}}{\rightleftharpoons}} H_2O^* + ^* \tag{C.14a}$$

$$r_{40} = k^f_{40}\theta_{H^*}\theta_{OH^*} - k^f_{41}\theta_{H_2O^*}\theta_{^*} \tag{C.14b}$$

$$OH^* + OH^* \underset{k^f_{43}}{\overset{k^f_{42}}{\rightleftharpoons}} H_2O^* + O^* \tag{C.15a}$$

$$r_{42} = k^f_{42}\theta^2_{OH^*} - k^f_{43}\theta_{H_2O^*}\theta_{O^*} \tag{C.15b}$$

C.3 Langmuir-Hinschelwood plus Eley-Rideal Model

This model, proposed by Nibbelke et al. [96], also uses elementary kinetics as a foundation. Here, a LH mechanism has an additional Eley-Rideal step. Gas-phase carbon monoxide can react with adsorbed oxygen to form carbon dioxide. While many in the literature argue that the Eley-Rideal step does not occur, a mechanism for reacting gas phase carbon monoxide on a surface fully covered by oxygen is critical to explaining some behaviour. The Eley-Rideal step is one means of providing this step. There is discussion in the literature about the Eley-Rideal step, with several groups suggesting that it does not occur on a platinum oxidation catalyst, and others suggesting that there is such a step [97].

C.3.1 CO Oxidation

In this model, CO adsobs to the surface in a single step. Oxygen adsorbs to the surface, and then splits to form two separate adsorbed oxygen atoms. Both adsobed and gas-phase

Equation	Parameter	Value	Units [a]	Source
C.11b	$k^J_{cLH,A}$			[66]
	S_0	0.046	unitless	
	γ	2.72e-5	$\mathrm{mol}_{NM}\ \mathrm{m}^{-2}_{NM}$	
	$k^J_{cLH,11}$			
	A_0	1.006E+13	mol s cm^{-1}	
	E_A	67.4	kJ mol^{-1}	
	$\frac{dE_A}{d\theta_H}$	6.0	kJ mol^{-1}	
C.12b	$k^J_{cLH,5}$			[66]
	S_0	0.75	unitless	
	γ	2.72e-5	$\mathrm{mol}_{NM}\ \mathrm{m}^{-2}_{NM}$	
	$k^J_{cLH,12}$			
	A_0	1.00E+13	mol s cm^{-1}	
	E_A	40.3	kJ mol^{-1}	
C.13b	$k^J_{cLH,38}$			[66]
	A_0	1.006E+13	mol s cm^{-1}	
	E_A	11.5	kJ mol^{-1}	
	$k^J_{cLH,39}$			
	A_0	1.569E+14	mol s cm^{-1}	
	E_A	74.9	kJ mol^{-1}	
C.14b	$k^J_{cLH,40}$			[66]
	A_0	1.006E+13	mol s cm^{-1}	
	E_A	17.4	kJ mol^{-1}	
	$k^J_{cLH,41}$			
	A_0	9.955E+12	mol s cm^{-1}	
	E_A	73.6	kJ mol^{-1}	
C.15b	$k^J_{cLH,42}$			[66]
	A_0	1.006E+13	mol s cm^{-1}	
	E_A	48.2	kJ mol^{-1}	
	$k^J_{cLH,43}$			
	A_0	6.392E+11	mol s cm^{-1}	
	E_A	41.0	kJ mol^{-1}	

---

[a] units converted from literature source. For example, 3.70×10^{21} mol cm s $\times$ 2.72×10^{-9} mol cm^{-2} = 1.006×10^{13} mol s cm^{-1}. In the original literature source, surface site density $\Gamma = 2.72\times 10^{-9}$ mol cm^{-2}.

Table C.3: LH Mechanism Parameters for H_2 Oxidation

CO are allowed to react with adsobed oxygen

$$CO + * \underset{k_1^b}{\overset{k_1^f}{\rightleftharpoons}} CO^* \tag{C.16a}$$

$$r_1 = k_1^f C_{CO} \theta_* - k_1^b \theta_{CO^*} \tag{C.16b}$$

Oxygen adsorbs and subsequently dissociates.

$$O_2 + * \xrightarrow{k_2^f} O_2^* \tag{C.17a}$$

$$r_{2/3} = k_2^f C_{O_2} \theta_* \tag{C.17b}$$

$$O_2 * + * \xrightarrow{k_2^f} 2O^* \tag{C.18a}$$

$$r_{2/3} = k_2^f C_{O_2} \theta_* \tag{C.18b}$$

The oxidation reaction may occur wither either both CO and oxygen adsorbed to the surface, or with only oxygen adsorbed. The product of oxidation, CO_2, quickly desorbs.

$$CO^* + O^* \xrightarrow{k_4^f} CO_2 + 2* \tag{C.19a}$$

$$r_4 = k_4^f \theta_{CO^*} \theta_{O^*} \tag{C.19b}$$

$$CO + O^* \underset{k_5^b}{\overset{k_5^f}{\rightleftharpoons}} OCO^* \tag{C.20a}$$

$$r_5 = k_5^f C_{CO^*} \theta_O - k_5^b \theta_{OCO^*} \tag{C.20b}$$

$$\mathrm{OCO}^* \xrightarrow{k_6^f} \mathrm{CO}_2 + * \tag{C.21a}$$

$$r_6 = k_6^f \theta_{OCO^*} \tag{C.21b}$$

$$\mathrm{O}_2 + \mathrm{s} \xrightarrow{k_7^f} \mathrm{O}_2\mathrm{s} \tag{C.22a}$$

$$r_{7/8} = k_7^f C_{O_2} \xi_S \tag{C.22b}$$

$$\mathrm{O}_2\mathrm{s} + \mathrm{s} \xrightarrow{k_8^f} 2\mathrm{Os} \tag{C.23a}$$

$$r_{7/8} = k_8^f C_{O_2} \xi_S \tag{C.23b}$$

$$\mathrm{CO}^* + \mathrm{Os} \xrightarrow{k_9^f} \mathrm{CO}_2 + \mathrm{s} + * \tag{C.24a}$$

$$r_9 = k_9^f C_{CO^*} \xi_O \tag{C.24b}$$

$$\mathrm{CO}_2 + \gamma \underset{k_{10}^b}{\overset{k_{10}^f}{\rightleftharpoons}} \mathrm{CO}_2\gamma \tag{C.25a}$$

$$r_{10} = k_{10}^f C_{CO_2} \delta_\gamma - k_{10}^b \delta_{CO_2} \tag{C.25b}$$

Equation	Parameter	Value	Units	Source
C.16b	A_1^f	9×10^5	m^3 mol^{-1} s^{-1}	[98, 99]
	A_1^b	5.65×10^{14}	s^{-1}	
	E_1^b	113	kJ mol^{-1}	
	$\frac{dE_A}{d\theta_{CO}}$	-8.5	kJ mol^{-1}	
C.16b	Alternative Value			[100] [a]
	A_1^b	8.16×10^9	s^{-1}	
	E_1^b	86.5	kJ mol^{-1}	
	$\frac{dE_A}{d\theta_{CO}}$	4.15	kJ mol^{-1}	
C.17b	A_2^f	1×10^5	m^3 mol^{-1} s^{-1}	[98, 99]
C.18b	A_3^f	1×10^5	m^3 mol^{-1} s^{-1}	[98, 99]
C.19b	A_4^f	2.81×10^{13}	s^{-1}	[99]
	E_1^b	96.8	kJ mol^{-1}	
C.20b	A_5^f	4.6×10^3	m^3 mol^{-1} s^{-1}	[98, 99]
	E_5^f	0.0	kJ mol^{-1}	
	A_5^b	248	s^{-1}	
	E_5^b	20.3	kJ mol^{-1}	
C.21b	A_6^f	20.5	s^{-1}	[98, 99]
	E_6^f	12.1	kJ mol^{-1}	

---

[a] page 131, Table 6.5 [100]

Table C.4: LH+ER Mechanism Parameters for CO Oxidation

C.4 Strong and Weakly Adsorbed Oxygen Mechanism

[137, 97, 103, 205, 273, 154, 155]

$$\mathrm{CO} +^{*} \underset{k^{b}_{Bou,S1}}{\overset{k^{f}_{Bou,S1}}{\rightleftharpoons}} \mathrm{L} \tag{C.26a}$$

$$r_{Bou,S1} = k^{f}_{Bou,S1} C_{CO} \theta_{*} - k^{b}_{Bou,S1} \theta_{L} \tag{C.26b}$$

$$\mathrm{O}_2 + 2^{*} \underset{k^{b}_{Bou,S2}}{\overset{k^{f}_{Bou,S2}}{\rightleftharpoons}} 2\mathrm{O}^{*} \tag{C.27a}$$

$$r_{Bou,S2} = k^{f}_{Bou,S2} C_{O_2} \theta_{*}^{2} - k^{b}_{Bou,S2} \theta_{O^{*}} \tag{C.27b}$$

$$\mathrm{L} + \mathrm{O}^{*} \overset{k^{f}_{Bou,S3}}{\rightarrow} \mathrm{CO}_2^{*} \tag{C.28a}$$

$$r_{Bou,S3} = k^{f}_{Bou,S3} \theta_{O^{*}} \theta_{L} \tag{C.28b}$$

$$\mathrm{CO}_2^{*} \overset{k^{f}_{Bou,S4}}{\rightarrow} \mathrm{CO}_2 +^{*} \tag{C.29a}$$

$$r_{Bou,S4} = k^{f}_{Bou,S4} \theta_{CO_2^{*}} \tag{C.29b}$$

Desorption of carbon dioxide is considered to be very fast. [97]

C.5 Multiple Binding Sites: A and B-Type Sites

The AB model is essentially a LH mechanism, but in a system with two slightly different types of surface sites. This model is predicated on the assumption of two different surface sites (type A and B), each with different activities for the respective components. The sites are assumed to be equally dispersed throughout the catalyst, and adsorbed species on one site can react with adsorbed species on the other. Of special note, one type of site is much more active towards oxygen adsorption than the other. This mechanim was studied using laminar flow on Pt foil at low pressures [199, 274]. Nett-Carrington and Herz [136] used a bimodal distribution of surface sites to model the reactions on a catalyst pellet, reporting that the surface reaction step was rate-limiting.

$$O_2 + 2^* \quad \underset{k_{AB,2}}{\overset{k_{AB,1}}{\rightleftharpoons}} \quad 2O^* \tag{C.30a}$$

$$r_{AB,} = k_{AB,1} C_{O_2} \theta_*^2 - k_{AB,2} \theta_{O^* 2} \tag{C.30b}$$

Oxygen adsorption is considered to be irreversible below 700 K [89, 90] (also see 4.1.6).

$$CO +^* \quad \underset{k_{AB,4}}{\overset{k_{AB,3}}{\rightleftharpoons}} \quad CO^* \tag{C.31a}$$

$$r_{AB,3} = k_{AB,3} C_{CO} \theta_* - k_{AB,4} \theta_{CO^*} \tag{C.31b}$$

$$CO^* + O^* \quad \xrightarrow{k_{AB,5}} \quad CO_2 + 2^* \tag{C.32a}$$

$$r_{AB,5} = k_{AB,5} \theta CO_* \theta O_* \tag{C.32b}$$

These reactions may occur on either type of site (either * or $\star$).

$$O_2 + 2^\star \quad \xrightarrow{k_{AB,6}} \quad 2O^\star \tag{C.33a}$$

$$r_{AB,6} = k_{AB,6} C_{O_2} \zeta_\star^2 \tag{C.33b}$$

Oxygen adsorption is considered to be irreversible below 700K [89, 90] (also see 4.1.6).

$$CO +^\star \quad \xrightarrow{k_{AB,7}} \quad CO^\star \tag{C.34a}$$

$$r_{AB,7} = k_{AB,7} C_{CO} \zeta_\star \tag{C.34b}$$

$$\mathrm{CO}^{\star} \xrightarrow{k_{AB,9}} \mathrm{CO}+^{\star} \tag{C.35a}$$

$$r_{AB,9} = k_{AB,9}\zeta_{CO^{\star}} \tag{C.35b}$$

$$\mathrm{CO}^{\star} + \mathrm{O}^{\star} \xrightarrow{k_{AB,10}} \mathrm{CO}_2 + \star + * \tag{C.36a}$$

$$r_{AB,10} = k_{AB,10}\zeta_{CO^{\star}}\theta_{O^{*}} \tag{C.36b}$$

$$\mathrm{CO}^{\star} + \mathrm{O}^{\star} \xrightarrow{k_{AB,10}} \mathrm{CO}_2 + 2\star \tag{C.36c}$$

$$r_{AB,10} = k_{AB,10}\zeta_{CO^{\star}}\zeta_{O^{\star}} \tag{C.36d}$$

$$\mathrm{CO}^{\star} + \mathrm{O}^{\star} \xrightarrow{k_{AB,10}} \mathrm{CO}_2 + * + \star \tag{C.36e}$$

$$r_{AB,10} = k_{AB,10}\theta_{CO^{*}}\zeta_{O^{\star}} \tag{C.36f}$$

Equation	Parameter	Value	Units	Source
A Sites				
C.30b	$k_{AB,1}$	O_2 ads		[199]
	S_0	0.05		
	γ	2.72×10^{-5}	$mol_{NM}\ m_{NM}^{-2}$	[66] *
C.30b	$k_{AB,2}$	O_2 des		[199, 66]
	v	3.7×10^{21}	s^{-1}	
	E_0	210.0	kJ mol^{-1}	
C.31b	$k_{AB,3}$	CO ads		[199]
	S_0	0.75		[199] †
	γ	2.72×10^{-5}	$mol_{NM}\ m_{NM}^{-2}$	[66]
C.31b	$k_{AB,4}$	CO des		[199]
	v	3.0×10^{19}	s^{-1}	
	E_0	183.0	kJ mol^{-1}	
	E_1	71.0	kJ mol^{-1}	
	$\frac{dE_{A,CO}}{dPt}$	112	kJ mol^{-1}	
C.32b	$k_{AB,5}$	CO_2 prod		[199]
	v	6.0×10^{19}	s^{-1}	‡
	E_0	90.0	kJ mol^{-1}	[199]
B Sites				
C.33b	$k_{AB,6}$	O_2 ads		[199]
	S_0	$\simeq 1$		
	γ	2.72×10^{-5}	$mol_{NM}\ m_{NM}^{-2}$	[66] §
C.34b	$k_{AB,7}$	CO ads		[199]
	S_0	0.75	in the absence of oxygen	
	$\frac{dE_{S_0,CO}}{d\theta_O}$	0.65		
C.35b	$k_{AB,9}$	CO des		[199]
	v	5.0×10^{21}	s^{-1}	
	E_0	220.0	kJ mol^{-1}	
	E_1	206.0	kJ mol^{-1}	
	$\frac{dE_A}{dO_{pt}}$	14	kJ mol^{-1}	
A and B Site Combinations				
C.36b	$k_{AB,10}$	CO_2 prod		[199]
	v	6.0×10^{21}	s^{-1}	
	E_0	105.0	kJ mol^{-1}	

Table C.5: Multiple Oxygen Sites - CO Oxidation

Equation	Parameter	Value	Units	Source
other constants are here				
C.37b	$k_6^{subsO,f}$			[190]
	$v^f_{subsO,6}$	282	s^{-1}	
	$E^f_{subsO,6}$	8.2	kcal mol^{-1}	
C.38b	$k_7^{subsO,f}$			[190]
	$v^f_{subsO,7}$	188	s^{-1}	
	$E^f_{subsO,7}$	8.2	kcal mol^{-1}	

Table C.6: Subsurface Oxygen Parameters - CO Oxidation

C.6 Subsurface Oxygen Sub-Mechanism

This sub-mechanism describes a means by which oxygen can be stored below the catalyst surface. Oertzen et al. state that subsurface oxygen's role in surface waves as providing temporary storage capacity [198, 190]. Oxygen can be temporarily stored below the surface, only to return to affect the propagation of reaction fronts on the surface.

$$O^* \xrightarrow{k^f_{subsO,6}} O^\dagger \tag{C.37a}$$

$$r_{subsO,6} = k^f_{subsO,6}\theta_{O^*} \tag{C.37b}$$

$$O^\dagger \xrightarrow{k^f_{subsO,7}} O^* \tag{C.38a}$$

$$r_{subsO,7} = k^f_{subsO,7}\theta_{O^\dagger} \tag{C.38b}$$

C.7 Compressed Oxygen Sub-Mechanism

This sub-mechanism describes a means by which islands of adsorbed oxygen are compressed due to slight repulsive forces between CO and O, and slight attractive forces between O adatoms. This has been observed before on Pd catalysts [275].

Compressed oxygen is not allowed to build up to excessive levels, and Equation C.42a allows compressed oxygen to reform back to typical adsorbed oxygen atoms.

$$CO + 2O^* \xrightarrow{k_1^f} CO^* + OO^* \tag{C.39a}$$

$$r_1 = k_1^f C_{CO} \theta_{O^*}^2 \tag{C.39b}$$

The adsorption of CO is the only step that can produced compressed oxygen (OO). Simply adsorbing more oxygen does not form the compressed oxygen species.

$$CO^* + O^* \xrightarrow{k_2^f} CO_2^* + 2^* \tag{C.40a}$$

$$r_2 = k_2^f \theta_{CO^*} \theta_{O^*} \tag{C.40b}$$

Equation C.40a is the same as the surface reaction shown in the classical LH mechanism in Equation Equation C.9a.

$$CO^* + OO^* \xrightarrow{k_3^f} CO_2 + O^* + ^* \tag{C.41a}$$

$$r_3 = k_3^f \theta_{CO^*} \theta_{OO^*} \tag{C.41b}$$

Equation C.41a is the surface reaction between compressed oxygen and adsorbed CO. A reasonable assumption is that this reaction proceeds at the same rate as the surface reaction between a typically adsorbed oxygen and CO. This assumption, however, does give the equation a good order-of-magnitude approximation.

$$OO^* + ^* \xrightarrow{k_4^f} 2O^* \tag{C.42a}$$

Equation	Parameter	Value	Units	Source
C.39b	k_1^f			
	A_1^f	1×10^9	mol cm^{-1} s	
	E_1^f	50	kJ mol^{-1}	
C.40b	k_2^f			[66]
	A_0	1.006×10^{12}	mol cm^{-1} s	
	E_A	108	kJ mol^{-1}	
	$\frac{dE_{A,CO}}{dPt}$	33	kJ mol^{-1}	
	$\frac{dE_{A,NO}}{dPt}$	-90	kJ mol^{-1}	
C.41b	k_3^f			
	A_3^f	1×10^{15}	mol cm^{-1} s	
	E_3^f	115	kJ mol^{-1}	
C.42b	k_4^f			
	A_3^f	1×10^{15}	mol cm^{-1} s	
	E_3^f	115	kJ mol^{-1}	

Table C.7: Compressed Oxygen Parameters - CO Oxidation

$$r_4 = k_4^f \theta_{OO^*} \theta_* \tag{C.42b}$$

This step allows the compressed oxygen to "dissociate" such that it occupies two separate sites instead of one. This step prevents excessive buildup of the compresed oxygen.

C.8 Vlachos Mechanism for H_2 + CO Oxidation

This is the mechanism presented by Vlachos and colleges [229, 253, 230, 144]. This mechanism uses a classical LH mechanism, but also considers the coupling reactions between CO and H_2 and H_2O, and also includes the COOH* and HCOO* intermediates.

C.8.1 Hydrogen Oxidation on Pt

$$H_2 + 2* \underset{k_{R2}}{\overset{k_{R1}}{\rightleftharpoons}} 2H^* \tag{C.43a}$$

$$r_{R1} = k_{R1} C_{H_2} \theta_*^2 - k_{R2} \theta_H^2 \tag{C.43b}$$

Equation	Parameter	Value	Units	Source
Equation C.43b	s_{R1}	0.129	unitless	[229, 230]
	$E_{a,R1}$	0	kJ mol^{-1}	
	k_{R2}	7.95×10^{12}	s^{-1}	
	$E_{a,R2}$	$93.1 - 10.7\frac{T}{T_{300K}} - 6\theta_H$	kJ mol^{-1}	

Table C.8: Vlachos Model Parameters

$$O_2 + 2* \underset{k_{R4}}{\overset{k_{R3}}{\rightleftharpoons}} 2O^* \tag{C.44a}$$

$$r_{Vl,3} = k_{R3} C_{O_2} \theta_*^2 - k_{R4} \theta_O^2 \tag{C.44b}$$

Equation	Parameter	Value	Units	Source
5.19	$k^f_{COH,1}$			[66]
	S_0	0.046	unitless	
	γ	2.72e-5	$\mathrm{mol}_{NM}\ \mathrm{m}_{NM}^{-2}$	
5.20	$k^f_{COH,2}$			[66]
	A_0	1.006E+13	mol s cm^{-1}	
	E_A	67.4	kJ mol^{-1}	
	$\frac{dE_A}{d\theta_H}$	6.0	kJ mol^{-1}	
3.11b	k^f_{14}			[66]
	A_0	1E+13	mol cm^{-1} s	
	E_A	126.4	kJ mol^{-1}	
	$\frac{dE_A}{d\theta_{CO}}$	33	kJ mol^{-1}	
	$\frac{dE_{A,CO-H}}{d\theta_{PtB-H}}$	10	kJ mol^{-1}	determined in subsection 5.9.4

Table C.9: CO-H Submechanism Parameters

C.9 CO-H

This sub-mechanism describes a means by which hydrogen in the gas phase may promote CO desorption [259, 260, 257, 233, 142], potentially increasing the availabilty of free sites. With the increase of free sites, oxygen has more opportunities to adsorb to the surface, potentially promoting CO oxidation and shifting the light-off curve to lower temperatures.

$$H_{2(g)} + 2\bullet \rightarrow 2H\bullet \tag{C.45}$$

Hydrogen adsorbs to a pseudo-site, PtB, represented by $\bullet$. This surface may also be thought of as the CO to which hydrogen has been stated to bind to[259, 260, 257, 233, 142]. Hydrogen has a very high mobility, and is the least sterrically hindered species under consideration.

$$2H\bullet \rightarrow H_{2(g)} + 2\bullet \tag{C.46}$$

Hydrogen that adsorbs to a surface may also desorb. The parameters (Table C.9) used for Equation C.45 and C.46 are taken from those used in Equation 3.11b. The critical addition that this mechanism makes is the addition of a dependency term to the standard CO desorption term (Equation C.8b). With the addition of this term, the activation energy of the desorption of CO depends upon the surface coverage of hydrogen on the pseudo-surface.

C.10 Carbon Deposition

The equations for carbon deposition are taken from the reactions published by Chatterjee et al. [66].

$$\mathrm{C}^* + \mathrm{O}^* \underset{k^f_{cLH,A7}}{\overset{k^f_{cLH,A6}}{\rightleftharpoons}} \mathrm{CO}^* + {}^* \tag{C.47a}$$

$$r_{cLH,A6} = k^f_{cLH,A6}\theta C_* \theta O_* - k^f_{cLH,A7}\theta CO_* \theta_* \tag{C.47b}$$

$$\mathrm{CO}^* + \mathrm{CO}^* \rightarrow \mathrm{C}^* + \mathrm{CO}_2^* \tag{C.47c}$$

D

Simulator Input Files and Parameters

Many different parameters needed to be defined before the simulator would function. These values were read in from various text-based input files. These parameters and their container files are described here. Earlier simulation work involved modifying these text files directly. A Matlab interface was used to modify these input files in later work.

D.1 Gas Properties

Properties of the various components were stored in the file `species.dat`. This file contained three sections, defining the properties of each of the gas species, surface species, and site species, respectively.

Every gas phase component had associated properties, and the thermodynamic and heat capacity properties needed to be defined. These properties were defined in the section `GasSpecies` in the `species.dat` file. Data used to describe the gas components were written in columns, which were, respectively: species index, species name, species mass, five columns of Cp coefficients, species standard enthalpy, species standard entropy, and diffusion volume.

Each gas species required that the parameters for heat capacity, standard enthalpy and standard entropy be numerically defined. Heat capacity of the gas was defined by the fourth-order polynomial in Equation D.1:

$$Cp = a + b \times T + c \times T^2 + d \times T^3 + e \times T^4 \tag{D.1}$$

index	species name	Heat Capacity Coefficients a	b	c	d	e
1	N_2	28.85	-1.569×10^{-3}	8.067×10^{-6}	-2.868×10^{-9}	0
2	CO	28.11	1.672×10^{-3}	5.363×10^{-6}	-2.218×10^{-9}	0
3	O_2	25.44	1.518×10^{-2}	-7.144×10^{-6}	-1.31×10^{-9}	0
4	CO_2	22.22	5.9711×10^{-2}	-3.495×10^{-5}	7.457×10^{-9}	0
5	H_2	32.19	1.92×10^{-3}	1.054×10^{-5}	-3.589×10^{-9}	0
6	H_2	29.06	-1.913×10^{-3}	3.997×10^{-6}	-8.69×10^{-10}	0

Table D.1: Gas Phase Heat Capacity. Units for the coefficents a, b, c, d and e are J mol^{-1} K^{-1}, J mol^{-1} K^{-2}, J mol^{-1} K^{-3}, J mol^{-1} K^{-4}, and J mol^{-1} K^{-5}, respectively.

index	species name	species mass (g mol^{-1})	standard enthalpy J mol^{-1} [276, 270]	standard entropy J mol^{-1} K^{-1} [276, 270]	diffusion volume m^3 [268, 269]
1	N_2	28	0	191.61	17.9
2	CO	28	-110530	197.67	18.9
3	O_2	32	0	205.138	16.6
4	CO_2	44	-393510	213.74	26.9
5	H_2O	18	-241820	188.83	12.7
6	H_2	2	0	130.684	7.07

Table D.2: Gas Phase Properties

This is the constant pressure heat capacity. The coefficients used for each species are given in Table D.1.

Other properties of the gas components were also defined. This includes molar mass, standard enthalphy, standard entropy and the diffusion volume used to calculate diffusion using the Fuller equation (see Equation A.6). These values are shown in Table D.2.

D.2 Site Species

On the surface of the catalyst are the active sites to which the reacting components bind. These sites were listed in this file, and their interactions with the reacting components are mathematically described in other locations. When it is assumed that there is only one type of surface species, only one type needed to be defined. Additional surface species types

index	species name	species mass (g mol^{-1})	site name	standard enthalpy (J mol^{-1})	standard entropy (J mol^{-1} K^{-1})
24	Pt_	0	platinum	0	0
25	Pt_O	0	platinum	-116000	0
26	Pt_O2	0	platinum	0	0
27	Pt_CO	0	platinum	-223500	0
28	Pt_OCO	0	platinum	-400500	0
44	H2O_Pt	0	platinum	-304600	0

Table D.3: Surface Species Properties

could be defined in the model, and were not used if not referenced. There was a limit of 9 surface site types in the model as used.

Differing surface site types were defined in columns in the section `SiteSpecies` in the file `species.dat`. A site index and sitename were assigned to each surface site type. For example, the following text was used in the input file:

```
5, platinumB
6, platinum
```

D.3 Surface Species Properties

Every component that adsorbs to or is formed on an active site is defined as a surface species. The thermodynamic properties of the various combinations of active site and the reacting component were described here. The columns in the section `SurfaceSpecies` in the `species.dat` file were, respectively: species index, species name, species mass, site name, species standard enthalpy, species standard entropy.

Properties of the surface species are defined, as shown in Table D.3.

D.4 Solid Material Properties

Properties of the solid materials and washcoat were defined in the file `material.dat`. The eleven columns were, respectively: material name, material density, three columns of thermal conductivity coefficients, three columns of heat capacity coefficients, pore size diameter, tortuosity, and finally porosity.

material name	density (kg m^3)	k$_s$			Cp$_s$		
		k$_{s,1}$	k$_{s,2}$	k$_{s,3}$	Cp$_{s,1}$	Cp$_{s,2}$	Cp$_{s,3}$
Washcoat1	1600	1.5	0.001	0	1020	0.0001	0
Substrate	1800	1.7	0.00035	0	950	0.051	0

Table D.4: Physical properties of the washcoat and solid material. Units for k$_{s,1}$, k$_{s,2}$ and k$_{s,3}$ are W·m^{-2}·K^{-1}, W·m^{-2}·K^{-2} and W·m^{-2}·K^{-3}, respectively. Units for Cp$_{s,1}$, Cp$_{s,2}$ and Cp$_{s,3}$ are J·kg^{-1}·K^{-1}, J·kg^{-1}·K^{-2} and J·kg^{-1}·K^{-3}, respectively.

material name	Pore Size Diameter (PSD) (m)	tortuosity (τ) (dimensionless)	porosity (ϵ) (dimensionless)
Washcoat1	5×10^{-9}	3	0.54
Substrate	1×10^{-8}	3	0.45

Table D.5: Physical properties of the washcoat and solid material.

The thermal conductivity of the material was calculated using the polynomial Equation D.2, with the corresponding coefficients from Table D.4.

$$k_s = k_{s,1} + k_{s,2} \times T + k_{s,3} \times T^2 \tag{D.2}$$

The heat capacity of the material also uses a polynomial to calculate the heat capacity at a given temperature. The coefficients used for each material may be found in Table D.5.

$$Cp_s = Cp_{s,1} + Cp_{s,2} \times T + Cp_{s,3} \times T^2 \tag{D.3}$$

D.5 Mechanisms

All reaction steps and associated parameters and reaction stoichiometry were defined in the input files. The reaction stoichiometry is defined in this step, as well as the type of reaction. Reactions may be either reversible or irreversible, and may be either an elementary sticking step (which calls the sticking function), an elementary step (which uses the Arrhenius equation), or a user-defined step. These reaction steps and parameters are shown in more detail in Appendix C and Appendix F.

A noble metal loading factor was defined in the model, to represent the concentration of surface sites.

The noble metal loading factor affects not only all the activities, but also the accumulation of adsorbed species. When this value is set too high, there is the possibility of a large amount of a reactant being present on the surface. When the reaction ignites, much of this reactant may react, yielding a much larger exotherm (~200 K) than is normally seen in experiments. This large exotherm may also be attributed in part to the numerical solver.

To ensure that the initial surface coverages in the simulator were acceptable, sufficient time was allowed such that the system would be settled before significant events occured. In a typically light-off simulation, light-off did not occur in the first 1200 times-steps (where 1 time-step = 1 second), affording the system sufficient time to come to an acceptable equilibrium state well in advance. In concentration step simulations, a typical step occured after 400 time-steps, ensuring that surface coverages were constant and that any small errors in the initial estimate would not influence the final result.

D.5.1 Surface Reaction

Surface reactions are modelled based on elementary mechanisms which are outlined in section B.1 and section B.2. Additions and changes to these models are described in subsection 4.5.4, section 5.4 and section 5.9.

The equations used to calculate rates are described in more detail in Appendix B.

D.6 Washcoat

A thickness of 2.33×10^{-5}m was assigned to the washcoat on the catalyst support.

D.7 Numerical Solver Parameters

The numerical solver required a relative error (between two iterations) of less than 1×10^{-6} before considering the solution for that time step to have converged and to move onto the next step. If convergence was not reached, the simulation would end with an error and not proceed to the next timestep.

Although the simulator used variable timestep sizes, a solution was outputted and saved to a datafile for every 1 second. This allowed easier comparision to experimental data, which was also written in 1 second increments.

D.8 Reactor Conditions

The inlet conditions were defined in simple text files, with each line representing a point in time. The simulator read these files in, and linearly interpolated between the defined points to determine the appropriate inlet conditions for the point in time that was currently being considered. Initial conditions were also defined in the input files. When the Matlab interface to the simulator, USI, was used, this program generated the necessary input files from data defined by the user in the interface.

D.8.1 Initial Temperature and Gas-Phase Concentrations in the Reactor

The initial reactor conditions were imposed with the assumption that there are no gradients in the system. The imposed initial solid temperature profile was uniform in temperature, as was the imposed initial gas concentration profile. The values imposed were defined in the file `calculation.init`.

D.8.2 Initial Surface Concentrations

The initial fractional surface concentrations were defined in the parameters and reaction mechanism file. The values used are stated in the simulation discussions.

D.8.3 Inlet Concentrations over Time

The inlet concentration profile over time for a temperature programmed reaction was defined in the file `calculation.cmp`. This file contained columns of data. Each column represented a gas composition, each row a point in time. At any given timestep in the simulation, the simulator linearly interpolated between the two most appropriate time steps (the defined point before and the defined point later than the current point in time) to determine the current inlet concentrations.

D.9 Simulator Keywords

Keywords were available in the simulator to accomplish specific tasks. The keyword 'nonexothermic' allowed the user to quickly and easily redefine the heat of reaction of all reactions to be zero. This keyword was used for select simulations during investigations into the role of adiabatic temperature rise on the promotion of CO light-off by the presence of H_2 (subsection 5.9.1).

E
Staging Queues software package and LabVIEW code

E.1 Introduction to LabVIEW

LabVIEW[72] is a graphical programming language from National Instruments designed to be used in the operation of laboratory equipment and data collection. This programming environment includes many libraries useful for creating graphical environments, interfacing with instruments, and processing data.

E.2 User Interface

The user interface has two parts - the first being the basic screen showing the commands that are running or have recently completed as well as handling file and manual command I/O. The second part of the user interface is the monitoring station, which graphically displays date from mass flow controllers, thermoelements, analyzers and other devices. The monitoring station vi is completely optional for the operation of the system, but it allows the operator to customize the shown data to be that of most interest to the experiment at hand. The monitoring station is simply a (relatively) small program that only *reads* data from tags in the DSC. As it is intended to only read data, it does not modify anything, and exists for the benefit of the operator.

E.3 Communication with Laboratory Equipment

The Datalogging and Supervisory Control (DSC) module from National Instruments extends the functionality of LabVIEW [72] to include the addressing of inputs and output via OPC and logging of data to a SQL database, among other features.

All input and output channels in the system are configured as DSC tags. Each tag has a specific address in the system, and addresses either a specific hardware channel, or is stored in memory. Each tag is logged to the database as a series of events, with each new recorded value being logged as timestamp/value pair. Values are determined to be new when they exceed a difference of 0.1% from the last measured value, or every 30 seconds, whichever event occurs earlier.

E.4 Queueing System

The software that drove the experiments and determined when to send new setpoints is the queuing system. This system was written by the author of the present work. The queuing system was essentially a means by which single commands may be executed in series, as a sequencer or state machine. These commands take the form of text commands, usually with parameters, and are detailed in section E.8. The core of the application involved a system of queues passing commands to a state machine. The state machine is essentially a large case statement that runs specific commands (and passes the stated parameters) when that command is called. The queuing system ensures that these commands are passed in the correct order and at the correct time, and allowed the ordering of commands to be modified during operation.

Commands such as INJECT (E.8) allow a new file with commands to be read and added to the queue in the appropriate order. The files are read on demand, and as such, may be modified between the start of an experiment and the reading of the file.

E.5 Parallel Routines

Many other routines run in parallel to the central queuing system. Routines to perform safety checks, perform calculations and convert between data types, as well as to monitor and report on the progress of the system run besides the main queuing system. These routines are essential to safe operation (for example, to stop the experiment if safe limits are exceeded) and general maintenance (for example, warnings in case hard disk space becomes limited). Regular configuration information is written to a text file, in case there is a need later to verify the data.

E.6 Input Scriptfiles

When starting the software, a command file was defined. This command file was loaded, and the commands within were executed in series.

The maximum length of an input line was by default defined as 120 characters, and was set to avoid buffer-overflow errors. Commands longer than 120 characters did not seem to be typical, however, should the need arise, this value was defined in a global variables file and may be modified as necessary.

Upon loading input files, the files were cleaned to a format easier for the system to understand. Empty lines were removed, and tabs and semi-colons were replaced with spaces. Whitespace was trimmed such that multiple spaces were trimmed to a single space. All text after a hash symbol (#) was ignored, allowing this symbol to be used for commenting out lines and comments in an input file.

Input files were allowed to load other input files, allowing for a more modular and cleaner operation. Repeated tasks were written into a single file, and then each time that task was to run, the file containing the necessary command sequence was loaded.

E.6.1 Global Operational Parameters

The global variables file used in this system were typically only written, if at all, in one location in the program. This type of variable is used such that every routine had *read* access to defined operational parameters. These parameters included the standard loop times, user-interface parameters and filenames, folders and locations. This file may be modified by the user, but during typical usage the file was predefined and not changed.

E.7 Output Files

Output files were written as a record of what the processor has done, and which commands have been executed as well as any errors enoucntered. Every command that completed successfully was written (with timestamp) to a log file. Every recognized error encountered by the system was also recorded to log files.

Experimental data was extracted from the SQL database on demand, as defined in the script files. The output file was a comma separated values list, with the header containing tag names and the data being written in columns of text values. This file was then easily imported into Microsoft Excel, or processed via BASH or MatLab scripts.

A log of gas usage was kept. The gas consumption was calculated by integrating the measured values of the mass flow controllers over time. The file was overwritten to a file named with a timestamp. Whenever the program was restarted, the data for gas consumption was reset to zero.

Data pertaining to the configuration of the system and tag properties was written upon demand such that the user may reference this information at a later date when diagnosing problems.

A snapshot of all current readings was also periodically written to a text file, such that in the event the operator has only minimal, or remote, access to the system, that the operator could still ascertain if the apparatus was functioning according to expectations.

E.8 Basic Queueing Script Commands

COMMENT

This command simply takes the input line and copies it into the log file. This was useful for describing the what is happening in the system for whomever reads the log or script files. This command does not affect any setpoints.
input parameters: text, up to line length limit
usage: `COMMENT text`
example: `COMMENT "this is the start of experiment 12"`

DRAMP

`DRAMP` will perform two simultaneous ramp functions. This is useful when performing an large concentration ramp, and controlling the inert gas at the same time. In this manner, the space velocity may also be more closely maintained than with a single concentration ramp.
usage: `DRAMP tag_name initial_point ramp_rate end_point tag_name initial_point ramp_rate end_point`
example: `DRAMP O2_soll_2001-h 20 0.5 40 N2_soll_20001-h 2000 -0.5 1980`

EXTRACT_TODAYS_DATA

All data for all datapoints for the current day (from midnight until the present moment) will be extracted to an appropriately named datafile.
input parameters: none
usage: `EXTRACT_TODAYS_DATA`

EXTRACT_DAILY_DATA

Extracts all data for specific day, from midnight (00:00:00) to midnight (23:59:59). When no input parameters are specified (or a value of 0), then this command extracts that current day's data (from midnight until the present moment) will be extracted to an appropriately named datafile. When the optional parameter is included, then this is used to specify for which day to extract data (0 = today, 1 = yesterday, 2 = the day before...). When the day being considered is not the current day, then all data for that day is extracted (midnight to midnight). The input parameter cannot be a negative number (data from the future may not be extracted from the database).
input parameters: days_previous (optional)
usage: `EXTRACT_TODAYS_DATA days_previous`
example: `EXTRACT_TODAYS_DATA 2`

FLUSH_QUEUE

This command empties the queue of all commands. After this command is run, there should be no more waiting tasks, and the system will be at a state where it is waiting for new commands to be specified. Setpoints made before this command are held.
input parameters: none
usage: `FLUSH_QUEUE`

INJECT

`INJECT` will read in a new script and begin running the commands found inside. This is especially useful for running a series of commands multiple times. For example, a temperature-programmed experiment may be run, but at several different concentrations. The concentrations may be defined in one script, and then everytime the temperature program is run,

it is run simply by injecting the temperature-program script, assuming that everytime it is run the commands are the same.
input parameters: input-file-name
example: `INJECT temperature_program.txt`

RAMP

`RAMP` will ramp a specified variable from a defined starting point to a defined end point at a given rate. The user must define the four require parameters for this function.
input parameters: tag_name - label of the tag to be controlled
initial_point - starting value
ramp_rate - rate at which the rate proceeds. The units are those of the controlled variable, per second. For example, the units of a mass flow controller are typically Ln hr^{-1}, and this the units of the ramp rate for a MFC would be Ln hr^{-1} s^{-1}.
end_point - the value at which the ramp will be completed
usage: `RAMP tag_name initial_point ramp_rate end_point`
example: `RAMP O2_soll_2001-h 20 0.5 40`

REPORT

also `REPORT_VALUE` Reads the current value of the selected tag and reports this value to the log file.
input parameters: tag-name
usage: `REPORT_VALUE tag_name`
example: `REPORT_VALUE TC_03`

SET

Gives a new setpoint to the specified tag. Should the value be outside the predefined range of the setpoint, the value is sent as the nearest point within the range. The units are defined in the tag configuration.
input parameters: tag-name - label of the system point that is to be given a new setpoint
usage: `SET tag-name value`

example: `SET N2_soll_20001-h 1000`

START_PHASE

The current time is stored to a local variable, and the name of the phase is changed.
input parameters: phase-name - label defining the phase. No spaces are allowed in this variable.
usage: `START_PHASE phase-name`
example: `START_PHASE temperature_ramp`

STOP

Stops the program. This is a hard stop, and the entire program will stop running. No setpoints are changed, and the signal to the watchdog (described in subsection 2.11.1) will cease.
input parameters: none
example: `STOP`

STOP_PHASE

Stops the current phase. The data for the phase is automatically extracted. The local variable defined in `START_PHASE` is used as the starting time point, and the current time is used as the end point.
input parameters: none
example: `STOP_PHASE`

TITLE

Sets the title of the experiment. The "Title" is a string variable, stored with all other variables. This is used to easily identify specific experiments within the data. This variable is also used to define a title for output experimental data files.
input parameters: title-name - short string (no spaces) that identifies a part of the current experiment
usage: `TITLE title-name`

example: `TITLE Exp038`

UPDATE

Sets the first given tag name with the value read from the second given tag. This may be used when a calculation is used to determine a new setpoint. Simple boundary checking is performed to ensure that the new setpoint is within the allowed bounds of the tag to be set. With skillful scripting, this can be used to perform 'intelligent' experiments. For example, the computer could perform an experiment at a given temperature, calculating the best temperature for the next experiment in the background based on analyzer results, and then set the new setpoint to that new desired temperature. Iterations of experiments could be performed, each time calculating a new temperature or concentration setpoint.
usage: `UPDATE tag-to-set tag-to-read`
example: `UPDATE N2_soll_2000L-h N2_ist_4000L-h`

WAIT

usage: `WAIT TIME number units`
example: `WAIT TIME 5 min`
Acceptable units are sec, min and msec. If no units are given, the default is sec. The WAIT command will wait to a maximum as defined in the maximum wait time variable (default is currently 120 min). After this time is reached, the command will time out and proceed.
example: `WAIT tag tag-name operator value`
example: `WAIT tag tag-name IN_RANGE lower_boundary upper_boundary`
example: `WAIT tag CO_30000ppm_MLT < 2000`
example: `WAIT tag TC_01 IN_RANGE 80 90`
Acceptable units are as defined in the tag configuration. Acceptable tags are any accessable, writable tags. Operators may be any of "<", "<=", "=", ">", ">=", or, if defined with an additional value, the "IN_RANGE" operator may be used. When the condition is met, the system proceeds as normal to the next step. When the condition is not met, the system will wait until it reaches the defined maximum wait time and then proceed normally.

WAIT_USER_ACKNOWLEDGEMENT

Displays a window on the screen with COMMENT, and waits until the operator clicks to acknowledge the message before proceeding.
usage: `WAIT_USER_ACKNOWLEDGEMENT` COMMENT

WRITE_TAG_CONFIG

This command will write the configuration of all the OPC tags in the system to a text file. There are no parameters for this command. useage: `WRITE_TAG_CONFIG`

DEFINE_GLOBAL

Redefine the maximum wait time for any single time-dependent step (WAIT TIME, WAIT TAG, or RAMP). The default value is 120 minutes.
usage: `DEFINE_GLOBAL global_variable_name value wait_time_in_minutes`
example: `DEFINE_GLOBAL WAIT_LONG_CMD 10`

If one of the above commands was not found, the system recorded an error message with the problematic command line, and then continued to the next command in the queue.

F

Model Parameters Summary

Index	Reaction	A / S^0	E_A / γ	Notes
1	O_2+2Pt_→2O_Pt	$S^0 = 0.07$	$\gamma = 2.72\times10^{-5}$	[66] [a]
4	H_2+2Pt_→2H_Pt	$S^0 = 0.046$	$\gamma = 2.72\times10^{-5}$	[66]
			$\theta_{Pt\_} = -1$	
5	H_2O+Pt_→H_2O_Pt	$S^0 = 0.75$	$\gamma = 2.72\times10^{-5}$	[66]
6	CO_2+Pt_→CO_2_Pt	$S^0 = 0.005$	$\gamma = 2.72\times10^{-5}$	[66]
7	CO+Pt_→CO_Pt	$S^0 = 0.84$	$\gamma = 2.72\times10^{-5}$	[66]
8	2O_Pt→O_2+2Pt_	$A = 1.0060 \times 10^{13}$	$E_A = 232.2$	[66] [b]
		$\frac{dE_A}{d\theta_{O\_Pt}} = 90$		see 4.1.6
11	2H_Pt→H_2+2Pt_	$A = 1.006 \times 10^{13}$	$E_A = 67.4$	[66]
			$\frac{dE_A}{d\theta_{H\_Pt}} = 6$	
12	H_2O_Pt→H_2O+Pt_	$A = 1.000 \times 10^{13}$	$E_A = 40.3$	[66]
13	CO_Pt→CO+Pt_	$A = 1.000 \times 10^{13}$	$E_A = 126.4$	[66, 148] [c]
			$\frac{dE_A}{d\theta_{CO\_Pt}} = 33$	see 4.1.6
			$\frac{dEa_{CO-H}}{d\theta_{PtB-H}} = 10$	see 5.9.2
14	CO_2_Pt→CO_2+Pt_	$A = 1.000 \times 10^{13}$	$E_A = 27.1$	[66]
38	O_Pt+H_Pt→OH_Pt+Pt_	$A = 1.006 \times 10^{13}$	$E_A = 77.5$	[d] see 5.4
39	OH_Pt+Pt_→O_Pt+H_Pt	$A = 1.569 \times 10^{14}$	$E_A = 74.9$	[66]
40	H_Pt+OH_Pt→H_2O_Pt+Pt_	$A = 1.006 \times 10^{13}$	$E_A = 17.4$	[66]
41	H_2O_Pt+Pt_→H_Pt+OH_Pt	$A = 9.955 \times 10^{12}$	$E_A = 73.6$	[66]
42	2OH_Pt→H_2O_Pt+O_Pt	$A = 1.000 \times 10^{13}$	$E_A = 48.2$	[66]
43	H_2O_Pt+O_Pt→2OH_Pt	$A = 6.392 \times 10^{11}$	$E_A = 41$	[66]
44	CO_Pt+O_Pt→CO_2_Pt+Pt_	$A = 1.006 \times 10^{12}$	$E_A = 108$	[66]
			$\frac{dE_A}{d\theta_{CO\_Pt}} = 33$	
			$\frac{dE_A}{d\theta_{NO\_Pt}} = -90$	
45	CO_2_Pt+Pt_→CO_Pt+O_Pt	$A = 1.006 \times 10^{13}$	$E_A = 161$	[66]
			$\frac{dE_A}{d\theta_{O\_Pt}} = -45$	

Table F.1: Parameter Set, based on a modified version of the parameter set presented in section C.2. A is in units of mol·mol_{NM}^{-1}·s^{-1}, E_A in units of kJ·mol^{-1}, and γ is in units of mol_{NM}·m_{NM}^{-2}. S^0, the sticking coefficient, is dimensionless.

---

[a] Temperature dependence from literature not used in the model presented here.

[b] Oxygen adsorption is assumed to be irreversible, and hence used with a value of A=0. See 4.1.6.

[c] This E_A value is critical and controversial. See 4.1.6.

[d] Values modified from [66]. This E_A value and the influence on selectivity is discussed in more detail in section 5.4.

Index	Reaction	A	E_A	Notes
46	C_Pt+O_Pt→CO_Pt+Pt_	1.006×10^{13} $\frac{dE_A}{d\theta_{CO\_Pt}} = -33$	0	[66]
47	CO_Pt+Pt_→C_Pt+O_Pt	1.006×10^{13} $\frac{dE_A}{d\theta_{O\_Pt}} = -45$	218.5	[66]

Table F.2: Carbon Deposition Parameter Set. See also section C.10 and subsection 4.5.8. A is in units of mol·mol$_{NM}^{-1}$·s^{-1} and E_A in units of kJ·mol^{-1}.

Index	Reaction	A	E_A	Notes
71	CO+2O_Pt→CO_Pt+OO_Pt	1.0×10^{12}	50	[a]
72	CO_Pt+OO_Pt→CO_2_Pt+O_Pt	1.0×10^{15}	115	[a]
73	OO_Pt+Pt_→2O_Pt	1.0×10^{15}	105	[a]

Table F.3: Parameters used for Compressed Oxygen Parameter steps. A is in units of mol·mol$_{NM}^{-1}$·s^{-1} and E_A in units of kJ·mol^{-1}.

---

[a] Due to a lack of good literature values, these are rough estimates. See subsection 4.5.4 and section C.7.

Index	Reaction	A	E_A	Notes
81	CO_2_Pt+H_Pt→CO_Pt+OH_Pt	8.03×10^{8} $\frac{dE_A}{d\theta_{O\_Pt}} = 60.3$ $\frac{dE_A}{d\theta_{H\_Pt}} = -6.3$ $\frac{dE_A}{d\theta_{H2O\_Pt}} = -45.6$ $\frac{dE_A}{d\theta_{CO\_Pt}} = 18.1$	23.7	[144]
82	CO_Pt+OH_Pt→CO_2_Pt+H_Pt	1.25×10^{9} $\frac{dE_A}{d\theta_{O\_Pt}} = -77.8$ $\frac{dE_A}{d\theta_{H\_Pt}} = 6.3$ $\frac{dE_A}{d\theta_{H2O\_Pt}} = 59$ $\frac{dE_A}{d\theta_{CO\_Pt}} = 44.6$	77.3	[144]

Table F.4: Parameters used for Compressed Oxygen Parameter steps. A is in units of mol·mol$_{NM}^{-1}$·s^{-1} and E_A in units of kJ·mol^{-1}.

Index	Reaction	A	E_A	Notes
94	2CO_Pt→CO_2_Pt+C_Pt	1.00×10^{9}	70	[a]

Table F.5: Parameters used for Boudouard steps. A is in units of mol·mol$_{NM}^{-1}$·s^{-1} and E_A in units of kJ·mol^{-1}.

---

[a] Due to a lack of good literature values, these are rough estimates. See 4.5.8.

Index	Reaction	A	E_A	Notes
95	$O\_Pt \rightarrow O_{ox}\_Pt$	1.006×10^{13}	70	[a]
96	$O_{ox}\_Pt \rightarrow O\_Pt$	1.006×10^{13}	110	[a]

Table F.6: Parameters used for oxidation of platinum steps. A is in units of $\text{mol}\cdot\text{mol}_{NM}^{-1}\cdot\text{s}^{-1}$ and E_A in units of $\text{kJ}\cdot\text{mol}^{-1}$.

---

[a] Due to a lack of good literature values, these are rough estimates.

G

Experiments Performed

Date and Time	Short Title	SV (hr^{-1})	O_2 (%)	CO (ppm)	CO_2 (ppm)	H_2O (%)	H_2 (ppm)
20050129.074206	036	25000	6	500	0	0	0
20050129.112534	036	25000	6	500	0	0	0
20050705.055129	036	25000	6	500	0	0	0
20050709.001005	036	25000	6	500	0	0	0
20050717.044213	036	25000	6	500	0	0	0
20050717.082357	036	25000	6	500	0	0	0
20050719.094116	036	25000	6	500	0	0	0
20050725.011036	036	25000	6	500	0	0	0
20050807.190156	036	25000	6	500	0	0	0
20050129.151021	037	25000	6	1000	0	0	0
20050129.185112	037	25000	6	1000	0	0	0
20050715.201806	037	25000	6	1000	0	0	0
20050715.235146	037	25000	6	1000	0	0	0
20050722.194426	037	25000	6	1000	0	0	0
20050808.001920	037	25000	6	1000	0	0	0
20050129.223037	038	25000	6	1500	0	0	0
20050130.021011	038	25000	6	1500	0	0	0
20050129.223037	038	25000	6	1500	0	0	0
20050130.054735	039	25000	6	2000	0	0	0
20050130.092440	039	25000	6	2000	0	0	0
20050721.010640	039	25000	6	2000	0	0	0
20050720.214207	039	25000	6	2000	0	0	0
20050808.191704	039	25000	6	2000	0	0	0

Table G.1: CO Light-Off (Ignition/Extinction) experiments performed.

Date and Time	T (K)	SV (hr^{-1})	O_2 (%)	CO (ppm)	CO_2 (ppm)	H_2O (%)	H_2 (ppm)	details details
20041207.232517	391	25000	6	0-1000-0	0	0	0	repeated steps
	373	25000	6	0-500-0	0	0	0	

Table G.2: CO concentration step experiments performed.

Date and Time	Short Title	SV (hr^{-1})	O_2 (%)	CO (ppm)	CO_2 (ppm)	H_2O (%)	H_2 (ppm)
20050409.153945	117	25000	6	250	0	10	0
20050409.190118	118	25000	6	375	0	10	0
20050409.222403	119	25000	6	500	0	10	0
20050410.014656	120	25000	6	750	0	10	0
20050410.051130	121	25000	6	1000	0	10	0
20050410.083419	122	25000	6	1500	0	10	0
20050410.115819	123	25000	6	2000	0	10	0

Table G.3: CO + H_2O Light-Off (Ignition/Extinction) experiments performed.

Date and Time	Short Title	SV (hr^{-1})	O_2 (%)	CO (ppm)	CO_2 (ppm)	H_2O (%)	H_2 (ppm)
20050409.153945	117	25000	6	250	0	10	0
20050311.220558	094	25000	6	500	0	0	500
20050312.045711	096	25000	6	1000	0	0	500
20050313.023216	096	25000	6	1000	0	0	2000
20050312.082247	097	25000	6	2000	0	0	500
20050313.054041	103	25000	6	2000	0	0	2000

Table G.4: CO + H_2 Light-Off (Ignition/Extinction) experiments performed.

Date and Time	T (K)	SV (hr^{-1})	O_2 (%)	CO (ppm)	CO_2 (ppm)	H_2O (%)	H_2 (ppm)
20050426.171556	308	25000	6	0-250-0	0	0	100
20060510.224033	366	25000	6	1000	0	0	0-500-2000
20050425.164635	347	25000	6	0-250-0	0	0	100
20050425.164635	347	25000	6	0-500-0	0	0	100
20050425.164635	347	25000	6	0-1000-0	0	0	100
20050425.164635	347	25000	6	0-2000-0	0	0	100

Table G.5: CO + H_2 concentration step experiments performed.

References

---

[1] Jan Kaspar, Paolo Fornasiero, and Neal Hickey. Automotive catalytic converters: current status and some perspectives. *Catalysis Today*, 77(4):419–449, 2003. doi:10.1016/S0920-5861(02)00384-X.

[2] J.C. Guibet and E. Faure-Birchem. *Fuels and Engines: Technology, Energy, Environment*, volume 1. Technip Editions, Paris, 1999.

[3] Government of Canada. *Regulatory Framework for Air Emissions*. 2007. ISBN 978-0-662-69717-6.

[4] Michael Bettencourt. More diesels models coming when cleaner fuel arrives. *The Globe and Mail*, May 18, 2006.

[5] Ricardo. Report shows small US shift to diesel. http://www.engineeringtalk.com, May 21 2003.

[6] J.D. Power and Associates. Global Demand for Diesel-Fueled Light Vehicles to Nearly Double During the Next 10 Years. press release, April 13 2006. http://www.jdpa.com/pdf/2006057.pdf.

[7] CANADIAN ENVIRONMENTAL PROTECTION ACT, 1999 On-Road Vehicle and Engine Emission Regulations. Canada Gazette Vol. 137, No. 1, January 2003.

[8] T. G. Kaufmann, A. Kaldor, G. F. Stuntz, M. C. Kerby, and L. L. Ansell. Catalysis science and technology for cleaner transportation fuels. *Catalysis Today*, 62(1):77–90, September 2000. doi:10.1016/S0920-5861(00)00410-7.

[9] M. Booth, J.G. Buglass, and J.F. Unsworth. Tailoring fuels for the new millennium. *Topics in Catalysis*, 16/17(1-4):39–46, 2001. doi:10.1023/A:1016670528451.

[10] Seth Dunn. Hydrogen futures: toward a sustainable energy system. *International Journal of Hydrogen Energy*, 27(3):235–264, 2002. doi:10.1016/S0360-3199(01)00131-8.

[11] Heather L. MacLean and Lester B. Lave. Evaluating automobile fuel/propulsion system technologies. *Progress in Energy and Combustion Science*, 29(1):1–69, 2003. doi:10.1016/S0360-1285(02)00032-1.

[12] Roberto Galiasso Tailleur. Diesel upgrading into a low emissions fuel. *Fuel Processing Technology*, 87(9):759–767, 2006. doi:10.1016/j.fuproc.2005.12.005.

[13] A comprehensive analysis of biodiesel impacts on exhaust emissions. Technical report, Assessment and Standards Division, Office of Transportation and Air Quality, U.S. Environmental Protection Agency, 2002. EPA420-P-02-001.

[14] Bruce Ainslie, Hadi Dowlatabadi, Naoko Ellis, Francis Ries, Mahbod Rouhany, and Hans Schreier. A review of environmental assessments of biodiesel displacing fossil diesel. Technical report, The Canola Council of Canada & Auto21 Network of Centres of Excellence, 2006.

[15] Carlo N Hamelinck and André P.C. Faaij. Outlook for advanced biofuels. *Energy Policy Volume 34*, 34(17):3268–3283, 2006. doi:10.1016/j.enpol.2005.06.012.

[16] Gurpreet Singh. Progress Report for Advanced Combustion Engine Research & Development. Technical report, Energy Efficiency and Renewable Energy Office of FreedomCAR and Vehicle Technologies U.S. Department of Energy, 2003.

[17] Richard Smokers, Raymond Gense, Rudolf Rijkeboer, and Arjan Dijkhuizen. Expert Judgement on the Long Term Possibilities of Conventional Emission Abatement Technologies for Passenger Cars. *Topics in Catalysis*, 30/31:439–443, 2004. doi:10.1023/B:TOCA.0000029787.60870.49.

[18] Paul Zelenka, Wolfgang Cartellieri, and Peter Herzog. Worldwide diesel emission standards, current experiences and future needs. *Applied Catalysis B: Environmental*, 10(1-3):3–28, 1996. doi:10.1016/0926-3373(96)00021-5.

[19] R.J. Farrauto and R.M. Heck. Environmental catalysis into the 21st century. *Catalysis Today*, 55(1-2):179–187, 2000. doi:10.1016/S0920-5861(99)00237-0.

[20] Ronald M. Heck and Robert J. Farrauto. Automobile exhaust catalysts. *Applied Catalysis A: General*, 221(1-2):443–457, 2001. doi:10.1016/S0926-860X(01)00818-3.

[21] Bruce I. Bertelsen. Future US Motor Vehicle Emission Standards and the Role of Advanced Emission Control Technology in Meeting Those Standards. *Topics in Catalysis*, 16/17(1-4):15–22, 2001. doi:10.1023/A:1016614310704.

[22] H. S. Gandhi, G. W. Graham, and R. W. McCabe. Automotive exhaust catalysis. *Journal of Catalysis*, 216(1-2):433–442, 2003. doi:10.1016/S0021-9517(02)00067-2.

[23] François Garin. Environmental catalysis. *Catalysis Today*, 89(3):255–268, 2003. doi:10.1016/j.cattod.2003.12.002.

[24] Shin'ichi Matsumoto. Recent advances in automobile exhaust catalysts. *Catalysis Today*, 90(3-4):183–190, 2004. doi:10.1016/j.cattod.2004.04.048.

[25] Mitsuru Hosoya and Masatoshi Shimoda. The application of diesel oxidation catalysts to heavy-duty diesel engines in Japan. *Applied Catalysis B: Environmental*, 10(1-3):83–97, 1996. doi:10.1016/0926-3373(96)00025-2.

[26] M. V. Twigg. Twenty-Five Years of Autocatalysts. *Platinum Metals Review*, 43(4):168–171, 1999.

[27] M. Shelef and R. W. McCabe. Twenty-five years after introduction of automotive catalysts: what next? *Catalysis Today*, 62(1):35–50, 2000. doi:10.1016/S0920-5861(00)00407-7.

[28] D.E. Webster. 25 years of catalytic automotive pollution control: a collaborative effort. *Topics in Catalysis*, 16/17(1-4):33–38, 2001. doi:10.1023/A:1016618411613.

[29] G.J.K. Acres and B. Harrison. The Development of Catalysts for Emission Control from Motor Vehicles: Early Research at Johnson Matthey. *Topics in Catalysis*, 28(1-4):3–11, 2004. doi:10.1023/B:TOCA.0000024329.85506.94.

[30] A. König, G. Herding, B. Hupfeld, Th. Richter, and K. Weidmann. Current Tasks and Challenges for Exhaust Aftertreatment Research. A Viewpoint from the Automotive Industry. *Topics in Catalysis*, 16/17(1-4):23–31, 2001. doi:10.1023/A:1016666327542.

[31] DIRECTIVE 98/69/EC OF THE EUROPEAN PARLIAMENT AND OF THE COUNCIL of 13 October 1998 relating to measures to be taken against air pollution by emissions from motor vehicles and amending Council Directive 70/220/EEC. *Official*

Journal of the European Communities, L 350:1–56, October 1998. `http://europa.eu.int/eur-lex/pri/en/oj/dat/1998/l_350/l_35019981228en00010056.pdf`.

[32] R. Burch. Knowledge and Know-How in Emission Control for Mobile Applications. *Catalysis Review*, 46:271–334, 2004. doi:10.1081/CR-200036718.

[33] Paul Greening. European vehicle emission legislation - present and future. *Topics in Catalysis*, 16/17(1-4):5–13, 2001. doi:10.1023/A:1016629326634.

[34] Günter Hörmandinger. Towards a new Euro-5 standard (20 Jan. 2005). Technical report, DG Environment, January 2005. `http://www.t-e.nu/docs/presentations/2005/2005-01_clean_car_seminar/2005-01_p4_towards_a_new_euro5_standard_hormandinger.pdf`.

[35] Transportation Division Environment Canada. Fleet average NO_x emission performance of 2004 model year light-duty vehicles, light-duty trucks and medium-duty passenger vehicles. internet, May 2006. `http://www.ec.gc.ca/cepareqistry/documents/regs/nox_avg/toc.cfm`.

[36] Dieselnet.com. Emission Standards - Canada - on road vehicles. internet, 2004. `http://www.dieselnet.com/standards/ca/`.

[37] Dieselnet.com. Emission Standards - USA - Cars and Light-Duty Trucks. internet, 2004. `http://www.dieselnet.com/standards/us/light.html`.

[38] Kuo-Ching Wu, Yu-Lan Tung, Yi-Ling Chen, and Yu-Wen Chen. Catalytic oxidation of carbon monoxide over gold/iron hydroxide catalyst at ambient conditions. *Applied Catalysis B: Environmental*, 53(2):111–116, 2004. doi:10.1016/j.apcatb.2004.05.008.

[39] G. Pattrick, E. van der Lingen, C. W. Corti, R. J. Holliday, and D. T. Thompson. Recent Developments in Gold-Based Catalyst Systems for Automotive Applications. Sixth International Congress on Catalysis & Automotive Pollution Control (CAPoC6), October 2003. `http://www.gold.org/discover/sci_indu/presentations/files/CAPoC6.pdf`.

[40] Sterling E. Voltz, Charles R. Morgan, David Liederman, and Solomon M. Jacob. Kinetic Study of Carbon Monoxide and Propylene Oxidation on Platinum Catalysts. *Industrial & Engineering Chemistry Product Research and Development*, 12(4):294–301, 1973. `http://pubs.acs.org/cgi-bin/archive.cgi/iepra6/1973/12/i04/pdf/i360048a006.pdf`.

[41] Se H. Oh and James C. Cavendish. Transients of monolithic catalytic converters. Response to step changes in feedstream temperature as related to controlling automobile emissions. *Industrial & Engineering Chemistry Product Research and Development*, 21(1):29–37, 1982. doi:10.1021/i300005a006.

[42] S. H. Oh and J. C. Cavendish. Mathematical modeling of catalytic converter lightoff. part ii: Model verification by engine-dynamometer experiments. *AIChE Journal*, 31(6):935–942, 1985. doi:10.1002/aic.690310609.

[43] S. H. Oh and J. C. Cavendish. Mathematical modeling of catalytic converter lightoff. part iii: Prediction of vehicle exhaust emissions and parametric analysis. *AIChE Journal*, 31(6):943–949, 1985. doi:10.1002/aic.690310610.

[44] Grigorios C. Koltsakis and Anastasios M. Stamatelos. Catalytic automotive exhaust aftertreatment. *Progress in Energy and Combustion Science*, 23(1):1–39, 1997. doi:10.1016/S0360-1285(97)00003-8.

[45] C. Dubien, D. Schweich, G. Mabilon, B. Martin, and M. Prigent. Three-way catalytic converter modelling: fast- and slow-oxidizing hydrocarbons, inhibiting species, and steam-reforming reaction. *Chemical Engineering Science*, 53(3):471–481, 1998. doi:10.1016/S0009-2509(97)00313-8.

[46] S. Siemund, J. P. Leclerc, D. Schweich, , M. Prigent, and F. Castagna. Three-way monolithic converter: Simulations versus experiments. *Chemical Engineering Science*, 51(15):3709–3720, 1996. doi:10.1016/0009-2509(96)00018-8.

[47] Zygourakis. Transient operation of monolith catalytic converters: a two-dimensional reactor model and the effects of radially nonuniform flow distributions. *Chemical Engineering Science*, 44(9):2075–2086, 1989. doi:10.1016/0009-2509(89)85143-7.

[48] J. P. Leclerc and D. Schweich. Modeling catalytic monoliths for automobile emission control. In H. de Lasa, G. Dogammau, and A. Ravella, editors, *Chemical Reactor Technology for Environmentally Safe Reactors and Products, Proceedings of the NATO Advanced Study Institute*, pages 547–576. Kluwer Academic Press, Dordrecht, 1992. ISBN: 978-0-7923-2032-6.

[49] Chaitanya S Sampara, Edward J Bissett, Matthew Chiemeleski, and Dennis Assanis. Global oxidation kinetics for platinum diesel oxidation catalysts. Poster at 20th North American Catalysis Society North American Meeting, June 2007.

[50] C. T. Campbell, G. Ertl, H. Kuipers, and J. Segner. A molecular beam study of the catalytic oxidation of CO on a Pt(111) surface. *Journal of Chemical Physics*, 73(11):5862–5873, 1980. doi:10.1063/1.440029.

[51] P. R. Norton, K. Griffiths, and P. E. Bindner. Interaction of O_2 with Pt(100) II. Kinetics and energetics. *Surface Science*, 138(1):125–147, 1984. doi:10.1016/0039-6028(84)90500-4.

[52] R. J. Behm, P. A. Thiel, P. R. Norton, and P. E. Bindner. The oxidation of CO on Pt(100): Mechanism and structure. *Surface Science*, 147(1):143–161, 1984. doi:10.1016/0039-6028(84)90172-9.

[53] Sohail Akhter and J. M. White. The effect of oxygen islanding on CO and H_2 oxidation on Pt(111). *Surface Science*, 171(3):527–542, 1986. doi:10.1016/0039-6028(86)91058-7.

[54] Deborah Holmes Parker, Michael E. Bartram, and Bruce E. Koel. Study of high coverages of atomic oxygen on the Pt(111) surface. *Surface Science*, 217(3):489–510, 1989. doi:10.1016/0039-6028(89)90443-3.

[55] D. H. Parker and B. E. Koel. Chemisorption of high coverages of atomic oxygen on the Pt(111), Pd(111), and Au(111) surfaces. *Journal of Vacuum Science & Technology A*, 8(3):2585–2590, 1990. doi:10.1116/1.576675.

[56] H. Akiyama, C. Moise, T. Yamanaka, K. Jacobi, and T. Matsushima. Selective modification of reaction sites for carbon monoxide oxidation on a platinum (113) surface. *Chemical Physics Letters*, 272(3-4):219–224, 1997. doi:10.1016/S0009-2614(97)88012-8.

[57] T. Zambelli, J. V. Barth, J. Wintterlin, and G. Ertl. Complex pathways in dissociative adsorption of oxygen on platinum. *Nature*, 390:495–497, 1997.

[58] W. F. Lin, M. S. Zei, and G. Ertl. Identification of the structure of a CO adlayer on a Pt(111) electrode. *Chemical Physics Letters*, 312(1):1–6, 1999. doi:10.1016/S0009-2614(99)00899-4.

[59] V. V. Gorodetskii, A. V. Matveev, P. D. Cobden, and B. E. Nieuwenhuys. Study of H_2, O_2, CO adsorption and $CO+O_2$ reaction on Pt(100), Pd(110) monocrystal surfaces. *Journal of Molecular Catalysis A: Chemical*, 158(1):155–160, 2000. doi:10.1016/S1381-1169(00)00060-1.

[60] B. L. M. Hendriksen and J. W. M. Frenken. CO Oxidation on Pt(110): Scanning Tunneling Microscopy Inside a High-Pressure Flow Reactor. *Physical Review Letters*, 89:046101, 2002. doi:10.1103/PhysRevLett.89.046101.

[61] Denise C. Ford, Ye Xu, and Manos Mavrikakis. Atomic and molecular adsorption on Pt(1 1 1). *Surface Science*, 587(3):159–174, 2005. doi:10.1016/j.susc.2005.04.028.

[62] I. Nakai, H. Kondoh, K. Amemiya, M. Nagasaka, T. Shimada, R. Yokota, A. Nambu, and T. Ohta. Mechanism of the CO oxidation reaction on O-precovered Pt(111) surfaces studied with near-edge x-ray absorption fine structure spectroscopy. *Journal of Chemical Physics*, 122:134709, 2005. doi:10.1063/1.1869415.

[63] T. Shamim, H. Shen, S. Sengupta, S. Son, and A. A. Adamczyk. A Comprehensive Model to Predict Three-Way Catalytic Converter Performance. *Journal of Engineering for Gas Turbines and Power*, 124(2):421–428, 2002. doi:10.1115/1.1424295.

[64] B.C. Gates. Models of metal catalysts: beyond single crystals. *Topics in Catalysis*, 14(1-4):173–180, 2000. doi:10.1023/A:1009031722028.

[65] J.M.A. Harmsen, J.H.B.J. Hoebink, and J.C. Schouten. Acetylene and carbon monoxide oxidation over a Pt/Rh/CeO_2/γ-Al_2O_3 automotive exhaust gas catalyst: kinetic modelling of transient experiments. *Chemical Engineering Science*, 56(6):2019–2035, 2001. doi:10.1016/S0009-2509(00)00498-X.

[66] Daniel Chatterjee, Olaf Deutschmann, and Jürgen Warnatz. Detailed surface reaction mechanism in a three-way catalyst. *Faraday Discussions*, 119:371–384, 2001. doi:10.1039/b101968f.

[67] Mingyong Sun, Eric B. Croiset, Robert R. Hudgins, Peter L. Silveston, and Michael Menzinger. Steady-State Multiplicity and Superadiabatic Extinction Waves in the Oxidation of CO/H_2 Mixtures over a Pt/Al_2O_3-Coated Monolith. *Industrial & Engineering Chemistry Research*, 42(1):37–45, 2003. doi:10.1021/ie020310l.

[68] Per-Anders Carlsson, Lars Österlund, Peter Thormählen, Anders Palmqvist, Erik Fridell, Jonas Jansson, and Magnus Skoglundh. A transient in situ FTIR and XANES study of CO oxidation over Pt/Al_2O_3 catalysts. *Journal of Catalysis*, 226(2):422–434, 2004. doi:10.1016/j.jcat.2004.06.009.

[69] PROFIBUS. internet. `http://www.profibus.com`.

[70] Johannes G. Khinast, Alexander Bauer, David Bolz, and Anthony Panarello. Mass-transfer enhancement by static mixers in a wall-coated catalytic reactor. *Chemical Engineering Science*, 58(3-5):1063–1070, 2003. doi:10.1016/S0009-2509(02)00648-6.

[71] Jimmie L. Williams. Monolith structures, materials, properties and uses. *Catalysis Today*, 69(1-4):3–9, 2001. doi:10.1016/S0920-5861(01)00348-0.

[72] National Instruments. LabVIEW. software. `http://www.ni.com/labview/`.

[73] GNU Project. Bash. internet. `http://www.gnu.org/software/bash/bash.html`.

[74] Mathworks. Matlab. software. `http://www.mathworks.com/`.

[75] Systat Software Inc. SigmaPlot. software. `http://systat.com/products/SigmaPlot/`.

[76] David S. Lafyatis, Graham P. Ansell, Steven C. Bennett, Jonathan C. Frost, Paul J. Millington, Raj R. Rajaram, Andrew P. Walker, and Todd H. Ballinger. Ambient temperature light-off for automobile emission control. *Applied Catalysis B: Environmental*, 18(1-2):123–135, 1988. doi:10.1016/S0926-3373(98)00032-0.

[77] Robert Joumard and Michel Andre. Cold start emissions of traffic. *The Science of The Total Environment*, 93:175–182, 1990. doi:10.1016/0048-9697(90)90106-5.

[78] Jordan K. Lampert, M. Shahjahan Kazi, and Robert J. Farrauto. Palladium catalyst performance for methane emissions abatement from lean burn natural gas vehicles. *Applied Catalysis B: Environmental*, 14(3-4):211–223, 1997. doi:10.1016/S0926-3373(97)00024-6.

[79] Françoise Duprat. Light-off curve of catalytic reaction and kinetics. *Chemical Engineering Science*, 57(6):901–911, 2002. doi:10.1016/S0009-2509(01)00409-2.

[80] Karthik Ramanathan, Vemuri Balakotaiah, and David H. West. Light-off criterion and transient analysis of catalytic monoliths. *Chemical Engineering Science*, 58(8):1381–1405, 2003. doi:10.1016/S0009-2509(02)00679-6.

[81] Amornmart Sirijaruphan, James G. Goodwin Jr., and Richard W. Rice. Investigation of the initial rapid deactivation of platinum catalysts during the selective oxidation of carbon monoxide. *Journal of Catalysis*, 221(2):288–293, 2004. doi:10.1016/S0021-9517(03)00247-1.

[82] Stan T. Kolaczkowski. Modelling catalytic combustion in monolith reactors - challenges faced. *Catalysis Today*, 47(1-4):209–218, 1999. doi:10.1016/S0920-5861(98)00301-0.

[83] M. Balenovic, J.H.B.J. Hoebink, A.C.P.M. Backx, and A.J.L. Nievergeld. Modeling of an automotive exhaust gas converter at low temperatures, aiming at control application. *SAE*, 1999.

[84] Louise Olsson and Bengt Andersson. Kinetic Modelling in Automotive Catalysis. *Topics in Catalysis*, 28(1-4):89–98, 2004. doi:10.1023/B:TOCA.0000024337.50617.8e.

[85] N. Matthess, D. Schweich, B. Martin, and F. Castagna. From light-off curves to kinetic rate expressions for three-way catalysts. *Topics in Catalysis*, 16/17(1-4):119–124, 2001. doi:10.1023/A:1016695101135.

[86] I. Manuel, C. Thomas, H. Colas, N. Matthess, and G. Djéga-Mariadassou. A New Approach in the Kinetic Modelling of Three-Way Catalytic Reactions. *Topics in Catalysis*, 30/31:311–317, 2004. doi:10.1023/B:TOCA.0000029768.22036.88.

[87] J.H.B.J. Hoebink, J.M.A. Harmsen, M. Balenovic, A.C.P.M. Backx, and J.C. Schouten. Automotive exhaust gas conversion: from elementary step kinetics to prediction of emission dynamics. *Catalysis Today*, 16/17(1-4):319–327, 2001. doi:10.1023/A:1016609031602.

[88] E. S. Kurkina and N. L. Semendyaeva. Oscillatory Dynamics of CO Oxidation on Platinum-Group Metal Catalysts. *Kinetics and Catalysis*, 46(4):453–463, 2005. doi:10.1007/s10975-005-0098-4.

[89] B. Kasemo and E. Törnqvist. Weighing Fractions of Monolayers: Application to the Adsorption and Catalytic Reactions of H_2, CO, and O_2 on Pt. *Phys. Rev. Lett.*, 44:1555–1558, 1980. doi:10.1103/PhysRevLett.44.1555.

[90] W. Tieber, W. Athenstaedt, and M. Leisch. 3D-Atom-probe study of oxygen-adsorption on stepped platinum surfaces. *Fresenius' Journal of Analytical Chemistry*, 358(1-2):116–118, 1997. doi:10.1007/s002160050359.

[91] S.-J. Han, C.-W. Lee, H. Yoon, and H. Kang. Discovery of CO_2 precursor in the reaction of CO and O on Pt(111). *Journal of Chemical Physics*, 116(7):2684–2687, 2002. doi:10.1063/1.1449948.

[92] V. P. Zhdanov and B. Kasemo. Kinetic phase transitions in simple reactions on solid surfaces. *Surface Science Reports*, 29(3):113–189, 1994. doi:10.1016/0167-5729(94)90009-4.

[93] S. Raimondeau and D. G. Vlachos. The role of adsorbate-layer nonuniformities in catalytic reactor design: multiscale simulations for CO oxidation on Pt. *Computers & Chemical Engineering*, 26(7-8):965–980, 2002. doi:10.1016/S0098-1354(02)00021-2.

[94] K. M. Ogle and J. M. White. The low temperature water formation reaction on Pt(111): A static SIMS and TDS study. *Surface Science*, 139(1):43–62, 1984. doi:10.1016/0039-6028(84)90007-4.

[95] Laurens K. Verheij and Markus B. Hugenschmidt. Hydrogen adsorption on oxygen covered Pt(111). *Surface Science*, 324(2-3):185–201, 1995. doi:10.1016/0039-6028(94)00697-0.

[96] R. H. Nibbelke, M. A. J. Campman, J. H. B. J. Hoebink, and G. B. Marin. Kinetic Study of the CO Oxidation over Pt/γ-Al_2O_3 and Pt/Rh/CeO_2/γ-Al_2O_3 in the Presence of H_2O and CO_2. *Journal of Catalysis*, 171(2):358–373, 1997. doi:10.1006/jcat.1997.1785.

[97] Abdennour Bourane and Daniel Bianchi. Oxidation of CO on a Pt/Al_2O_3 Catalyst: From the Surface Elementary Steps to Light-Off Tests I. Kinetic Study of the Oxidation of the Linear CO Species. *Journal of Catalysis*, 202(1):34–44, 2001. doi:10.1006/jcat.2001.3242.

[98] Rob H. Nibbelke. *Steady state, transient and non-linear kinetics in automotive exhaust gas catalysis*. PhD thesis, Technische Universiteit Eindhoven, 1998. `http://alexandria.tue.nl/extra2/9801572.pdf`.

[99] L.S. Mukadi and R.E. Hayes. Modelling the three-way catalytic converter with mechanistic kinetics using the Newton-Krylov method on a parallel computer. *Computers and Chemical Engineering*, 26(3):439–455, 2002. doi:10.1016/S0098-1354(01)00763-3.

[100] Jan Harmsen. *Kinetic Modelling of the Dynamic Behaviour of an Automotive Three-Way Catalyst under Cold-Start Conditions*. PhD thesis, Technische Universiteit Eindhoven, 2001. `http://alexandria.tue.nl/extra2/200113165.pdf`.

[101] Gerardine G. Botte, James A. Ritter, and Ralph E. White. Comparison of finite difference and control volume methods for solving differential equations. *Computers*

& Chemical Engineering, 24(12):2633–2654, 2000. doi:10.1016/S0098-1354(00)00619-0.

[102] Hewlet Packard. Fortran. software. `http://www.hp.com/go/fortran`.

[103] Abdennour Bourane and Daniel Bianchi. Oxidation of CO on a Pt/Al_2O_3 Catalyst: From the Surface Elementary Steps to Light-Off Tests II. Kinetic Study of the Oxidation of Adsorbed CO Species Using Mass Spectroscopy. *Journal of Catalysis*, 209(1):114–125, 2002. doi:10.1006/jcat.2002.3605.

[104] A. Bourane, O. Dulaurent, and D. Bianchi. Heats of Adsorption of Linear and Multibound Adsorbed CO Species on a Pt/Al2O3 Catalyst Using in Situ Infrared Spectroscopy under Adsorption Equilibrium. *Journal of Catalysis*, 196(1):115–125, 2000. doi:10.1006/jcat.2000.3030.

[105] Prisca Pillonel, Salim Derrouiche, Abdennour Bourane, François Gaillard, Philippe Vernoux, and Daniel Bianchi. Impact of the support on the heat of adsorption of the linear CO species on Pt-containing catalysts. *Applied Catalysis A: General*, 278(2):223–231, 2005. doi:10.1016/j.apcata.2004.10.001.

[106] Abdennour Bourane, Salim Derrouiche, and Daniel Bianchi. Impact of Pt dispersion on the elementary steps of CO oxidation by O2 over Pt/Al_2O_3 catalysts. *Journal of Catalysis*, 228(2):265–468, 2004. doi:10.1016/j.jcat.2004.08.020.

[107] OriginLab Corporation. Origin. software. `http://www.originlab.com`.

[108] S. Salomons, R.E. Hayes, M. Votsmeier, A. Drochner, H. Vogel, S. Malmberg, and J. Gieshof. On the use of mechanistic CO oxidation models with a platinum monolith catalyst. *Applied Catalysis B: Environmental*, 70(1-4):305–313, 2007. doi:10.1016/j.apcatb.2006.01.022.

[109] Stephen Salomons, Alfons Drochner, Herbert Vogel, Martin Votsmeier, Stephan Malmberg, Jürgen Gieshoff, and R.E. Hayes. Validation of CO oxidation models for a Pt diesel oxidation catalyst. In *4th International Conference on Environmental Catalysis, Heidelberg, Germany*, June 2005. 4th International Conference on Environmental Catalysis `http://ssalomons.fastmail.fm/200506-Salomons_et_al-Heidelberg_ICEC4_poster-CO_oxidation_models.pdf`.

[110] Irving Langmuir. Part II - Heterogeneous reactions - Chemical reactions on surfaces. *Transactions of the Faraday Society*, 17:607–620, 1922. doi:10.1039/TF9221700607.

[111] Irving Langmuir. The mechanism of the catalytic action of platinum in the reactions $2CO + O_2 = 2CO_2$ and $2H_2 + O_2 = 2H_2O$. *Transactions of the Faraday Society*, 17:621–654, 1922. doi:10.1039/TF9221700621.

[112] Hiromichi Arai and Masato Machida. Thermal stabilization of catalyst supports and their application to high-temperature catalytic combustion. *Applied Catalysis A: General*, 131(2):161–176, 1996. doi:10.1016/0926-860X(95)00294-4.

[113] Ronald M. Heck, Suresh Gulati, and Robert J. Farrauto. The application of monoliths for gas phase catalytic reactions. *Chemical Engineering Journal*, 82(1-3):149–156, 2001. doi:10.1016/S1385-8947(00)00365-X.

[114] T. Haakana, E. Kolehmainen, I. Turunen, J.-P. Mikkola, and T. Salmi. The development of monolith reactors: general strategy with a case study. *Chemical Engineering Science*, 59(22-23):5629–5635, 2004. doi:10.1016/j.ces.2004.07.112.

[115] Pedro Avila, Mario Montes, and Eduardo E. Miró. Monolithic reactors for environmental applications - A review on preparation technologies. *Chemical Engineering Journal*, 109(1-3):11–36, 2005. doi:10.1016/j.cej.2005.02.025.

[116] M.G. Poirier, H. Sapoundjiev, S. Salomons, and R.E. Hayes. Pressure drop reduction by using monolith in a pilot-scale flow reversal reactor. In *CSC2002 Vancouver*, June 2002. CSC2002 Vancouver CA2 IRC 1 Environmental Catalysis 14:20 00490.

[117] Barbara Marinacci. *Linus Pauling in His Own Words : Selections From his Writings, Speeches and Interviews*. Touchstone, 1995. ISBN 0684813874.

[118] webmineral.com. Cordierite mineral data. internet, May 2004. `http://web.archive.org/web/*/http://webmineral.com/data/Cordierite.shtm`.

[119] Wikipedia. Cordierite. internet.

[120] Keisuke Tashiro, Shigeru Ito, Akiko Oba, and Tomohiro Yokomizo. Development of oxidation catalyst for diesel passenger car. *JSAE Review*, 16(2):131–136, 1995. doi:10.1016/0389-4304(95)00005-R.

[121] Li Xiao, Peiyan Lin, Wendong Wang, Zhibo Yang, Yilu Fu, and Shouming Yu. A novel preparation route of three-way catalysts. *Topics in Catalysis*, 16/17(1-4):107–113, 2001. doi:10.1023/A:1016691000226.

[122] Karl Arnby, Johan Assiks, Per-Anders Carlsson, Anders Palmqvist, and Magnus Skoglundh. The effect of platinum distribution in monolithic catalysts on the oxidation of CO and hydrocarbons. *Journal of Catalysis*, 233(1):176–185, 2005. doi:10.1016/j.jcat.2005.04.031.

[123] Pio Forzatti and Luca Lietti. Catalyst deactivation. *Catalysis Today*, 52(2-3):165–181, 1999. doi:10.1016/S0920-5861(99)00074-7.

[124] Ulla Lassi. *Deactivation Correlations of Pd/Rh Three-way Catalysts Designed for Euro IV Emission Limits - Effect of Ageing Atmosphere, Temperature and Time.* PhD thesis, Department of Process and Environmental Engineering, University of Oulu, University of Oulu, Oulu Finland 2003, February 2003. `http://herkules.oulu.fi/isbn9514269543/`.

[125] Anna Holmgren. Monolith catalysts for car exhaust: experimental and theoretical studies of oxygen storage, flow and mass transfer. Licentiate thesis, Department of Chemical Reaction Engineering, Chalmers University of Technology, Göteborg, Sweden, 1997. `http://www.cre.chalmers.se/staff/old_phd/anna/lic/lic_avh/liccover.htm`.

[126] F. Cabello Galisteo, R. Mariscal, M. López Granados, J.L.G. Fierro, R.A. Daley, and J.A. Anderson. Reactivation of sintered Pt/Al_2O_3 oxidation catalysts. *Applied Catalysis B: Environmental*, 59(3-4):227–233, 2005. doi:10.1016/j.apcatb.2005.02.004.

[127] H.-J. Freund and M.W. Roberts. Surface chemistry of carbon dioxide. *Surface Science Reports*, 25(8):225–273, 1996. doi:10.1016/S0167-5729(96)00007-6.

[128] R. Rajasree, J. H. B. J. Hoebink, and J. C. Schouten. Transient kinetics of carbon monoxide oxidation by oxygen over supported palladium/ceria/zirconia three-way catalysts in the absence and presence of water and carbon dioxide. *Journal of Catalysis*, 223(1):36–43, 2004. doi:10.1016/j.jcat.2003.12.014.

[129] H. Conrad, G. Ertl, and J. Küppers. Interactions between oxygen and carbon monoxide on a Pd(111) surface. *Surface Science*, 76(2):323, 1978. doi:10.1016/0039-6028(78)90101-2.

[130] T. Engel and G. Ertl. *Advances in Catalysis*, volume 28, chapter Elementary Steps in the Catalytic Oxidation of Carbon Monoxide on Platinum Metals, pages 1–78. Elsevier Inc., 1979. ISBN 0-12-007828-7.

[131] G. Rupprechter, T. Dellwig, H. Unterhalt, and H.-J. Freund. CO adsorption on Ni(100) and Pt(111) studied by infrared-visible sum frequency generation spectroscopy: design and application of an SFG-compatible UHV-high-pressure reaction cell. *Topics in Catalysis*, 15(1):19–26, 2001. doi:10.1023/A:1009063611629.

[132] Claus D. Makowka, Charles P. Slichter, and J. H. Sinfelt. Probe of the Surface of a Heterogeneous Catalyst: Double NMR of Carbon Monoxide Chemisorbed on Highly Dispersed Platinum. *Physical Review Letters*, 49(6):379–382, 1982. doi:10.1103/PhysRevLett.49.379.

[133] A. K. Santra and D. W. Goodman. Catalytic oxidation of CO by platinum group metals: from ultrahigh vacuum to elevated pressures. *Electrochimica Acta*, 47(22-23):3595–3609, 2002. doi:10.1016/S0013-4686(02)00330-4.

[134] András Szabó, Michael A. Henderson, and John T. Yates Jr. Oxidation of CO by oxygen on a stepped platinum surface: Identification of the reaction site. *The Journal of Chemical Physics*, 96(8):6191–6202, 1992. doi:10.1063/1.462636.

[135] J. H. Craig, Jr. and J. L. Hock. ESD study of CO adsorbed on platinum. *Surface Science*, 102(1):89–98, 1981. doi:10.1016/0039-6028(81)90309-5.

[136] Laura C. Nett-Carrington and Richard K. Herz. Spatiotemporal patterns within a porous catalyst: dynamic carbon monoxide oxidation in a single-pellet reactor. *Chemical Engineering Science*, 57(8):1459–1474, 2002. doi:10.1016/S0009-2509(02)00046-5.

[137] Abdennour Bourane, Olivier Dulaurent, and Daniel Bianchi. Comparison of the Coverage of the Linear CO Species on Pt/Al_2O_3 Measured under Adsorption Equilibrium Conditions by Using FTIR and Mass Spectroscopy. *Journal of Catalysis*, 195(2):406–411, 2000. doi:10.1006/jcat.2000.2962.

[138] G. Ertl, M. Neumann, and K. M. Streit. Chemisorption of CO on the Pt(111) surface. *Surface Science*, 64(2):393–410, 1977. doi:10.1016/0039-6028(77)90052-8.

[139] M. M. Schubert, M. J. Kahlich, H. A. Gasteiger, and R. J. Behm. Correlation between CO surface coverage and selectivity/kinetics for the preferential CO oxidation over $Pt/\gamma\text{-}Al_2O_3$ and $Au/\alpha\text{-}Fe_2O_3$: an in-situ DRIFTS study. *Journal of Power Sources*, 84(2):175–182, 1999. doi:10.1016/S0378-7753(99)00314-6.

[140] Edward J. Bissett, Se H. Oh, and Robert M. Sinkevitch. Pt surface kinetics for a PrOx reactor for fuel cell feedstream processing. *Chemical Engineering Science*, 60(17):4709–4721, 2005. doi:10.1016/j.ces.2005.02.069.

[141] P. R. Norton, J. A. Davies, and T. E. Jackman. Absolute coverages of CO and O on Pt(111); Comparison of saturation CO coverages on Pt(100), (110) and (111) surfaces. *Surface Science*, 122(1):L593–L600, 1982. doi:10.1016/0039-6028(82)90054-1.

[142] M. J. Kahlich, H. A. Gasteiger, and R. J. Behm. Kinetics of the Selective CO Oxidation in H_2-Rich Gas on Pt/Al_2O_3. *Journal of Catalysis*, 171(1):93–105, 1997. doi:10.1006/jcat.1997.1781.

[143] G.S. Zafiris and R.J. Gorte. CO Oxidation on $Pt/\alpha\text{-}Al_2O_3(0001)$: Evidence for Structure Sensitivity. *Journal of Catalysis*, 140(2):418–423, 1993. doi:10.1006/jcat.1993.1095.

[144] A.B. Mhadeshwar and D.G. Vlachos. A thermodynamically consistent surface reaction mechanism for CO oxidation on Pt. *Combustion and Flame*, 142(3):289–298, 2005. doi:10.1016/j.combustflame.2005.01.019.

7

[145] Daniel Chatterjee. *Detaillierte Modellierung von Abgaskatalysatoren // Detailed Modeling of Automotive Catalytic Converters*. PhD thesis, Interdisziplinäres Zentrum für Wissenschaftliches Rechnen (IWR) Fakultät für Chemie und Geowissenschaften, October 2001. `http://www.ub.uni-heidelberg.de/archiv/1799`.

[146] David K. Zerkle, Mark D. Allendorf, Markus Wolf, and Olaf Deutschmann. Understanding Homogeneous and Heterogeneous Contributions to the Platinum-Catalyzed Partial Oxidation of Ethane in a Short-Contact-Time Reactor. *Journal of Catalysis*, 196(1):18–39, 2000. doi:10.1006/jcat.2000.3009.

[147] Paul J. Berlowitz, Charles H. F. Peden, and D. Wayne Goodman. Kinetics of carbon monoxide oxidation on single-crystal palladium, platinum, and iridium. *Journal of Physical Chemistry*, 92(18):5213 – 5221, 1988. doi:10.1021/j100329a030.

[148] O. Deutschmann, R. Schmidt, F. Behrendt, and J. Warnatz. Numerical Modeling of Catalytic Ignition. *Symposium (International) on Combustion*, 26:1747–1754, 1996.

[149] Richard K. Herz and Samuel P. Marin. Surface chemistry models of carbon monoxide oxidation on supported platinum catalysts. *Journal of Catalysis*, 65(2):281–296, 1980. doi:10.1016/0021-9517(80)90306-1.

[150] Rob H. Nibbelke, Arthur J. L. Nievergeld, Jozef H. B. J. Hoebink, and Guy B. Marin. Development of a transient kinetic model for the CO oxidation by O_2 over a $Pt/Rh/CeO_2/\gamma$-Al_2O_3 three-way catalyst. *Applied Catalysis B: Environmental*, 19(3-4):245–259, 1998. doi:10.1016/S0926-3373(98)00076-9.

[151] Petr Kocí, Frantisek Stepánek, Milan Kubícek, and Milos Marek. Meso-scale modelling of CO oxidation in digitally reconstructed porous Pt/γ-Al_2O_3 catalyst. *Chemical Engineering Science*, 61(10):3240–3249, 2006. doi:10.1016/j.ces.2005.12.008.

[152] B. C. Stipe, M. A. Rezaei, and W. Ho. Atomistic studies of O_2 dissociation on Pt(111) induced by photons, electrons, and by heating. *The Journal of Chemical Physics*, 107(16):6443–6447, 1997. doi:10.1063/1.474304.

[153] Martin Berdau, Stefan Moldenhauer, Ayman Hammoudeh, Jochen H. Block, and Klaus Christmann. Interaction of oxygen with Pt(210): formation of new oxygen states at higher exposures. *Surface Science*, 446(3):323–333, 2000. doi:10.1016/S0039-6028(99)01173-5.

[154] Abdennour Bourane and Daniel Bianchi. Oxidation of CO on a Pt/Al_2O_3 Catalyst: From the Surface Elementary Steps to Light-Off Tests V. Experimental and kinetic model for light-off tests in excess of O_2. *Journal of Catalysis*, 222(2):499–510, 2004. doi:10.1016/j.jcat.2003.11.019.

[155] Salim Derrouiche and Daniel Bianchi. Experiments and kinetic model regarding the induction period observed during the oxidation by O_2 of adsorbed CO species on Pt/Al_2O_3 catalysts. *Journal of Catalysis*, 230(2):359–374, 2005. doi:10.1016/j.jcat.2004.12.011.

[156] Frank Eisert and Arne Rosén. In situ investigation of the catalytic reaction $H_2 + 1/2O_2 \rightarrow H_2O$ on Pt(111) with second-harmonic generation. *Phys. Rev. B*, 54(19):14061–14065, 1996. doi:10.1103/PhysRevB.54.14061.

[157] P. Légaré. Interaction of oxygen with the Pt(1 1 1) surface in wide conditions range. A DFT-based thermodynamical simulation. *Surface Science*, 580(1-3):137–144, 2005. doi:10.1016/j.susc.2005.02.017.

[158] John L. Gland, Galen B. Fisher, and Edward B. Kollin. The hydrogen-oxygen reaction over the Pt(111) surface: Transient titration of adsorbed oxygen with hydrogen. *Journal of Catalysis*, 77(1):263–278, 1982. doi:10.1016/0021-9517(82)90167-1.

[159] W. X. Li, L. Osterlund, E. K. Vestergaard, R. T. Vang, J. Matthiesen, T. M. Pedersen, E. Laegsgaard, B. Hammer, and F. Besenbacher. Oxidation of Pt(110). *Physical Review Letters*, 93(14):146104, 2004. doi:10.1103/PhysRevLett.93.146104.

[160] Zhenping Qu, Mojie Cheng, Weixin Huang, and Xinhe Bao. Formation of subsurface oxygen species and its high activity toward CO oxidation over silver catalysts. *Journal of Catalysis*, 229(2):446–458, 2005. doi:10.1016/j.jcat.2004.11.043 S0021-9517(04)00566-4.

[161] Grazyna Antczak and Gert Ehrlich. The beginnings of surface diffusion studies. *Surface Science*, 589(1-3):52–66, 2005. doi:10.1016/j.susc.2005.05.049.

[162] J. Wintterlin, R. Schuster, and G. Ertl. Existence of a 'hot' atom mechanism for the dissociation of O_2 on Pt(111). *Phys. Rev. Lett.*, 77:123–126, 1996. doi:10.1103/PhysRevLett.77.123.

[163] J. R. Stetter and K. F. Blurton. Selective Oxidation of Hydrogen in Carbon Monoxide/Air Streams. Application to Environmental Monitoring. *Ind. Eng. Chem. Prod. Res. Dev.*, 16(1):22–25, 1977. `http://pubs.acs.org/cgi-bin/archive.cgi/iepra6/1977/16/i01/pdf/i360061a004.pdf`.

[164] J. Hall, I. Zoric, and B. Kasemo. Reaction of fast CO molecules with CO, NO or O_2 preadsorbed on Pt(111) surface; a search for Eley-Rideal reaction mechanism. *Surface Science*, 269-270:460–464, 1992. doi:10.1016/0039-6028(92)91292-J.

[165] A. Eichler and J. Hafner. Reaction channels for the catalytic oxidation of CO on Pt(111). *Physical Review B*, 59(8):5960–5967, 1999. doi:10.1103/PhysRevB.59.5960.

[166] A. V. Walker and D. A. King. Reaction of gaseous oxygen with adsorbed carbon on Pt(110)(1x2). *Journal of Chemical Physics*, 112(4):1937–1945, 2000. doi:10.1063/1.480822.

[167] Xue-Qing Gong, P. Hu, and R. Raval. The catalytic role of water in CO oxidation. *Journal of Chemical Physics*, 119(12):6324–6334, 2003. doi:10.1063/1.1602053.

[168] V. F. Kharlamov. Chemisorbed Atoms and Molecules of Reactants As Active Sites in Heterogeneous Catalysis. *Kinetics and Catalysis*, 46(4):464–471, 2005. doi:10.1007/s10975-005-0099-3.

[169] G. Padmavathi, K.K. Chaudhuri, D. Rajeshwer, G. Sreenivasa Rao, K.R. Krishnamurthy, P.C. Trivedi, K.K. Hathi, and N. Subramanyam. Kinetics of n-dodecane dehydrogenation on promoted platinum catalyst. *Chemical Engineering Science*, 60(15):4119–4129, 2005. doi:10.1016/j.ces.2005.01.039.

[170] O. Pozdnyakova, D. Teschner, A. Wootsch, J. Kröhnert, B. Steinhauer, H. Sauer, L. Toth, F.C. Jentoft, A. Knop-Gericke, Z. Paál, and R. Schlögl. Preferential CO oxidation in hydrogen (PROX) on ceria-supported catalysts, part I: Oxidation state and surface species on Pt/CeO_2 under reaction conditions. *Journal of Catalysis*, 237(1):1–16, 2006. doi:10.1016/j.jcat.2005.10.014.

[171] R. A. Shigeishi and David A. King. The oxidation of carbon monoxide on platinum 111: Reflection-absorption infrared spectroscopy. *Surface Science*, 75(2):L397–L400, 1978. doi:10.1016/0039-6028(78)90264-9.

[172] R. J. Baxter and P. Hu. Insight into why the langmuir-hinshelwood mechanism is generally preferred. *The Journal of Chemical Physics*, 116(11):4379–4381, 2002. doi:10.1063/1.1458938.

[173] V. Nevoral, P. Kocí, M. Kubícek, I. Schreiber, and M. Marek. Continuation and bifurcations in TWC microkinetics. `http://www.phy.bme.hu/deps/chem_ph/Etc/Reactor2003/posters/Nevoral.pdf`, 2003.

[174] Petr Kocí, Milan Kubícek, and Milos Marek. Periodic forcing of three-way catalyst with diffusion in the washcoat. *Catalysis Today*, 98(3):345–355, 2004. doi:10.1016/j.cattod.2004.08.002.

[175] Petr Kocí, Vladislav Nevoral, Martin Záhrubský, Milan Kubícek, and Milos Marek. Nonlinear dynamics of automobile exhaust gas converters: the role of nonstationary kinetics. *Chemical Engineering Science*, 59(22-23):5597–5605, 2004. doi:10.1016/j.ces.2004.07.115.

[176] Appendix. Oscillatory Heterogeneous Catalytic Systems. *Catalysis Today*, 105(2):I–II, 2005. doi:10.1016/S0920-5861(05)00345-7.

[177] P. Hugo and M. Jakubith. Dynamisches Verhalten und Kinetik der Kohlenmonoxid-Oxidation am Platin-Katalysator. *Chemie Ingenieur Technik*, 44(6):383–387, 1972. doi:10.1002/cite.330440608.

[178] H. Beusch, P. Fieguth, and E. Wicke. Thermisch und kinetisch verursachte Instabilitäten im Reaktionsverhalten einzelner Katalysatorkörner. *Chemie Ingenieur Technik*, 44(7):445–451, 1972. doi:10.1002/cite.330440702.

[179] Anca Faur Ghenciu. Review of fuel processing catalysts for hydrogen production in PEM fuel cell systems. *Current Opinion in Solid State and Materials Science*, 6(5):389–399, 2002. doi:10.1016/S1359-0286(02)00108-0.

[180] Patricia K. Tsai, Ming G. Wu, and M. Brian Maple. Oscillatory oxidation of CO over Pt at pressures from 10 to 760 torr. *Journal of Catalysis*, 127(2):512–523, 1991. doi:10.1016/0021-9517(91)90181-3.

[181] G. Ertl, P. R. Norton, and J. Rüstig. Kinetic Oscillations in the Platinum-Catalyzed Oxidation of CO. *Physical Review Letters*, 49(2):177–180, 1982. doi:10.1103/PhysRevLett.49.177.

[182] David T. Lynch and Sieghard E. Wanke. Oscillations during CO oxidation over supported metal catalysts III. Mathematical modeling of the observed phenomena. *Journal of Catalysis*, 97(2):456–468, 1986. doi:10.1016/0021-9517(86)90017-5.

[183] B.L.M. Hendriksen, S.C. Bobaru, and J.W.M. Frenken. Bistability and oscillations in CO oxidation studied with scanning tunnelling microscopy inside a reactor. *Catalysis Today*, 105(2):234–243, 2005. doi:10.1016/j.cattod.2005.02.041.

[184] B. C. Sales, J. E. Turner, and M. B. Maple. Oscillatory oxidation of CO over Pt, Pd and Ir catalysts: Theory. *Surface Science*, 114(2-3):381–394, 1982. doi:10.1016/0039-6028(82)90692-6.

[185] J. Wintterlin, S. Völkening, T. V. W. Janssens, T. Zambelli, and G. Ertl. Atomic and Macroscopic Reaction Rates of a Surface-Catalyzed Reaction. *Science*, 278:1931–1934, 1997. doi:10.1126/science.278.5345.1931.

[186] Masanari Nagasaka, Hiroshi Kondoh, Ikuyo Nakai, and Toshiaki Ohta. Oxygen island formation on Pt(111) studied by dynamic Monte Carlo simulation. *Journal of Chemical Physics*, 122:044715, 2005. doi:10.1063/1.1835270.

[187] V. A. Burrows, S. Sundaresan, Y. J. Chabal, and S. B. Christman. Studies on self-sustained reaction-rate oscillations II. The role of carbon and oxides in the oscillatory oxidation of carbon monoxide on platinum. *Surface Science*, 180(1):110–135, 1987. doi:10.1016/0039-6028(87)90039-2.

[188] C. D. Lund, C. M. Surko, M. B. Maple, and S. Y. Yamamoto. Model discrimination in oscillatory CO oxidation on platinum catalysts at atmospheric pressure. *Surface Science*, 459(3):413–425, 2000. doi:10.1016/S0039-6028(00)00482-9.

[189] J. Lauterbach, K. Asakura, and H. H. Rotermund. Subsurface oxygen on Pt(100): kinetics of the transition from chemisorbed to subsurface state and its reaction with CO, H_2 and O_2. *Surface Science*, 313(1-2):52–63, 1994. doi:10.1016/0039-6028(94)91156-8.

[190] A. von Oertzen, A. Mikhailov, H. H. Rotermund, and G. Ertl. Subsurface oxygen in the CO oxidation reaction on Pt(110): Experiments and mathematical modelling. *J. Phys. Chem. B.*, 102(25):4966–4981, 1998. doi:10.1021/jp981285t.

[191] Harm Hinrich Rotermund, Michael Pollmann, and Ioannis G. Kevrekidis. Pattern formation during the CO-oxidation involving subsurface oxygen. *Chaos: An Interdisciplinary Journal of Nonlinear Science*, 12(1):157–163, 2002. doi:10.1063/1.1448809.

[192] Noah McMillan, Tanmay Lele, Christopher Snively, and Jochen Lauterbach. Subsurface oxygen formation on Pt(1 0 0): Experiments and modeling. *Catalysis Today*, 104(2):244–253, 2005. doi:10.1016/j.cattod.2005.02.042.

[193] N. A. Collins, S. Sundaresan, and Y. J. Chabal. Studies on self-sustained reaction-rate oscillations III. The carbon model. *Surface Science*, 180(1):136–152, 1987. doi:10.1016/0039-6028(87)90040-9.

[194] Geoffrey R. Wilson and W. Keith Hall. Studies of the hydrogen held by solids XVIII. Hydrogen and oxygen chemisorption on alumina- and zeolite-supported platinum. *Journal of Catalysis*, 17(2):190–206, 1970. doi:10.1016/0021-9517(70)90091-6.

[195] Geoffrey R. Wilson and W. Keith Hall. Studies of the hydrogen held by solids. XIX. H_2 and O_2 chemisorption on silica-supported platinum. *Journal of Catalysis*, 24(2):306–314, 1972. doi:10.1016/0021-9517(72)90074-7.

[196] David T. Lynch and Sieghard E. Wanke. Oscillations during CO oxidation over supported metal catalysts I. Influence of catalyst history on activity. *Journal of Catalysis*, 88(2):333–344, 1984. doi:10.1016/0021-9517(84)90010-1.

[197] M. Eiswirth, J. Bürger, P. Strasser, and G. Ertl. Oscillating Langmuir-Hinshelwood Mechanisms. *Journal of Physical Chemistry*, 100(49):19118–19123, 1996. doi:10.1021/jp961688y.

[198] A. von Oertzen, A. Mikhailov, H. H. Rotermund, and G. Ertl. Subsurface oxygen formation on the Pt(110) surface: experiment and mathematical modeling. *Surface Science*, 350(1-3):259–270, 1996. doi:10.1016/0039-6028(95)01276-1.

[199] R. Kissel-Osterrieder, F. Behrendt, J. Warnatz, U. Metka, H.-R. Volpp, and J. Wolfrum. Experimental and Theoretical Investigations of CO Oxidation on Platinum: Bridging the Pressure and Materials Gap. *Proceedings of the Combustion Institute*, 28:1341–1348, 2000. `http://www.pci.uni-heidelberg.de/pci/hvolpp/d_hvpublic/51_syc00.pdf`.

[200] Keith R. McCrea, Jessica S. Parker, and Gabor A. Somorjai. The Role of Carbon Deposition from CO Dissociation on Platinum Crystal Surfaces during Catalytic CO Oxidation: Effects on Turnover Rate, Ignition Temperature, and Vibrational Spectra. *Journal of Physical Chemistry B*, 106(42):10854–10863, 2002. doi:10.1021/jp014679k S1089-5647(01)04679-X.

[201] Markus M. Schubert, Hubert A. Gasteiger, and R. Jürgen Behm. Surface Formates as Side Products in the Selective CO Oxidation on Pt/γ-Al_2O_3. *Journal of Catalysis*, 172(1):256–258, 1997. doi:10.1006/jcat.1997.1856.

[202] Zoltán Paál, Attila Wootsch, Robert Schlögl, and Ute Wild. Carbon accumulation, deactivation and reactivation of Pt catalysts upon exposure to hydrocarbons. *Applied Catalysis A: General*, 282(1-2):135–145, 2005. doi:10.1016/j.apcata.2004.12.027.

[203] Adriana D. Ballarini, Sergio R. de Miguel, Estanislao L. Jablonski, Osvaldo A. Scelza, and Alberto A. Castro. Reforming of CH_4 with CO_2 on Pt-supported catalysts - Effect of the support on the catalytic behaviour. *Catalysis Today*, 107-108:481–486, 2005. doi:10.1016/j.cattod.2005.07.058.

[204] Abolghasem Shamsi and Christopher D. Johnson. Effect of pressure on the carbon deposition route in CO_2 reforming of $^{13}CH_4$. *Catalysis Today*, 84(1-2):17–25, 2003. doi:10.1016/S0920-5861(03)00296-7.

[205] Abdennour Bourane and Daniel Bianchi. Oxidation of CO on a Pt/Al_2O_3 Catalyst: From the Surface Elementary Steps to Light-Off Tests III. Experimental and Kinetic Model for Lights-Off Tests in Excess CO. *Journal of Catalysis*, 209(1):126–134, 2002. doi:10.1006/jcat.2002.3606.

[206] A. Brad Anton and David C. Cadogan. The mechanism and kinetics of water formation on Pt(111). *Surface Science*, 239(3):L548–L560, 1990. doi:10.1016/0039-6028(90)90217-V.

[207] Stephen Salomons, Martin Votsmeier, R.E. Hayes, Alfons Drochner, Herbert Vogel, and Jürgen Gieshoff. CO+H_2 Oxidation on a Pt based Monolith Diesel Oxidation Catalyst. *Catalysis Today*, 117(4):491–497, 2006. doi:10.1016/j.cattod.2006.06.001.

[208] Stephen Salomons, R.E. Hayes, Alfons Drochner, Herbert Vogel, Martin Votsmeier, and Jürgen Gieshoff. Validation of CO+H_2 Oxidation Models for a Pt-based Monolith Diesel Oxidation Catalyst. In *6th International Workshop on Catalytic Combustion, Ischia, Italy*. 6th International Workshop on Catalytic Combustion (IWCC 6), September 2005. 6th International Workshop on Catalytic Combustion (IWCC 6).

[209] J. W. Döbereiner. *J. Chem. (Schweiger)*, 38(1):321, 1823.

[210] George B. Kauffman. Johann Wolfgang Dobereiner's Feuerzeug. *Platinum Metals Review*, 43(3):122–128, 1999.

[211] J. N. Armor. Catalysis and the hydrogen economy. *Catalysis Letters*, 101(3-4):131 – 135, 2005. doi:10.1007/s10562-005-4877-3.

[212] G. E. Gdowski and R. J. Madix. The kinetics and mechanism of the hydrogen-oxygen reaction on Pt(S)-[9(111) x (100)]. *Surface Science*, 119(2-3):184–206, 1982. doi:10.1016/0039-6028(82)90292-8.

[213] Miquel Salmeron. The Nature of the Catalytic Sites for H_2 Dissociation. *Topics in Catalysis*, 36(1-4):55–63, 2005. doi:10.1007/s11244-005-7862-6.

[214] S. Horch, H. T. Lorensen, S. Helveg, E. Laegsgaard, I. Stensgaard, K. W. Jacobsen, J. K. Nørskov, and F. Besenbacher. Enhancement of surface self-diffusion of platinum atoms by adsorbed hydrogen. *Nature*, 398:134–136, 1999. doi:10.1038/18185.

[215] T. Wahnström, E. Fridell, S. Ljungström, B. Hellsing, B. Kasemo, and A. Rosén. Determination of the activation energy for OH desorption in the H_2 + O_2 reaction on Polycrystalline Platinum. *Surface Science*, 223(3):L905–L912, 1989. doi:10.1016/0039-6028(89)90662-6.

[216] S. Ljungström, B. Kasemo, A. Rosen, T. Wahnström, and E. Fridell. An experimental study of the kinetics of OH and H_2O formation on Pt in the H_2 + O_2 reaction. *Surface Science*, 216(1-2):63–92, 1989. doi:10.1016/0039-6028(89)90644-4.

[217] W. R. Williams, C. M. Marks, and L. D. Schmidt. Steps in the reaction hydrogen + oxygen .dblharw. water on platinum: hydroxy desorption at high temperatures. *Journal of Physical Chemistry*, 96(14):5922–5931, 1992. doi:10.1021/j100193a051.

[218] Seyed-A. Seyed-Reihani and Gregory S. Jackson. Effectiveness in catalytic washcoats with multi-step mechanisms for catalytic combustion of hydrogen. *Chemical Engineering Science*, 59(24):5937–5948, 2004. doi:10.1016/j.ces.2004.07.028.

[219] Jazaer Dawody, Lisa Eurenius, Hussam Abdulhamid, Magnus Skoglundh, Eva Olsson, and Erik Fridell. Platinum dispersion measurements for $Pt/BaO/Al_2O_3$, NO_x storage catalysts. *Applied Catalysis A: General*, 296(2):157–168, 2005. doi:10.1016/j.apcata.2005.07.060.

[220] S. Völkening, K. Bedürftig, K. Jacobi, J. Wintterlin, and G. Ertl. Dual-Path Mechanism for Catalytic Oxidation of Hydrogen on Platinum Surfaces. *Physical Review Letters*, 83:2672–2675, 1999. doi:10.1103/PhysRevLett.83.2672.

[221] P. V. Snytnikov, V. A. Belyaev, and V. A. Sobyanin. Kinetic model and mechanism of the selective oxidation of co in the presence of hydrogen on platinum catalysts. *Kinetics and Catalysis*, 48(1):93–102, 2007. doi:10.1134/S0023158407010132.

[222] J. Harris, B. Kasemo, and E. Törnqvist. The water reaction on platinum: An example of a precursor mechanism? *Surface Science*, 105(2-3):L288–L296, 1981. doi:10.1016/0039-6028(81)90005-4.

[223] Cristina Pedrero, Toshio Waku, and Enrique Iglesia. Oxidation of CO in H_2-CO mixtures catalyzed by platinum: Alkali effects on rates and selectivity. *Journal of Catalysis*, 233(1):242–255, 2005. doi:10.1016/j.jcat.2005.04.005.

[224] Christian Sachs. *Untersuchung von Reaktionsmechanismen auf Oberflächen mittels Rastertunnelmikroskopie Zur Wasserstoffoxidation auf den Oberflächen Platin(111) und Rhodium(111) Investigation of Reaction Mechanisms on Surfaces with Scanning Tunneling Microscopy*. PhD thesis, FU Berlin, December 2001.

[225] C. Sachs, M. Hildebrand, S. Völkening, J. Wintterlin, and G. Ertl. Spatiotemporal Self-Organization in a Surface Reaction: From the Atomic to the Mesoscopic Scale. *Science*, 293(5535):1635–1638, 2001. doi:10.1126/science.1062883.

[226] C. Sachs, M. Hildebrand, S. Völkening, J. Wintterlin, and G. Ertl. Reaction fronts in the oxidation of hydrogen on Pt(111): Scanning tunneling microscopy experiments

and reaction-diffusion modeling. *The Journal of Chemical Physics*, 116(13):5759–5773, 2002. doi:10.1063/1.1453964.

[227] V. Yakhnin and M. Menzinger. Stationary and traveling hot spots in the catalytic combustion of hydrogen in monoliths. *Chemical Engineering Science*, 58(21):4559–4567, 2002. doi:10.1016/S0009-2509(02)00356-1.

[228] J. Wei. *Advances in catalysis*, 24:57, 1975. `http://www.sciencedirect.com/science/bookseries/03600564`.

[229] A. B. Mhadeshwar and D. G. Vlachos. Microkinetic Modeling for Water-Promoted CO Oxidation, Water-Gas Shift, and Preferential Oxidation of CO on Pt. *Journal of Physical Chemistry B*, 108(39):15246–15258, 2004. doi:10.1021/jp048698g.

[230] A.B. Mhadeshwar and D.G. Vlachos. Is the water-gas shift reaction on Pt simple? Computer-aided microkinetic model reduction, lumped rate expression, and rate-determining step. *Catalysis Today*, 105(1):162–172, 2005. doi:10.1016/j.cattod.2005.04.003.

[231] Scott G. Davis, Ameya V. Joshi, Hai Wang, and Fokion Egolfopoulos. An optimized kinetic model of H_2/CO combustion. *Proceedings of the Combustion Institute*, 30(1):1283–1292, 2005. doi:10.1016/j.proci.2004.08.252.

[232] Edward J. Bissett and Se H. Oh. PrOx reactor model for fuel cell feedstream processing. *Chemical Engineering Science*, 60(17):4722–4735, 2005. doi:10.1016/j.ces.2005.02.068.

[233] S. H. Oh and R. M. Sinkevitch. Carbon Monoxide Removal from Hydrogen-Rich Fuel Cell Feedstreams by Selective Catalytic Oxidation. *Journal of Catalysis*, 142(1):254–262, 1993. doi:10.1006/jcat.1993.1205.

[234] Olga Korotkikh and Robert Farrauto. Selective catalytic oxidation of CO in H_2: fuel cell applications. *Catalysis Today*, 62(2-3):249–254, 2000. doi:10.1016/S0920-5861(00)00426-0.

[235] Xinsheng Liu, Olga Korotkikh, and Robert Farrauto. Selective catalytic oxidation of CO in H_2: structural study of Fe oxide-promoted Pt/alumina catalyst. *Applied Catalysis A: General*, 226(1-2):293–303, 2002. doi:10.1016/S0926-860X(01)00915-2.

[236] T. V. Choudhary and D. W. Goodman. CO-free fuel processing for fuel cell applications. *Catalysis Today*, 77(1-2):65–78, 2002. doi:10.1016/S0920-5861(02)00233-X.

[237] Attila Wootsch, Claude Descormea, and Daniel Duprez. Preferential oxidation of carbon monoxide in the presence of hydrogen (PROX) over ceria-zirconia and alumina-supported Pt catalysts. *Journal of Catalysis*, 225(2):259–266, 2004. doi:10.1016/j.jcat.2004.04.017.

[238] Rajesh K. Ahluwalia, Qizhi Zhang, Donald J. Chmielewski, Kevin C. Lauzze, and Michael A. Inbody. Performance of CO preferential oxidation reactor with noble-metal catalyst coated on ceramic monolith for on-board fuel processing applications. *Catalysis Today*, 99(3-4):Pages 271–283, 2005. doi:10.1016/j.cattod.2004.10.015.

[239] Tugba Ince, Gökhan Uysal, A. Nilgün Akin, and Ramazan Yildirim. Selective low-temperature CO oxidation over Pt-Co-Ce/Al_2O_3 in hydrogen-rich streams. *Applied Catalysis A: General*, 292:171–176, 2005. doi:10.1016/j.apcata.2005.06.002.

[240] A. Jhalani and L.D. Schmidt. Preferential CO Oxidation in the Presence of H_2, H_2O and CO_2 at Short Contact-times. *Catalysis Letters*, 104(3-4):103–110, 2005. doi:10.1007/s10562-005-7937-9.

[241] Zhenping Qu, Mojie Cheng, Chuan Shi, and Xinhe Bao. Low-temperature selective oxidation of CO in H_2-rich gases over Ag/SiO_2 catalysts. *Journal of Molecular Catalysis A: Chemical*, 239(1-2):22–31, 2005. doi:10.1016/j.molcata.2005.05.033.

[242] Shuailin Zhou, Zhongshan Yuan, and Shudong Wang. Selective CO oxidation with real methanol reformate over monolithic Pt group catalysts: PEMFC applications. *International Journal of Hydrogen Energy*, 31(7):924–933, 2006. doi:10.1016/j.ijhydene.2005.07.014.

[243] Paul Chin, Xiaolei Sun, George W. Roberts, and James J. Spivey. Preferential oxidation of carbon monoxide with iron-promoted platinum catalysts supported on metal foams. *Applied Catalysis A: General*, 302(1):22–31, 2006. doi:10.1016/j.apcata.2005.11.030.

[244] Shuailin Zhou, Zhongshan Yuan, and Shudong Wang. Selective CO oxidation with real methanol reformate over monolithic Pt group catalysts: PEMFC applications. *International Journal of Hydrogen Energy*, in press:in press, 2005. doi:10.1016/j.ijhydene.2005.07.014.

[245] Akkarat Manasilp and Erdogan Gulari. Selective CO oxidation over Pt/alumina catalysts for fuel cell applications. *Applied Catalysis B: Environmental*, 37(1):17–25, 2002. doi:10.1016/S0926-3373(01)00319-8.

[246] George W. Roberts, Paul Chin, Xiaolei Sun, and James J. Spivey. Preferential oxidation of carbon monoxide with Pt/Fe monolithic catalysts: interactions between external transport and the reverse water-gas-shift reaction. *Applied Catalysis B: Environmental*, 46(3):601–611, 2003. doi:10.1016/j.apcatb.2003.07.002.

[247] Masashi Kotobuki, Akiko Watanabe, Hiroyuki Uchida, Hisao Yamashita, and Masahiro Watanabe. Reaction mechanism of preferential oxidation of carbon monoxide on Pt, Fe, and Pt-Fe/mordenite catalysts. *Journal of Catalysis*, 236(2):262–269, 2006. doi:10.1016/j.jcat.2005.09.026.

[248] Grigorios C. Koltsakis and Anastasios M. Stamatelos. Modeling dynamic phenomena in 3-way catalytic converters. *Chemical Engineering Science*, 54(20):4567–4578, 1999. doi:10.1016/S0009-2509(99)00130-X.

[249] Urs Dogwiler, Peter Benz, and John Mantzaras. Two-Dimensional Modelling for Catalytically Stabilized Combustion of a Lean Methane-Air Mixture With Elementary Homogeneous and Heterogeneous Chemical Reactions. *Combustion and Flame*, 116:243–258, 1999.

[250] O. Deutschmann, L. I. Maier, U. Riedel, A. H. Stroemman, and R. W. Dibble. Hydrogen assisted catalytic combustion of methane on platinum. *Catalysis Today*, 59(1-2):141–151, 2000. doi:10.1016/S0920-5861(00)00279-0.

[251] M. Rinnemo, O. Deutschmann, F. Behrendt, and B. Kasemo. Experimental and numerical investigation of the catalytic ignition of mixtures of hydrogen and oxygen on platinum. *Combustion and Flame*, 111(4):312–326, 1997. doi:10.1016/S0010-2180(97)00002-3.

[252] Olaf Deutschmann. *Interactions between transport and chemistry in catalytic reactors*. Fakultät für Chemie der Ruprecht-Karls-Universität Heidelberg, 2001. Habilitationsschrift.

[253] A. B. Mhadeshwar, H. Wang, and D. G. Vlachos. Thermodynamic Consistency in Microkinetic Development of Surface Reaction Mechanisms. *J. Phys. Chem. B*, 107(46):12721–12733, 2003. doi:10.1021/jp034954y.

[254] Rui Hu, Shiping Huang, Zhiping Liu, and Wenchuan Wang. Water formation on Pt(1 1 1) surfaces at high temperatures studied by kinetic Monte Carlo simulations. *Applied Surface Science*, 242(3-4):353–361, 2005. doi:10.1016/j.apsusc.2004.08.038.

[255] D. M. Collins and W. E. Spicer. The adsorption of CO, O_2, and H_2 on Pt - II. Ultraviolet photoelectron spectroscopy studies. *Surface Science*, 69(1):114–132, 1977. doi:10.1016/0039-6028(77)90164-9.

[256] M A Barteau, E I Ko, and R J Madix. The Adsorption of CO, O_2, and H_2 on Pt(100)-(5 x 20). *Surface Science*, 102(1):99–117, 1981. doi:10.1016/0039-6028(81)90310-1.

[257] J. R. Stetter and Keith F. Blurton. Catalytic Oxidation of CO and H_2 Mixtures in Air. *Ind. Eng. Chem. Prod. Res. Dev.*, 19(2):214–215, 1980. doi:10.1021/i360074a016.

[258] N. D. Hoyle, P. Kumarasamy, V. A. Self, P. A. Sermon, and M. S. W. Vong. Catalysis of H_2, CO and alkane oxidation-combustion over Pt/Silica catalysts: evidence of coupling and promotion. *Catalysis Today*, 47(1-4):45–49, 1999. doi:10.1016/S0168-1923(98)00108-7.

[259] Vaniah H. Baldwin, Jr. and John B. Hudson. Coadsorption of Hydrogen and Carbon Monoxide on (111) Platinum. *Journal of Vacuum Science and Technology*, 8:49–52, 1971. doi:10.1116/1.1316351.

[260] David W. Dabill, Stephen J. Gentry, H. Bryan Holland, and Alan Jones. The oxidation of hydrogen and carbon monoxide mixtures over platinum. *Journal of Catalysis*, 53(1):164–167, 1978. doi:10.1016/0021-9517(78)90016-7.

[261] B. Atalik and D. Uner. Structure sensitivity of selective CO oxidation over Pt/γ-Al_2O_3. *Journal of Catalysis*, 241(2):268–275, 2006. doi:10.1016/j.jcat.2006.04.029.

[262] W. Hauptmann, A. Drochner, H. Vogel, M. Votsmeier, and J. Gieshoff. Global kinetic models for the oxidation of NO on platinum under 4 lean conditions. *Topics in Catalysis*, 42-43(1-4):157–160, 2007. doi:10.1007/s11244-007-0170-6.

[263] S. Malmberg, M. Votsmeier, J. Gieshoff, N. Söger, L. Mußmann, A. Schuler, and A. Drochner. Dynamic phenomena of scr-catalysts containing fe-exchanged zeolites - experiments and computer simulations. *Topics in Catalysis*, 42-43:33–36, 2007. doi:10.1007/s11244-007-0146-6.

[264] R. Litto, R.E. Hayes, and B. Liu. Capturing fugitive methane emissions from natural gas compressor buildings. *Journal of Environmental Management*, 84(3):347–361, 2007.

[265] J.F. Knoth, A. Drochner, H. Vogel, J. Gieshoff, M. Kögel, M. Pfeifer, and M. Votsmeier. Transport and reaction in catalytic wall-flow filters. *Catalysis Today*, 105(3-4):598–604, 2005. doi:10.1016/j.cattod.2005.06.050.

[266] Martin Votsmeier, Jürgen Gieshoff, Markus Kögel, Markus Pfeifer, Jens Felix Knoth, Alfons Drochner, and Herbert Vogel. Wall-flow filters with wall-integrated oxidation catalyst: A simulation study. *Applied Catalysis B: Environmental*, 70(1-4):233–240, 2007. doi:10.1016/j.apcatb.2005.12.032.

[267] Frank P. Incropera and David P. DeWitt. *Introduction to Heat Transfer*. John Wiley and Sons, 3 edition, 1996.

[268] Christie J. Geankoplis. *Transport Processes and Unit Operations*. Prentice Hall PTR, 3rd edition, 1993. ISBN 0-13-930439-8.

[269] E. N. Fuller, P. D. Schettler, and J. C. Giddings. A New Method for the Prediction of Gas Phase Diffusion Coefficients. *Ind. Eng. Chem.*, 58(5):18–27, 1966. doi:10.1021/ie50677a007.

[270] http://webbook.nist.gov/. internet, May 2005. `http://webbook.nist.gov/`.

[271] Samy L. Mukadi. Summary of Elementary Mechanisms. ckfluid@yahoo.ca CK-FLUID.INC. 8232-128 Avenue, Edmonton, Alberta T5E 0E6, Canada, June 2003.

[272] M. A. Khan and Khwaja Yaldram. Role of sticking coefficients in catalytic reactions on a surface. *Surface Science*, 219(3):445–452, 1989. doi:10.1016/0039-6028(89)90520-7.

[273] Abdennour Bourane and Daniel Bianchi. Oxidation of CO on a Pt/Al_2O_3 Catalyst: From the Surface Elementary Steps to Light-Off Tests IV. Kinetic study of the reduction by CO of strongly adsorbed oxygen species. *Journal of Catalysis*, 220(1):3–12, 2003. doi:10.1016/S0021-9517(03)00267-7.

[274] R. Kissel-Osterrieder, F. Behrendt, and J. Warnatz. Dynamic Monte Carlo simulations of catalytic surface reactions. *Proceedings of the Combustion Institute*, 28(1):1323–1330, 2000. `http://www.iwr.uni-heidelberg.de/sfb359/PP/Preprint2000-27.ps.gz`.

[275] S. H. Kim, J. Méndez, J. Wintterlin, and G. Ertl. Enhanced reactivity of adsorbed oxygen on Pd(111) induced by compression of the oxygen layer. *Physical Review B*, 72:155414, 2005. doi:10.1103/PhysRevB.72.155414.

[276] M.W. Chase Jr. *NIST-JANAF Themochemical Tables, J. Phys. Chem. Ref. Data, Monograph 9*, volume J. Phys. Chem. Ref. Data, Monograph 9. Fourth edition edition, 1998.